Millimeter-Wave Detector Systems and Applications in the Study of Quiescent Galaxy Evolution

by

Jeremy Meinke

A Dissertation Presented in Partial Fulfillment
of the Requirements for the Degree
Doctor of Philosophy

Approved April 2023 by the
Graduate Supervisory Committee:

Philip Mauskopf, Chair
Ricardo Alarcon
Evan Scannapieco
Georgios Trichopoulos

ARIZONA STATE UNIVERSITY

May 2023

ABSTRACT

Millimeter astronomy unlocks a window to the earliest produced light in the universe, called the Cosmic Microwave Background (CMB). Through analysis of the CMB, overarching features about the universe's evolution and structure can be better understood. Modern millimeter-wave instruments are constantly seeking improvements to sensitivity in the effort to further constrain small CMB anisotropies in both temperature and polarization. As a result, detailed investigations into lesser-known processes of the universe are now becoming possible.

Here I present work on the millimeter-wavelength analysis of $z \approx 1$ quiescent galaxy samples, whose conspicuous quenching of star formation is likely the result of active galactic nuclei (AGN) accretion onto supermassive black holes. Such AGN feedback would heat up a galaxy's surrounding circumgalactic medium (CGM). Obscured by signal from cold dust, I isolate the thermal Sunyaev-Zel'dovich effect, a CMB temperature anisotropy produced by hot ionized gas, to measure the CGM's average thermal energy and differentiate between AGN accretion models. I find a median thermal energy that best corresponds with moderate to high levels of AGN feedback. In addition, the radial profile of cold dust associated with the galaxy samples appears to be consistent with large-scale clustering of the universe.

In the endeavor of increasingly efficient millimeter-wave detectors, I also describe the design process for novel multichroic dual-polarization antennas. Paired with extended hemispherical lenslets, simulations of these superconducting antennas show the potential to match or exceed performance compared to similar designs already in use. A prototype detector array, with dual-bowtie and hybrid trapezoidal antennas coupled to microwave kinetic inductance detectors (MKIDs) has been made and is under preparation to be tested in the near future.

Finally, I also present my contributions to the cryogenic readout design of the Ali CMB Polarization Telescope (AliCPT), a large-scale CMB telescope geared towards searching the Northern Hemisphere sky for a unique 'B-mode' polarization expected to be produced by primordial gravitational waves. Cryogenic readout is responsible for successful interfacing between room temperature electronics and sensitive detectors operating on AliCPT's sub-Kelvin temperature focal plane. The development of millimeter-wave instruments and future endeavors show great potential for the overall scientific community.

ACKNOWLEDGMENTS

I would like to begin by reflecting upon the past nearly six years from when I first arrived at Arizona State. I have learned a lot from the great classes and faculty here at ASU and in the department of physics. To my primary advisor, Phil Mauskopf, thank you for welcoming me into your lab group even though I had little initial experience in the field. Your enthusiasm and support as I became evermore immersed in the realm of millimeter astronomy was invaluable. Especially when you nudged me forward the time I showed interest in the SZ science meetings, which gradually evolved into my primary project and two papers that I am very proud of.

Of course, I have to also thank my secondary advisor, Evan Scannapieco. His guidance and alternate point of view helped keep me focused these final years of my studies. In addition, a huge thank you is required for Seth Cohen and the rest of the SZ science group. Seth's positivity and encouragement is contagious, and I always looked forward to those meetings. I will forever now view our weekly SZ science meetings as the pinnacle of meeting standards. I also would like to thank the rest of my committee, Ricardo Alacron and Georgios Trichopoulos, for being the best supportive graduate committee I could have asked for. I appreciate the various support from collaborators outside of ASU as well, such as Brad Johnson, Maria Salatino, and many others.

In addition, a huge thank you is required to everyone past and present of the lab, especially the help I've received in the final few years of my research. I'm well aware of my naturally quiet disposition, but I always felt comfortable and welcomed in that sunless basement habitat.

I also have to thank the support of my family throughout this entire process, especially my parents, sister and brother in-law, that helped make everything easier.

Last but not least, thank you to all of my teachers, from kindergarten through grad school, who saw potential in that one quiet kid near the back of the classroom.

This research was aided by the use of High Performance Computing (HPC) *Agave* Research Computing at Arizona State University.

"you are an aperture through which the universe looks at itself"

- Alan Watts

TABLE OF CONTENTS

CHAPTER Page

CHAPTER Page

CHAPTER Page

LIST OF TABLES

LIST OF FIGURES

Figure Page

Figure Page

Chapter 1

INTRODUCTION

Journeying throughout the universe in all directions is a primordial and noticeably unique distribution of light. Originating from a location commonly known as the surface of last scattering, this light was released from when the early universe became transparent after the formation of neutral hydrogen. With much fewer free electrons, light had reduced scattering and began to decouple from baryonic matter. Such an event occurred throughout the universe at roughly the same redshift and temperature to produce the near-uniform, well-characterized, blackbody spectrum of the Cosmic Microwave Background (CMB) known today. Modern millimeter astronomy seeks to examine the small perturbations within the CMB spectrum which reveal important details about the evolution and structure of our universe. In order to further such investigations, continuous advancements are needed in instrumentation. The next evolution of CMB instruments could thus benefit from novel design solutions.

1.1 The Standard Model

The current standard model of cosmology is the Lambda Cold Dark Matter (ΛCDM) version of the FLRW (Friedmann-Lamaître-Robertson-Walker), which sets the age of the universe at roughly 13.8 billion years old. This is simple yet well-matching to observations, producing Friedmann equation solutions as

$$\left(\frac{\dot{a}}{a}\right)^2 = H^2 = \frac{8\pi G\rho}{3} - \frac{kc^2}{a^2} + \frac{\Lambda c^2}{3}, \tag{1.1}$$

where $a = (1+z)^{-1}$ is the dimensionless scale factor related to redshift z, G is the gravitational constant, ρ is the mean relativistic mass density, c is the speed of light, k

is the curvature of the universe, and Λ is the cosmological constant. In a flat ($k = 0$) universe the present-day mean or critical density becomes

$$\rho_0 = \frac{3H_0^2}{8\pi G}, \tag{1.2}$$

where H_0 is the Hubble constant. A set of normalized density parameters Ω are thus defined as the ratio with respect to ρ_0, producing (Maoz, 2016; Condon and Matthews, 2018)

$$\left(\frac{H}{H_0}\right)^2 = \frac{\rho}{\rho_0} = \frac{\Omega_m}{a^3} + \Omega_\Lambda + \frac{\Omega_r}{a^4}, \tag{1.3}$$

where Ω_0, Ω_Λ, and Ω_r are the total matter, vacuum, and radiation densities, respectively, in units of the critical density. Throughout this dissertation, parameters within the limits found by Planck Collaboration et al. (2016c, 2020b) are adopted as $H_0 = 68$ [km s^{-1} Mpc^{-1}], $\Omega_m = 0.31$, $\Omega_\Lambda = 0.69$, and a baryonic density of $\Omega_b = 0.049$ (a sub-component of matter density). The radiation term Ω_r only dominates at high redshifts ($z > 3500$) and so is considered negligible for most observational studies (Condon and Matthews, 2018).

1.2 Cosmic Microwave Background

A few minutes after it began, the universe was already substantially cooled while remaining in thermal equilibrium. This cooling resulted from inflation of the very early universe and its continued expansion. Annihilation between matter and antimatter produced photons that dominated the energy of the early universe while keeping the remaining baryonic matter in thermal equilibrium via scattering. After annihilation, stable light nuclei formed between protons and neutrons in a period referred to as primordial nucleosynthesis (Pathria and Beale, 2011). As the neutron fraction (neutrons per baryon, $q = \mathrm{N}_n/\mathrm{N}_B = n_n/n_B \approx 0.12$) at this time reflects, a

substantial portion of the protons remained free. This effect would become key as the photon-baryon plasma continued to cool in thermal equilibrium.

At $\sim 380,000$ years or $< 0.003\%$ of its present age, the universe reached another important event called recombination. After nucleosynthesis, plenty of both free protons and electrons were available to begin forming neutral hydrogen. However, the high temperature and density of photons prevented them from becoming stable until the surrounding plasma further cooled. This is shown to have happened at $\mathrm{T} \approx 3000\mathrm{K}$, following the Saha equation for the neutral hydrogen fraction,

$$f_{\mathrm{H}} = \frac{n_{\mathrm{H}}}{n_p + n_{\mathrm{H}}} = (1 - f_{\mathrm{H}})^2 s, \tag{1.4}$$

with hydrogen and proton number density, n_{H} and n_p, respectively. Where solving for the neutral hydrogen fraction f_{H} yields

$$f_{\mathrm{H}} = \frac{1 + 2s - \sqrt{1 + 4s}}{2s}, \tag{1.5}$$

with parameter s,

$$s = 4\zeta(3)\sqrt{\frac{2}{\pi}}(1 - 2q)\eta \left(\frac{k_B \mathrm{T}}{m_e c^2}\right)^{3/2} \exp\left(\frac{\mathrm{Ry}}{k_B \mathrm{T}}\right), \tag{1.6}$$

for a baryon-to-photon ratio of $\eta = 6 \times 10^{-10}$, Boltzmann constant $k_{\mathrm{B}} = 1.381$ [kg m^2 s^{-2} K^{-1}], and electron mass $m_e = 9.109 \times 10^{-31}$ [kg]. At which point a high neutral hydrogen fraction, $f_{\mathrm{H}} > 99\%$, indicates when nearly all free protons and electrons were combined (Pathria and Beale, 2011). With few free electrons available for scattering, the universe became transparent and the photons traveled unimpeded. Thus, this is often also referred to as the surface of last scattering, with the resulting photons being called the Cosmic Microwave Background (CMB).

As the CMB photons were in thermal equilibrium with their surroundings up to recombination, they are well described by the Planck black-body distribution using

Bose-Einstein statistics,

$$B(\nu, \mathrm{T}) = \frac{2h\nu^3}{c^2} \frac{1}{e^{h\nu/k_B\mathrm{T}} - 1}, \tag{1.7}$$

expressed here in terms of power per unit area per steradian per unit frequency at frequency ν, where $h = 6.626$ [kg m^2 s^{-1}] is the Planck constant and $c = 2.998$ [m s^{-1}] is the speed of light in vacuum. The CMB is extremely well-characterized by the Planck distribution of eq. (1.7) with a present temperature of $\mathrm{T_{CMB}} = 2.725$K (Fixsen, 2009).

Meanwhile the number density for a blackbody distribution of photons is

$$n_\gamma(\mathrm{T}) = \frac{8\pi}{c^3} \int_0^\infty \frac{\nu^2}{\exp\big(h\nu/k_\mathrm{B}\mathrm{T}\big) - 1} \, \mathrm{d}\nu = 16\pi\zeta(3) \left(\frac{k_\mathrm{B}\mathrm{T}}{hc}\right)^3, \tag{1.8}$$

with ζ being the Reimann-Zeta function. For CMB photons, this yields a present-day density of $n_{\gamma,\mathrm{CMB}} \approx 4.1 \times 10^8$ per cubic meter [m^{-3}]. This is orders of magnitudes larger than the average stellar photon density, though CMB photons only contribute a small fraction to the total energy density in today's universe (Maoz, 2016).

1.2.1 Anisotropies

While the primary CMB is extremely well-fit to the Planck distribution, it still contains smaller directional dependent fluctuations. The CMB temperature dipole term was the first of such to be observed and is attributed to the Doppler shift relative to the observer's velocity with respect to the CMB. From this dipole term the motion of the earth, our solar system, and the local galaxy group relative to the CMB rest frame can be determined (Planck Collaboration et al., 2020a).

Smaller-scale temperature anisotropies also occur, as shown in Fig. 1.1 from the *Planck* satellite, at a level of $\mathcal{O}(10^{-5})$ (Lewis and Challinor, 2006). Primary anisotropies originating at the surface of last scattering are driven by acoustic oscillations and diffusion (Silk) damping (Hu and Dodelson, 2002; Silk, 1968). Gravitational

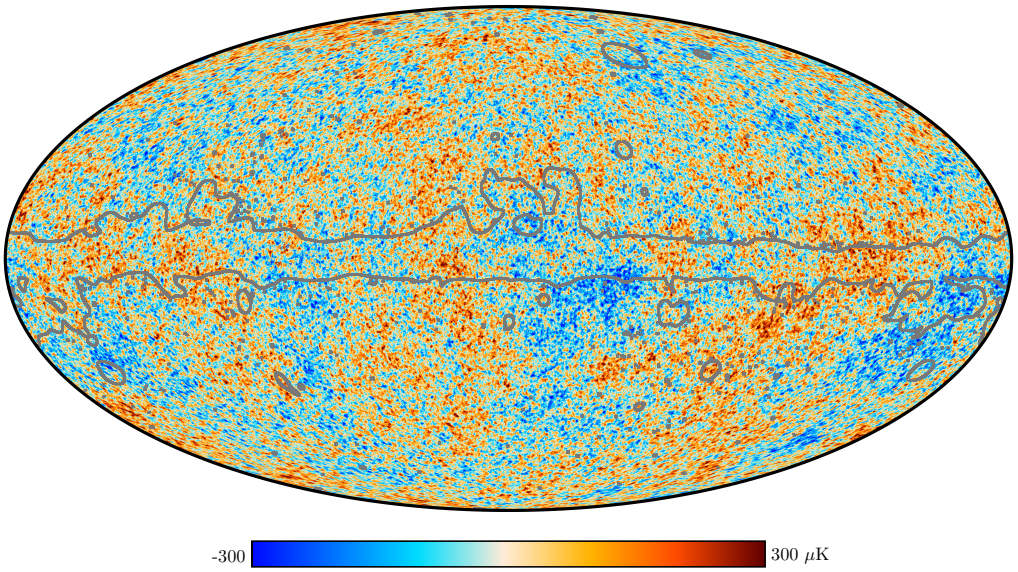

Figure 1.1: Cosmic Microwave Background temperature map from Planck Collaboration et al. (2020a), with the primary monopole and dipole terms removed. The faint gray outline corresponds to where residuals of foreground emissions (most notably along the galactic plane) are expected to be significant.

redshifting via the Sachs-Wolfe effect also produces anisotropies both at the surface of last scattering and afterwards as a result of perturbations in the gravitational potential (Sachs and Wolfe, 1967).

As the CMB is found in all directions, it is often convenient to describe it in terms of spherical harmonics on the sky,

$$T(\theta, \phi) = \sum_{\ell,m} a_{\ell,m} Y_{\ell,m}(\theta, \phi) \tag{1.9}$$

where $Y_{\ell,m}$ are the mutually orthogonal spherical harmonic terms upon the surface of a sphere, and $a_{\ell,m}$ are the spherical harmonic coefficients. Hence the CMB monopole term $Y_{0,0}(\theta, \phi) = 1$ has a coefficient corresponding to the average CMB blackbody temperature $a_{0,0} = \mathrm{T_{CMB}} = 2.725\mathrm{K}$. Higher-order anisotropies are broken into variance with respect to multipole ℓ,

$$C_\ell = \langle a^*_{\ell,m} a_{\ell,m} \rangle = \frac{1}{2\ell + 1} \sum_{m=-\ell}^{\ell} a^*_{\ell,m} a_{\ell,m}, \tag{1.10}$$

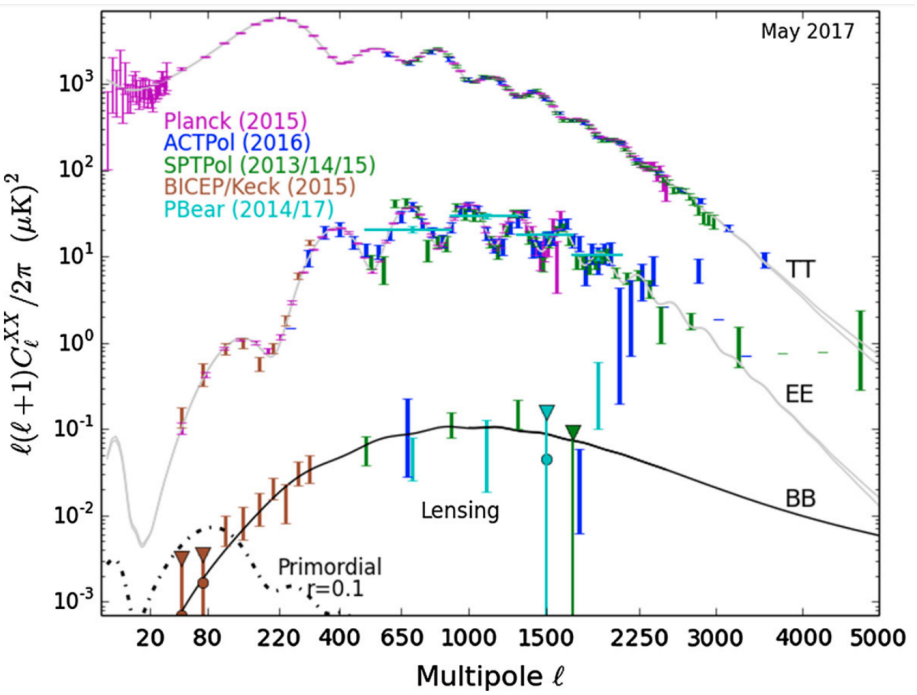

Figure 1.2: Power spectrum of the CMB from (Hubmayr et al., 2018). TT, EE, and BB correspond to the cross-correlation power spectrum of the temperature, E-mode, and B-mode polarization components of the CMB, respectively.

while the CMB angular power spectrum is often discussed in scale invariant terms of $D_\ell = \ell(\ell+1)C_\ell/2\pi$. The uppermost plotted line in Fig. 1.2 (Hubmayr et al., 2018) shows the temperature cross-correlation power spectrum (denoted as C_ℓ^{TT}) alongside polarization components discussed further below. These anisotropies found in the CMB angular power spectrum help constrain various cosmological parameters to further understand our universe.

1.2.2 Sunyaev-Zel'dovich Effect

One highly studied anisotropy occurs when CMB photons pass through hot ionized gas. Via inverse-Compton scattering, these photons are scattered to higher energies, causing a shift in their spectrum. This was first shown by Sunyaev and Zel'dovich (Sunyaev and Zeldovich, 1972). A redshift-independent thermal Sunyaev-Zel'dovich

(tSZ) for non-relativistic scattering shifts the CMB spectrum as,

$$\frac{\Delta T_{\rm tSZ}}{T_{\rm CMB}} = y\left(x\frac{\exp(x)+1}{\exp(x)-1}-4\right), \tag{1.11}$$

with the dimensionless Compton-y parameter defined as

$$y \equiv \int dl\, \sigma_T \frac{n_e k_{\rm B}\left(T_e - T_{\rm CMB}\right)}{m_e c^2}, \tag{1.12}$$

where σ_T is the Thomson cross section, n_e is the electron number density, and T_e is the electron temperature. The integral is performed over the line-of-sight distance l, and the dimensionless frequency x is given by $x \equiv h\nu/k_B T_{\rm CMB} = \nu/56.81\,{\rm GHz}$. The first definitive detection of the tSZ was presented by Birkinshaw et al. (1984) in three large galaxy clusters.

There is also a fainter kinetic Sunyaev-Zel'dovich (kSZ) that arises from a bulk motion of the ionized gas relative to CMB rest frame along our line of sight:

$$\frac{\Delta T_{\rm kSZ}}{T_{\rm CMB}} = -\tau\frac{v_p}{c}, \tag{1.13}$$

where τ is the optical depth and v_p is the peculiar velocity of the gas relative to the CMB. This kSZ effect was first confirmed via observations in 2012 (Hand et al., 2012; Mroczkowski et al., 2012).

Both the tSZ and kSZ are commonly used for identifying and further analyzing large structures where gas is most readily found, such as galaxies and galaxy clusters (e.g. Mauskopf et al., 2000; Reichardt et al., 2013; Bleem et al., 2015; Soergel et al., 2016; Spacek et al., 2016; Schaan et al., 2021; Meinke et al., 2021, etc.).

1.2.3 Polarization

Alongside the temperature components already stated, the CMB also has important polarization characteristics, with CMB photons polarized at a level of $\mathcal{O}(10^{-6})$ as

a result of Thomson scattering at recombination. A common polarization metric, the Stokes parameters are not rotationally invariant on the celestial sphere (Kamionkowski et al., 1997). Thus, a consistent standard was established with two polarization terms called E- and B- modes, named as such from gradient and curl properties like the electric and magnetic field, respectively (also referred to as 'G-' and 'C-' modes). Polarization at last scattering can occur from quadrupolar temperature perturbations (Kosowsky, 1996; Kamionkowski et al., 1997; Hu and White, 1997). A scalar perturbation produces solely E-mode polarization, which is expected to dominate. Gravitational waves could also produce tensor perturbations near last scattering, enabling faint B-mode polarization (Kamionkowski et al., 1997; Hu and White, 1997).

The observed cross-correlation angular power spectrum for E- and B- mode polarizations are shown in Fig. 1.2. E-mode polarization was first detected at the start of this millennium (Kovac et al., 2002). Meanwhile the B-mode is noticeably fainter, up to nearly three orders of magnitude less than that of the E-mode, and is obscured by secondary sources such as gravitational lensing (Hanson et al., 2013). As a result, the primary B-mode polarization from primordial gravitational waves has yet to be experimentally shown, likely due to both the detection sensitivity required and foreground contamination. BICEP2 originally postulated detection of B-modes from gravitational waves (Ade et al., 2014), but later results instead pointed to contaminant foreground dust as the source of origin (BICEP2/Keck Collaboration et al., 2015).

Polarization anisotropies in the CMB also exist from various origins, much like the aforementioned temperature fluctuations. One notable example is a polarized Sunyaev-Zel'dovich (pSZ) effect, created from a remote CMB temperature quadrupole relative to the electron gas where the scattering occurs. The largest pSZ terms are expected to be $\propto \tau$ and $\propto \tau^2$, though at orders of magnitude comparable to or

lower than that of primordial B-modes and thus challenging for detection due to contamination from other sources (Sazonov and Sunyaev, 1999; Carlstrom et al., 2002; Mroczkowski et al., 2019; Hotinli et al., 2022).

1.2.4 Lensing

Gravitational lensing also affects both the CMB temperature and polarization components, as CMB photons can be deflected by gravitational wells. The first reported observation of CMB gravitational lensing was in 2011 with the initial ACT (Atacama Cosmology Telescope) temperature maps (Das et al., 2011). E-modes, the most prominent polarization mode, can be partly converted into B-modes when lensed (Lewis and Challinor, 2006). This property also contributes to and can overwhelm B-modes produced via gravitational waves. Lensing is noticeable in the B-mode power spectrum as in Fig. 1.2, especially at higher ℓ multipoles.

1.3 Circumgalactic Medium

The evolution of a galaxy is heavily dictated and reflected by the properties of its circumgalactic medium (CGM), especially as only roughly 10% of a galaxy's baryonic matter is associated with stars (Walter et al., 2020). The CGM encompasses all the diffuse gas and processes that reside outside of a galaxy's interstellar medium (ISM) but within its virial radius and surrounding intergalactic medium (IGM)(Tumlinson et al., 2017). The standard view of galaxy evolution requires the accretion of IGM gas onto galactic halos, where it contributes to the ISM and star formation (White and Rees, 1978). Meanwhile opposing processes like stellar feedback from supernovae (Ceverino and Klypin, 2009) and outflows from the central supermassive black hole, cycle material and energy back into the surrounding CGM. A concise visualization of these processes are shown in Fig. 1.3 from Tumlinson et al. (2017).

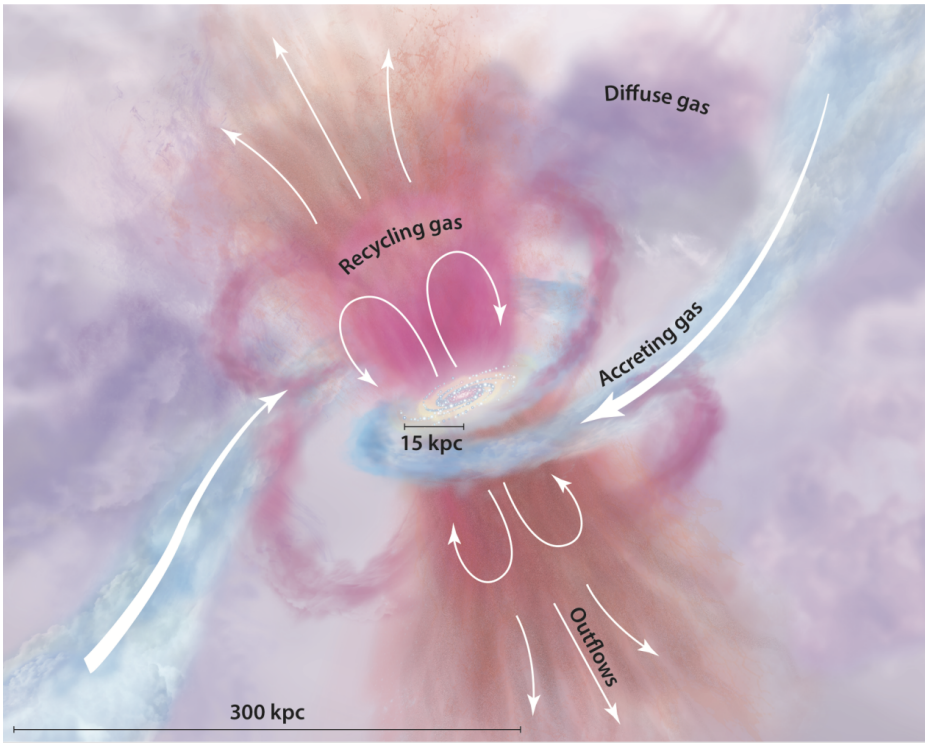

Figure 1.3: An artistic depiction of CGM processes around a galaxy, from Tumlinson et al. (2017). Outflowing and recycled gas are shown as orange and pink. Inflowing material from the IGM is shown as blue, accreting onto the galaxy center and disk. Purple shows resultant diffuse gas of the CGM likely produced through a mixing of all such sources.

The faint diffuse nature of the CGM makes it a challenging feature to observe. Many different methods are utilized to analyze the CGM. Transverse absorption line studies using bright background sources, often quasars, are one of the more common methods to constrain gas composition, temperature, and density in the CGM Savage et al. (2014); Werk et al. (2014); Borthakur et al. (2015); Werk et al. (2016). Stacking of spectra for multiple targets also enables absorption line analysis. Other methods include emission line mapping, spectroscopy absorption via the galaxy's starlight, and a variety of hydrodynamical simulations (Tumlinson et al., 2017).

1.3.1 Thermal Energy via the tSZ Effect

In a separate realm of measurements, the CGM can also be studied through the tSZ effect described in Section 1.2.2 and eqs. (1.11) & (1.12). The tSZ effect is created as CMB photons pass through and inverse-Compton scatter off hot, ionized gas (Sunyaev and Zeldovich, 1972). The resulting CMB anisotropy has a distinctive frequency dependence, which causes a deficit of photons below and an excess above $\nu_{\rm null} = 217.6$ GHz, ideal for studies with millimeter-wave data.

Ionized gas is most readily found in the ISM and CGM of galaxies (and galaxy clusters). As the Compton-y parameter is proportional to both n_e and T_e, it provides a measure of the total pressure along the line-of-sight. Therefore by integrating the tSZ signal over a patch of sky (solid angle $\mathrm{d}\boldsymbol{\theta}$), the volume integral of the pressure can be obtained, and from it the total thermal energy $E_{\rm th}$ in the CGM associated with a source (e.g. Scannapieco et al., 2008; Mroczkowski et al., 2019). Taking eq. (1.12), the integral as in (Spacek et al., 2016) becomes

$$\int y(\boldsymbol{\theta})\,\mathrm{d}\boldsymbol{\theta} = \iint \frac{\sigma_T n_e k_B T_e}{m_e c^2}\,\mathrm{d}l\,\mathrm{d}\boldsymbol{\theta} = \frac{\sigma_T}{m_e c^2 D_{\rm a}^2}\int n_e k_B T_e\,\mathrm{d}V\,, \tag{1.14}$$

where $D_{\rm a}$ is the (redshift dependent) angular diameter distance of the source, V is volume defined by the solid angle and line-of-sight, and the gas is assumed to be hot $T_e \gg \mathrm{T_{CMB}}$. The integral thus is transformed into an electron pressure ($P_e = n_e k_B T_e$) within a volume. This can be related to total thermal energy for a fully ionized gas consisting of hydrogen and helium (Spacek et al., 2016; Pandey et al., 2019),

$$E_{\rm th} = \frac{3}{2}\left(\frac{2+A}{1+A}\right)\int n_e k_B T_e\,\mathrm{d}V = \frac{3}{2}\left(\frac{8-5Y}{4-2Y}\right)\int n_e k_B T_e\,\mathrm{d}V \simeq 2.9\int n_e k_B T_e\,\mathrm{d}V\,, \tag{1.15}$$

which may be solved using either the cosmological number abundance of helium $A = 0.08$, or primordial mass fraction of helium $Y = 0.24$. Combining eqs. (1.14) & (1.15)

yields a thermal energy from the integrated Compton-y as,

$$E_{\rm th} = 2.9 \frac{m_e c^2 D_{\rm a}^2}{\sigma_T} \int y(\boldsymbol{\theta})\, \mathrm{d}\boldsymbol{\theta} = 2.9 \times 10^{60} \mathrm{erg} \left(\frac{D_{\rm a}}{\mathrm{Gpc}} \right)^2 \frac{\int y(\boldsymbol{\theta})\, \mathrm{d}\boldsymbol{\theta}}{10^{-6}\ \mathrm{arcmin}^2}. \tag{1.16}$$

As a result, eq. (1.16) relates a measured tSZ signal around a target galaxy to the thermal energy of its surrounding CGM. This method provides a useful tool when certain processes are expected to significantly affect CGM energy.

1.3.2 Galaxy Quenching and Active Galactic Nuclei Feedback

Much is still unknown about the evolution of our universe's most massive galaxies and the processes that shaped them. These elliptical galaxies consist of a central massive black hole, surrounded by a bulge of old, red stars. An additional mechanism is needed to explain the lack of young stars in these galaxies (Silk and Rees, 1998; Somerville and Davé, 2015). The prevailing consensus reached is that star formation is quenched by feedback on the surrounding environment by active galactic nuclei (AGN) (Granato et al., 2004; Scannapieco and Oh, 2004; Croton et al., 2006; Bower et al., 2006). Observations of galaxy stellar mass are well explained by AGN feedback, showing a 'downsizing' or drop in star formation rate for progressively lower masses with decreasing redshift (Cowie et al., 1996; Treu et al., 2005; Drory and Alvarez, 2008). This is contrary to hierarchical models of galaxy formation with no feedback present (Rees and Ostriker, 1977; White and Frenk, 1991).

Yet, many aspects of AGN feedback remain uncertain, with two commonly proposed feedback models. In 'quasar mode' feedback, the CGM surrounding the galaxy is impacted by a powerful outburst when the supermassive black hole is accreting most rapidly. In this case, the CGM is heated such that the gas cooling time is much longer than the Hubble time, suppressing further star formation until today. These models are supported by observations of high-velocity flows of ionized gas associated

with the black holes accreting near the Eddington rate (Harrison et al., 2014; Greene et al., 2014; Lansbury et al., 2018; Miller et al., 2020). Unfortunately, uncertainty arises in the mass and energy flux from such quasars due to uncertain estimates of the outflowing material's distance from the central source (Wampler et al., 1995; de Kool et al., 2001; Chartas et al., 2007; Feruglio et al., 2010; Dunn et al., 2010; Veilleux et al., 2013; Chamberlain et al., 2015).

Second, in 'radio mode' feedback, cooling material is more gradually prevented from forming stars by jets of relativistic particles that arise during periods of lower accretion rates. Here, the CGM is maintained at a roughly constant temperature and entropy, as low levels of gas cooling are continually balanced by energy input from the relativistic jets. Such models are supported by AGN observations of lower power jets of relativistic plasma (Fabian, 2012). These couple efficiently to the volume-filling hot atmospheres of galaxies clusters (McNamara et al., 2000; Churazov et al., 2001; McNamara et al., 2016), but may or may not be significant for balancing cooling in less massive gravitational potentials (Werner et al., 2019).

A promising method for distinguishing between these feedback models is by inspecting the energy held within the CGM. Outlined in Section 1.3.1, the tSZ effect is produced from interactions between CMB photons and hot ionized gas of the CGM. Therefore, thermal energy of the CGM can be determined from the tSZ effect according to eq. (1.16).

The overall level of feedback is tied to the CGM's observed thermal energy. However, this is likely a combination of various mechanisms. To estimate the contribution due to gravitational heating, it can be assumed that the gas collapses and virializes along with an encompassing spherical dark matter halo, and is heated to the virial temperature $T_{\rm vir}$. This gives

$$E_{\rm th,halo}(M_{13}, z) = 1.5 \times 10^{60}\ {\rm erg}\ M_{13}^{5/3}\ (1+z), \tag{1.17}$$

where M_{13} is the mass of the halo in units of $10^{13}\mathrm{M}_{\odot}$ (Spacek et al., 2016). In photometric-only studies like those in the following chapters, a conversion from halo mass to galaxy stellar mass is needed. For massive elliptical galaxies, this is done using the observed relation between black hole mass and halo circular velocity for massive quiescent galaxies (Ferrarese, 2002), and the relation between black hole mass and bulge dynamical (Marconi and Hunt, 2003). As shown in Spacek et al. (2016), this gives

$$E_{\mathrm{th,gravity}}(M_{\star}, z) \approx 5 \times 10^{60}\ \mathrm{erg}\ \frac{M_{\star}}{10^{11}\mathrm{M}_{\odot}}\ (1+z)^{-3/2}, \tag{1.18}$$

representing the expected total thermal energy around a galaxy of stellar mass $M_{\star}$, ignoring both radiative cooling and feedback. Unfortunately this estimate has an uncertainty of about a factor of two, which is significantly larger than the uncertainty in most measurements. Regardless, observational results larger than that of eq. (1.18) would suggest the presence of additional non-gravitational heating, particularly as cooling losses are not included. To estimate the addition of quasar-mode feedback heating, a simple model described in Scannapieco and Oh (2004) is used,

$$E_{\mathrm{th,feedback}}(M_{\star}, z) \approx 4 \times 10^{60}\ \mathrm{erg}\ \epsilon_{k,0.05}\ \frac{M_{\star}}{10^{11}\mathrm{M}_{\odot}}\ (1+z)^{-3/2}, \tag{1.19}$$

where $\epsilon_{k,0.05}$ is the fraction of bolometric luminosity from the quasar associated with an outburst, normalized by a fiducial value of 5%, which is typical of quasar models (e.g. Scannapieco and Oh, 2004; Thacker et al., 2006; Costa et al., 2014). A standard assumption of $\epsilon_{k,0.05} = 1$ is often valid in these cases (Spacek et al., 2017; Meinke et al., 2021). The sum of heating due to gravity (eq. 1.18), and quasar-mode AGN feedback (eq. 1.19) produces an upper expected limit of E_{th} to compare with observations via eq. (1.16). However, these models still have about a factor of two uncertainty and do not incorporate any form of energy losses.

Furthermore, radio-mode feedback is expected to produce thermal energies somewhere between these two limits, where jets provide continuous heating that more closely balances the cooling processes within galaxies, never reaching energy magnitudes comparable to eq. (1.19). Thus, the primary goal of current observations is to compare with theory and discern the potential presence of AGN feedback.

1.4 Interstellar Dust

Another significant component of galaxies is the presence of dust, mostly situated or at least noticeable in the ISM. Interpretation of galaxy photometry and spectra must take into account the effect of dust extinction, or scattering and absorption of visible, ultraviolet (UV), and near-infrared (NIR) starlight due to dust grain particles. Such grains have a variety of shapes, sizes, and compositions (Draine and Lazarian, 1998; Draine, 2011). This dust also then emits or re-radiates thermal energy at lower frequencies.

In far-infrared (FIR) and millimeter wavelengths, dust emission is often described as a gray-body or modified blackbody distribution,

$$I_d(\nu) = \nu^\beta B(\nu, T_d), \tag{1.20}$$

where β is the dust spectral emissivity index, T_d is the dust temperature, and $B(\nu, T_d)$ is the Planck blackbody distribution of eq. (1.7). Inclusion of the modification term ν^β is representative of limitations to the possible energies emitted due to the physical sizes of dust grains. Analysis of CMB or its anisotropies like the tSZ have to contend with dust emission. This occurs both from a galactic dust foreground of our Milky Way, and from any target or neighboring galaxies of a sample. Although the tSZ effect is redshift independent, high-redshift galaxy studies also have to grapple with

central dust emission that becomes redshifted to lower frequencies and can more greatly obscure tSZ signals.

1.5 Millimeter-Wave Bands and Atmospheric Windows

Millimeter astronomy is commonly defined between wavelengths of 1 and 10 millimeters (frequencies between $30 - 300$ GHz). This is also synonymous with the extremely high frequency (EHF) band as defined by the International Telecommunication Union (ITU) (International Telecommunication Union, 2020). Millimeter-waves are often contained within the broader microwave regime definition ($0.3 - 300$ GHz), and sometimes considered within or overlapping with the radio spectrum. As the scientific motivation and antenna design frequencies discussed here mainly reside between $30 - 300$ GHz, the millimeter definition will be used.

At these millimeter wavelengths, ground based telescopes also have to contend with the atmosphere. Atmospheric effects are reduced through the careful selection of a dry high-altitude site, and frequency bands designed to operate outside strong absorption lines. Precipitable water vapor (PWV), i.e. the amount of water vapor vertically integrated within the atmosphere, is a key value in calculating useful atmospheric models. A PWV of 4.0 mm is often considered dry (Meier Valdés, E. A. et al., 2021). Prime targets for ground telescope sites are those with extremely low PWV (i.e. dry), as atmospheric absorption from water vapor is desired to be kept at a minimum. For example, ALMA, located in the Atacama desert, has a PWV < 2.0 mm (Otarola et al., 2019).

Fig. 1.4 shows the transmission windows up to 400 GHz for PWV values of 1.00 and 2.00 mm as calculated from the publicly available CSO Atmospheric Transmission Interactive Plotter (Pardo et al., 2001; CSO, 2007). This model takes a PWV and

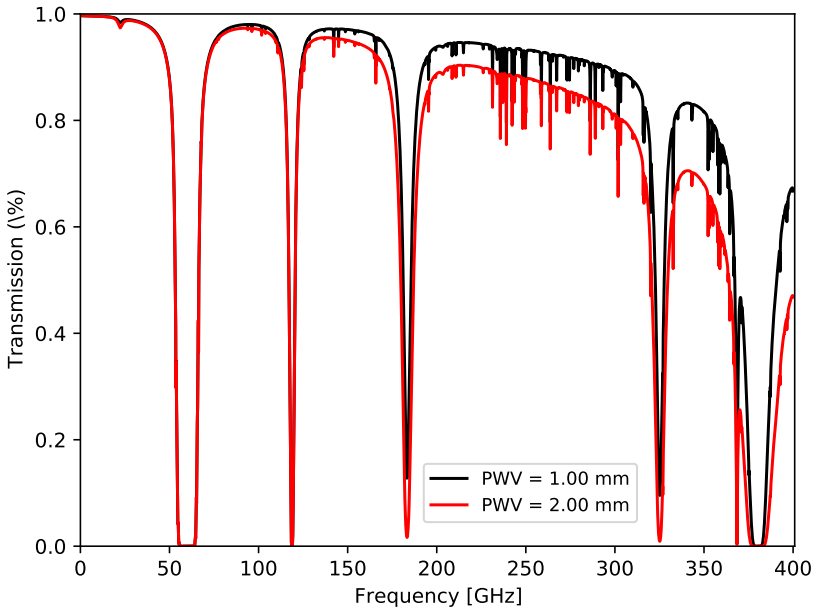

Figure 1.4: Atmospheric transmission window between 1 and 400 GHz for precipitable water vapor (PWV) values of 1.00 and 2.00 mm as calculated from the publicly available CSO Atmospheric Transmission Interactive Plotter (Pardo et al., 2001; CSO, 2007). This model is for the Mauna Kea location, where multiple observatories reside. Absorption of water vapor and oxygen divide the frequencies into separate atmospheric windows. Thus, ground instruments often operate in one or more bands centered near 40, 90, 150, 220, 280, or 350 GHz.

frequency range input to calculate atmosphere transmission at Mauna Kea, another major dry high-altitude location used for multiple observatories.

The atmosphere can also be avoided through the use of balloon-borne or satellite missions. Various balloon-borne telescopes at millimeter and sub-millimeter wavelengths have been launched, including BOOMERanG, MAXIMA, and BLAST (de Bernardis et al., 2000; Hanany et al., 2000; Pascale et al., 2008). Relevant millimeter-wave space telescopes include COBE, WMAP, and *Planck* (Mather et al., 1990; Jarosik et al., 2011; Planck Collaboration et al., 2020a). These often have frequency bands near those used for ground-based telescopes, which enables easier comparison to one another.

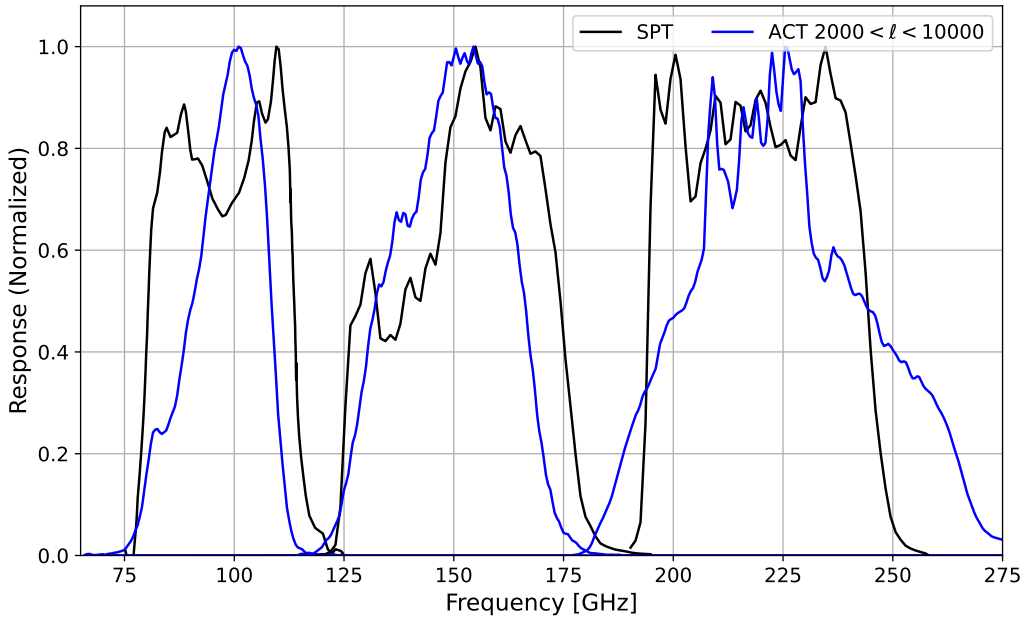

Figure 1.5: Frequency bandpasses used in analysis throughout this paper for the South Pole Telescope (SPT) and Atacama Cosmology Telescope (ACT). Each are situated in three frequency bands near 100, 150, and 220 GHz. The original ACT bands are used with a multipole cut of $2000 < \ell < 10000$, to represent large angular scale filtering and consistency with the maximum SPT limit of $\ell_{\rm max} = 10000$.

This dissertation uses data from both the South Pole Telescope (SPT) and Atacama Cosmology Telescope (ACT), whose bands used are shown in Fig. 1.5. The SPT-SZ bands (without large scale ℓ from *Planck*) were extracted from Chown et al. (2018), while the ACT bands (combined with *Planck* data) are publicly available[1] per detector and multipole ℓ (Naess et al., 2020). As such, an ℓ cut was made on ACT to remove large angular scales ($2000 < \ell$) and any ℓ greater than the SPT limit of $10,000$.

1.6 A Brief History of CMB Observations

Much of the progress in millimeter astronomy can be accredited to the push for continuously refined measurements of the CMB. The very first direct detection of

[1] https://lambda.gsfc.nasa.gov/product/act/actpol_dr5_coadd_maps_info.html

the CMB was measured by Penzias and Wilson in 1964 as excessive antenna noise (Penzias and Wilson, 1965). With a steady supply of theory postulating about the CMB and its anisotropies (Silk, 1968; Zeldovich and Sunyaev, 1969, etc.), instruments specifically designed for CMB detection followed suit. Setups with basic feedhorn antennas, often in a differential radiometer manner, were used to constrain the CMB dipole term shortly thereafter (Conklin, 1969; Henry, 1971; Corey and Wilkinson, 1976; Smoot et al., 1977; Cheng et al., 1979; Smoot and Lubin, 1979).

Verification from such initial measurements then turned attention to improving sensitivity for better anisotropy detection. Multiple satellite experiments like Relikt, COBE (Cosmic Microwave Background Explorer), and then WMAP (Wilkinson Microwave Anisotropy Probe) were subsequently launched (Strukov and Skulachev, 1984; Smoot et al., 1990; Bennett et al., 2003; Page et al., 2003). Balloon-based telescopes with novel bolometer detector configurations were also being deployed (e.g., BOOMERANG, MAXIMA, Mauskopf et al., 1997; Masi et al., 1999; Crill et al., 2003; Rabii et al., 2006).

Nowadays, this process has coalesced into a continuous development of new millimeter telescope technology for observing the CMB's temperature and polarization components. Prominent instruments since include the *Planck* satellite (Planck Collaboration et al., 2020a), ALMA (Wootten and Thompson, 2009), SPT (Carlstrom et al., 2011; Sobrin et al., 2022), ACT (Das et al., 2011; Thornton et al., 2016), MUSTANG (Dicker et al., 2014), BICEP (Keating et al., 2003; Soliman et al., 2018), plus many more current or upcoming like AliCPT (Salatino et al., 2020), BICEP Array (BICEP/Keck Collaboration et al., 2022), Simon's Observatory (Xu et al., 2020), TolTEC (Wilson et al., 2020), and more.

For the purpose of this dissertation, I consider the millimeter-wave instrumentation and observational timeline to be divided into five separate areas, as shown in

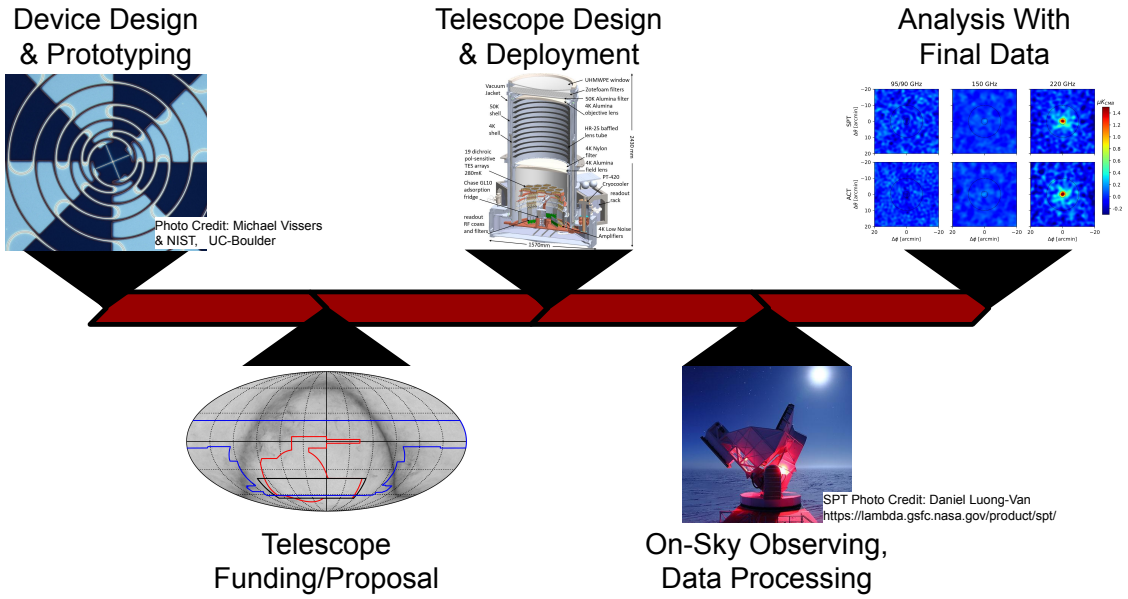

Figure 1.6: A generalized timeline of millimeter astronomy instrumentation from device design and prototyping to final data products released to the public.

Fig. 1.6. These by no means create a concise or comprehensive timeline, but help to emphasize distinctions between them, though in reality they can often intersect. The first step is the designing and prototyping of devices, which is really a continuous activity. Improved observations require improved technology that applies to all facets, such as antennas, detectors, electronics, cryogenics, optics, etc. Compiling such advancements into a new millimeter-wave instrument is the second area, where a specific proposal is put forth to offer new or better observations. The third utilizes those resources in the telescope design, assembly, and deployment. Also here, smaller technical and often forgotten details in the design are addressed. Then the fourth distinct area involves pointing the instrument on-sky for observing. Challenges in data collection and processing are tackled. All of which culminates in the fifth and final step of analyzing the final processed data. Often released to the public after a given time, this final data allows for a wide range of scientific analysis to take place.

1.7 Dissertation Outline

The information presented in this dissertation is arranged as follows:

- The initial tSZ stacking analysis of $138,235$ quiescent galaxies near redshifts of $z \approx 1$ are described in chapter 2. This uses millimeter-wave maps from the South Pole Telescope (SPT) to isolate the tSZ from dust emission around the target galaxies and glean information about quiescent galaxy formation. Results hinting at potential feedback from active galactic nuclei (AGN) are found.

- Chapter 3 is an expansion of the work conducted in Chapter 2. It incorporates recently released millimeter-wave data maps from the Atacama Cosmology Telescope (ACT) along with SPT to analyze $z \approx 1$ selections of up to $387,627$ quiescent galaxies. The work dives deeper into data cleaning and analysis methods to allow for detailed inspection of radial profiles around said galaxies. Stronger evidence for AGN feedback is observed, in addition to interesting information from the analysis of dust. This includes a dust radial profile consistent with the large-scale clustering of galaxies, and estimations of the sample's galactic dust mass.

- Chapter 4 pivots to the device design phase of the millimeter astronomy timeline shown in Fig. 1.6. It focuses on the design and development of multichroic dual-polarization lenslet-coupled antennas for millimeter-wave detectors. A novel log-periodic hybrid trapezoidal design is simulated, with further discussion on relevant considerations in antenna selection.

- The implementation and fabrication of such prototype antennas paired with microwave kinetic inductance detectors (MKIDs) is then discussed in chapter 5.

That describes the prototype MKID array as a whole, and various steps to conduct testing upon it.

- Chapter 6 presents the cryogenic readout design for the Ali CMB polarization telescope (AliCPT), set to be deployed on the Tibetan Plateau. It includes mechanical, electrical, and thermal considerations to accurately read signals from up to $32,376$ detectors of AliCPT.

- Finally, the conclusion in chapter 7 discusses the next steps in millimeter and CMB astronomy, with a look to the future generation of telescopes currently under development.

Chapter 2

THE THERMAL SUNYAEV-ZEL'DOVICH EFFECT FROM MASSIVE, QUIESCENT $0.5 \leq z \leq 1.5$ GALAXIES

This chapter is a slightly modified version of the 2021 article published in The Astrophysical Journal (ApJ), Volume 913, Page 88 (Meinke et al., 2021), with permission from the co-authors.

2.1 Introduction

Measurements of the tSZ effect over the last decade have been focused on detecting and characterizing high-mass cosmic structures with the highest gas thermal energies, namely galaxy clusters (e.g. Planck Collaboration et al., 2011; Reichardt et al., 2013; Planck Collaboration et al., 2016a; Hilton et al., 2018). On the other hand, pushing to lower mass halos has proven to be much more challenging. While in one case, evidence of a tSZ decrement caused by outflowing gas associated with a single luminous quasar was found in ALMA measurements (Lacy et al., 2019), most such constraints have involved averaging over many objects. In this regard, Chatterjee et al. (2010) used data from the Wilkinson Microwave Anisotropy Probe and Sloan Digital Sky Survey (SDSS) around both quasars and galaxies to find a tentative $\approx 2\sigma$ tSZ signal suggesting AGN feedback; Hand et al. (2011) used data from SDSS and the Atacama Cosmology Telescope (ACT) to find a $\approx 1\sigma - 3\sigma$ tSZ signal around galaxies; Gralla et al. (2014) used the ACT to find a $\approx 5\sigma$ tSZ signal around AGNs; Ruan et al. (2015) used SDSS and Planck to find $\approx 3.5\sigma - 5.0\sigma$ tSZ signals around both quasars and galaxies; Crichton et al. (2016) used SDSS and ACT to find a $3\sigma - 4\sigma$ SZ signal around quasars; Hojjati et al. (2017) used data from Planck and the Red Cluster

Sequence Lensing Survey to find a $\approx 7\sigma$ tSZ signal suggestive of AGN feedback; and (Hall et al., 2019) used ACT, Herschel, and the Very Large Array data to measure the tSZ effect around $\approx 100,000$ optically selected quasars, finding a 3.8σ signal that provided a joint constraint on AGN feedback and mass of the quasar host halos at $z \gtrsim 2$.

Recent measurements have also been made around massive galaxies. At $z \lesssim 0.5$, Greco et al. (2015) used SDSS and Planck data to compute the average tSZ signal from a range of over 100,000 'locally brightest galaxies' (LBGs). This sample was large enough to derive constraints on $E_{\rm th}$ as a function of galaxy stellar mass $M_\star$ for objects with $M_\star \gtrsim 2 \times 10^{11} M_\odot$. More recently, Schaan et al. (2021) and Amodeo et al. (2021) combined microwave maps from ACT DR5 and Planck with in the galaxy catalogs from the Baryon Oscillation Spectroscopic Survey (BOSS), to study the gas associated with these galaxy groups. They measured the tSZ signal at $\approx 10\sigma$ along with a weaker detection of the kinetic Sunyaev-Zel'dovich effect (Sunyaev and Zeldovich, 1980), which constrains the gas density profile. They were able to compare these results to cosmological simulations (Battaglia et al., 2010; Springel et al., 2018) to find that the feedback employed in these models was insufficient to account for the gas heating observed at $\approx$ Mpc scales.

At redshifts $0.5 \lesssim z \lesssim 1.5$ the SZ signal from massive quiescent galaxies was studied by Spacek et al. (2016, 2017). These are precisely the objects for which AGN feedback is thought to quench star formation and thus where a significant excess tSZ signal is expected (e.g. Scannapieco et al., 2008). To obtain this faint signal, Spacek et al. (2016) performed a stacking analysis using the VISTA Hemisphere Survey and Blanco Cosmology Survey data overlapping with 43 deg^2 at 150 and 220 GHz from the 2011 South Pole Telescope (SPT) data release, finding a $\approx 2-3\sigma$ signal hinting at non-gravitational heating. Spacek et al. (2017) used SDSS and the Wide-Field

Infrared Survey Explorer (WISE) data overlapping with 312 deg^2 of 2008/2009 ACT data at 148 and 220 GHz, finding a marginal detection that was consistent with gravitational-only heating models.

Here we build on these measurements by making use of data from WISE, the Dark Energy Survey, and the 2500 square-degree survey of the southern sky taken by the SPT, which includes measurements at 95, 150, and 220 GHz. The increase in frequency and sky coverage allows us to obtain a 10.1σ detection of the tSZ effect around $z \approx 1$ galaxies. This lets us move from the marginal detections and upper limits presented in our previous work to measurements that can be applied to future simulations to strongly distinguish between feedback models.

The structure of this chapter is as follows: In Section 2.2 we describe the data sets used for our analysis and contrast that with our previous work. In Section 2.3 we describe our galaxy selection procedure, and the overall properties of the sample of massive, moderate-redshift, quiescent galaxies we use for the stacking analysis presented in Section 2.4. In Section 2.5, we contrast our measurements with the work from other groups as well as with simple feedback models. Conclusions are given in Section 2.6.

2.2 Data

For our analysis, we use three public datasets, two to detect and select galaxies, and one to make our tSZ measurements. As discussed in section 2.3, selecting and carrying out photometric fitting of passive galaxies at $0.5 \lesssim z \lesssim 1.5$ requires data that spans optical, near infrared, and mid-infrared wavelengths. Thus we make use of optical and near-infrared data from DES data release 1 (Abbott et al., 2018), which are already matched to AllWISE data spanning 3-25 μm (Schlafly et al., 2019). For detecting the tSZ effect, we use millimeter-wave observations from the SPT-SZ survey

(Bocquet et al., 2019). The three datasets, which overlap over an area of ≈ 2500 deg^2, are described in more detail below.

2.2.1 DES

DES DR1 is based on optical and near-infrared imaging from 345 nights between August 2013 to February 2016 by the Dark Energy Camera mounted on the 4-m Blanco telescope at Cerro Tololo Inter-American Observatory in Chile. The data covers ≈ 5000 deg^2 of the South Galactic Cap in five photometric bands: grizY. These five bands have point-spread functions of g = 1.12, r = 0.96, i = 0.88, z = 0.84, and Y = 0.90 arcsec FWHM (Abbott et al., 2018). The survey has exposure times of 90s for griz and 45s for Y band, yielding a typical single-epoch PSF depth at S/N = 10 for g $\lesssim$ 23.57, r $\lesssim$ 23.34, i $\lesssim$ 22.78, z $\lesssim$ 22.10 and Y $\lesssim$ 20.69 mag (Abbott et al., 2018). Here and below, all magnitudes are quoted in the AB system (i.e. Oke and Gunn, 1983).

2.2.2 WISE

The AllWISE catalog is based on the Wide-field Infrared Survey Explorer (WISE) NASA Earth orbit mission (Wright et al., 2010; Mainzer et al., 2011). In 2010 WISE carried out an all-sky survey of the sky in bands W1, W2, W3 and W4, centered at 3.4, 4.6, 12 and 22 μm, respectively (Schlafly et al., 2019). The 40 cm diameter infrared telescope was equipped with four 1024x1024 pixel focal plane detector arrays cooled by a dual-stage solid hydrogen cryostat. The whole sky was surveyed 1.2 times in all four bands at a full sensitivity. After the hydrogen ice in the outer cryogen tank evaporated, WISE surveyed an additional third of the sky in three bands, with the W1 and W2 detectors operating at near full sensitivity while the W3 focal plane operated at a lower sensitivity (Mainzer et al., 2011).

AllWISE uses the work of the WISE mission by combining data from the cryogenic and post-cryogenic survey, which yields a deeper coverage in the W1 and W2. The added sensitivity of AllWISE extends the limit of detection of luminous distant galaxies because their apparent brightness at 4.6 μm (W2) no longer declines significantly with increasing redshift. The increased sensitivity yields better detection of those galaxies for redshift $z > 1$. This is crucial for our galaxy detection and selection because we are especially looking for luminous distant galaxies at a redshift $z > 1$.

2.2.3 SPT-SZ

The SPT-SZ survey (Chown et al., 2018) covers 2500 deg^2 of the southern sky between 2007 to 2011 in three different frequencies: 95 GHz and 150 GHz, which lie on either side of the maximum tSZ intensity decrement ($\sim$ 128 GHz), and 220 GHz, which is very near $\nu_{\rm null}$ = 217.6 GHz where there is no change in the CMB signal due to the tSZ effect. The South Pole Telescope (SPT) is a 10 m telescope located within 1 km of the geographical South Pole and consists of a 960-element bolometer array of superconducting transition edge sensors. The maps used in this analysis are publicly available[1] combined maps of the SPT with data from the all-sky Planck satellite (with similar bands at 100, 143, and 217 GHz). Each combined map has a beam resolution of 1.85′, and is provided in a HEALPix (Hierarchical Equal Area isoLatitude Pixelation) format with $N_{\rm side}$ = 8192 (Chown et al., 2018). For comparison, the previous analysis of Spacek et al. (2016) relied on the 2011 SPT data release covering a limited 95 deg^2 at only 150 and 220 GHz (Schaffer et al., 2011). The addition of the 95 GHz band allows for better extraction of the tSZ component, while the larger available field increases the galaxy sample size for reduced noise.

[1] https://lambda.gsfc.nasa.gov/product/spt/index.cfm

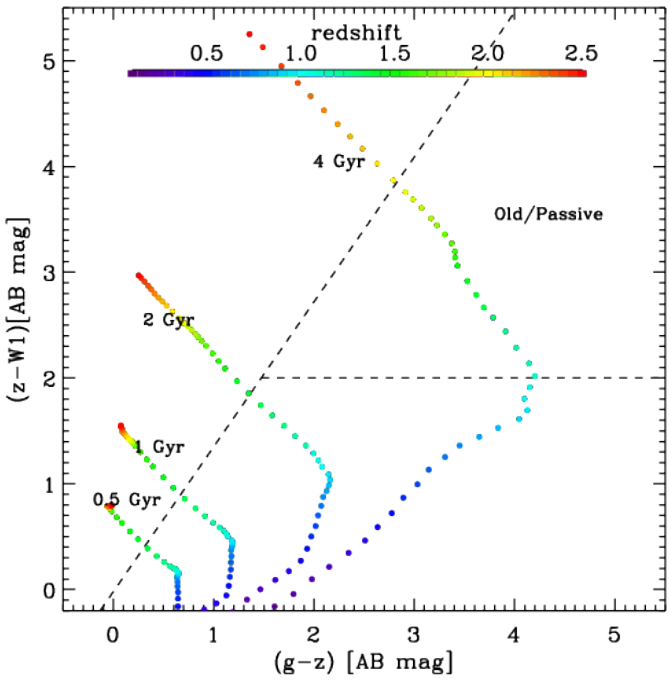

Figure 2.1: Color-color plot showing selection region for passive galaxies. This is slightly modified from Spacek et al. (2017). These are BC03 models with age as indicated. This pre-selection is only used to query the DES database, with the final selection based on SED-fit parameters.

2.3 Defining the Galaxy Sample

2.3.1 Selection

We carried out our initial galaxy selection using the DES database server at NOAO, called NOAO-Lab. In order to start with a manageable sample, we applied a cut in color-color space designed to select old galaxies with low star-formation rates at approximately $1.0 \leq z \leq 1.5$ in the initial database query, as shown in Fig. 2.1. We used mag_auto from the DES in *grizy* bands, along with *W1* and *W2* PSF-magnitudes (converted to AB-system) from AllWISE (Wright et al., 2010; Mainzer et al., 2011) joined to the main DES table. The bands and color-selection used here are slightly different than Spacek et al. (2017) used in SDSS Stripe 82.

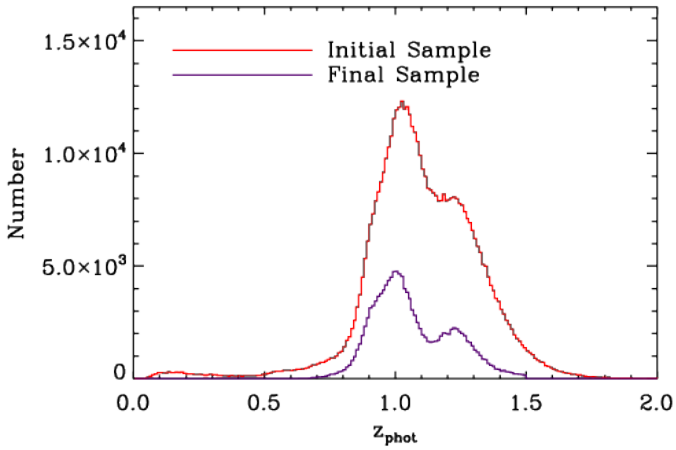

Figure 2.2: Six-band photometric redshift distribution of the initial color-selected sample (red). As expected, the majority of the sample is at $z > 1$. The final sample after selecting based on goodness-of-fit, redshift, age, and SSFR is shown in purple.

The NOAO Data lab allows direct queries in SQL via Jupyter notebook on their server. The lines we used to make the color selection were:

`((mag_auto_z_dered-(w1mpro+2.699)) <= (1.37*mag_auto_g_dered-1.37*mag_auto_z_dered-0.02))` and `((mag_auto_z_dered-(w1mpro+2.699) )>=2.0)`.

2.3.2 Photometric Fitting

After the galaxies were selected, photometric redshifts were computed using EAZY (Brammer et al., 2008) and the seven broad bands *grizyW1W2*. In calling EAZY, we used the CWW+KIN (Coleman et al., 1980; Kinney et al., 1996) templates, and did not allow for linear combinations. Since we are looking for red galaxies and have a gap in wavelength coverage between *y*-band and *W1*, we were worried that allowing combinations of templates would yield unreliable redshifts, where e.g., a red template was fit to the IR-data and a blue one was fit to the optical data and they meet in the wavelength gap. The resulting redshift distribution is shown in Fig. 2.2, which clearly shows that we selected galaxies in the desired range.

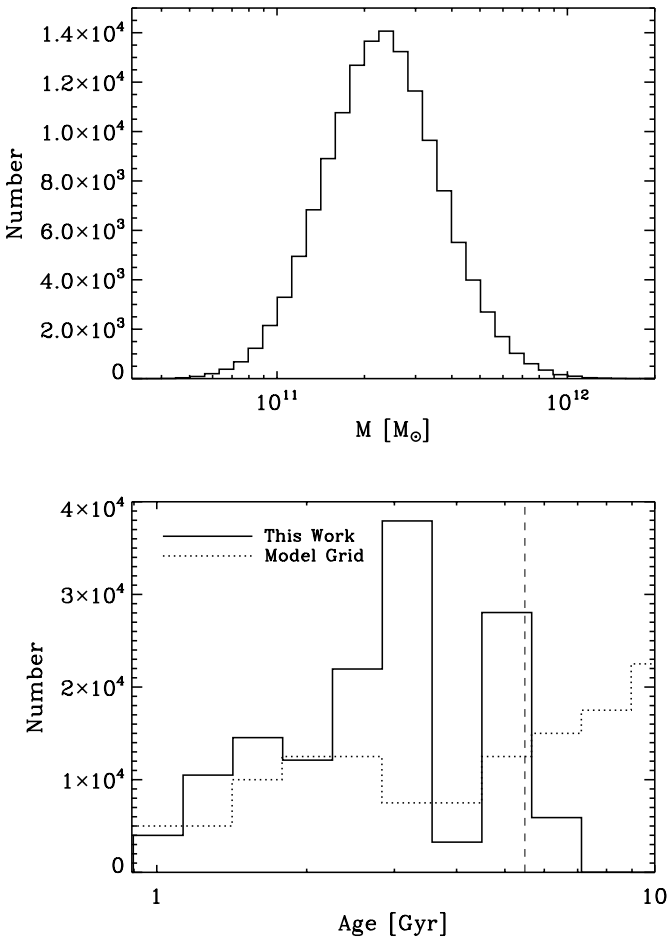

Figure 2.3: *Top:* Stellar mass distribution of the sample after selecting based on SED parameters (Meinke et al., 2021). *Bottom:* Age histogram of the sample. Note that, at a given redshift, the ages are restricted to be younger than the age of the universe at that redshift. The black dashed line shows the age of the universe at $z = 1.1$. The dotted line shows the scaled distribution of all available Bruzual and Charlot (2003) models on the grid.

Once the redshifts were measured, we fit the spectral energy distributions (SEDs) using our own code, following the method used in Spacek et al. (2017), to which the reader is referred for more details. Briefly, a grid of BC03 (Bruzual and Charlot, 2003) models with exponentially declining star formation rates (SFRs) was fit over a range of stellar ages, SFHs (i.e., τ), and dust-extinction values ($0 < A_V < 4$). Our code uses BC03 models assuming a Salpeter initial mass function (IMF), but in

$\log_{10}\left(\frac{M_\star}{\mathrm{M}_\odot}\right)$	N	$\overline{z}$	$\widetilde{z}$	$\log_{10}\left(\frac{\overline{M}}{\mathrm{M}_\odot}\right)$	$\log_{10}\left(\frac{\widetilde{M}}{\mathrm{M}_\odot}\right)$	$\overline{Age}$ [Gyr]	$\overline{D_\mathrm{a}}^2$ [Gpc^2]	$\widetilde{D}_\mathrm{a}^2$ [Gpc^2]
$10.9-11.0$	3376	0.94	0.95	10.96	10.96	1.69	2.76	2.78
$11.0-11.1$	8241	0.97	0.96	11.06	11.06	2.05	2.79	2.81
$11.1-11.2$	15738	1.00	0.98	11.16	11.16	2.47	2.83	2.84
$11.2-11.3$	23448	1.03	1.01	11.25	11.25	2.86	2.87	2.87
$11.3-11.4$	27723	1.07	1.04	11.35	11.35	3.19	2.91	2.91
$11.4-11.5$	24877	1.09	1.07	11.45	11.45	3.52	2.93	2.94
$11.5-11.6$	17246	1.11	1.09	11.55	11.54	3.71	2.95	2.96
$11.6-11.7$	9501	1.13	1.13	11.65	11.64	3.88	2.97	3.00
$11.7-11.8$	4396	1.15	1.16	11.74	11.74	4.01	2.99	3.03
$11.8-11.9$	1625	1.17	1.21	11.84	11.84	4.14	3.01	3.06
$11.9-12.0$	506	1.21	1.25	11.94	11.93	4.13	3.04	3.09

Table 2.1: Statistics of 0.1-wide dex stellar mass bins from $\log_{10}(M_\star/M_\odot) = 10.9-12.0$. Both mean and median are listed for redshift, mass, and angular-diameter-distance-squared (D_a).

comparison with the literature, we convert all stellar masses to the value assuming a Chabrier IMF (0.24 dex offset; Santini et al. (2015)). As in Spacek et al. (2017), we choose as our final sample all galaxies with age$>$ 1 Gyr, $SSFR < 0.01\mathrm{Gyr}^{-1}$, $0.5 < z_\mathrm{phot} < 1.5$, and reduced $\chi^2 < 5$.

2.3.3 Removing Known Contaminants

Before using this catalog, there are several contaminants that must be removed. We therefore remove sources from the *ROSAT* Bright and Faint Source catalogs (BSC and FSC; Voges et al., 1999). We additionally remove known clusters from *ROSAT* (Piffaretti et al., 2011) and *Planck* (Planck Collaboration et al., 2016b). Sources from the *AKARI/FIS* Bright Source Catalog (Yamamura et al., 2010) and

the *AKARI/IRC* Point Source Catalog (Ishihara, D. et al., 2010) were also removed along with galactic molecular clouds by cross-matching with the Planck Catalogue of Galactic Cold Clumps (Planck Collaboration et al., 2016d) and compact sources from the nine-band Planck Catalog of Compact Sources (Planck Collaboration et al., 2014). We also remove sources from the *IRAS* Point Source Catalog Joint IRAS Science (1994). We *do not* remove the SZ sources selected from the SPT by (Bleem et al., 2015). In all cases, sources with a possible contaminant within $4.0'$, to match the beam of the SPT-SZ data, are flagged and those sources are removed from further consideration. This left 138,235 massive and quiescent $z \gtrsim 0.5$ galaxies to include in our SZ stacks. This final sample is shown as the purple line in Fig. 2.2 and stellar mass distribution shown in Fig. 2.3. These galaxies were partitioned into 12 logarithmic stellar mass bins of width $\Delta\log_{10}(M_\star/M_\odot) = 0.1$ ranging from $\log_{10}(M_\star/M_\odot)$ =10.9 to 12.0. The mean and median redshift, mass, and angular-diameter-distance-squared for each of these bins are listed in Table 2.1. These small mass bins were chosen to more accurately fit the dust model discussed in Section 2.4, which has a dependence on redshift and potential non-linearity with $\log_{10}(M_\star/M_\odot)$.

2.3.4 Comparison with Previous Work

Our current sample has several advantages to previous work in Spacek et al. (2016) and Spacek et al. (2017). As compared to Spacek et al. (2017), the DES data is deeper than the SDSS data, which provides for better SED-fits in addition to fainter sources. In addition, the use of the AllWISE data is superior to the Wise All-Sky Survey (Wright et al., 2010) used in Spacek et al. (2017), because it includes more observing time from the extended NEOWISE mission (Mainzer et al., 2011). Again, this helps the fidelity of the SED-fits. Second, we have slightly altered the color selection, as given above, so as to better include galaxies in the desired redshift

range of $0.5 \leq z \leq 1.5$. This was successful as shown in Fig. 2.2, as compared to Fig. 3 of Spacek et al. (2017).

The third difference is the choice of photometric redshift template. Our color-selection aims to find very red galaxies as templates designed to work on the most general sets of galaxies are not ideal. This is mainly, but not only, due to large 4000 Å breaks. After testing all the available templates for EAZY, we found that the best-fits were given by the empirical CWW+KIN templates, because the elliptical galaxy template had a sufficiently large 4000 Å break. We found that 86% of our galaxies were best-fit by either the "E" or "Sbc" CWW templates. By contrast, Spacek et al. (2017) used the EAZY V1.0 templates, which are based on population synthesis models.

Finally, Spacek et al. (2016) relied on the 2011 SPT data release covering a limited 95 deg^2 at only 150 and 220 GHz (Schaffer et al., 2011), while the more recent data release used here both includes the 95 GHz band and covers a significantly larger area (2500 sq. deg.). This is also a much larger region than the $\approx$ 300 deg^2 of ACT data used in Spacek et al. (2017). All four of these improvements contribute to the present study having much higher signal-to-noise measurements than our previous work.

2.4 Stacking and Filtering

Once the catalog of galaxies described in Table 2.1 was determined, images were taken around each galaxy location on the combined SPT-SZ maps at all three frequencies. In the conversion from the HEALPix map format, we set the Cartesian pixel resolution of the images to $0.05'$ ($\approx$ 74 pixels per HEALPix pixel), so the full $60'$x$60'$ images contain 1201x1201 pixels. As the SPT region is far from the equatorial plane, the right ascension must be accurately scaled to the cosine of the declination. We

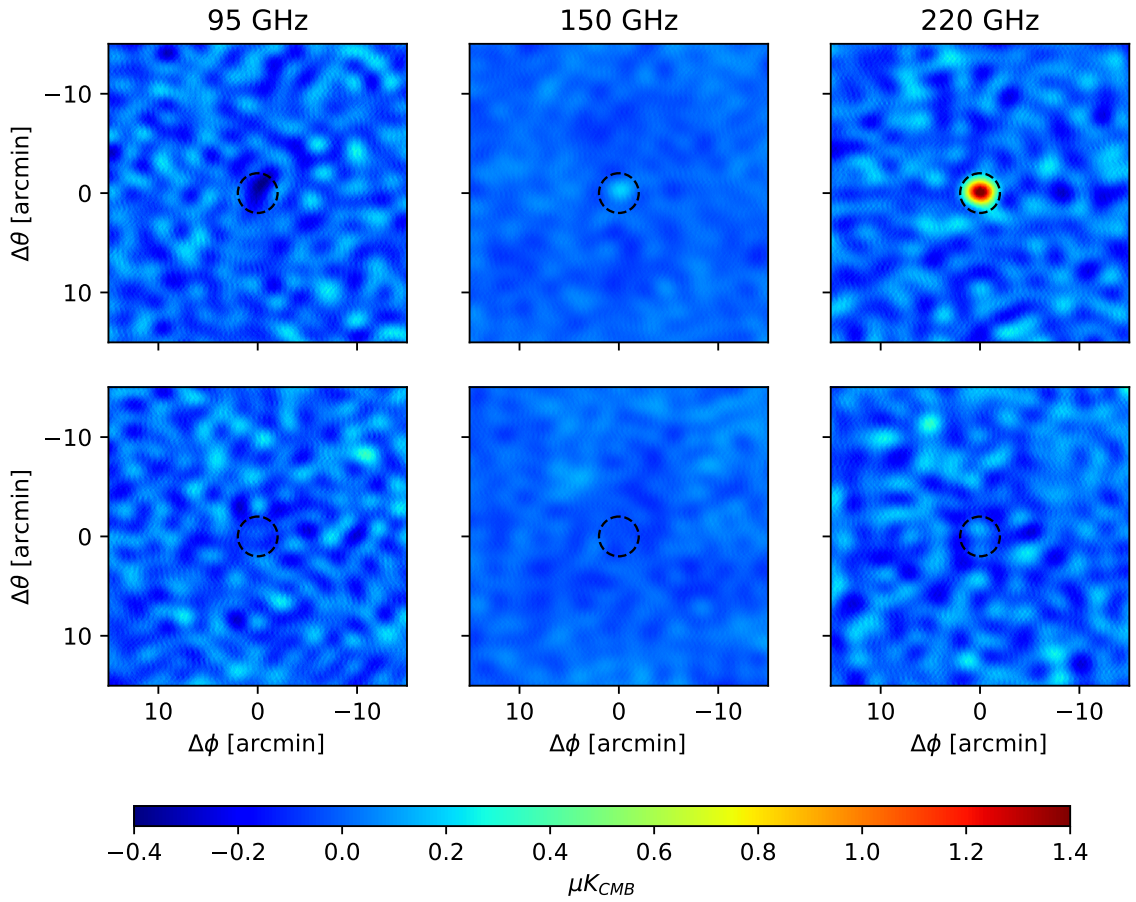

Figure 2.4: 30′x30′ filtered stacks at 95 (Left), 150 (Middle), and 220 (Right) GHz for all (N=138235) galaxies (*Top*), and random points (*Bottom*, N=138235 out of the generated 869878). The center dashed circle in each represents the 2.0′ radius top-hat aperture discussed in Section 2.5.

constructed averaged co-added stacked images from the individual galaxies, resulting in one stacked image per frequency per bin.

To remove large-scale CMB and dust fluctuations, we applied a 5′ high-pass Gaussian filter to each averaged frequency stack. We used an iterative Gaussian method alongside the high-pass filter to minimize central signal loss in the process. This involved the following steps of:

1. Apply 5′ high-pass filter to the stacked image.

2. Fit the high-pass filtered image center with a symmetric 2D Gaussian. A maximum FWHM of 1.5 times the map resolution or $2.775'$ was used to ensure no large runaway fits, as a $z = 1$ galaxy would have an angular size $\approx 1'$ (for a diameter of 0.5 Mpc proper or 1.0 Mpc comoving).

3. The resultant fit is then subtracted from the image before high-pass filtering used in Step 1.

4. Steps $1-3$ above are repeated until the Gaussian fit amplitude of Step 2 is less than the image's surrounding noise, or the fit FWHM has $< 10\sigma$ certainty.

5. Return the final high-pass filtered image after Step 4 condition is met.

To account for any residual bias offset from SPT maps, galaxy selection, and filtering procedure, we also generated a set of random points in the SPT field. After an identical $4'$ cut of contaminant sources, 869,878 random points were obtained. They were then stacked, averaged, and high-pass filtered as outlined above for the galaxies. Measurements such as those listed in Section 2.5 include corrections obtained from these residual bias offsets. The stacked and filtered images around galaxies are illustrated in the upper panels of Fig. 2.4, while the comparison stacks for the random points are illustrated in the lower panels of the figure. There is a clearly visible signal in the galaxy stacks not seen in the random stacks.

2.5 Results

2.5.1 Two Component Fitting

To extract the central signal from each filtered frequency stack, we used a circular top-hat aperture of $2.0'$ radius. This is large enough to contain the majority of the

central signal while minimizing noise introduced from any other surrounding sources. Additional apertures and sizes were also investigated as detailed in Appendix 2.5.2. To correct for beam and filter effects, we scaled all apertures with respect to $S^{-1}_{\nu,\mathrm{beam}}$, where $S_{\nu,\mathrm{beam}}$ is the aperture signal detected from a normalized central source convolved to the beam FWHM of 1.85′, and filtered as in Section 2.4. The final 2.0′ top-hat aperture used here has a scale factor of 1.03, indicating all but 3% of an unresolved central source is within the aperture. Table 2.2 lists the 2.0′ top-hat measurements after bias correction and scaling.

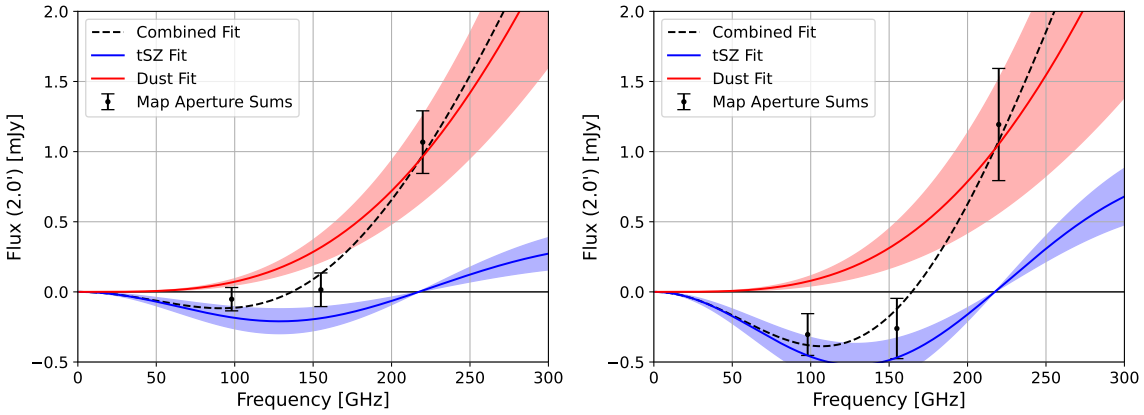

Figure 2.5: Intensity spectrum of our two-component fit for the two highest stellar mass bins ($\log_{10}(M_\star/M_\odot) = 11.8-11.9$ and $11.9-12.0$). The shaded tSZ and dust regions represent 1σ error. The points are the 2.0′ top-hat aperture values as listed in Table 2.2, placed at each frequency band center. *Left:* For $\log_{10}(M_\star/M_\odot) = 11.8-11.9$ bin (N=1625 galaxies). *Right*: For $\log_{10}(M_\star/M_\odot) = 11.9-12.0$ bin (N=506 galaxies).

From our aperture measurements, we used a two-component fitting model consisting of tSZ (y) and $z = 0$ dust in the 220 GHz band (D_{220}),

$$S_\nu = \int \Delta T_\nu(\boldsymbol{\theta}) d\boldsymbol{\theta} = f_x \int y(\boldsymbol{\theta}) d\boldsymbol{\theta} + d_{\nu,220} \int D_{220}(\boldsymbol{\theta}) d\boldsymbol{\theta}, \tag{2.1}$$

where $f_x \equiv T_{\mathrm{CMB}}[x\,(e^x+1)/(e^x-1)-4]$ of the tSZ signal (from eq. 1.11), and $d_{\nu,220}$ is the gray-body dust spectrum conversion from CMB temperature at frequency band ν to CMB temperature in the 220 GHz band at $z = 0$:

$$d_{\nu,220} \equiv \left[\frac{(1+z)\,\nu}{220\mathrm{GHz}}\right]^\beta \frac{B[(1+z)\,\nu, T_{\mathrm{dust}}]}{B(220\mathrm{GHz}, T_{\mathrm{dust}})} \left.\frac{dT}{dB(\nu,T)}\right|_{T_{\mathrm{CMB}}} \left.\frac{dB(220\mathrm{GHz},T)}{dT}\right|_{\mathrm{T_{CMB}}}, \tag{2.2}$$

$\log_{10}\left(\frac{M_\star}{M_\odot}\right)$	$S_\nu = \int \Delta T_\nu(\boldsymbol{\theta}) d\boldsymbol{\theta}$ [μK arcmin^2]			$\int D_{220}(\boldsymbol{\theta}) d\boldsymbol{\theta}$	$\int y(\boldsymbol{\theta}) d\boldsymbol{\theta}$
	95 GHz	150 GHz	220 GHz	μK arcmin^2	10^{-6}arcmin^2
$10.9 - 11.0$	-3.66 ± 2.95	-0.02 ± 2.40	2.40 ± 3.80	$0.34^{+0.43}_{-0.44}$	$0.78^{+0.63}_{-0.63}$
$11.0 - 11.1$	-0.72 ± 1.89	2.20 ± 1.54	9.07 ± 2.44	$0.98^{+0.31}_{-0.33}$	$0.47^{+0.41}_{-0.42}$
$11.1 - 11.2$	-1.04 ± 1.37	2.15 ± 1.12	3.47 ± 1.77	$0.46^{+0.21}_{-0.22}$	$0.15^{+0.30}_{-0.30}$
$11.2 - 11.3$	-2.79 ± 1.13	-0.06 ± 0.92	5.73 ± 1.46	$0.57^{+0.18}_{-0.19}$	$0.87^{+0.25}_{-0.25}$
$11.3 - 11.4$	-1.55 ± 1.04	0.37 ± 0.85	5.37 ± 1.34	$0.50^{+0.15}_{-0.17}$	$0.59^{+0.23}_{-0.23}$
$11.4 - 11.5$	0.44 ± 1.10	3.72 ± 0.90	13.94 ± 1.42	$1.26^{+0.25}_{-0.30}$	$0.44^{+0.27}_{-0.28}$
$11.5 - 11.6$	-5.59 ± 1.31	-0.90 ± 1.07	9.28 ± 1.69	$0.80^{+0.21}_{-0.23}$	$1.69^{+0.29}_{-0.30}$
$11.6 - 11.7$	-4.16 ± 1.76	-0.07 ± 1.44	11.71 ± 2.27	$0.93^{+0.25}_{-0.29}$	$1.52^{+0.39}_{-0.40}$
$11.7 - 11.8$	-6.09 ± 2.58	-0.11 ± 2.10	17.59 ± 3.33	$1.34^{+0.37}_{-0.41}$	$2.27^{+0.57}_{-0.59}$
$11.8 - 11.9$	-2.66 ± 4.24	0.44 ± 3.46	26.14 ± 5.47	$1.75^{+0.53}_{-0.57}$	$2.23^{+0.94}_{-0.95}$
$11.9 - 12.0$	-15.52 ± 7.60	-7.53 ± 6.19	29.21 ± 9.79	$1.81^{+0.80}_{-0.84}$	$5.57^{+1.65}_{-1.65}$

Table 2.2: $2.0'$ top-hat integrated temperatures determined from their respective frequency stacks (95, 150, and 220 GHz) for 0.1-wide dex stellar mass bin subsets of the galaxy catalog. These values were extracted from the high-pass filtered stacks with the random point bias offsets subtracted, and scaled for beam correction. The last two columns show the Dust and tSZ values obtained via component fit of eq. (2.1).

where β is the dust emissivity spectral index, and $B(\nu, T)$ is the Planck distribution. The tSZ and dust terms are integrated over SPT bandpasses extracted from Chown et al. (2018), as the SPT+Planck maps are dominated by the SPT response for our small angular scales ($< 5'$). We use conservative values of $\beta = 1.75 \pm 0.25$ and $T_{\rm dust} = 20 \pm 5$K within the bounds of previous studies (Draine, 2011; Addison et al., 2013; Planck Collaboration: et al., 2014). Unlike investigations such as Greco et al. (2015), these values impact final results due to our higher redshift and better map resolution, that lead to an increased dust detection at lower frequencies. We treat the dust parameters as Gaussian priors, fitting for a Gaussian distribution of β and T_{dust} with $\sigma_\beta = 0.25$ and $\sigma_{T_{dust}} = 5$. The reported best fit y and D_{220} are the 50th percentile (median) obtained. Error from the priors are calculated as the bounds containing 1σ (68.27%), added in quadrature with the fit error. The uncertainty in our dust parameters determined this way contributes up to 10% of our final reported errors.

The integrated aperture temperatures of Table 2.2 are fit according to eq. (2.1) with their median redshifts, yielding dust and tSZ signals as listed in the final two columns in this table. The dust is kept in units of μK CMB at $z = 0$ redshift and $\nu = 220$GHz for easy comparison, as dust is largest in the 220 GHz band.

We find a $0.8 - 4.2\sigma$ dust signal ranging between $0.34 - 1.81\mu$K arcmin^2 at 220 GHz for our mass bins. The highest dust S/N values occur in the larger mass bins, and show a trend of increasing dust with mass. The overall signal to noise detection of dust in our data is 9.8σ, and the dust fit is heavily determined by the integrated 220 GHz values, which is also the noisiest of the three SPT bands.

For the tSZ signal, we see a negligible $0.5 - 3.5\sigma$ detection in the lower mass bins between $10.9 \lesssim \log_{10}(M_\star/M_\odot) \lesssim 11.5$. From $\log_{10}(M_\star/M_\odot) = 11.5 - 12.0$ however, we observe a S/N up to 5.6σ. The four highest bins centered at 11.65, 11.75, 11.85,

and 11.95 yield integrated y values of $1.52^{+0.39}_{-0.40}$, $2.27^{+0.57}_{-0.59}$, $2.23^{+0.94}_{-0.95}$, and $5.57^{+1.65}_{-1.65}$ 10^{-6} arcmin^2, respectively. The overall signal to noise ratio of our tSZ detection is 10.1σ, which is a vast improvement from the $2-3\sigma$ measurements we were able to obtain from previous data sets (Spacek et al., 2016, 2017).

Fig. 2.5 shows the intensity spectrum of the dust and tSZ signals from our two-component fit for the two highest bins using the $2.0'$ top-hat aperture. The dust spectrum is near the Rayleigh-Jeans limit, but it still contributes a significant signal at the lower frequencies when compared to the fainter tSZ. Some of the dust fit uncertainty arises from our inability to accurately determine the dust emissivity (β) and temperature ($T_{\rm dust}$), and would likely be helped by future experiments with more frequency channels.

The Compton-y measurements can further be converted to thermal energy following eq. (1.16), as was done in Section 2.5.3. Numerous steps were taken to verify the stacking process. Fits done with different apertures and sizes are outlined in the following Section 2.5.2, while Section 2.5.4 details the reproduction of previous studies (Planck Collaboration et al., 2013; Greco et al., 2015) to validate the stacking code used and compare catalog selection criteria.

2.5.2 Impact of Aperture Size

The aperture shape and size used in the integrated sums at each frequency has a large influence on the final two-component fit of eq. (2.1). It needs to be large enough to encompass most of the signal from our galaxies without being too large to introduce extra noise and nearby source contamination.

Table 2.3 shows the $\log_{10}(M_\star/M_\odot)$ 0.1-wide bin Compton-y fits, alongside the final stellar mass correction power-law parameters E_{pk} and α for three other potential aperture choices. A $3.0'$ FWHM Gaussian aperture is chosen as a similar comparison

to our main 2.0′ top-hat used. Two larger apertures: a 4.0′ top-hat, and a 6.0′ Gaussian are also selected to highlight the additional noise they incur.

2.5.3 Correction for Stellar Mass Uncertainty

At $0.5 \leq z \leq 1.5$ redshifts, our photometrically selected galaxies yield higher uncertainties in stellar mass compared to previous spectroscopic studies (Greco et al., 2015). To quantify our uncertainties in stellar mass, we performed two Monte Carlo tests. Using the final sample, we first perturbed the photometry using the 1-σ photometric errors for each galaxy and band, and re-ran the SED-fitting code. This was repeated 100 times for each galaxy, and the standard deviation was computed for each galaxy. We found the mean uncertainty, due to photometric errors, to be $\sigma_{\log(M_p)} \simeq 0.140$ dex. Similarly, we repeated the procedure, this time keeping the photometry fixed but perturbing the photometric redshift using a 5% uncertainty in $1+z$, or $\sigma_z \approx 0.05(1+z)$. Again, this was repeated 100 times for each galaxy, and we found the mean uncertainty, due to photometric redshift errors, to be $\sigma_{\log(M_z)} \simeq 0.074$ dex. These two numbers were combined in quadrature to give a total estimated uncertainty in stellar mass of $\sigma_{\log(M)} \simeq 0.16$ dex.

This 0.16 dex uncertainty is large enough to 'flatten' our 0.1 dex stellar mass bin measurements, by shifting a significant number of galaxies near the peak of the mass distribution into wings where they can overwhelm signal from the much smaller galaxy counts at low and high masses. As an illustration of this effect, Fig. 2.8 in Appendix 2.5.4 shows the results of an additional 0.16 dex uncertainty applied to the low-redshift galaxies recreated from Greco et al. (2015).

Our high redshift galaxies also contain this additional artifact from stellar mass uncertainty, but amplified further due to the narrower distribution of our sample. We correct for this by fitting our ($\log_{10}$) stellar mass distribution to a Gaussian, with a

	$\log_{10}\left(\frac{M_\star}{M_\odot}\right)$	Top-Hat		Gaussian	
		$2.0'$	$4.0'$	$3.0'$	$6.0'$
$\int y(\boldsymbol{\theta})d\boldsymbol{\theta}$ [10^{-6} arcmin^2]	$10.9-11.0$	$0.78^{+0.63}_{-0.63}$	$1.23^{+1.35}_{-1.35}$	$0.72^{+0.61}_{-0.61}$	$0.90^{+1.02}_{-1.02}$
	$11.0-11.1$	$0.47^{+0.41}_{-0.42}$	$0.79^{+0.87}_{-0.87}$	$0.55^{+0.40}_{-0.40}$	$0.61^{+0.66}_{-0.66}$
	$11.1-11.2$	$0.15^{+0.30}_{-0.30}$	$0.15^{+0.63}_{-0.63}$	$0.14^{+0.29}_{-0.29}$	$0.31^{+0.48}_{-0.48}$
	$11.2-11.3$	$0.87^{+0.25}_{-0.25}$	$0.79^{+0.52}_{-0.52}$	$0.81^{+0.24}_{-0.24}$	$0.91^{+0.39}_{-0.39}$
	$11.3-11.4$	$0.59^{+0.23}_{-0.23}$	$1.10^{+0.48}_{-0.48}$	$0.59^{+0.22}_{-0.22}$	$0.91^{+0.36}_{-0.36}$
	$11.4-11.5$	$0.44^{+0.27}_{-0.28}$	$0.00^{+0.52}_{-0.53}$	$0.39^{+0.25}_{-0.27}$	$0.06^{+0.39}_{-0.41}$
	$11.5-11.6$	$1.69^{+0.29}_{-0.30}$	$2.42^{+0.60}_{-0.61}$	$1.63^{+0.28}_{-0.29}$	$2.12^{+0.46}_{-0.46}$
	$11.6-11.7$	$1.52^{+0.39}_{-0.40}$	$1.76^{+0.81}_{-0.82}$	$1.38^{+0.38}_{-0.39}$	$1.65^{+0.62}_{-0.62}$
	$11.7-11.8$	$2.27^{+0.57}_{-0.59}$	$2.90^{+1.18}_{-1.19}$	$2.20^{+0.56}_{-0.57}$	$2.42^{+0.90}_{-0.91}$
	$11.8-11.9$	$2.23^{+0.94}_{-0.95}$	$0.32^{+1.99}_{-2.02}$	$2.06^{+0.91}_{-0.92}$	$1.12^{+1.50}_{-1.53}$
	$11.9-12.0$	$5.57^{+1.65}_{-1.65}$	$3.78^{+3.47}_{-3.47}$	$4.91^{+1.59}_{-1.60}$	$3.45^{+2.63}_{-2.63}$
$E_{\rm pk}$ [10^{60} erg]		$5.98^{+1.02}_{-1.00}$	$7.62^{+1.83}_{-2.06}$	$5.76^{+0.99}_{-0.96}$	$7.17^{+1.44}_{-1.55}$
α		$3.77^{+0.60}_{-0.74}$	$2.93^{+0.94}_{-1.33}$	$3.65^{+0.60}_{-0.76}$	$2.88^{+0.82}_{-1.08}$

Table 2.3: Results for alternate aperture shapes and sizes: the fiducial $2.0'$ radius top-hat, a larger $4.0'$ radius top-hat, a $3.0'$ FWHM Gaussian, and a $6.0'$ FWHM Gaussian. Listed are their respective Compton-y parameter fits found from eq. (2.1), and the final two rows showing the stellar mass uncertainty correction power-law fit parameters E_{pk} and α. As expected, the additional noise from the larger apertures results in worse fits. The $3.0'$ Gaussian aperture behaves similar to that of our $2.0'$ top-hat chosen for the main results.

mass peak of $\log_{10}(M_{\star,\mathrm{pk}}/M_{\odot}) = 11.36 \pm 0.001$ and $\sigma = 0.20 \pm 0.001$. This allows for easy deconvolution of the 0.16 dex stellar mass uncertainty, yielding an unconvolved distribution of $\sigma_{\mathrm{uncon.}} = \sqrt{(0.20)^2 - (0.16)^2} = 0.12$. We assign a simple power-law energy-mass function to the unconvolved distribution following:

$$E_{\mathrm{th}}(M_{\star}) = E_{\mathrm{pk}} \left(\frac{M_{\star}}{M_{\star,\mathrm{pk}}} \right)^{\alpha}, \tag{2.3}$$

where $M_{\star,\mathrm{pk}} = 2.29 \times 10^{11} M_{\odot}$. In our case it is also more convenient to write eq. 2.3 as a log-log relation:

$$\mathcal{E}(\mu) = \log_{10}(E_{\mathrm{th}})(\mu) = \log_{10}(E_{\mathrm{pk}}) + \alpha \left(\mu - \mu_{pk} \right), \tag{2.4}$$

where $\mu = \log_{10}(M_{\star}/\mathrm{M}_{\odot})$, the $\log_{10}$ stellar mass.

We assign the energies of this model to the unconvolved ($\sigma = 0.12$) $\log_{10}(M_{\star}/M_{\odot})$ distribution and convolve (forward-model) them with our 0.16 dex uncertainty. This brings our mass distribution back to the original $\sigma = 0.20$ Gaussian fit. The now-convolved assigned energies can then be placed in similar 0.1 dex stellar mass bins and fit to our measured SPT values to find E_{pk} and α. Fig. 2.6 shows the probability contour of our two-parameter fit (*inset*) and the corresponding convolved power-law relation with shaded 2σ. Then Fig. 2.7 shows the unconvolved energy-mass relation alongside the thermal energies extracted from Greco et al. (2015).

This analysis reveals that thermal energy is indeed noticeably flattened at low and high mass bins for our stellar mass uncertainty of 0.16 dex. We extract a basic energy-stellar mass relation following eq. (2.3) with $E_{\mathrm{pk}} = 5.98^{+1.02}_{-1.00} \times 10^{60}$ erg and $\alpha = 3.77^{+0.60}_{-0.74}$, indicative of the expected signal after stellar mass uncertainty correction. This relation also corresponds closely to the lower redshift investigations of Planck Collaboration et al. (2013); Greco et al. (2015).

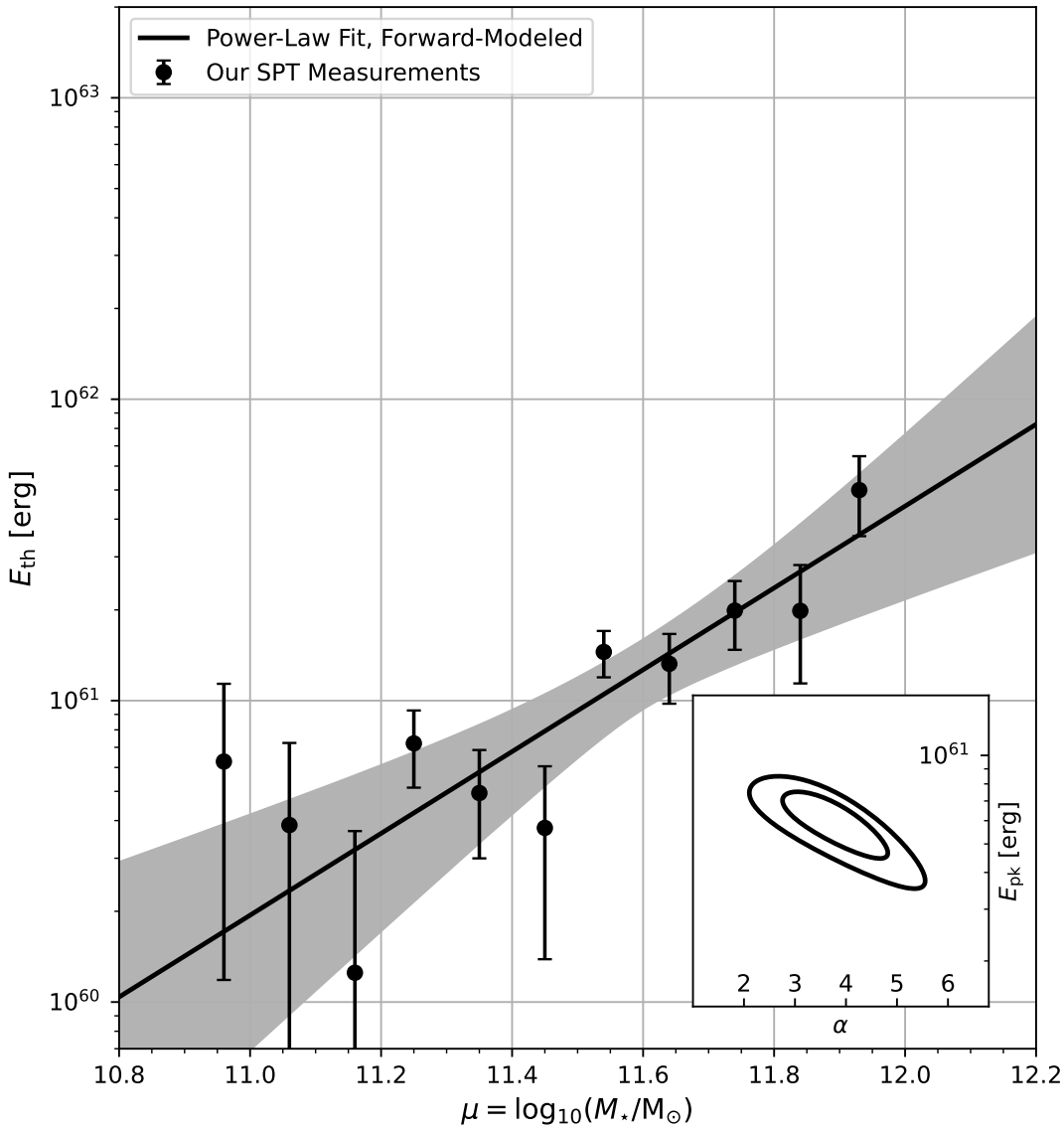

Figure 2.6: Energy-Stellar Mass plot of measured stellar mass bin values (*black circles*) and the best power-law fit (eq. 2.3, $E_{\rm pk} = 5.98^{+1.02}_{-1.00} \times 10^{60}$ erg, $\alpha = 3.77^{+0.60}_{-0.74}$) with shaded 2σ, forward-modeled to factor in stellar mass uncertainty. *Inset:* Probability contour for the unconvolved power-law parameters $E_{\rm pk}$ and α, with lines at 1σ, and 2σ.

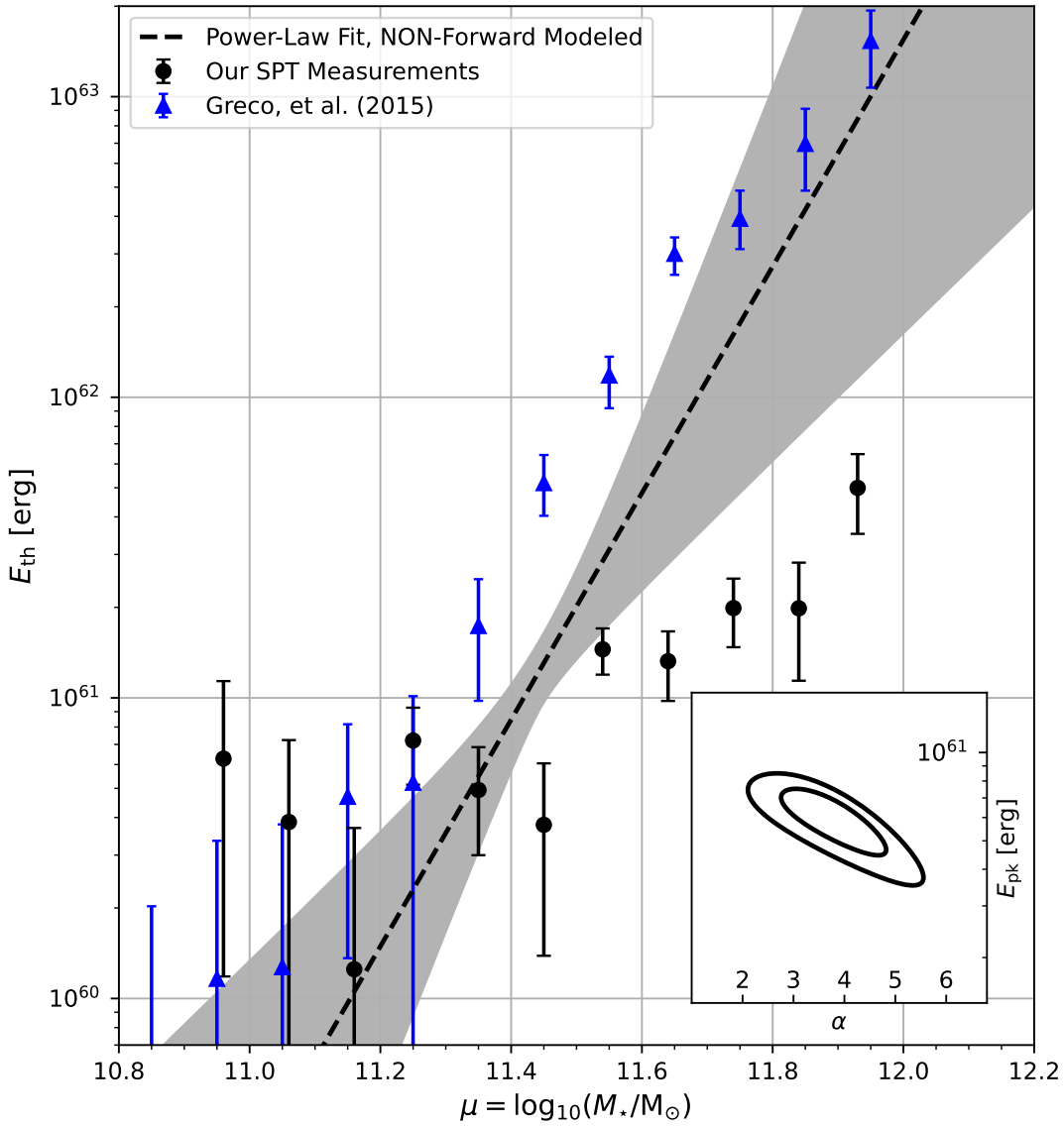

Figure 2.7: Energy-Stellar Mass plot of measured stellar mass bin values (*black circles*) and the best power-law fit (eq. 2.3, $E_{\rm pk} = 5.98^{+1.02}_{-1.00} \times 10^{60}$ erg, $\alpha = 3.77^{+0.60}_{-0.74}$) with shaded 2σ, now shown without forward-modeling. Also included are converted measurements from Greco et al. (2015) (*blue triangles*). Our non-forward-modeled power-law fit is roughly consistent with the points from Greco et al. (2015).

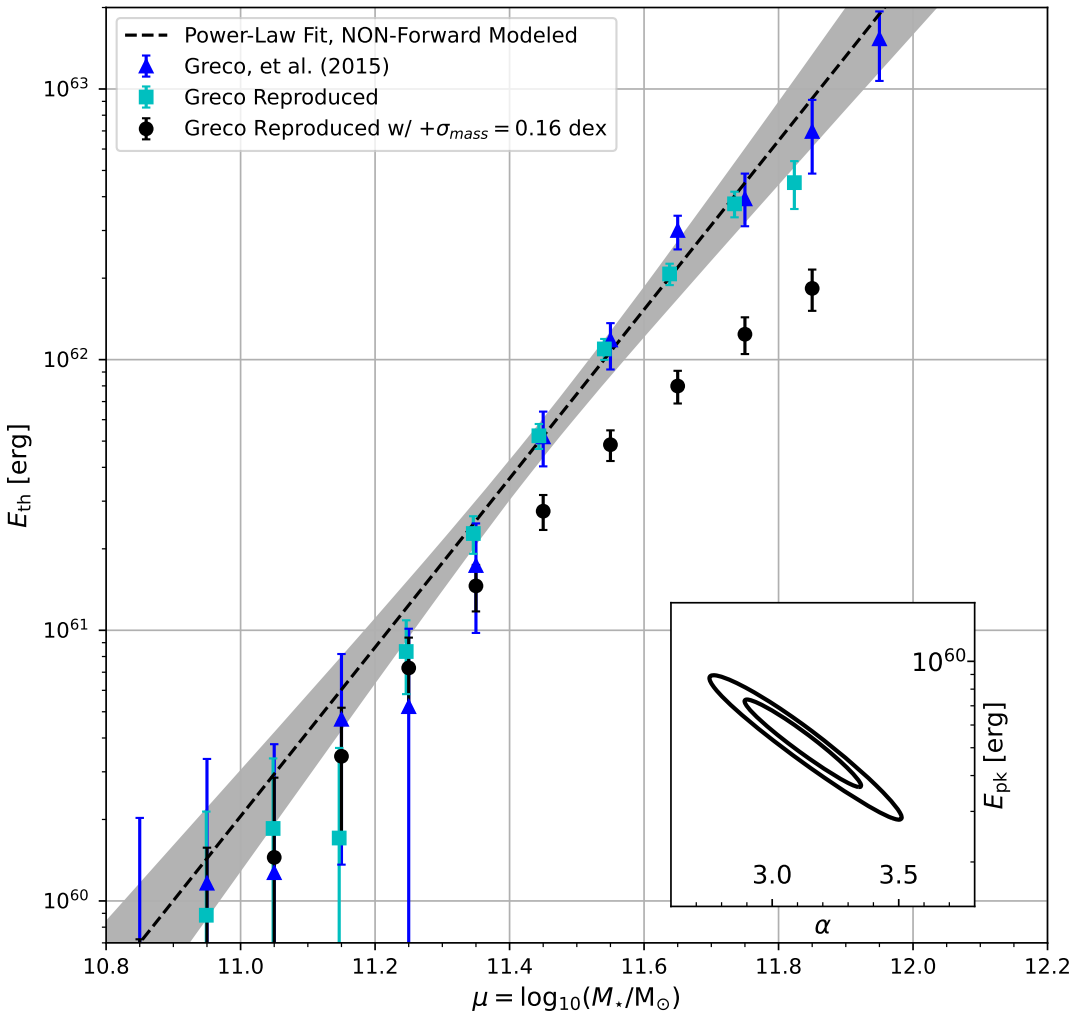

Figure 2.8: Low-z galaxies observed in Greco et al. (2015) converted to thermal energy (*blue triangles*). We also recreated the low-z galaxy sample as described in Greco et al. (2015); Planck Collaboration et al. (2013) and obtained similar results (*cyan squares*). Finally, a major concern with our high-z SPT galaxies is the larger uncertainty in mass ($\sigma_m = 0.16$ dex). Using the recreated low-z galaxies, an additional $\sigma_m = 0.16$ dex uncertainty in mass shows diluted signal in the higher stellar mass bins, indicating our high-z galaxies contain this effect (*black circles*). Error bars represent 1σ uncertainties. We also then show our unconvolved (non-forward-modeled) energy-mass function of eq. (2.3) applied to the flattened bins, producing a slope that aligns well with the original values.

2.5.4 *Reproduction of Previous Low Redshift Results*

To ensure there were no unknown errors in the stacking procedure and code, we reconstructed the locally brightest galaxy catalog used in the studies of Planck Collaboration et al. (2013); Greco et al. (2015) and stacked them with the Planck Modified Internal Linear Combination Algorithm (MILCA) Compton-y map.

The catalog was selected in identical fashion as was done in Planck Collaboration et al. (2013); Greco et al. (2015). Starting from the spectroscopic New York University Value Added Galaxy Catalog[2] (Blanton et al., 2005), which uses the Sloan Digital Sky Survey (SDSS) DR7, $r < 17.7$ magnitude and $z > 0.03$ cuts were first applied. Then any smaller neighbors of the catalog were removed by selecting only galaxies brighter than all other sample galaxies within a 1000 km/s redshift difference and a projected distance of 1.0 Mpc. This method was then repeated with a separate photometric catalog, photoz2 (Cunha et al., 2009). After a final removal of any galaxies within Planck point sources and 40% galactic masks, 243364 galaxies were obtained. This is marginally lower than that reported in Planck Collaboration et al. (2013), likely from a slightly stricter removal of flagged galaxies or updated masks. Since spectroscopic and low redshift, these have a lower stellar mass uncertainty of ≈ 0.1 dex (Blanton and Roweis, 2007) than our photometric and high-z catalog (≈ 0.16 dex). We bin the low-z galaxies in similar $\log_{10}(M_\star/M_\odot)$ 0.1-wide mass bins.

The map used for stacking is a component-separated Modified Internal Linear Combination Algorithm (MILCA) from Planck DR2 [3] (Planck Collaboration et al., 2016e). This map has units of micro Compton-y and a FWHM of $10'$. For simplicity, we use an R = $10'$ radius top-hat aperture and mean-subtract with an annulus from R to R+FWHM. The average equal-weighted signals from mass bins of

[2] https://sdss.physics.nyu.edu/vagc/

[3] https://irsa.ipac.caltech.edu/data/Planck/release_2/all-sky-maps/ysz_index.html

$10.0 < \log_{10}(M_\star/M_\odot) < 11.9$ are shown in Fig. 2.8, converted to thermal energy as in eq. (1.16). Even without simulations for inverse-variance weighting and variable aperture radii, our results compare well with those of Greco et al. (2015) also plotted in Fig. 2.8.

To determine the effect of our larger ≈ 0.16 dex mass uncertainty in our original high-z catalog, we apply a 0.16 dex Gaussian uncertainty to all low-z galaxy masses. By doing a new weighted mass binning according to the likelihood of each galaxy to be in each respective bin, we calculate the new average thermal energies with the 0.16 dex mass uncertainty (also shown in Fig. 2.8). These values reveal a dimming of the signal at high masses, due to contamination from low mass galaxies shifted higher from the uncertainty. This is likely to be similar for our high-z galaxies, and provides a challenge to be accurately corrected. Our method aimed at correcting for this (in Section 2.5.3 and eq. 2.3) can similarly be applied to these purposely dimmed values to obtain $E_{\rm pk} = 0.53^{+0.14}_{-0.11} \times 10^{60}$ erg and $\alpha = 3.12^{+0.12}_{-0.19}$ about a peak mass of $\log_{10}(M_{\star,\rm pk}/M_\odot) = 11.8$. As shown in Fig. 2.8, this aligns well with the expected original results and the slope α is near the $3.77^{+0.60}_{-0.74}$ extracted from our SPT sample in Section 2.5.3.

Later studies (Hill et al., 2018) have also shown a residual two-halo effect occurs for this low redshift catalog, more so evident at the low masses. In some instances, the two-halo contribution was shown to dominate, but further investigation will be needed to translate this to our higher redshift galaxies.

2.5.5 Implications for AGN Feedback

While detailed constraints on AGN models are best carried out with comparisons to full numerical simulations, we can nevertheless draw general inferences from our constraints on $E_{\rm th}$. The first of these is the remarkable similarity between our $z \approx 1$

results and the Greco et al. (2015) at $z \approx 0.1$. It is important to note that these samples were selected by applying slightly different criteria. In our case, we apply cuts on age > 1 Gyr, $SSFR < 0.01$ Gyr^{-1}, while Greco et al. (2015) selects locally brightest galaxies, defined as brighter than all other sample galaxies within a 1000 km/s redshift difference and projected distance 1.0 Mpc. On the other hand, a wide range of theoretical models suggest a good match between the most massive quiescent galaxies at moderate redshifts and the central galaxies of massive halos in the nearby universe (e.g Moster et al., 2013; Schaye et al., 2015; Pillepich et al., 2018).

This lack of significant evolution of thermal energy in the CGM around massive galaxies since $z \approx 1$ parallels the lack of significant evolution in the luminosity function of these galaxies (e.g. van Dokkum et al., 2010; Muzzin et al., 2013). All in all, this trend is slightly more compatible with models in which AGN feedback is dominated by radio mode contributions. This is because in such models, gas accretion contributes to CGM heating and radiative losses will contribute to CGM cooling. Whenever cooling exceeds heating, jets will arise that quickly push the gas up to the constant temperature and entropy at which cooling is inefficient. In quasar models on the other hand, the energy input from feedback occurs once at high redshift, and gas is heated to the point that cooling is extremely inefficient up until today. In this case, gravitational heating will increase $E_{\rm th}$ without any significant mechanism to oppose it. However, the particulars of this evolution are highly dependent on the history of galaxy and halo mergers between $0 < z \lesssim 1$. Hence, it is possible that some types of quasar dominated models may be compatible with our measurements.

A second major inference is the overall level of feedback. As an estimate of the magnitude of gravitational heating, we can assume that the gas collapses and virializes along with an encompassing spherical dark matter halo, and is heated to the virial temperature $T_{\rm vir}$ following eq. (1.17). For massive elliptical galaxies, we can convert

from halo mass to galaxy stellar mass using the observed relation between black hole mass and halo circular velocity (Ferrarese, 2002), and the relation between black hole mass and bulge dynamical (Marconi and Hunt, 2003), as shown in Spacek et al. (2016) that produces eq. (1.18).

This is the total thermal energy expected around a galaxy of stellar mass $M_\star$ ignoring both radiative cooling and feedback. For a mean redshift of ≈ 1.1 and $M_{\star,\mathrm{pk}} = 2.29 \times 10^{11} M_\odot$ this gives $\approx 4 \times 10^{60}$ erg. Note that this estimate has an uncertainty of about a factor of two, which is significantly larger than the uncertainty in our measurements. Nevertheless it is somewhat lower than $E_{\mathrm{pk}} = 5.98^{+1.02}_{-1.00} \times 10^{60}$ erg, suggesting the presence of additional non-gravitational heating, particularly as cooling losses are not included in eq. (1.18).

As a simple estimate of heating due to quasar-mode feedback, we make use of the model described in Scannapieco and Oh (2004) to yield eq. (1.19). For the peak mass and average redshift of our sample, this gives $\approx \epsilon_{k,0.05} 3 \times 10^{60}$ erg. Taking $\epsilon_{k,0.05} = 1$ and adding this to contribution from $E_{\mathrm{th,gravity}}$ above gives a total energy of $\approx 7 \times 10^{60}$ erg. This is on the high side of our measurements, but as it does not account for any energy losses, appears to be a somewhat better match than models without non-gravitational heating.

Finally, radio mode models are expected to fall somewhere between these two limits, with jets supplying power to roughly balance cooling processes, but never adding a large burst of additional energy of the type, estimated in eq. (1.19). This would suggest a somewhat better match to the data than pure-gravitational heating models, but again with far too much theoretical uncertainty to draw any definite conclusions.

A third major inference from our measurements comes from the slope of eq. (2.3), which is significantly steeper than in our simple models. This is most likely due to

uncertainties in the halo-mass stellar mass relation, which are particularly large for the most massive $z \approx 1$ galaxies (Wang et al., 2013; Lu et al., 2015; Moster et al., 2018; Kravtsov et al., 2018; Behroozi et al., 2010, 2019). This represents a major change in the field from only a few years ago, in which tSZ detections at halo masses smaller than galaxy clusters were only marginal, and provided only weak constraints on feedback. Rather, our measurements, along with other recent constraints (Schaan et al., 2021; Amodeo et al., 2021), make it clear that observations are fast outstripping theoretical estimates, and that future close comparisons between measurements and full simulations will yield significant new insights into the history of AGN feedback.

2.5.6 Two-Halo Effect

It is important to recognize that our measurements include the contribution not only from the selected galaxies, but also from the excess of galaxies clustered around them. This so-called two-halo contribution is described in detail in Hill et al. (2018) where it is shown to be significant for lower redshift galaxies and clusters. To estimate the impact of this effect on our $z \approx 1$ sample, we can again make use of a simple model for gravitational heating as given by eq. (1.17). This allows us to compute the excess energy due to the neighboring halos within a radius R perpendicular to a central galaxy of halo mass M_0 as

$$\begin{aligned} E_{\rm therm,2halo} = b(M_0) \int_{10^{11}\,{\rm M}_\odot}^{10^{16}\,{\rm M}_\odot} \frac{dn(M,z)}{dM}\, E_{\rm th,halo}(M,z)\, b(M)\, dM \\ \times \int_{-100R}^{100R} 2\pi \int_0^R dr\, r\, \xi(\sqrt{r^2+l^2}, z)\, dr\, dl, \end{aligned} \tag{2.5}$$

where we account for the excess of neighboring halos with masses between $10^{11} - 10^{16}$ $\rm M_\odot$ within a cylinder of radius R and length $200R$. In this expression, $dn(M,z)/dM$ is the number density of dark matter halos per unit mass, $\xi(r,z)$ is the dark matter correlation function, and $b(M) = 1 + (\nu^2 - 1)/1.69$ (with $\nu \equiv 1.69\sigma(M,z)^{-1}$) is

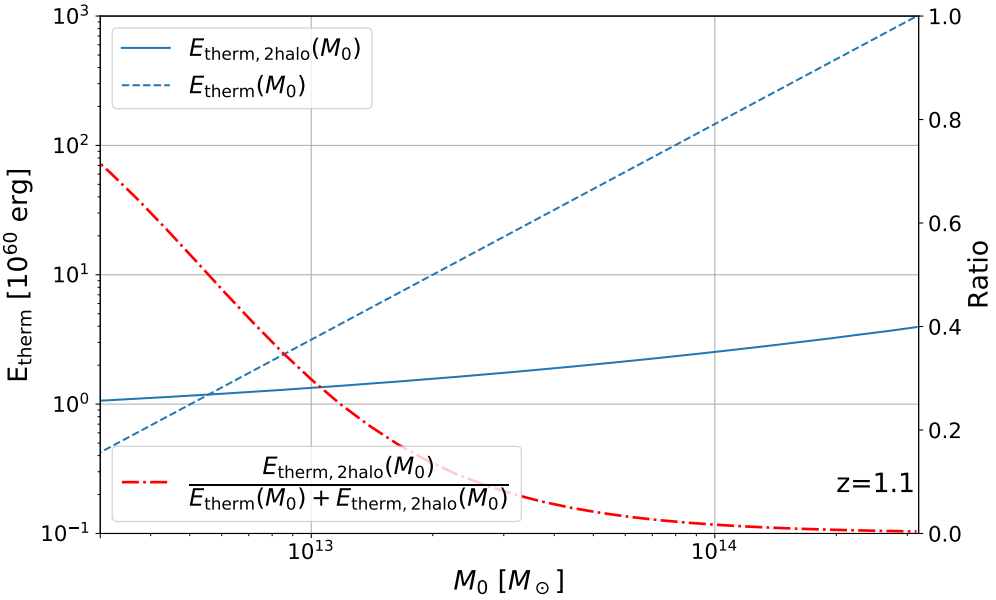

Figure 2.9: Contribution to the thermal energy from a two-halo term (Meinke et al., 2021). The dashed blue line is an estimate of the gravitational thermal energy in the CGM of a galaxy with a given halo mass (x-axis). The solid blue line estimates the total thermal energy in a cylinder (radius = 2 Mpc x len = 400 Mpc) centered and stacked on a galaxy with a given halo mass. This estimate uses the 2-point correlation function to include galaxies within the cylinder given the mass of the central galaxy, M_0 (see details in the text). All data is for z=1.1. The red dot-dashed line indicates the ratio of the energy in the cylinder to the sum of both curves and uses the y-axis to the right, which shows that the central halo dominates the total energy when its mass exceeds $\approx 10^{13} M_\odot$ or when $E_{\rm th}$ exceeds $\approx 3 \times 10^{60}$ erg.

bias factor that accounts for mass-dependent differences between the underlying dark matter density field and the distribution of massive dark matter halos (Mo and White, 1996).

In Fig. 2.9 we compare the energy in the central halo given by eq. (1.17) to the two-halo contribution given by eq. (2.5), over the range of halo masses from $M_0 = 10^{12.5} - 10^{14.5}\, M_\odot$. In this figure, we use the Code for Anisotropies in the Microwave Background (Lewis and Challinor, 2011) to compute the dark matter correlation function, $\xi(r, z)$, and the rms fluctuations at a redshift z within a sphere containing a mass M, $\sigma(M, z)$, and we compute the number density of halos, $dn/dM(M, z)$, according to the standard Press and Schechter (1974) formula.

While the relationship between galaxy stellar mass and halo mass at $z \approx 1.1$ is uncertain as mentioned above, the fact that the central halo becomes $E_{\rm th,halo} \gg E_{\rm therm,2halo}$ when the total thermal energy exceeds $\approx 3 \times 10^{60}$ erg suggests that the majority of our measurements are in the range for which the central halo is dominant. The reason that the two halo term is significantly less important than at $z \approx 0$ is because the dark matter structures have had less time to collapse, meaning that the matter correlation function ξ is significantly smaller than at $z \approx 1$ than it is today. Thus, although this effect merits careful consideration in comparisons with simulations, it is less likely to complicate the analysis to the degree it does for more local samples (e.g. Schaan et al., 2021). In addition, although this cannot be computed directly from eq. (2.5), the two halo contribution is likely to become more important on sightlines with large impact parameters from the selected galaxies, and thus it is important to keep in mind when interpreting the tSZ radial profile, a topic to which we turn our attention in the next section.

2.5.7 Radial Profile

The radial profile of the tSZ signal has been recently studied at lower redshifts with the latest ACT release at similar angular resolution (Schaan et al., 2021). To compare against this study, we apply the same procedure as in Schaan et al. (2021) to compute this profile: summing within a cap or top-hat shape of radius R, and subtracting the neighboring pixels out to $\sqrt{2}R$ to remove the surrounding background offset such as from the primary CMB. In this case we abstain from the high-pass filtering done in our main stellar mass bin analysis.

The profile of our SPT galaxies is shown in Fig. 2.10, where it is compared to the CMASS sample in Schaan et al. (2021) which has a mean redshift of $z = 0.55$ and mean $\log_{10}(M_\star/M_\odot)$ in linear units is $\approx 2 \times 10^{11} M_\odot$. As a preliminary analysis,

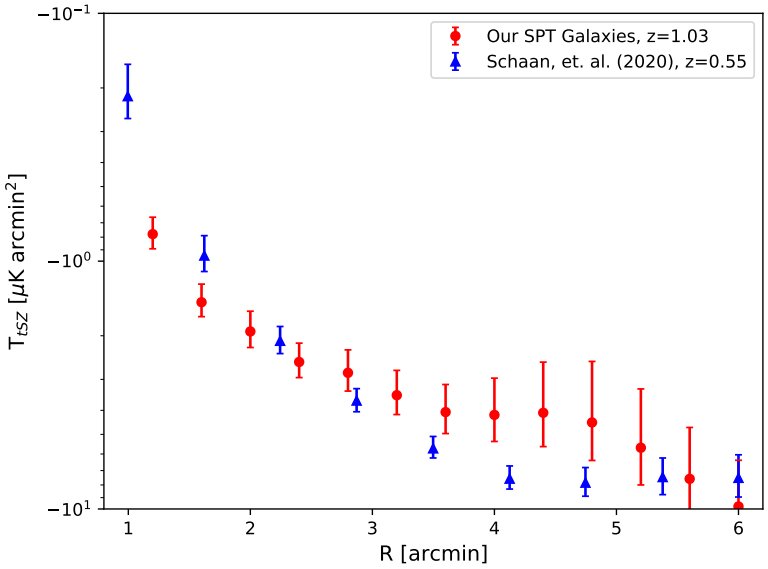

Figure 2.10: Radial profile of our complete (N=138235) SPT galaxy catalog (*red circles*, $1' = 1.01$ comoving Mpc $= 0.50$ proper Mpc @ $z = 1.03$), alongside the recent profile from Schaan et al. (2021) (*blue triangles*, $1' = 0.61$ comoving Mpc $= 0.39$ proper Mpc @ $z = 0.55$). The y-axis is in units of integrated CMB temperature at 150 GHz (μK arcmin^2). The two profiles are similar even with their difference in redshift.

we stack all N=138,325 SPT galaxies, and apply the same style aperture from $R = 1.2 - 6.2'$ radius, at each band. We then use our two-component fit of eq. (2.1) using the median redshift of $z = 1.03$, and dust parameters T $= 20 \pm 5$K and $\beta = 1.75 \pm 0.25$ applied as before. The final tSZ values are converted to integrated CMB temperature with respect to 150 GHz, as in Schaan et al. (2021). The two tSZ profiles have very similar overall shapes. Our profile however is slightly less defined with larger uncertainty, due to being at higher redshift and a smaller sample size. A more detailed comparison, such as by mass-binning and fitting to profile models, is left for future work.

2.6 Discussion

From $z \approx 1$ to $z \approx 0$, dark matter halos continue to merge and accrete material, but the growth of massive galaxies over this redshift range is minimal, with

$\log_{10}(M_\star/M_\odot) = 11.15$ galaxies growing in mass by less than 0.2 dex (Muzzin et al., 2013). To explain this surprising trend, theoretical models have been forced to invoke significant energy input from AGN, which heats the medium surrounding massive galaxies to temperatures high enough to prevent it from cooling and forming further generations of stars. On the other hand, such AGN feedback is largely unconstrained by observations.

Here we make use of measurements of the tSZ effect to derive direct constraints that can be applied to such models. As the total tSZ distortion along a given sightline is proportional to the line-of-sight integral of the pressure, the total signal summed over the area of sky around any object is proportional to the volume integral of the pressure, or the total thermal energy. This means that by summing the Compton distortions over the patches of sky around galaxies, we can directly measure the thermal energy of the CGM surrounding them.

We apply this technique to constrain the signal of 138,235 $z \approx 1$ galaxies, selected from the DES and WISE surveys. Data from the SPT at 95, 150, and 220 GHz were stacked around the galaxies, spatially filtered to separate the signal from primary CMB fluctuations, and fit with a gray-body model to remove the dust contribution, which is detected with a signal to noise ratio of 9.8σ. The resulting tSZ around these galaxies is detected with an overall signal to noise ratio of 10.1σ, which is large enough to allow us to partition the galaxies into 0.1 dex stellar mass bins from $M_\star = 10^{10.9} M_\odot$ - $10^{12} M_\odot$, which have corresponding tSZ detections of up to 5.6σ. We also observe significantly more dust at these frequencies than previous low redshift studies (Planck Collaboration et al., 2013; Greco et al., 2015), and a noticeable increase in dust signal with larger mass bins.

As the stellar mass distribution of our selected galaxies is highly peaked at $M_{\star,\mathrm{pk}} = 2.3 \times 10^{11} M_\odot$, the 0.16 dex uncertainty in our photometric fits to the masses is large

enough to 'flatten' our measurements, shifting a significant number of galaxies near the distribution peak into wings where they can overwhelm signal from the much smaller galaxy counts at low and high masses. To correct for this effect, we carry out a two parameter fit for the unconvolved energy-mass relation that best fits our data, of the form $E_{\rm th} = E_{\rm pk}\left(M_\star/M_{\star,\rm pk}\right)^\alpha$. In this case, we find an amplitude at the mass peak of $E_{\rm pk} = 5.98^{+1.02}_{-1.00} \times 10^{60}$ erg and a slope of $\alpha = 3.77^{+0.60}_{-0.74}$. This, however, would not take into account any inherent biases in our stellar mass uncertainty, such as a potentially smaller uncertainty for our brighter, more massive galaxies.

This aligns well with previous $z \approx 0$ studies, indicating a good match between the thermal energy of the CGM surrounding the most massive quiescent galaxies at moderate redshifts, and the central galaxies of massive halos in the nearby universe. When compared to theoretical models, our energy-mass relation best corresponds to moderate radio mode feedback. Purely gravitational heating predictions are slightly lower than the final results, while quasar-mode AGN feedback models are slightly higher. However, all of these models have wide enough uncertainties that definitive conclusions are difficult to be drawn from them. This means that observations are no longer in the regime of marginal detections, and are quickly outstripping the capabilities of theoretical estimates. This further highlights the need for improved theoretical models to keep pace with the ever-increasing observational capabilities.

The limitations in our observational analysis primarily stem from our ability to accurately fit and remove the large dust component such as seen in the galaxy stacks in Fig. 2.4 and the dust fit in Fig. 2.5. The dust fit amplitude is set mainly by the 220 GHz band, and we use a spectral emissivity index β and dust temperature $\rm T_{dust}$ with large uncertainty due to our inability to fit them with only three frequency bands. The addition of a similar resolution survey at far-infrared frequencies would provide a better fit of all thermal dust parameters.

We also recognize there is a likely two-halo contribution term for these stacking type measurements, which was shown to be large in Hill et al. (2018) for lower redshift galaxies and clusters. While simple models such as presented in Section 2.5.6 suggest that the contribution of this effect to the total SZ signal is small for the majority of our $z \approx 1$ galaxies, the exact significance of the two-halo contribution to our measurements of the radial profile are yet to be determined.

An initial radial tSZ profile of our entire galaxy sample in Section 2.5.7 highlights the similarities with lower redshift studies (Schaan et al., 2021). Additional investigation will be needed to refine and compare to profile models, including the impact of additional sources such as the aforementioned two-halo term.

Similar resolution surveys across more of the sky, such as planned with the next generation Atacama Cosmology Telescope instrument (Advanced ACTPol Koopman et al., 2018), will enable a larger sampling area. Likewise, advances in spatial resolution, such as will be possible using the TolTEC camera being built for the 50-meter Large Millimeter-wave Telescope (Bryan et al., 2018), will allow for a cleaner separation between the tSZ signal, which comes primarily from the CGM, and the dust signal, which comes primarily from the underlying galaxy. Such developments promise to yield dramatic new insights into the physical processes that shaped the most massive galaxies in the universe.

Chapter 3

EVIDENCE OF EXTENDED DUST AND FEEDBACK AROUND $z \approx 1$ QUIESCENT GALAXIES VIA MILLIMETER OBSERVATIONS

This chapter is a slightly modified version of a manuscript submitted for publication in The Astrophysical Journal (ApJ), with permission from the co-authors.

3.1 Introduction

As already discussed in Section 1.3 and the previous investigation in Chapter 2, massive elliptical galaxies show reduced star formation best thought to be quenched through AGN feedback. Two common models are frequently proposed. The first and stronger of the two, 'quasar mode' feedback impacts a galaxy's CGM when the supermassive black hole accretes rapidly to produce extreme outbursts. This torrent of energy heats the CGM such that the gas cooling time is longer than the Hubble time and suppresses star formation to this day. Meanwhile 'radio-mode' feedback has the supermassive black hole at low accretion rates produce jets of relativistic particles that act as a more continuous heating mechanism. This instead is thought to balance gas cooling processes, but may not be significant for lower mass gravitational potentials (Werner et al., 2019).

The relationship of eq. (1.16) allows thermal energy of the CGM to be probed via the tSZ effect (Section 1.2.2) and compared to feedback models. It also means that improvements in the sensitivity and angular resolution of tSZ measurements translate directly to better constraints on thermal energy. Thus, cosmic structures with higher gas thermal energies, galaxy clusters, are most easily detected and indeed, have been the focus of tSZ measurements over the last decade (e.g. Planck Collaboration et al.,

2011; Reichardt et al., 2013; Planck Collaboration et al., 2016a; Hilton et al., 2018; Lokken et al., 2022).

Further challenges arise when going to lower mass halos. Bright targets such as quasars with abundant amounts of outflowing gas are detectable in tSZ on an individual basis using ALMA (Lacy et al., 2019; Brownson et al., 2019). However, averaging over many objects is currently required for appreciable detection of most samples. Chatterjee et al. (2010) stacked quasars and galaxies with data from the Wilkinson Microwave Anisotropy Probe (WMAP) and Sloan Digital Sky Survey (SDSS) to find a tentative $\approx 2\sigma$ tSZ signal suggesting AGN feedback; Hand et al. (2011) used data from SDSS and the Atacama Cosmology Telescope (ACT) to see a $\approx 1\sigma - 3\sigma$ tSZ signal around galaxies; Gralla et al. (2014) found a $\approx 5\sigma$ detection for AGNs with ACT; Ruan et al. (2015) used SDSS and Planck to find $\approx\ 3.5\sigma - 5.0\sigma$ tSZ signals around both quasars and galaxies; Crichton et al. (2016) used SDSS and ACT to find a $3\sigma - 4\sigma$ SZ signal around quasars; Hojjati et al. (2017) found a $\approx 7\sigma$ tSZ detection suggestive of AGN feedback with data from Planck and the Red Cluster Sequence Lensing Survey; and (Hall et al., 2019) used ACT, Herschel, and the Very Large Array data to measure the tSZ effect around $\approx 100,000$ optically selected quasars, finding a 3.8σ signal that provided a joint constraint on AGN feedback and mass of the $z \gtrsim 2$ quasar host halos.

Recent measurements have also been made around massive galaxies. Greco et al. (2015) used SDSS and Planck data to compute the average tSZ signal from a range of over 100,000 'locally brightest galaxies' (LBGs) at $z \lesssim 0.5$. This sample was large enough to derive constraints on $E_{\rm th}$ as a function of galaxy stellar mass $M_\star$ for objects with $M_\star \gtrsim 2 \times 10^{11}$ $\mathrm{M}_\odot$. At redshifts $0.5 \lesssim z \lesssim 1.5$ Spacek et al. (2016, 2017) studied the tSZ signal from massive quiescent galaxies. These are prime candidates for which AGN feedback is thought to quench star formation and where a significant

excess tSZ signal is expected to be produced in the CGM (e.g. Scannapieco et al., 2008). Spacek et al. (2016) performed a stacking analysis with the 150 and 220 GHz South Pole Telescope's (SPT) 2011 data release, using a 43 $\deg^2$ overlap with VISTA Hemisphere Survey and Blanco Cosmology Survey data to select samples of up to 3394, finding a $\approx 2-3\sigma$ signal hinting at non-gravitational heating. While Spacek et al. (2017) used SDSS and the Wide-Field Infrared Survey Explorer (WISE) data overlapping with 312 $\deg^2$ of 2008/2009 ACT data at 148 and 220 GHz, finding a marginal detection that was consistent with gravitational-only heating models. With the latest SPT release covering 2500 $\deg^2$, Meinke et al. (2021) stacked nearly $140,000$ quiescent galaxies selected in a similar process from the Dark Energy Survey (DES) and WISE, to obtain a combined 10.1σ detection of tSZ at $z \approx 1$. They found the signal was most consistent with moderate forms of AGN feedback models.

Other measurements with the latest *Planck* y-maps have been successfully conducted on nearby targets. Support for AGN feedback in local galaxy groups was found by Pratt et al. (2021). While Bregman et al. (2022) observed a 4.0σ detection of the tSZ effect in 11 local L^* spiral galaxies.

The recent ACT DR5 data release (Mallaby-Kay et al., 2021) has unlocked additional parts of the sky for detailed analysis. Schaan et al. (2021) and Amodeo et al. (2021) combined microwave maps from ACT and Planck with galaxy catalogs from the Baryon Oscillation Spectroscopic Survey (BOSS), to study the gas associated with these galaxy groups. They constrained the gas density profile through measurements of the tSZ signal at $\approx 10\sigma$ and a weaker detection of the kinetic Sunyaev-Zel'dovich effect (kSZ, Sunyaev and Zeldovich, 1980), which is caused by peculiar motions. They were able to compare these results to cosmological simulations (Battaglia et al., 2010; Springel et al., 2018) to find that the feedback employed in these models was insufficient to account for the gas heating observed at $\approx$ Mpc scales. Meanwhile Calafut

et al. (2021) and Vavagiakis et al. (2021) used SDSS and ACT to detect kSZ measurements consistent with one another. Vavagiakis et al. (2021) also found up to a 12σ detection of the tSZ in their galaxy groups and clusters. A novel oriented stacking method was also used in Lokken et al. (2022) on DES clusters to identify tSZ associated with the cosmic web. These are just a first step in a new wave of tSZ and kSZ analyses as more data becomes available.

A significant difficulty in accurate tSZ detection is the presence and removal of dust. This becomes all the more important for higher redshift samples in far-infrared and millimeter bands. Many tSZ studies have sought to simply remove this contaminant source, although there have also been an increasing number of mid- and far-infrared (MIR; FIR) studies with a primary emphasis on the dust associated with galaxies (Berta et al., 2016; Gobat et al., 2018). Dust is an excellent tracer of galaxy characteristics such as star formation and gas, and is a key component in understanding galaxy dynamics (Santini et al., 2014; Calura et al., 2016; Donevski et al., 2020). Despite having a lower star formation rate, dust in quiescent galaxies is still significant. A recent study by Magdis et al. (2021) highlights a noticeable increase in dust-to-stellar mass ratio for quiescent galaxies between $z = 0$ and $z = 1$.

Here we expand upon the work of Meinke et al. (2021) (Chapter 2) by including the recent millimeter-wave data from ACT DR5 and conducting a more detailed analysis of dust. Using the same quiescent galaxy selection method with DES and WISE, we now analyze data from where the SPT and ACT telescopes overlap within $\approx 2,100$ deg^2 in the Southern Hemisphere. An ACT-only analysis is also conducted over the larger ACT field, which shares $\approx 4,600$ deg^2 with DES and WISE. We apply a two-component fit to separate the tSZ and dust components, both in bins by radial profile and stellar mass. We compare these profiles to expectations and other relevant studies, detecting signals up to 11.6σ tSZ and 21.5σ dust in the centermost radial

bins. Divided into stellar mass bins, we calculate the thermal energy and dust mass versus stellar mass. We then compare our thermal energies to current simple feedback models to provide needed constraints for future simulations.

In Section 3.2 we describe all data sets used for our analysis. In Section 3.3 we outline our galaxy selection procedure, and the overall properties of the massive, moderate-redshift, quiescent galaxies we use for stacking. In Section 3.4, we detail all considerations and stacking processes used (Section 3.4.1-3.4.9), followed by our various results extracted from both the dust and tSZ associated with our samples (Section 3.4.10-3.4.15). Discussions are given in Section 3.5.

3.2 Data

Our analysis uses five public datasets: two for galaxy selection, and three to conduct our stacking analysis upon. For selection, we make use of optical and near-infrared data from DES data release 1 (Abbott et al., 2018), which are already matched to AllWISE data spanning $3 - 25$ μm (Schlafly et al., 2019). We select and carry out photometric fitting of passive galaxies at $0.5 \lesssim z \lesssim 1.5$ that requires this large span of wavelengths. Finally, the maps we stack include millimeter-wave observations from both the SPT-SZ (Bocquet et al., 2019) and ACT surveys (Naess et al., 2020), along with a Planck component-separated CMB map (Planck Collaboration et al., 2020a). The datasets are described in more detail below. Footprints of DES, SPT-SZ and ACT DR5 are shown in Fig. 3.1.

3.2.1 DES

DES DR1 consists of optical and near-infrared imaging from 345 nights between August 2013 to February 2016 by the Dark Energy Camera mounted on the 4-m Blanco telescope at Cerro Tololo Inter-American Observatory in Chile. The data

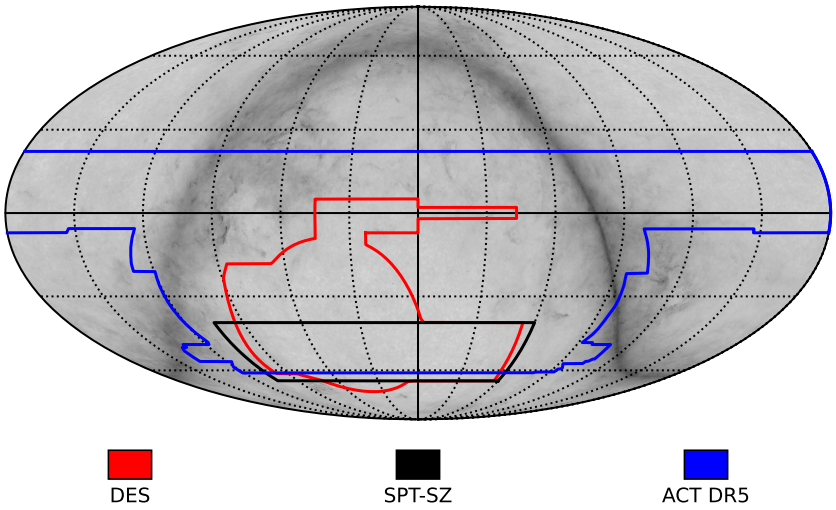

Figure 3.1: Mollweide (equatorial) projected sky footprints showing the coverage of DES (*red*), SPT-SZ (*black*), and ACT (*blue*) surveys used in this analysis. The *Planck* HFI 353 GHz is shown in the background. This was made with the help of publicly available resources at https://lambda.gsfc.nasa.gov/toolbox/footprint/.

covers $\approx$ 5000 deg^2 of the South Galactic Cap in five photometric bands: grizY. These five bands have point-spread functions of g = 1.12 arcsec, r = 0.96 arcsec, i = 0.88 arcsec, z = 0.84 arcsec, and Y = 0.90 arcsec FWHM (Abbott et al., 2018). The survey has exposure times of 90s for griz and 45s for Y band, yielding a typical single-epoch PSF depth at S/N = 10 for g $\lesssim$ 23.57, r $\lesssim$ 23.34, i $\lesssim$ 22.78, z $\lesssim$ 22.10 and Y $\lesssim$ 20.69 mag (Abbott et al., 2018). Here and below, all magnitudes are quoted in the AB system (i.e. Oke and Gunn, 1983).

3.2.2 WISE

The AllWISE catalog is derived from data from the 40 cm diameter Wide-field Infrared Survey Explorer (WISE) NASA Earth orbit mission (Wright et al., 2010; Mainzer et al., 2011). WISE carried out an all-sky survey in 2010 of the sky in bands W1, W2, W3 and W4, centered at 3.4, 4.6, 12 and 22 μm, respectively (Schlafly

et al., 2019). AllWISE uses the post-cryogenic data of the WISE mission to produce a deeper coverage in W1 and W2, which are the two bands used here.

The added sensitivity of AllWISE extends the detection limit of luminous distant galaxies because their apparent brightness at 4.6 μm (W2) no longer declines significantly with increasing redshift. The increased sensitivity yields better detection of those galaxies for redshift $z > 1$, which are the primary focus of this analysis.

3.2.3 SPT-SZ

The SPT-SZ survey (Chown et al., 2018) covered $2,500$ deg^2 of the southern sky between 2007 to 2011 in three different frequencies: 95 GHz and 150 GHz, which lie on either side of the maximum tSZ intensity decrement ($\approx$ 128 GHz), and 220 GHz, which is very near the tSZ null frequency, $\nu_{\rm null} = 217.6$ GHz. The South Pole Telescope (SPT) is a 10 m telescope located within 1 km of the geographical South Pole and consists of a 960-element bolometer array of superconducting transition edge sensors.

The SPT maps used in this analysis are publicly available[1] combined maps of SPT and all-sky Planck satellite (with similar bands at 100, 143, and 217 GHz). Each combined map has a provided beam resolution of $1.85'$ FWHM, and is given in a HEALPix (Hierarchical Equal Area isoLatitude Pixelation) format with $N_{\rm side} = 8192$ (Chown et al., 2018).

3.2.4 ACT

The DR5 data release from the Atacama Cosmology Telescope (ACT) contains combined maps from observations during 2008-2018 (ACT-MBAC and ACTpol, Naess

[1] https://lambda.gsfc.nasa.gov/product/spt/index.cfm

et al., 2020; Mallaby-Kay et al., 2021). These are publicly available[2] and cover $\approx 18,000\,\mathrm{deg}^2$, predominantly in the Southern Hemisphere. ACT uses a 6 m telescope with transition edge bolometer detectors. The provided maps include three frequency bands centered near 90, 150, and 220 GHz. For our purpose, we use the combined ACT+*Planck*, day+night, source-free frequency maps. These have provided FWHM resolutions of $2.1'$, $1.3'$, and $1.0'$, respectively. ACT maps differ from SPT and *Planck* by projection; instead given in CAR (Plate-Carrée), cylindrical coordinates of right ascension and declination.

3.2.5 Planck

The *Planck* Satellite was launched in 2009 by the European Space Agency and operated from 30 to 857 GHz in 9 total frequency bands. Taking measurements until 2013, *Planck* proved invaluable to the study of CMB anisotropies and the early Universe. Its third and ultimate data release in 2018 included full-sky frequency and component-separated maps (Planck Collaboration et al., 2020a). Of importance to us are the *Planck* CMB maps generated from various component separation techniques (Planck Collaboration et al., 2020d). Here we have elected to use the *Planck* SMICA (Spectral Matching Independent Component Analysis) SZ-free CMB map with SZ sources projected out, to safely remove large-scale CMB anisotropies around our sample area. This map has a resolution of $5.0'$ FWHM, provided in HEALPix format with $N_{\mathrm{side}} = 2048$. All of the *Planck* products mentioned are publicly available[3].

[2] https://lambda.gsfc.nasa.gov/product/act/actpol_prod_table.cfm

[3] https://irsa.ipac.caltech.edu/data/Planck/release_3/docs/

3.3 Defining the Galaxy Sample

3.3.1 Selection

We carried out our initial galaxy selection using the DES database server at NOAO, called NOAO-Lab. In order to start with a manageable sample, we applied a cut in color-color space designed to select old galaxies with low star-formation rates at approximately $1.0 \leq z \leq 1.5$ in the initial database query, as previously shown in Meinke et al. (2021). We used mag_auto from the DES in *grizy* bands, along with *W1* and *W2* PSF-magnitudes (converted to AB-system) from AllWISE (Wright et al., 2010; Mainzer et al., 2011) joined to the main DES table. The bands and color-selection used here are slightly different than Spacek et al. (2017) used in SDSS Stripe 82.

The NOAO Data lab allows direct queries in SQL via Jupyter notebook on their server. The lines we used to make the color selection were:

`((mag_auto_z_dered-(w1mpro+2.699)) <= (1.37*mag_auto_g_dered-1.37*mag_auto_z_dered-0.02))` and `((mag_auto_z_dered-(w1mpro+2.699))>=2.0)`.

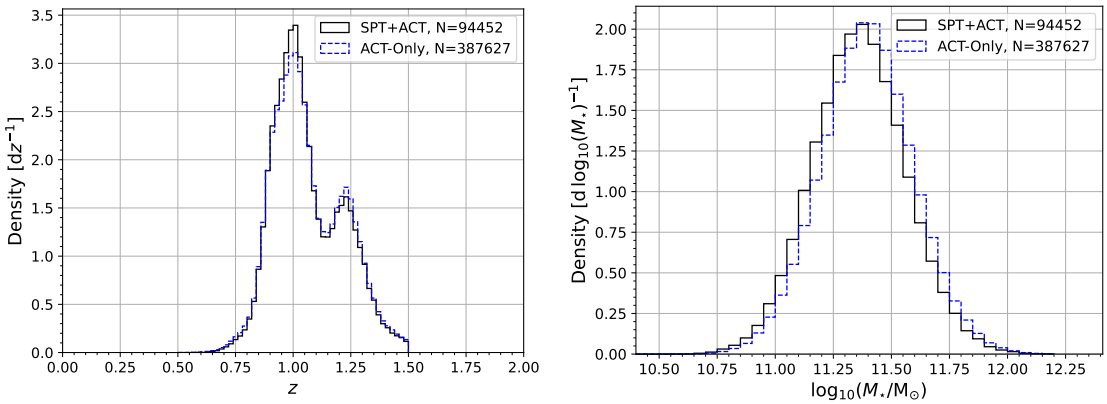

(a) Redshift Histogram

(b) $\log_{10}$ Stellar Mass Histogram

Figure 3.2: (a) Redshift and (b) $\log_{10}$ stellar mass distributions of the two samples, SPT+ACT (*black*) and ACT-Only (*blue, dashed*). After SED selection, normalized by count N and bin-width.

3.3.2 *Photometric Fitting*

After the galaxies were selected, photometric redshifts were computed using EAZY (Brammer et al., 2008) and the seven broad bands *grizyW1W2*. In calling EAZY, we used the CWW+KIN (Coleman et al., 1980; Kinney et al., 1996) templates, and did not allow for linear combinations. Since we are looking for red galaxies and have a gap in wavelength coverage between *y*-band and *W1*, we were worried that allowing combinations of templates would yield unreliable redshifts, where e.g., a red template was fit to the IR-data and a blue one was fit to the optical data and they met in the wavelength gap.

Catalog	N	$\widetilde{z}$	$\overline{z}$	$\log_{10}(\widetilde{M_\star}/\mathrm{M}_\odot)$	$\log_{10}(\overline{M_\star}/\mathrm{M}_\odot)$
SPT+ACT	$94,452$	1.031	1.063	11.36	11.41
ACT-Only	$387,627$	1.037	1.066	11.40	11.44

Table 3.1: Galaxy catalogs used in this analysis with redshifts and stellar mass statistics. Both catalogs were selected from DES and WISE as described in Section 3.3.

Once the redshifts were measured, we fit the spectral energy distributions (SEDs) using our own code, following the method in Spacek et al. (2017), to which the reader is referred for more details. Briefly, a grid of BC03 (Bruzual and Charlot, 2003) models with exponentially declining star formation rates (SFRs) was fit over a range of stellar ages, SFHs (i.e., τ), and dust-extinction values ($0 < A_V < 4$). Our code uses BC03 models assuming a Salpeter initial mass function (IMF), but to facilitate comparisons with the literature, we convert all stellar masses to the value assuming a Chabrier IMF (0.24 dex offset; Santini et al. (2015)). As in Spacek et al. (2017), we choose as our final sample all galaxies with age$>$ 1 Gyr, $SSFR < 0.01\mathrm{Gyr}^{-1}$,

$0.5 < z_{\rm phot} < 1.5$, and reduced $\chi^2 < 5$. Final redshift and stellar mass distributions are shown in Fig. 3.2.

Unlike Meinke et al. (2021) (Chapter 2), we do not directly remove any galaxies near source contaminants in order to limit potential radial profile biases. However both SPT and ACT maps are provided with bright sources already masked, as discussed further below.

3.4 Analysis

A summary with examples for many of the Python methods used here, including a custom Bayesian estimation code, is publicly available online[4].

3.4.1 Neighboring Sources

The SPT-SZ maps contain an applied mask of all bright 150 GHz sources greater than 50 mJy. This was done in Chown et al. (2018), through the removal of all signal within $5'$ and apodization with a $5'$ Gaussian beam. For our purposes these locations result in a large hole that potentially skews measurements. We avoid them by using the SPT-SZ provided mask to remove any targets within $20'$ of a masked pixel. A custom map depicting minimum distance to the nearest masked pixel, shown in Fig. 3.3, is used for this filtering purpose. The SPT+ACT random catalog described in Section 3.4.5 also applies this removal process.

Similarly, we have chosen to use the source-free ACT maps. They however differ from SPT-SZ, as all sources removed were done so using a finer matched filter and fitting procedure (Naess et al., 2020). We have found this source removal process has a minimal effect on our stacking results.

[4]https://github.com/JeremyMeinke/mm_astronomy_stacking

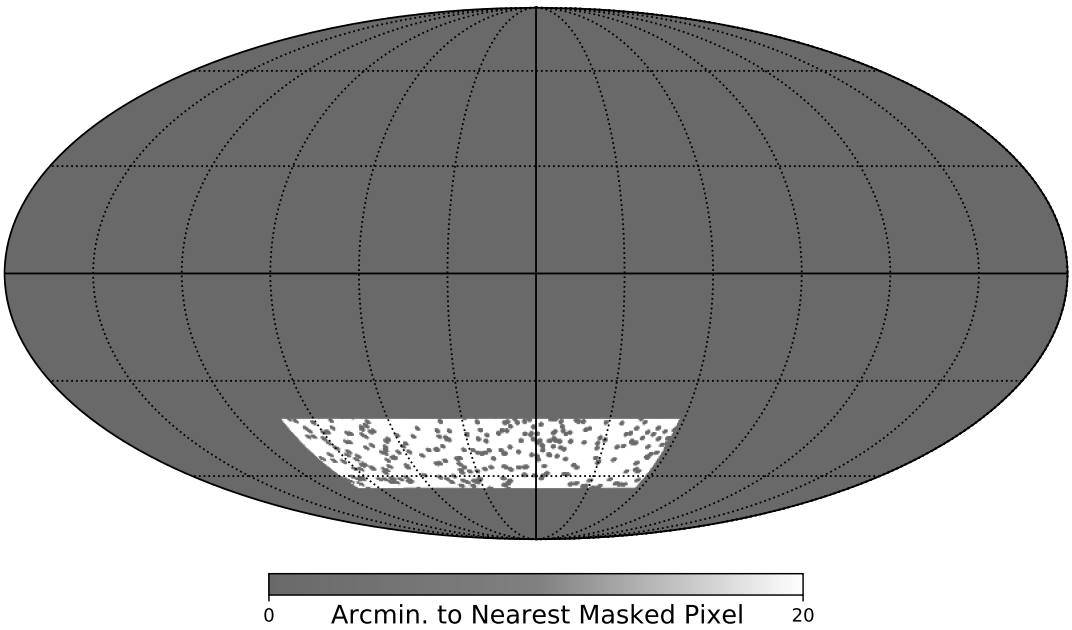

Figure 3.3: Mollweide (equatorial) projected map showing the distance to the nearest masked pixel for the SPT-SZ mask used in Chown et al. (2018). For our radial profile stacking needs, we have dropped any galaxies within $20'$ of a masked pixel.

3.4.2 Map Processing

The SPT and ACT maps span similar frequency bands and regions of the sky, making them ideal products for tSZ and dust comparisons. However, we employ multiple steps to further process the maps into similar formats and ensure all likely systemic differences are minimized. Notably:

- The maximum spherical harmonic or Legendre polynomial degree $\ell_{\rm max}$, differs between the provided maps of SPT ($\ell_{\rm max} = 10,000$) and ACT ($\ell_{\rm max} = 30,000$). For consistency, we elect to use the smaller limit of $\ell_{\rm max} = 10,000$ on each, cutting all higher-order terms within ACT. This removes ACT fluctuations at near pixel-size scales and introduces greater correlation between neighboring pixels, but otherwise does not significantly influence our results.

- Respective beam functions of all frequencies were replaced with a Gaussian beam of $2.10'$ FWHM. This corresponds to the lowest resolution map (ACT 90GHz). The operation was done on the spherical harmonics ($a_{\ell m}$), with the aforementioned cutoff at $\ell_{\max} = 10,000$.

- To remove any potential discrepancies due to projection differences, all ACT maps in their original Plate-Carée projection were converted into the SPT's HEALPix format with $N_{side} = 8192$. They were first transformed to spherical harmonics, beam and pixel window function corrections applied, and transformed into the final HEALPix map.

- For each frequency map, the SMICA CMB map was masked with the corresponding instrument's boundary mask and converted into spherical $a_{\ell m}$ coefficients. The pixel window function was replaced with the $N_{side} = 8192$ HEALPix pixel window function of the final map format. The CMB map was then subtracted from the desired frequency map(s). This approach is akin to a high-pass filter, removing all large-scale CMB anisotropies to help reduce overall noise at small angular scales and correlation at larger scales.

- The HEALPix projection does not lend itself to uniform stacking of individual pixels and we also seek to place our target galaxies in the direct center of measurements. Thus, all cutouts were made on a gnomonic-projected grid with a pixel resolution of $0.05'$ directly centered on the target galaxies. A HEALPix map with $N_{side} = 8192$ has pixel side lengths of roughly $0.18'$, so we are purposely oversampling for finer alignment. Bilinear interpolation was used to prevent any artificial beam effects from the pixel window function and allow additional precision in positioning. Final image cutouts of our SPT+ACT sample are shown in Fig. 3.4 in both SPT and ACT processed maps. As outlined in

the following subsection, final measurements were conducted on each individual galaxy cutout and then averaged together.

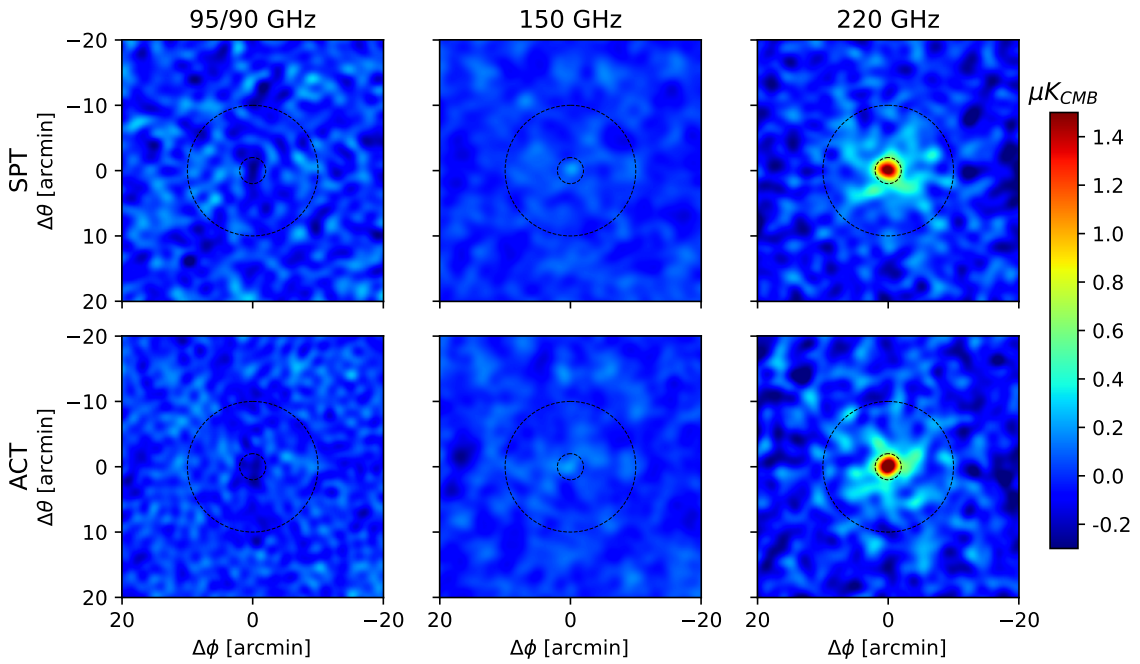

Figure 3.4: SPT+ACT galaxy stacks ($N = 94,452$) for their respective SPT and ACT frequency maps, processed according to Section 3.4.2. A gradient was also removed from each image. Dashed circles correspond to radii of $2.0'$ and $10'$.

3.4.3 Radial Profile

With the smoothed and CMB-subtracted frequency maps, we measure the radial profile around all galaxies in our catalog. We choose to create radial bins with uniform widths of $0.50'$, out to a radius of $20.0'$. For our mean redshift of roughly ≈ 1.1 this translates to a furthest comoving distance of 21 Mpc $\approx 14h^{-1}$ Mpc. Gnomonic projection cutouts were made around each galaxy with a pixel size of $0.05'$. Cutouts were mean subtracted, and radial bin averages as described above were measured on each catalog location individually. All samples of interest were then averaged with equal weight to create a final radial profile per map.

With three frequencies, we are able to fit both the tSZ and the dust that obscures it. However, any attempts to fit potential mean offsets from CMB or foreground signals would result in overfitting. For this reason we assume all profiles go to zero at large radii. We calculate the average signal in the three largest bins $(18.5 - 20.0')$ and subtract it as an offset from the entire radial profile for each frequency map. This method also subtracts any large-scale extragalactic background light (EBL) that might have further biased results. We recognize this subtraction likely truncates a non-zero signal, but at $20'$ consider it negligible in amplitude and detection. For completeness, we test the effect by comparing different numbers of furthest bin subtractions from one $(19.5 - 20.0')$ to ten $(15.0 - 20.0')$, which results in a shift of $< 0.5\sigma$ for 95 and 150 GHz radial bin measurements, and $< 1.0\sigma$ for 220 GHz. The 220 GHz causes the most noticeable shift due to it containing the highest S/N at large radii as a result of extended dust emission.

Fig. 3.5 shows these described radial profiles for the $N = 94,452$ SPT+ACT galaxies as measured on the SPT maps, alongside a bootstrap resampled random catalog profile to highlight the lack of any unexpected bias. Our method for calculating uncertainty and random catalog are outlined in the Sections below.

3.4.4 Uncertainties

Correct evaluation of our results requires an accurate calculation of uncertainties. This not only pertains to the error within a radial bin, but also correlation between its neighbors. We employ a bootstrap resampling procedure to construct a covariance matrix across all maps and radial average bins. This is done by resampling our galaxy catalog with replacement and with the same number of objects as the original. We repeat this process for a large number of resamples $(4,000)$ and measure the radial profile in identical fashion to Section 3.4.3. The offset correction done by subtraction

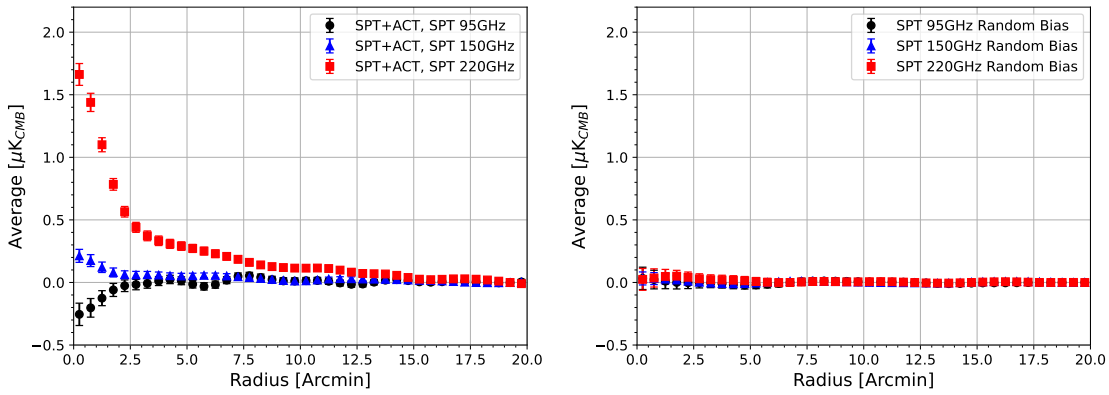

(a) Galaxy Radial Profile (b) Random Radial Profile

Figure 3.5: Measured radial profiles as detailed in Section 3.4.3 for: (a) all $N = 94,452$ galaxies within the SPT+ACT field overlap as measured on the SPT frequency maps of 95, 150, and 220 GHz. (b) Profile of estimated bias in the same SPT maps and SPT+ACT field overlap, calculated from bootstrap resampling a catalog of randomly generated positions (Section 3.4.5).

of three largest radial bins' average $(18.5' - 20.0')$ likely skews these calculations and results in underestimated noise near large radii. For this reason and low overall S/N at large radii, we elect to not use any radial bins above $15'$.

The covariance matrix per frequency map is determined from the corresponding distribution of bootstrapped profiles. The radial tSZ and dust covariance matrices are also calculated via fitting each bootstrap resample to the two-component fit outlined below in Section 3.4.8 and shown in Section 3.4.6.

This bootstrapped covariance estimation assumes the noise is independent between each galaxy. However for our sample, radial measurements out to a radius of $20'$ will on average have a few dozen catalog neighbors. A spatial overlap will thus cause correlation between these neighboring galaxies. This concern has been noted by others, such as Schaan et al. (2021), that found bootstrap resampling produced $\approx 10\%$ underestimation of error at $\geq 6'$ in their circular apertures. The severity of this effect in our analysis is a primary challenge as well. Our subtraction of the large-scale CMB may marginally reduce some correlation. Aperture choice would

also be influential. However, our radial profile S/N drops by roughly a factor of three between the center and $6'$, with the tSZ falling below 2σ by $8'$. As a result, any profile fits should be largely controlled by the inner radial bins and any effects due to underestimated error are considered minor. Additional avenuesfor checking this that we may explore further could include implementation of block bootstrapping, or generating and stacking maps of Gaussian noise.

3.4.5 Random Catalog Comparison

To validate our procedure outlined above, we also generate random samples of $1,000,000$ points uniformly distributed within the SPT and ACT catalog footprints. From these, we measure the radial profile (following Section 3.4.3) and bootstrap resample subsets with the same size as our desired galaxy catalog(s). The resultant bootstrap mean corresponds to the expected bias of our sample's background. Fig. 3.5b) shows our bias result of the SPT maps within the SPT-ACT overlap field. Throughout all radial bins the random bootstrap mean stays within 1σ of zero, indicating no additional bias is present.

3.4.6 Correlation Matrices

As discussed in Section 3.4.4, a large number (4000) of bootstrap resampled catalogs were constructed from each galaxy catalog. Covariance matrices for each respective frequency map were then made from these bootstrap resamples and used through our two-component fitting procedure of Section 3.4.8. Correlation between radial bins is also important for our profile analysis described in Section 3.4.3. Thus, we fit our two-component tSZ and dust model to all aforementioned bootstrap resamples to correctly estimate the correlation between neighboring radial bins. Fig. 3.6 shows the radial correlation matrices for each catalog (SPT+ACT, ACT-Only) and

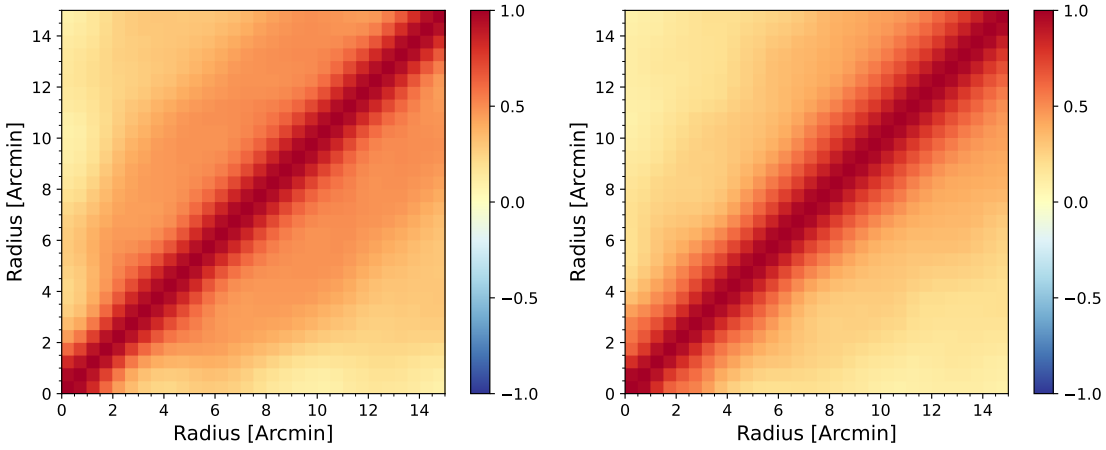

(a) SPT+ACT Dust Correlation Matrix

(b) SPT+ACT tSZ Correlation Matrix

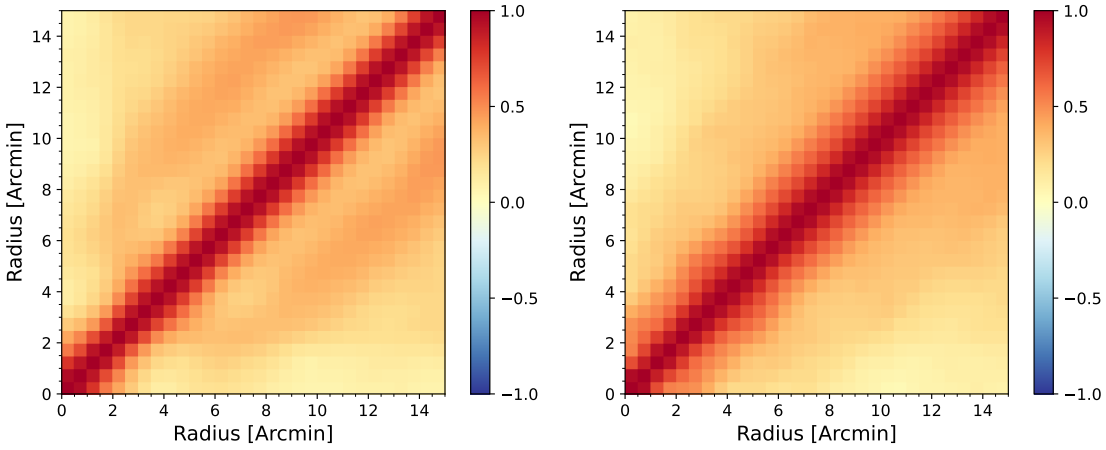

(c) ACT-Only Dust Correlation Matrix

(d) ACT-Only tSZ Correlation Matrix

Figure 3.6: Radial bin $(0 - 15')$ correlation matrices for the dust (*left*) and tSZ (*right*) two-component fit (Section 3.4.8) of 4000 bootstrap resamples outlined in Section 3.4.4 for SPT+ACT (*top*) and ACT-Only (*bottom*) galaxy catalogs.

fit component (dust, tSZ). The most significant effect would be from our beam resolution, with minor contributions likely as a result of residual foreground components not accounted for and structure of the surrounding signals. As shown in Fig. 3.6, neighboring radial bins are not independent from one another.

3.4.7 *Fitting Procedure*

All fits reported are conducted via Bayesian estimation with the assumption that our measurements are normally distributed but not necessarily independent. The likelihood function is related to our fit residuals $(\mathbf{X}_i - \hat{\mathbf{X}}_i)$ and covariance matrix $(\mathbf{C})$ as

$$\mathcal{L}(\psi|X) = p(X|\psi) \propto \exp\left[-\frac{1}{2}(\mathbf{X}_i - \hat{\mathbf{X}}_i)^T \times \mathbf{C}^{-1} \times (\mathbf{X}_i - \hat{\mathbf{X}}_i)\right], \tag{3.1}$$

incorporating parameters with discrete predefined ranges and priors $p(\psi)$. The posterior distributions are obtained as

$$p(\psi|X) = \frac{p(X|\psi)p(\psi)}{\int p(X|\psi')p(\psi')d\psi'}, \tag{3.2}$$

where we normalize across all combinations of fit parameters (ψ'). This is calculated for the ψ-dimensional array for all possible parameter combinations and implemented via our own custom Python code. Each parameter's reported best fit is classified as the median (50th percentile) after the posterior is marginalized over all other parameter ranges. Similarly, the 1σ bounds are calculated as the 16th and 84th percentiles.

3.4.8 *Two Component Fitting*

From our aperture measurements, we used a two-component fitting model consisting of tSZ (y) and the dust spectral intensity at $\nu_0 = 353$ GHz in the source's rest frame $I_r(\nu_0)$ with units [W Hz^{-1}m^{-2}sr^{-1}],

$$\delta T(\nu) = y\, g(\nu)\, T_{CMB} + \frac{I_r(\nu_0)}{(1+z)^2}\,\frac{I_o(\nu)}{I_r(\nu_0)}\,\frac{dT}{dB(\nu,T)}\bigg|_{T_{\rm CMB}}, \tag{3.3}$$

where $g(\nu) = [x\ (e^x+1)/(e^x-1) - 4]$ of the tSZ signal (eq. 1.11) and $B(\nu, T)$ is the Planck function. The $(1+z)^{-2}$ term arises from redshift corrections due to time

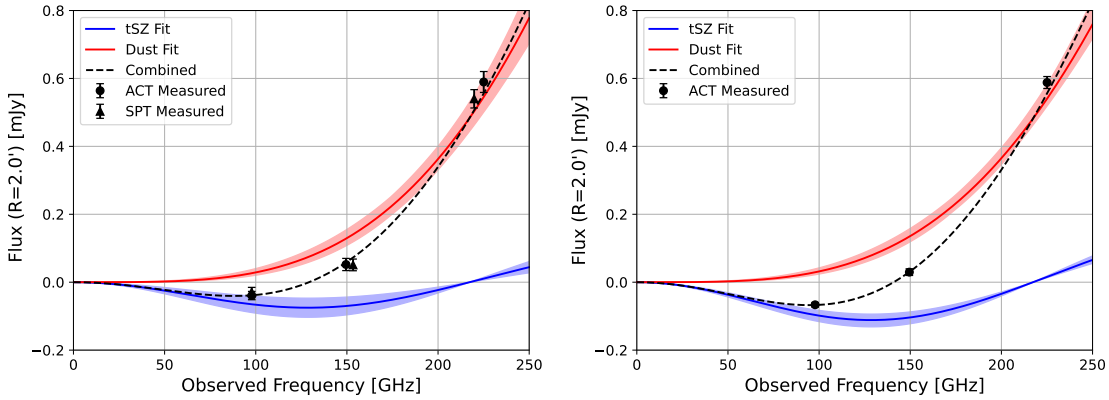

(a) SPT+ACT Intensity Plot (b) ACT-Only Intensity Plot

Figure 3.7: Observed intensity spectrum within a $2.0'$ circular aperture for: (a) SPT+ACT ($N = 94,452$) and (b) ACT-Only ($N = 387,627$). Measured ACT (*black, circles*) and SPT (*black, triangles*) values are placed at each frequency map band-center, determined by integrating over their respective response. Dust (*red*) and tSZ (*blue*) are shown with shaded 2σ bounds determined from the two-component fit of eq. (3.3).

dilation and energy. $I_o(\nu)$ is the specific dust intensity in the observed frequency band ν. It is converted to the rest frame band $\nu\,(1+z)$,

$$I_o(\nu) = (1+z)\; I_r\left[\nu\;(1+z)\right], \tag{3.4}$$

where we assume a gray-body dust spectrum for I_r with a dust temperature (T_d) and spectral emissivity index (β). Thus, the intensity term from eq. (3.3) can be written as

$$\frac{I_o(\nu)}{I_r(\nu_0)} = (1+z)\left[\frac{\nu\;(1+z)}{\nu_0}\right]^{\beta} \frac{B[\nu\;(1+z), T_d]}{B(\nu_0, T_d)}, \tag{3.5}$$

normalized with respect to $I_r(\nu_0)$. This normalization term helps define a reference frequency for all measurements while reducing the correlation between dust temperature and intensity amplitude when near the Rayleigh-Jeans limit. Equation 3.3 is integrated over each respective map's frequency band response. The SPT bands were extracted from Chown et al. (2018), as the SPT+Planck maps are dominated by the SPT response for most of our angular scales. Full ACT bandpasses were available as a

function of position, detector array, and multipole ℓ. We average each ACT response across our field of observation, all detectors, and with a cut of $2,000 < \ell <= \ell_{\rm max}$. The $\ell = 2,000$ minimum was chosen to reflect our angular scales of interest and subtraction of the large-scale CMB (Section 3.4.2). The observed flux in mJy integrated within a simple circular aperture of $R = 2.0'$ radius is shown in Fig.3.7 for our SPT+ACT and ACT-Only catalogs, respectively. This circular aperture is further used in our stellar mass binning shown in Section 3.4.13.

The two component fit described above was also applied to each set of frequency measurements per radial bin for all listed catalogs in Table 3.1. We assume priors as outlined in Table 3.2 for all fits. Uniform priors are set for the Compton-y ($0 \leq y \leq 4 \times 10^{-7}$) and dust intensity in the 220 GHz rest frame ($0 \leq I_r(\nu_0) \leq 4 \times 10^{-24}$ W Hz^{-1}m^{-2}sr^{-1}). In the event of fits near zero indicating low signal to noise, we shift these uniform priors to include slight negative values. Thus, in the absence of a signal we will then correctly produce a result centered about zero. Gaussian priors were assumed for the additional parameters of dust emissivity ($\beta = 1.75 \pm 0.25$) and dust temperature ($T_{\rm d} = 20 \pm 3$ K). These Gaussian priors were chosen to align within standard ranges (Dunne and Eales, 2001; Draine, 2011; Addison et al., 2013; Magdis et al., 2021), but were not set as free uniform parameters due to our limited number of maps to fit. The resultant dust parameter fits are found to be highly constrained to within 1.5σ of the prior mean. This method allows us to include additional uncertainty associated with our lack of information about the dust in our sample(s) without overfitting.

Our samples were selected with low SFRs and thus should have minimal radio sources at these frequencies. However if non-negligible radio contamination was present in the lower frequency bands, our two-component fit would then underesti-

Parameter	Description	Prior
y	Compton-y [unitless]	$[0^{\dagger},\ 4 \times 10^{-7}]$
$I_r(\nu_0)$	Dust Intensity [W Hz^{-1}m^{-2}sr^{-1}]	$[0^{\dagger},\ 4 \times 10^{-23}]$
β	Dust Emissivity [unitless]	$G(1.75, 0.25^2)$
$T_{\rm d}$	Dust Temperature [K]	$G(20, 3^2)$

Table 3.2: Two component fit parameters (from eq. 3.3) and given priors used on each catalog and radial bin. Gaussian $G(\mu, \sigma^2)$ priors are assumed for dust emissivity $\beta = 1.75 \pm 0.25$, and temperature $T_{\rm d} = 20 \pm 3$ K. †A realistic lower limit of zero is used on the uniform free parameters unless the fit is poor and near zero. In which case, the lower limit is shifted negative to allow for accurate fitting around zero and avoid artificially inflated values.

mate the tSZ signal. Meanwhile the dust fit would be either over- or under-estimated, dependent upon the radio source's spectrum into the higher bands.

3.4.9 Profile Fits

As detailed above, we obtain profiles for both the tSZ and dust responses per radial average bin from our frequency maps. The dominant source is expected to be a central point source associated with our target sample. However, we also expect an extended secondary profile term due to spatial correlations with neighboring galaxies.

A few different profile models could be considered, such as a generalized Navarro-Frenk-White (NFW) profile like that conducted by (Amodeo et al., 2021), or basic power-law models for two-point correlation clustering measurements (Coil et al., 2017). However, our $2.1'$ beam and $z \approx 1$ redshift would result in highly degenerate and correlated NFW parameter fits, while a power-law model cannot easily be forward-modeled with the beam since it diverges to infinity as $r \to 0$. As we are primarily interested in the power-law slope at radii away from the center, we opt for a simple pseudo-power-law approximation that can be made using a type of King or

isothermal model (King, 1962):

$$f(r) = \frac{A_{\rm k}}{r_0}\left(1+\frac{r^2}{r_0^2}\right)^{-\frac{\gamma}{2}}, \tag{3.6}$$

with an amplitude $A_{\rm k}$, comoving core radius r_0, and that now instead converges to $A_{\rm k}/r_0$ as $r \to 0$. Converted to a function of projected angle (θ) through the line-of-sight, this gives

$$f(\theta) = A_{\rm k}\frac{\Gamma(\frac{1}{2})\Gamma(\frac{\gamma-1}{2})}{\Gamma(\frac{\gamma}{2})}\left(1+\frac{(D_c\theta)^2}{r_0^2}\right)^{\frac{1-\gamma}{2}}, \tag{3.7}$$

where D_c is the comoving distance. This profile is best defined as a function of angle θ, as it must be convolved with the beam for accurate comparison to our measured values. For a combined model of a point source plus King ($\delta + f$) convolved with the beam (b) can be described as,

$$F(\theta) := \iint_{-\infty}^{\infty}\left[\delta(\boldsymbol{\theta}') + f(\boldsymbol{\theta}')\right] b(\boldsymbol{\theta}-\boldsymbol{\theta}')d\boldsymbol{\theta}'. \tag{3.8}$$

Our final beam as described in Section 3.4.2 is a Gaussian with FWHM= $2.1'$, but with an $\ell_{\rm max} = 10,000$ cutoff. Compared to convolution with a perfect Gaussian beam this can produce a 10% difference for a central point source, but has a negligible effect on our broader King profile of eq. (3.7). For this reason we elect to assume a perfect Gaussian beam to simplify the King convolution, but maintain the exact beam (with $\ell_{\rm max}$ cut) for the point source defined below as $b(\theta)$. These yield a profile function with one integral that we compute numerically,

$$F(\theta) = A_{\rm ps}b(\theta) + \int_0^{\infty}\exp\left(-\frac{\theta^2+\theta'^2}{2\sigma_{\rm beam}^2}\right)J_0\left(i\frac{\theta\theta'}{\sigma_{\rm beam}^2}\right)\frac{f(\theta')}{\sigma_{\rm beam}^2}\theta' d\theta', \tag{3.9}$$

where J_0 is the Bessel function of the first kind and the size of our Gaussian beam as $\sigma_{\rm beam} = 0.8918'$. This eq. (3.9) allows us to set a lower bound for the profile's central point source component and examine the extended profile slope.

3.4.10 Dust

Our resultant dust from the two-component fit per radial bin is shown in Fig. 3.8. We observe up to a 16.6σ and 21.5σ detection of dust in the center of SPT+ACT and ACT-Only catalogs respectively. Beyond the beam's FWHM, detection in both cases monotonically decreases to 5.3σ at $10'$ and down further to 2.0σ at $15.0'$ where noise begins to dominate. Of particular interest is the shape of our dust profile, which has a definitive central source similar to the beam along with a sloped extended signal.

We expect the dust profile to consist of an unresolved central source associated with our target galaxies, and a secondary extended profile tied to the two-point correlation function of neighboring galaxies. We fit the convolved point source plus King model of eqs. (3.7) and (3.9) to our dust profile up to $15'$ ($\approx$ 15.2 comoving Mpc). This cutoff is meant to avoid incorporating low S/N radial bins and reduce any residual impact from the offset correction discussed in Section 3.4.4.

Parameter	Description	Prior	SPT+ACT	ACT-Only
$A_{\rm ps}$ [10^{-23} W Hz^{-1}m^{-2}sr^{-1}]	Pt. Src. Amp.	[0, 4.0]	$2.24^{+0.22}_{-0.20}$	$2.32^{+0.18}_{-0.18}$
A_k [10^{-24} W Hz^{-1}m^{-2}sr^{-1}]	King Amp.	[0, 4.0]	$1.26^{+0.20}_{-0.18}$	$1.52^{+0.20}_{-0.16}$
γ [unitless]	King Slope	[1.0, 4.0]	$2.52^{+0.16}_{-0.13}$	$2.90^{+0.14}_{-0.12}$
r_0 [Comoving Mpc]	Core Radius	3.0	–	–

Table 3.3: Dust profile fit parameters for eq. (3.9), applied priors, and resultant fits for our SPT+ACT and ACT-Only catalogs. The King amplitude and slope will be positively correlated. We set the core radius to a constant larger than the beam due to its inherent degeneracy with the amplitudes.

We assume fit parameters with priors as outlined in Table 3.3. As core radius (r_0) has inherent degeneracy with the amplitudes we instead hold r_0 as a constant larger than the beam, selecting $r_0 = 3.0$ comoving Mpc. Due to this degeneracy and inability to resolve our central source, this fit is not an attempt to fully separate the

one- and two- component contributions within the profile. However, it provides us the opportunity to determine other characteristics such as the extended profile slope at larger radii.

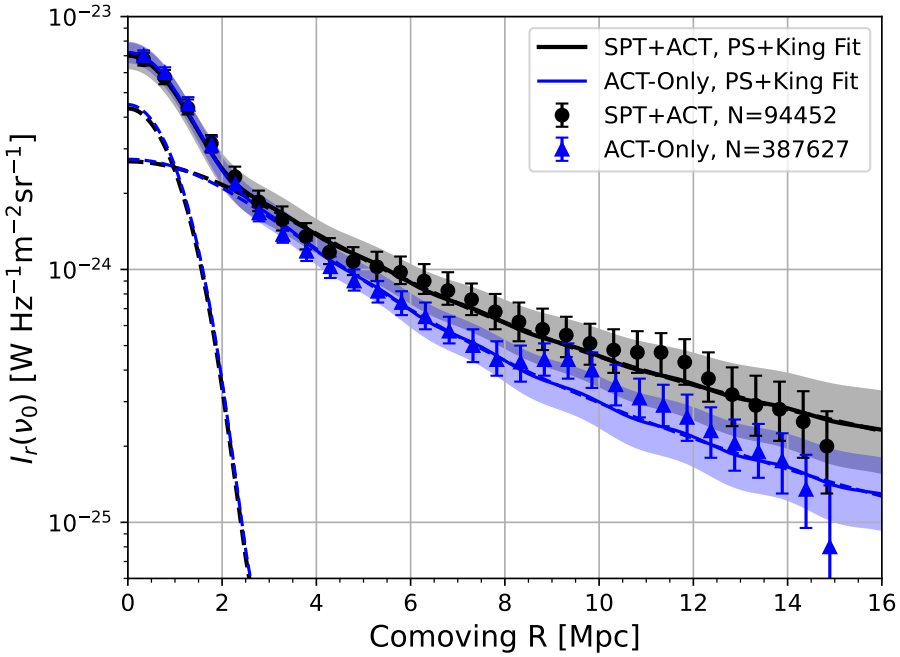

Figure 3.8: Dust radial profile and best fit point source + King model as defined in Section 3.4.10, shown here with core radius $r_0 = 3.0$ comoving Mpc for SPT+ACT (*black*) and ACT-Only (*blue*) catalogs. Shaded regions represent 2σ uncertainty of the combined fit. Dashed lines correspond to the separate best fit point source and King components.

The radial bin dust profile and resultant fits are shown in Fig. 3.8 for a core radius of $r_0 = 3.0$ comoving Mpc. We have separately checked the impact of different core radii. For instance, if a core radius of $r_0 = 5.0$ comoving Mpc was chosen instead, it would result in a $\approx 10\%$ increase of our dust's point source ($A_{\rm ps}$), with a $\approx 5 - 10\%$ decrease in the King ($A_{\rm k}$) amplitude. Increasing the core radius also has a noticeable effect on the King slope, due to heightened dependence on the noisier high radial bins and our limited range of $15'$. A core radius of $r_0 = 5.0$ comoving Mpc produces steeper dust slopes (γ) by a factor $\approx 25\%$.

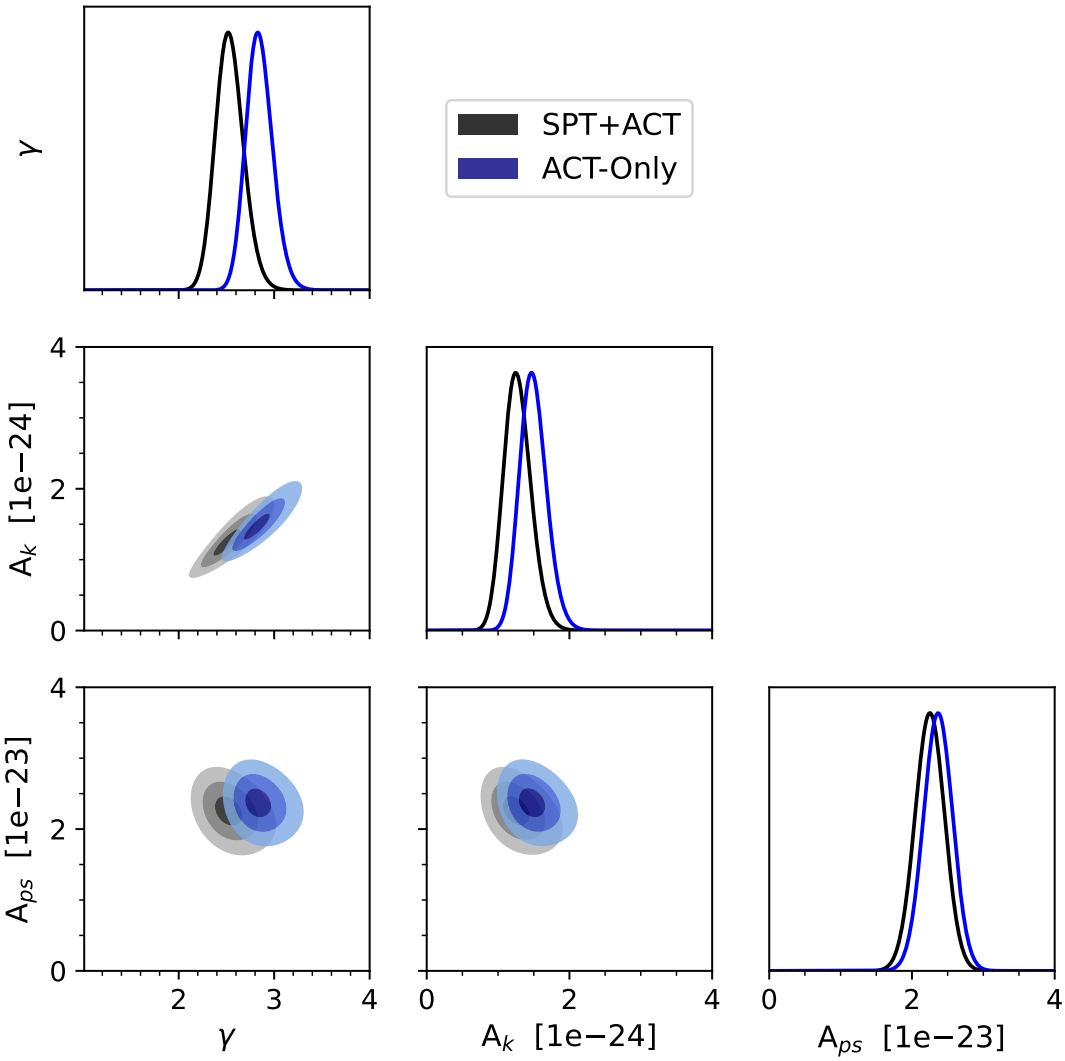

Figure 3.9: Posterior corner plot of the dust profile fit for our SPT+ACT (*blue*) and ACT-Only (*black*) galaxy catalogs. From dark to light, the three shaded contour regions correspond to the 1σ, 2σ, and 3σ levels.

Our dust profile fits are shown in Table 3.3 and Fig. 3.8 for both catalogs. The resultant posterior distributions are shown in the corner plot of Fig. 3.9. The point source ($A_{\rm ps}$) and King ($A_{\rm k}$) amplitudes are fit at a $10.7-12.9\sigma$ and $6.6-8.4\sigma$ level, respectively, and are consistent (within 2σ) between galaxy samples. The best fit King slopes are $2.52^{+0.16}_{-0.13}$ and $2.90^{+0.14}_{-0.12}$ for SPT+ACT and ACT-Only. These are slightly steeper than reported power law slopes from galaxy clustering studies ($\gamma = 1.5-2.0$, Eftekharzadeh et al., 2015; Coil et al., 2017; Amvrosiadis et al., 2018), likely as a result of the difference between our King model and a power-law, which diverge near and below the core radius. Since our King model is designed to level off as it nears the core radius, it would have to fit a steeper slope to be comparable with that of a power-law. Additionally, our necessary zeroing of the frequency profiles at large radii (Section 3.4.3) results in an underestimation of the dust by a small constant which would contribute to steeper slope fits. To test this, we incorporated an additional constant offset term in our profile fit and found it to be insignificant. The best fit offset was less than our measured signal at $15'$, within 1σ of zero, and simply increased the fit uncertainty of our other parameters while marginally decreasing the slope γ by $< 5\%$.

Thus, we can still conclude that our extended dust has a shape consistent with that expected from the two-point correlation function of neighboring galaxies and structure. Overall, we have shown here that at our $z \approx 1$ redshifts, dust in the millimeter bands contains useful insights into intergalactic structure and can be detected at a high significance.

3.4.11 Dust Mass

Also of interest is the mean dust mass associated with our galaxy samples, which can be estimated from the rest-frame dust intensities $I_r(\nu_0)$ found from eq. (3.3). The

dust mass follows,

$$M_{\rm d} = \frac{D_{\rm c}^2 \int I_r(\nu_0) d\Omega}{\kappa(\nu_0) B(\nu_0, T_{\rm d})}, \tag{3.10}$$

where $\kappa(\nu_0)$ is the dust mass opacity coefficient or absorption cross-section per unit mass [$\mathrm{m^2\ kg^{-1}}$] at our reference frequency of 353GHz. We take $T_d = 20 \pm 3$ K as used previously in our two-component fit. The final error is determined by standard error propagation of both $I_r(\nu_0)$ and $T_{\rm d}$.

Unfortunately $\kappa(\nu_0)$ is overall poorly constrained. Further potential uncertainty arises as $\kappa(\nu_0)$ values in literature are often derived from dust observations or models designed for the Milky Way or other local galaxies, which may slightly differ compared to our $z \approx 1$ quiescent samples. At $\nu_0 = 353$ GHz, or $\lambda_0 = 850$ μm, commonly used $\kappa(\nu_0)$ values range from $0.04 - 0.15$ $\mathrm{m^2 kg^{-1}}$ (Li and Draine, 2001; Dunne and Eales, 2001; Draine, 2003; Dunne et al., 2003; Casey, 2012). Thus, we take a conservative approach and assume a center value of $\kappa(\nu_0) = 0.08$ $\mathrm{m^2 kg^{-1}}$, while acknowledging this can fluctuate by a factor of two.

As evident by the previous subsection, we observe a dust profile containing both a central point source and extended neighboring structures. However, our beam introduces difficulty in accurate separation of them. As a lower bound for the expected central dust, we take the fit point source component: $\int I_r(\nu_0) d\Omega = A_{\rm ps} \int b(\theta) d\Omega$, integrated over the beam solid angle. In contrast, we also integrate within a $R = 2.0'$ circular aperture instead, assuming that the central point source will dominate any extended dust structure within this radius. Our results for each catalog are shown in Table 3.4.

The lower limit to our dust mass - extracted solely from the point source component ($A_{\rm ps}$) from Section 3.4.10 - indicates consistent dust masses of $8.45^{+0.10}_{-0.12}$ and $8.46^{+0.09}_{-0.12}$ $\log_{10}(\mathrm{M_\odot})$ for the complete SPT+ACT and ACT-Only catalogs, respectively. In comparison, an upper limit to the dust mass - simply integrating within a radius

Parameter	SPT+ACT		ACT-Only	
	$A_{\rm ps}$	$R = 2.0'$	$A_{\rm ps}$	$R = 2.0'$
$\log_{10}(M_{\rm d}/{\rm M}_\odot)$	$8.45^{+0.10}_{-0.12}$	$8.82^{+0.09}_{-0.11}$	$8.46^{+0.09}_{-0.12}$	$8.85^{+0.09}_{-0.11}$
$\log_{10}(M_{\rm d}/\overline{M_\star})$	$-2.96^{+0.10}_{-0.12}$	$-2.59^{+0.09}_{-0.11}$	$-2.98^{+0.09}_{-0.12}$	$-2.59^{+0.09}_{-0.11}$

Table 3.4: Dust mass associated with our central point source fit shown in Fig. 3.8 and Table 3.3, and for all dust within $R = 2.0'$. Dust-to-stellar mass ratio is also shown. For a $\kappa(\nu_0) = 0.08$ m^{2}kg^{-1}, which we recognize might fluctuate by a further factor of two or 0.30 dex.

of $R = 2.0'$ - produces dust masses 0.37 and 0.39 dex larger. The ratio of dust mass to stellar mass show even greater consistency between catalogs, ranging from -2.98 (lower limit using $A_{\rm ps}$) to -2.59 (upper limit using $R = 2.0'$) orders of magnitude. For smaller sample sizes when profiles cannot be well-constrained, such as when binning by stellar mass, the circular $R = 2.0'$ aperture is still possible. We employ this generalized method in Section 3.4.13 to analyze our dust-to-stellar mass relation.

While these dust masses are on the high side expected for galaxies with low SFRs, other studies have found similar results for massive galaxies with increasing redshift (Santini et al., 2014; Calura et al., 2016; Gobat et al., 2018). There are also indications that this increase in dust-to-stellar mass with redshift is more extreme for quiescent galaxies than dusty star-forming ones (Donevski et al., 2020; Magdis et al., 2021). The additional uncertainty from $\kappa(\nu_0)$ prevents us from drawing any strong conclusions. However, as our dust masses appear to be within an acceptable range compared to these previous studies, we can treat them as another verification of our stacking and analysis process. Determination of dust mass in this manner also highlights the potential for similar use in future sub-mm and FIR investigations.

3.4.12 Compton-y

In comparison with the dust measured above, we expect our tSZ profile to be similar but not identical in shape. Unlike dust, we expect the tSZ from our target galaxies to have a broader one-halo distribution associated with hot ionized gas, which spans throughout the CGM out to $\approx 0.5 - 1.0$ comoving Mpc. With our 2.1′ FWHM beam, most of this central component will still be unresolved. We also expect a steeper profile slope, as the extended tSZ is a tracer for hot gas that is less prevalent in lower-mass neighbors.

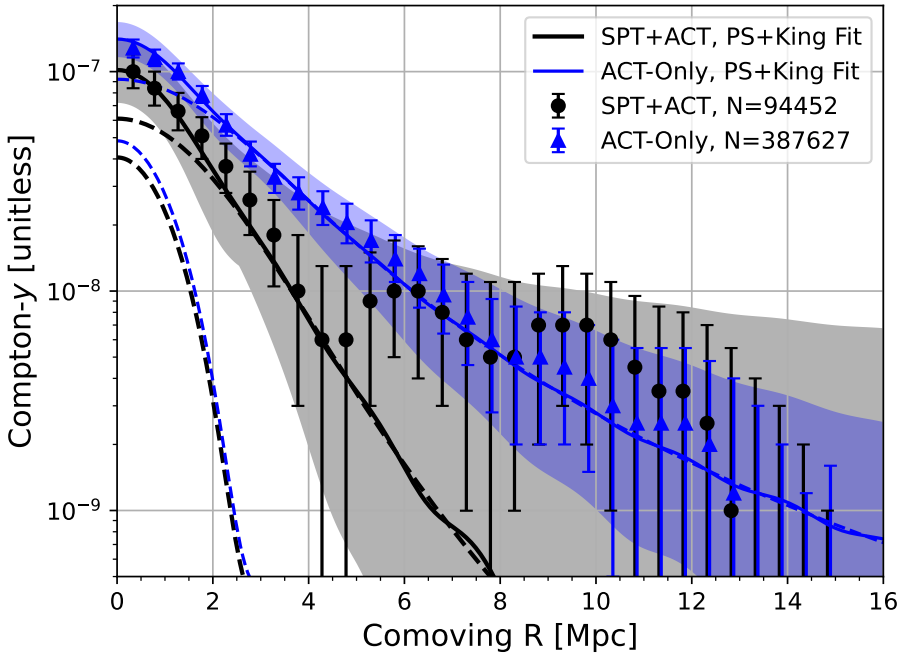

Figure 3.10: Compton-y radial profile for our quiescent galaxy catalogs; SPT+ACT (*black, triangles*) and ACT-Only (*blue, circles*). Alongside their best fit (*solid*), shaded 2σ bounds, and individual point source and King components (*dashed*).

The Compton-y component from our two-component fit of eq. (3.3) per radial bin is shown in Fig. 3.10 for each complete catalog. Here the difference in sample size is apparent, as the centermost radial bins for SPT+ACT ($N = 94,452$) detect the tSZ at up to 5.5σ, while ACT-Only ($N = 387,627$) is up to 11.6σ. Of equal importance

is the distance at which the S/N drops below 2σ. This occurs at a radius of $4.0'$ (4.0 comoving Mpc) for SPT+ACT, versus $8.0'$ (8.1 comoving Mpc) for ACT-Only. So while we do observe extended tSZ larger than the beam, noise begins to dominate much quicker than observed with dust, especially for SPT+ACT. Therefore we elect to only fit our profiles up to $10'$ (10.1 comoving Mpc).

We assume tSZ profile fit priors given in Table 3.5. Due to degeneracy between the central point source and King model, we assume a core radius again of $r_0 = 3.0$ comoving Mpc. It should be noted that just as with the dust, this profile fit does not fully isolate the one- and two- component contributions due to our inherent central degeneracy between the King and point source models as a result of the beam. Our main goal in applying this fit is to demonstrate the presence of extended tSZ, and compare the resultant King slope to that found for dust. We again checked the effect of using different core radii and see similar trends as with the dust; increasing core radius to $r_0 = 5.0$ comoving Mpc yields a $\approx 25\%$ increase in tSZ point source amplitude ($A_{\rm ps}$), $\leq 5\%$ decrease in King amplitude ($A_{\rm k}$), and $\approx 40\%$ increase in slope (γ). The change in slope with core radius here is larger than observed with dust, due to the faster rate at which our tSZ profile S/N drops.

Parameter	Description	Prior	SPT+ACT	ACT-Only
$A_{\rm ps}$ $[10^{-7}]$	Pt. Src. Amp.	[0, 8]	$2.1^{+1.2}_{-1.2}$	$2.5^{+0.8}_{-0.8}$
$A_{\rm k}$ $[10^{-8}]$	King Amp.	[0, 20]	$7.5^{+5.1}_{-3.7}$	$7.3^{+1.9}_{-1.5}$
γ [unitless]	King Slope	[1.0, 10.0]	$6.2^{+2.3}_{-2.1}$	$4.0^{+0.6}_{-0.4}$
r_0 [Comoving Mpc]	Core Radius	3.0	–	–

Table 3.5: Compton-y profile fit parameters for eq. (3.9), given priors, and resultant fits on our SPT+ACT and ACT-Only catalogs. We set the core radius to a constant larger than the beam due to its inherent degeneracy with the amplitudes.

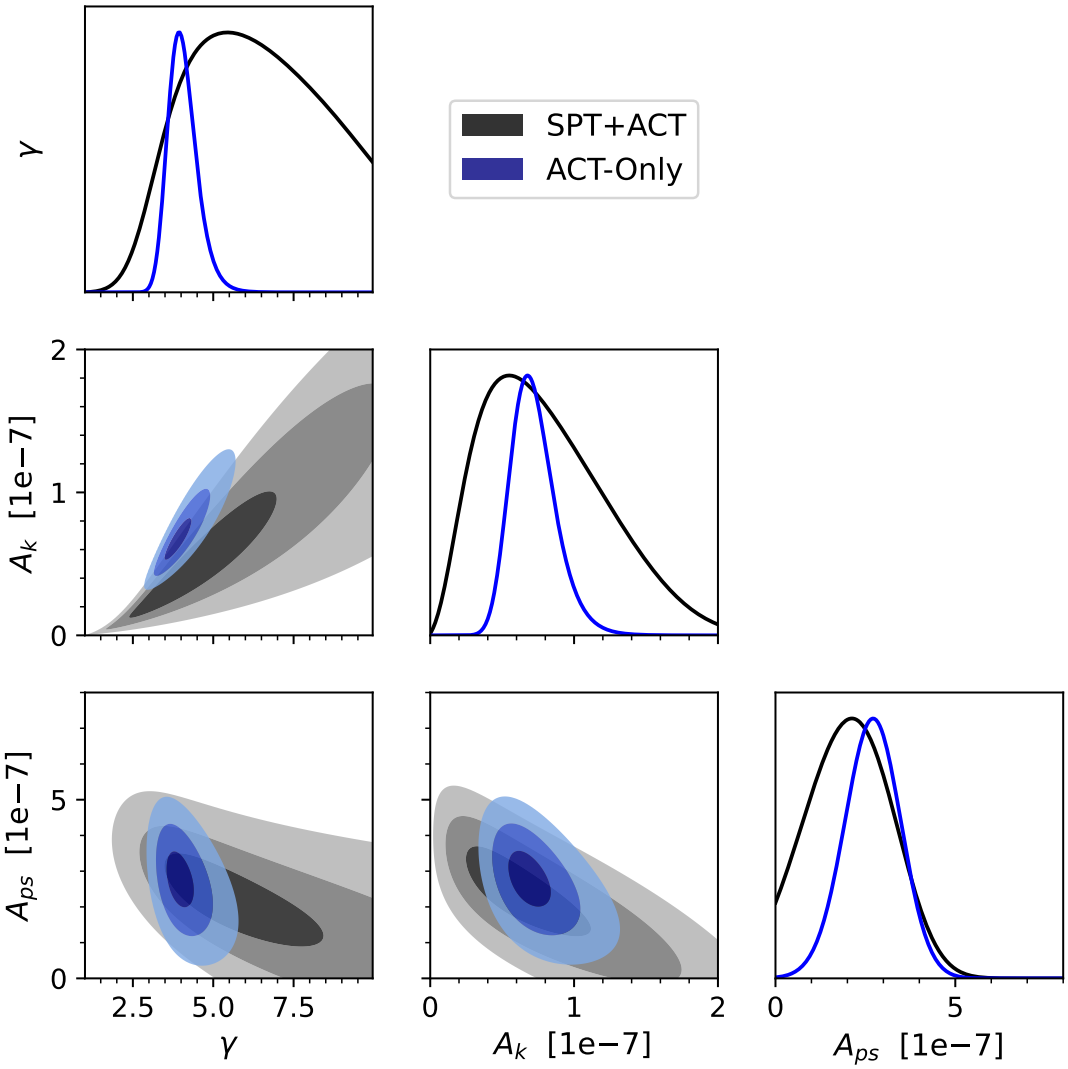

Figure 3.11: Posterior corner plot of the tSZ profile fit for our SPT+ACT (*blue*) and ACT-Only (*black*) galaxy catalogs. From dark to light, the three shaded contour regions correspond to the 1σ, 2σ, and 3σ levels.

Our fit results are shown in Table 3.5 and plotted alongside our measurements in Fig. 3.10. The marginalized posterior distributions are shown in Fig. 3.11. Indicative of the quick S/N drop-off, the King model for the SPT+ACT sample is poorly constrained. Point source amplitudes ($A_{\rm ps}$) are detected with 1.8σ and 3.1σ significance for SPT+ACT and ACT-Only, respectively. They are also within 1σ of each other, showing overall consistency. The King slopes of $\gamma = 6.2^{+2.3}_{-2.1}$ and $4.0^{+0.6}_{-0.4}$ indicate a sharper decline in tSZ two-point correlation than that of dust, as possible from a nonlinear relationship between ionized gas and lower mass neighbors. An uneven presence of radio contamination in the profile's outer vs inner radius, could also increase our reported slope via tSZ fit underestimation.

3.4.13 Stellar Mass Binning

We also wish to measure the dust mass and thermal energy from our galaxies as a function of stellar mass, similar to previous studies (Planck Collaboration: et al., 2014; Greco et al., 2015; Meinke et al., 2021). Hence we no longer are concerned with a profile fit, but rather the total integrated signal over a solid angle expected to be dominated by the primary central source.

A circular top-hat aperture with radius of $R = 2.0'$ is selected to integrate within, on all frequency maps per stellar mass bin. The two-component fit of eq. (3.3) is then applied to each sample and bin. Errors are calculated via bootstrap resampling from the same resample catalogs as Section 3.4.4.

We separate our catalogs into stellar mass bins with widths of 0.1 in $\log_{10}(M_\star/\mathrm{M}_\odot)$, over a range from $10.9 - 12.0$ and $10.8 - 12.1$ dex for our SPT+ACT and ACT-Only samples, respectively. Additional bins were possible in the latter due to its larger number of total galaxies. The impact of bin size was checked and found to be negligible, as wider 0.2 dex-wide bins produced similar results, but created fewer

points of measurement for the subsequent stellar mass uncertainty correction to be applied in Section 3.4.14.

Integrated Compton-y values are converted to thermal energies via eq. (1.16) and are shown versus stellar mass in Fig. 3.12. These align closely to the previous investigation in Meinke et al. (2021), showing a clear trend of increasing thermal energy versus stellar mass. For our mass range we expect the relation between thermal energy ($E_{\rm th}$) and stellar mass to be sufficiently described by a simple power-law model. As our analysis is conducted in terms of $\mu = \log_{10}(M_\star/\mathrm{M}_\odot)$, we write this energy-mass relation as a log-log model,

$$\mathcal{E}(\mu) = \log_{10}(E_{\rm th})(\mu) = \log_{10}(E_{\rm pk}) + \alpha\left(\mu - \mu_{pk}\right), \tag{3.11}$$

where α is the slope, $\mu_{pk} = \log_{10}(M_{\star,\rm pk}/\mathrm{M}_\odot)$ is the $\log_{10}$ peak stellar mass, and $E_{\rm pk}$ is the thermal energy at the peak stellar mass.

We conduct a similar analysis using the two-component fit's dust result to determine our dust mass (via Section 3.4.11) as a function of stellar mass. These are shown in Fig. 3.13. Here we again assume a log-log power-law relation,

$$\mathcal{M}_d(\mu) = \log_{10}(M_{\rm d})(\mu) = \log_{10}(M_{\rm d,pk}) + \alpha_{\rm d}\left(\mu - \mu_{\rm pk}\right), \tag{3.12}$$

where $\alpha_{\rm d}$ is the slope, and $M_{\rm d,pk}$ is the dust mass at the peak stellar mass. Both power-law equations of eqs. (3.11) & (3.12) describe the expected relation versus stellar mass prior to any contributions that may arise from stellar mass uncertainty, discussed below.

3.4.14 Stellar Mass Uncertainty

The main caveat in the stellar mass bin approach is our catalogs' inherent stellar mass uncertainty. We find our SED fitting in Section 3.3 has a stellar mass uncertainty

of $\sigma_{\rm SED} = 0.16$ dex, due in part from our high redshift and use of only photometric data (Meinke et al., 2021). Thus, to accurately fit measured stellar mass bins with the energy and dust mass vs stellar mass functions of eqs. (3.11) & (3.12), we must correctly incorporate our stellar mass uncertainty. Luckily our quiescent galaxy mass distributions are well fit by Gaussians of the form $G(\mu_{\rm pk}, \sigma_q^2)$, with $\sigma_q = 0.20$ dex for both and $\mu_{\rm pk}$ listed in Table 3.6. Applying uncertainty, the average $\log_{10}$ thermal energy within a stellar mass bin centered on $\log_{10}$ mass μ_i becomes,

$$\overline{\mathcal{E}}(E_{\rm pk}, \alpha, \mu_i) = \frac{\int_8^{15} \mathcal{E}(\mu)\ w(\mu, \mu_i)\ d\mu}{\int_8^{15} w(\mu, \mu_i)\ d\mu} \tag{3.13}$$

and similarly for average $\log_{10}$ dust mass,

$$\overline{\mathcal{M}}_d(M_{\rm d,pk}, \alpha_{\rm d}, \mu_i) = \frac{\int_8^{15} \mathcal{M}_d(\mu)\ w(\mu, \mu_i)\ d\mu}{\int_8^{15} w(\mu, \mu_i)\ d\mu}, \tag{3.14}$$

where $w(\mu, \mu_i)$ is the effective weight of a galaxy with $\log_{10}$ stellar mass μ to appear within the mass bin defined from $\mu_{i-1/2}$ to $\mu_{i+1/2}$,

$$w(\mu, \mu_i) = G(\mu - \mu_{\rm pk}, \sigma_\mu^2) \int_{\mu_{i-1/2}}^{\mu_{i+1/2}} G(\mu' - \mu, \sigma_{\rm SED}^2)\ d\mu', \tag{3.15}$$

with $\sigma_\mu^2 = \sigma_q^2 - \sigma_{\rm SED}^2$, corresponding to the standard deviation of our expected true mass distribution if no stellar mass uncertainty was present. The first Gaussian term is the weight of a galaxy selected with the true mass μ, while the integral and second Gaussian term is the chance that said galaxy actually appears in the mass bin between $\mu_{i-1/2}$ and $\mu_{i+1/2}$ due to our stellar mass uncertainty.

Equations (3.13) & (3.14) take the ideal generalized power-law functions from eqs. (3.11) & (3.12) and forward-model them into expected observations within a stellar mass bin. To clarify, this method is synonymous with the past energy-mass approach in Meinke et al. (2021), which was not described in as much detail.

Equation (3.13) was fit to the energy-mass bins found for each catalog. We refrain from fitting any bins with $S/N < 1\sigma$ to avoid introducing spurious bias. The forward-modeled best fits and 2σ uncertainties are shown in Fig. 3.12. The inset plot shows

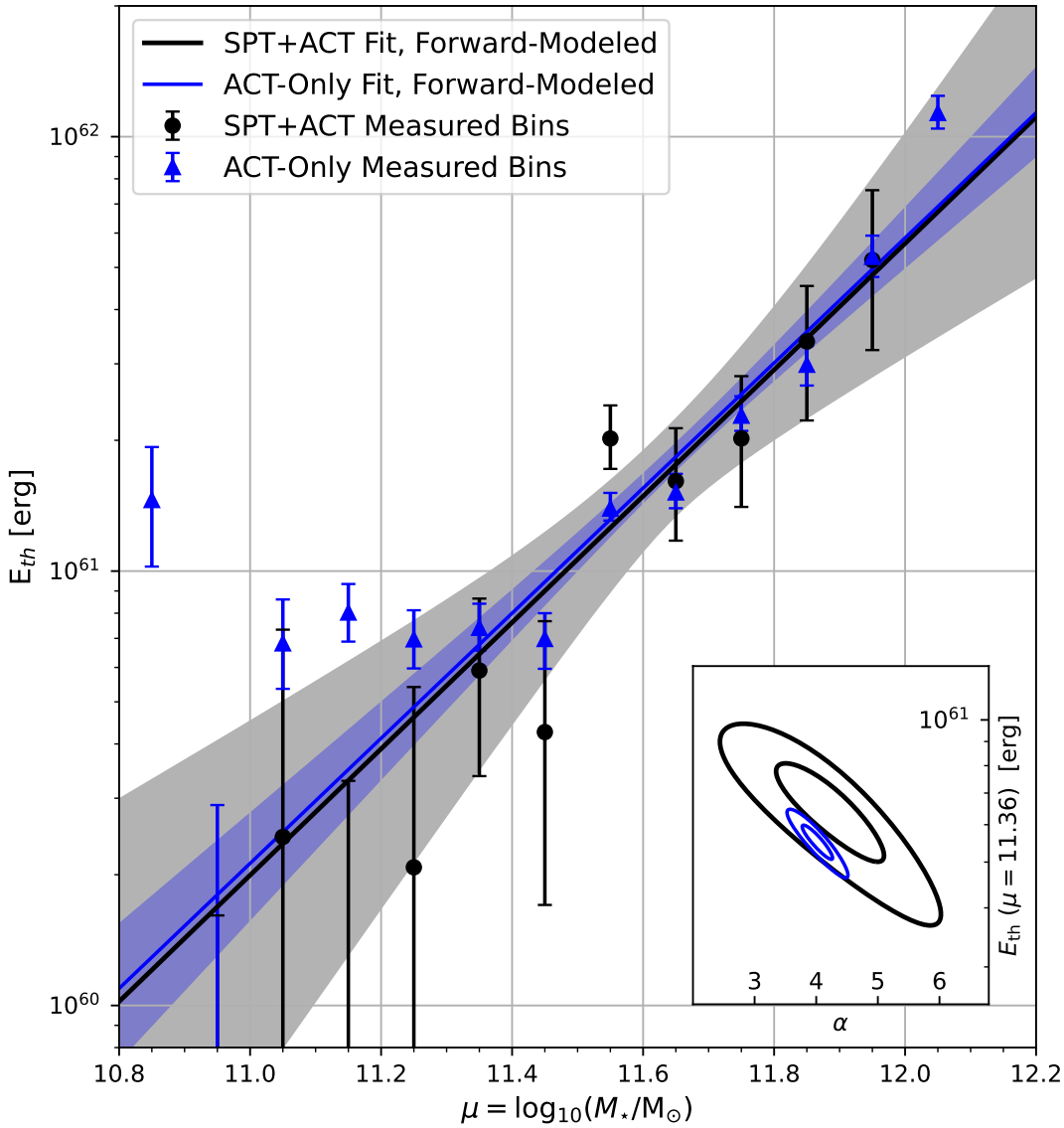

Figure 3.12: SPT+ACT (*black, circles*) and ACT-Only (*blue, triangles*) galaxies' energy in 0.1 dex stellar mass bins with associated energy-mass fit as described in Table 3.6 after forward-modeling our stellar mass uncertainty (Section 3.4.14). The shaded fit regions correspond to forward-modeled 2σ levels. Inset: 1- and 2-σ bounds of the (non-forward-modeled) fit parameters $E_{\mathrm{th}}(\mu = 11.36$ dex), and slope α. We show $E_{\mathrm{th}}(\mu = 11.36$ dex) instead of E_{pk} here as the samples contain different peak masses.

the posterior distributions of α and $E_{\rm th}(\mu = 11.36$ dex). We display $E_{\rm th}(\mu = 11.36$ dex) instead of $E_{\rm pk}$ in order to compare catalogs, as they have different peak masses ($\mu_{\rm pk}$). Best fit values for $E_{\rm pk}$ and α are shown in Table 3.6, compared to previous SPT results (Meinke et al., 2021). All three catalogs show agreeing slopes (α) within 1σ, $4.04^{+0.88}_{-0.87}$ for SPT+ACT and $4.00^{+0.25}_{-0.24}$ for ACT-Only. These slopes uphold a strong trend of observations that indicate only CGM in the most massive galaxies and clusters produce significant levels of thermal energy (Greco et al., 2015). Some plateauing at lower stellar mass may be present as well, evident by the low mass bin outliers in our ACT-Only measurements. Energies at peak mass ($E_{\rm pk}$) are also significant, at a level of 4.4σ for SPT+ACT and 15.8σ for ACT-Only.

Catalog	$\mu_{\rm pk}$	$E_{\rm pk}$	α	$M_{\rm d,pk}$	$\alpha_{\rm d}$
	$\left[\log_{10}(M_\star/{\rm M}_\odot)\right]$	$[10^{60}{\rm erg}]$	[unitless]	$[10^8{\rm M}_\odot]$	[unitless]
SPT+ACT	11.36	$6.66^{+1.60}_{-1.46}$	$4.04^{+0.88}_{-0.87}$	$6.18^{+0.66}_{-0.66}$	$2.58^{+0.45}_{-0.43}$
ACT-Only	11.40	$8.00^{+0.51}_{-0.50}$	$4.00^{+0.25}_{-0.24}$	$6.70^{+0.56}_{-0.55}$	$2.23^{+0.34}_{-0.34}$
SPT-Only†	11.36	$5.98^{+1.02}_{-1.00}$	$3.77^{+0.60}_{-0.74}$	–	–

Table 3.6: Forward-modeled energy and dust mass versus stellar mass fits of eqs. (3.11) & (3.12) following the inclusion stellar mass uncertainty via eqs. (3.13), (3.14), & (3.15). For our two quiescent galaxy samples and †previous energy-stellar mass fit from Meinke et al. (2021) (SPT-Only). †Our methods differ slightly from those in Meinke et al. (2021) due to changes in beam, map processing, and $S/N < 1\sigma$ cut. Dust mass was calculated from eq. (3.10) for a $\kappa(\nu_0) = 0.08$ m^{2}kg^{-1}, which we recognize might fluctuate by a further factor of two or 0.30 dex.

In similar fashion, eq. (3.14) was fit to the measured dust versus stellar mass bins found for each catalog. We again refrain from fitting any bins with $S/N < 1\sigma$ to avoid introducing spurious bias. The forward-modeled best fits and 2σ uncertainties are shown in Fig. 3.13. The inset plot shows the posterior distributions of $\alpha_{\rm d}$ and $M_{\rm d}(\mu = 11.36$ dex). Fits for $M_{\rm d,pk}$ and $\alpha_{\rm d}$ are shown in Table 3.6.

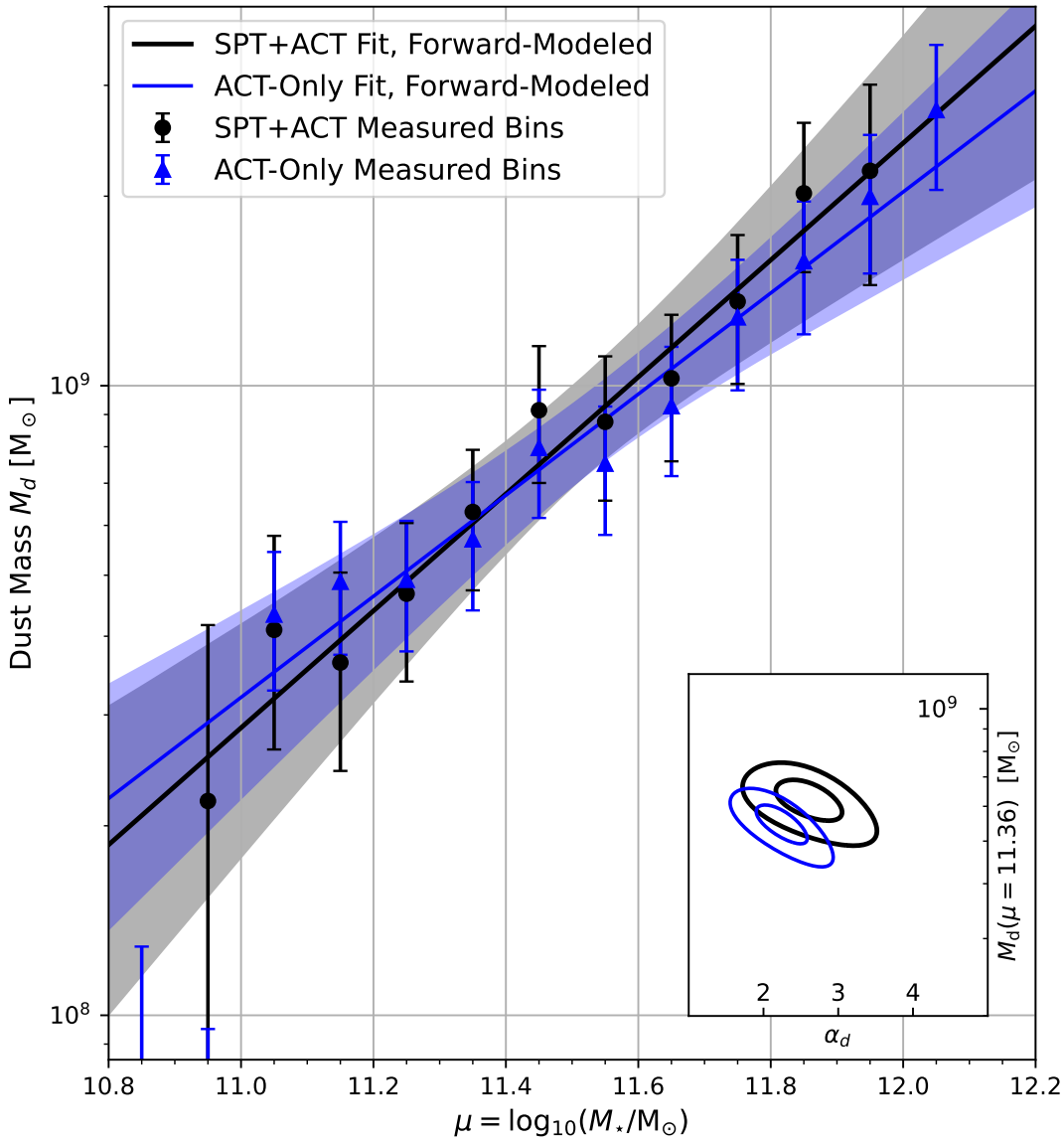

Figure 3.13: SPT+ACT (*black, circles*) and ACT-Only (*blue, triangles*) galaxies' dust mass in 0.1 dex stellar mass bins with associated dust-stellar mass fit as in 3.6 after forward-modeling our stellar mass uncertainty (Section 3.4.14). The shaded fit regions correspond to forward-modeled 2σ levels. Inset: 1- and 2-σ bounds of the non-forward-modeled fit parameters $M_{\rm d}(\mu = 11.36$ dex), $\alpha_{\rm d}$. We show $M_{\rm d}(\mu = 11.36$ dex) instead of $M_{\rm d,pk}$ here as the samples contain different peak stellar masses.

Dust mass at the peak stellar masses were detected at a 9.4σ level for SPT+ACT and 12.1σ for ACT-Only. Both catalogs show agreeing slopes ($\alpha_{\rm d}$) within 1σ, $2.58^{+0.45}_{-0.43}$ for SPT+ACT and $2.23^{+0.34}_{-0.34}$ for ACT-Only. As these slopes are greater than 1, they highlight a non-linear relationship between dust and stellar mass that indicates increasingly massive quiescent galaxies have a higher dust-to-stellar mass ratio. However, this trend may only be present in the high stellar mass regime due to our narrow galaxy mass distribution.

We also consider the potential of neighboring two-halo contributions that may falsely inflate these measurements. Discussed in more detail in Meinke et al. (2021) with the same $R = 2.0'$ aperture corresponding to a radius of ≈ 2.0 comoving Mpc, a central halo will be expected to dominate the tSZ signal for thermal energies exceeding $\approx 3 \times 10^{60}$ erg or halo masses larger than $\approx 10^{13}{\rm M}_{\odot}$. This is determined under the assumption that the gas in all neighboring halos is heated to virial temperature $T_{\rm vir}$. As all our reported thermal energies with $S/N > 1\sigma$ in Fig. 3.12 reside above 3×10^{60} erg, we conclude the two-halo contribution within them are negligible compared to their respective measured uncertainties.

We also consider our dust mass measurements in Fig. 3.13 to be the expected upper limit. As discussed in Section 3.4.11, the $R = 2.0'$ aperture produces a result roughly 0.30 dex greater than a separate conservative estimate via evaluation of the dust profile in Section 3.4.10. As the assumed dust mass opacity coefficient $\kappa(\nu_0) = 0.08\ {\rm m}^2{\rm kg}^{-1}$ contains a further factor of two or 0.30 dex uncertainty, any contributions from neighbors are likely within this uncertainty. Hence, we refrain from drawing any large conclusions aside from the relation indicated by our dust-to-stellar mass slope fit, as we expect $\kappa(\nu_0)$ to not vary significantly between our stellar mass bins.

3.4.15 Implications for AGN Feedback

Our constraints on $E_{\rm th}$ allow us to glean information about AGN feedback, though detailed comparisons with AGN models are best carried out alongside full numerical simulations. First, comparisons with previous work in Meinke et al. (2021) show strong similarities in their energy-mass fit. This is as expected, due to an overlap of target galaxy samples and use of SPT data. However, as before we also see significant similarities with the lower redshift ($z \approx 0.1$) results from Greco et al. (2015), even though they used locally bright galaxies as opposed to our age > 1 Gyr, $SSFR < 0.01$ Gyr^{-1}, quiescent galaxies. There are a variety of theoretical models that suggest a good match between the most massive quiescent galaxies at moderate redshifts and the central galaxies of massive halos in the nearby universe (e.g, Moster et al., 2013; Schaye et al., 2015; Pillepich et al., 2018).

Such lack of thermal energy evolution in the CGM around massive galaxies since $z \approx 1$ mirrors what occurs for the luminosity function of these galaxies (e.g. van Dokkum et al., 2010; Muzzin et al., 2013). This trend could be more indicative of radio-mode AGN feedback, where gas accretion contributes to CGM heating and radiative losses to CGM cooling. Whenever cooling surpasses heating, jets will arise that quickly push the gas up to a constant temperature and entropy at which cooling is inefficient. On the other hand, quasar models instead produce an energy input from feedback which occurs once at high redshift, heating the gas such that cooling is extremely inefficient up until today. As a result, gravitational heating will increase $E_{\rm th}$ without any significant mechanism to oppose it. However, specifics of this evolution are highly dependent on the history of galaxy and halo mergers between $0 < z \lesssim 1$. Hence, it is possible that some types of quasar dominated models may be compatible with our measurements.

A second major inference is the overall level of feedback. To estimate the magnitude of gravitational heating, we can assume that the gas collapses and virializes along with an encompassing spherical dark matter halo, and is heated to the virial temperature $T_{\rm vir}$. This gives the relation in eq. (1.17). We can convert from halo mass to galaxy stellar mass using the observed relation between black hole mass and halo circular velocity for massive quiescent galaxies (Ferrarese, 2002), and the relation between black hole mass and bulge dynamical (Marconi and Hunt, 2003). As shown in Spacek et al. (2016) this gives eq. (1.18), which represents the expected total thermal energy around a galaxy of stellar mass $M_\star$ ignoring both radiative cooling and feedback.

For a mean redshift of $z \approx 1.1$ this yields $\approx 3.8 \times 10^{60}$ erg and $\approx 4.1 \times 10^{60}$ erg for our $M_{\star,\rm pk} = 2.29 \times 10^{11} {\rm M}_\odot$ (SPT+ACT) and $2.51 \times 10^{11} {\rm M}_\odot$ (ACT-Only), respectively. Unfortunately this estimate has an uncertainty of about a factor of two, which is significantly larger than the uncertainty in our measurements. Regardless, these are lower than the $E_{\rm pk} = 6.66^{+1.60}_{-1.46} \times 10^{60}$ erg and $8.00^{+0.51}_{-0.50} \times 10^{60}$ erg respectively, that we found in Section 3.4.13. These suggest the presence of additional non-gravitational heating, particularly as cooling losses are not included in eq. (1.18).

To estimate quasar-mode feedback heating we use a simple model described in Scannapieco and Oh (2004), given by eq. (1.19) where $\epsilon_{k,0.05}$ is the fraction of bolometric luminosity from the quasar associated with an outburst, normalized by a fiducial value of 5%, which is typical of quasar models (e.g. Scannapieco and Oh, 2004; Thacker et al., 2006; Costa et al., 2014). Taking $\epsilon_{k,0.05} = 1$ for our samples' mean redshifts and peak masses, this gives $\approx 3.0 \times 10^{60}$ erg (SPT+ACT) and $\approx 3.3 \times 10^{60}$ erg (ACT-Only). Adding these to the contributions from $E_{\rm th,gravity}$ above gives a total energy of $\approx 6.8 \times 10^{60}$ erg and $\approx 7.4 \times 10^{60}$ erg, respectively. Including this additional energy from quasar-mode AGN feedback better matches our results of

$E_{\rm pk} = 6.66^{+1.60}_{-1.46} \times 10^{60}$ erg and $8.00^{+0.51}_{-0.50} \times 10^{60}$ erg than heating from gravity alone. It also does not account for any energy losses.

Meanwhile, radio mode models are expected to fall somewhere between these two limits, with jets supplying power to roughly balance cooling processes, but never adding a large burst of additional energy near that of eq. (1.19). This would suggest values slightly below our measurements, but again with too much theoretical uncertainty to draw any definite conclusions.

A third major inference from our measurements comes from the slope of eq. (3.11), which is significantly steeper than in our simple models. This is most likely due to uncertainties in the halo-mass stellar mass relation, which are particularly large for massive $z \approx 1$ galaxies (Wang et al., 2013; Lu et al., 2015; Moster et al., 2018; Kravtsov et al., 2018; Behroozi et al., 2010, 2019). Recent studies alongside our own (Schaan et al., 2021; Amodeo et al., 2021; Meinke et al., 2021; Vavagiakis et al., 2021) make it clear that observations are now fast outpacing theoretical estimates, a major change from several years ago when only galaxy cluster sized halos were capable of being moderately detected. Future comparisons between measurements and full simulations will yield key new insights into the processes behind AGN feedback.

3.5 Discussion

Many galaxies from $z \approx 1$ to present day, starting with the most massive, undergo a process that quenches new star formation. The proposed likely culprit is feedback from accretion onto supermassive black holes, which would have a noticeable impact on the surrounding CGM. By probing the CGM for signs of heating via the redshift-independent tSZ effect, we can begin to differentiate between various AGN accretion models and provide much needed constraints for theoretical simulations.

Here we have selected $N = 387,627$ old quiescent galaxies with low SFR at $0.5 \leq z \leq 1.5$ from DES and WISE within the ACT millimeter telescope field. A subset of $N = 94,452$ galaxies are further used to incorporate data from SPT for an analysis across multiple instruments. These quiescent galaxies are ideal candidates to show strong heating via feedback. A detailed set of map processing (Section 3.4.2) is conducted to mitigate any systematic differences between SPT and ACT, applying a uniform $2.1'$ FWHM Gaussian beam across all maps that reside near 95/150/220 GHz. We then subtract a $5.0'$ resolution *Planck* SMICA SZ-Free CMB map to remove large-scale CMB fluctuations uncorrelated with our target galaxies.

When stacked, we observe separable dust and tSZ profiles from both galaxy catalogs. Further split into stellar mass bins, we show a clear thermal energy versus stellar mass relation influenced by our photometric uncertainty in stellar mass. Often simply discarded in tSZ analysis, we also use the dust to estimate the associated dust mass for our samples.

This work builds off of previous $z \approx 1$ quiescent galaxy stacking conducted by Spacek et al. (2017); Meinke et al. (2021). Our analysis here is enhanced from the prior via use of the recent ACT data release (Naess et al., 2020; Mallaby-Kay et al., 2021), improved map processing, and a heightened focus on the radial profile and dust mass of our target galaxies. Others have also begun a more concerted effort to analyze the galactic structure of the tSZ and kSZ (Schaan et al., 2021; Amodeo et al., 2021; Calafut et al., 2021; Vavagiakis et al., 2021; Lokken et al., 2022).

Firstly, the dust profile of our SPT+ACT and ACT-Only galaxies produce up to 16.6σ and 21.5σ detection respectively, for radial bins with widths of $0.5'$. Profile detection with $S/N \geq 2\sigma$ is found out to $15'$ (15.2 comoving Mpc). We observe a dust profile shape for each sample indicative of a central point source associated with our galaxies and an extended profile that traces the two-point correlation function

of neighboring galaxies and structure. To obtain a slope for the extended dust, we fit a point source plus King model as described in Section 3.4.9, finding slopes of $\gamma = 2.52^{+0.16}_{-0.13}$ and $2.90^{+0.14}_{-0.12}$. These are $20-80\%$ greater than power-law fits conducted in galaxy cluster studies ($\gamma \approx 1.5-2.0$, Eftekharzadeh et al., 2015; Coil et al., 2017). We attribute most of this discrepancy to a divergence between the King and power-law models when near or below our core radius of $r_0 = 3.0$ comoving Mpc.

Such dust profile analysis might also provide a novel method to constrain a catalog's intergalactic medium (IGM) and central halo mass, wherein a similar catalog of known halo mass or bias factor is used to compare two-point correlation terms traced by the observed extended dust. However a correct comparison requires careful consideration of all systematic differences in catalog selection and accurate removal of dust associated with the central source(s).

Secondly, the high S/N detection of dust allows us to convert our dust intensity fit in the $\nu_0 = 353$ GHz rest frame to a dust mass as shown in eq. (3.10). The primary difficulty in this approach is an existing uncertainty in the dust mass opacity or absorption cross-section coefficient, where we take an intermediate value of $\kappa(\nu_0) = 0.08$ $\mathrm{m^2 kg^{-1}}$ while acknowledging this may vary by a factor of two (Draine, 2003; Dunne et al., 2003; Casey, 2012). We then consider reasonable lower and upper limits to isolate the dust solely associated with our central galaxies: the lower limit from the point source fit of our aforementioned profile fit, which has noted degeneracy with the King model at small radii; and an upper limit through integration within a circular aperture of $R = 2.0'$ radius.

These result in a $\log_{10}$ dust mass range from $8.45^{+0.10}_{-0.12}$ to $8.82^{+0.09}_{-0.11}$ $\log_{10}(\mathrm{M}_\odot)$ for SPT+ACT and $8.46^{+0.09}_{-0.12}$ to $8.85^{+0.09}_{-0.11}$ $\log_{10}(\mathrm{M}_\odot)$ for ACT-Only. As a dust-to-stellar mass ratio, these become $-2.96^{+0.10}_{-0.12}$ to $-2.59^{+0.09}_{-0.11}$ $\log_{10}(M_\mathrm{d}/\mathrm{M}_\star)$ and $-2.98^{+0.09}_{-0.12}$ to $-2.59^{+0.09}_{-0.11}$ $\log_{10}(M_\mathrm{d}/\mathrm{M}_\star)$, respectively. Other studies involving massive or quiescent

galaxies at $z \approx 1$ have found $\log_{10}(M_{\rm d}/{\rm M}_\star) \approx -3.5$ to -2.7 (Gobat et al., 2018; Magdis et al., 2021). As our dust mass contains an additional 0.30 dex uncertainty from $\kappa(\nu_0)$, we conclude our values are in agreement, but do not draw any larger inferences. This consistency is notable however, as it echoes reports of higher dust-to-stellar mass ratios for massive galaxies at $z \approx 1$ than those at nearby lower redshifts (Santini et al., 2015; Magdis et al., 2021).

Thirdly, we inspect our tSZ radial profile and obtain a clear central detection, up to 5.5σ in our SPT+ACT catalog and 11.6σ in ACT-Only. However our detection falls off much more rapidly than for dust, dropping below 2σ at $4.0'$ (4.0 comoving Mpc) and $8.0'$ (8.1 comoving Mpc), respectively. As a result compared to dust, we find steeper King slopes of $\gamma = 6.2^{+2.3}_{-2.1}$ and $4.0^{+0.6}_{-0.4}$, which indicate a sharper decline in the tSZ two-point correlation or two-halo term. This is within expectations, since the neighboring lower mass galaxies should contain reduced or cooler levels of ionized gas at a nonlinear relationship to stellar mass (Hill et al., 2018). We also note that radio contamination would produce an underestimated fit of the tSZ, while uneven relation of radio contaminates versus radii could affect fit slopes as well. This effect is likely marginal for our redshift and frequency bands.

We also fit the tSZ point source amplitudes at 1.8σ significance for SPT+ACT and 3.1σ for ACT-Only. These profiles and fits as shown in Fig. 3.10 indicate a clear extended tSZ signal. However, also evident is the inherent degeneracy between our combined point source plus King model brought about by the map resolution. This results in an inability to accurately separate the central one-halo tSZ from its two-halo counterpart and limit further detailed analysis.

Fourthly, we focused on measurements split into 0.1 dex stellar mass bins. In a more generalized approach than our profiles above, we separated the tSZ and dust integrated within a $R = 2.0'$ radius circular aperture. These signals were then con-

verted into thermal energy (eq. 1.16) and dust mass (eq. 3.10), respectively. Power-law relations were defined for both thermal energy and dust mass versus stellar mass (eqs. 3.11 & 3.12), scaled with respect to peak mass ($M_{\star,\mathrm{pk}}$) of 2.29×10^{11} $\mathrm{M}_{\odot}$ for SPT+ACT and 2.51×10^{11} $\mathrm{M}_{\odot}$ for ACT-Only. However, to accurately fit our measurements we also incorporated and forward-modeled a stellar mass uncertainty of 0.16 dex that arises from our SED fitting of photometric data.

Our thermal energy to stellar mass power-law fit produces energies of $E_{\mathrm{pk}} = 6.66^{+1.60}_{-1.46} \times 10^{60}$ erg for SPT+ACT and $8.00^{+0.51}_{-0.50} \times 10^{60}$ erg for ACT-Only, at their peak mass. These values only appear inconsistent due to their different peak masses. The power-law slopes are found to be within 1σ of each other, with $\alpha = 4.04^{+0.88}_{-0.87}$ and $4.00^{+0.24}_{-0.24}$, respectively. These slopes are significantly steeper than our simple feedback models in Section 3.4.15. This can likely be attributed to model uncertainties in the halo-to-stellar mass relation for massive $z \approx 1$ galaxies (Wang et al., 2013; Moster et al., 2018; Behroozi et al., 2019). Our fits, shown in Fig. 3.12, are also consistent with the previous investigation of Meinke et al. (2021) and lower redshift measurements by Greco et al. (2015).

Meanwhile, our dust to stellar mass power-law fit produces dust masses of $M_{\mathrm{d,pk}} = 6.18^{+0.66}_{-0.66} \times 10^{8}$ $\mathrm{M}_{\odot}$ for SPT+ACT and $6.70^{+0.56}_{-0.55} \times 10^{8}$ $\mathrm{M}_{\odot}$ for ACT-Only, at peak stellar mass. With power-law slopes of $\alpha_{\mathrm{d}} = 2.58^{+0.45}_{-0.43}$ for SPT+ACT and $2.23^{+0.34}_{-0.34}$ for ACT-Only. Our slope fits are more trustworthy than the aforementioned dust masses due to the uncertainties in dust mass opacity $\kappa(\nu_0)$ that would only scale our measurements and not affect the fit slope α_{d}. As our slopes indicate a greater than linear relation ($\alpha_{\mathrm{d}} > 1$), we conclude that massive $z \approx 1$ quiescent galaxies have an increasing dust-to-stellar mass ratio for our sample. Notably this may only be valid for our high and narrow stellar mass range.

Finally, we compare the stellar mass binned energy fit to those predicted by simple theoretical feedback models in Section 3.4.15. Our values more closely align with heating due to quasar-mode feedback rather than gravitational-only feedback. However, both theoretical models have uncertainties of roughly a factor of two that result in the models overlapping in the same regime that our energy fit is found. Additionally, a third option of radio-mode feedback would also be situated in-between. Hence, we conclude our values are strong indicators that some form of AGN feedback is present, but the exact process and amount is unable to be determined when compared to theory. This highlights the need for improved theoretical and simulation models to keep pace with observations.

With the development of better instruments in both noise, resolution, and sky coverage, observations will continue to improve the characterization of galactic structures. We have demonstrated here that such detailed analysis at $z \approx 1$ is currently possible and will greatly benefit from improved resolution for future analysis. The latest generation of telescopes includes SPT-3G (Benson et al., 2014; Sobrin et al., 2022) and TolTEC (Austermann et al., 2018; Wilson et al., 2020) which are more than capable of improving upon this work. TolTEC in particular, currently being deployed on the 50 m Large Millimeter Telescope, will grant a $\geq 5\times$ better resolution. This will enable the ability to resolve the tSZ mainly associated with the CGM and separate it from the potentially still unresolved dust which comes primarily from the underlying galaxy.

Chapter 4

DESIGN OF MULTICHROIC DUAL-POLARIZATION MILLIMETER-WAVE ANTENNAS

Observational astronomy is continuously driven by technological improvements and innovations. At millimeter wavelengths, such advancements are frequently dictated by the end goal of achieving more detailed observations of the CMB. This is evident in a variety of manners, including improvements in telescope design, readout electronics, signal chains, superconducting detector design, etc. Not to be forgotten however, is the significance of the optical coupling process present at the telescope's focal plane and responsible for efficiently delivering signal from incident photons to their respective detector sensor elements.

This chapter details the design of planar multichroic, dual-polarization, lenslet-coupled, superconducting antennas for their potential use in millimeter wavelength detectors. Concepts, design methodology, and simulations of the technology are described in the subsequent sections. This is meant to showcase the primary antenna design steps conducted, in the hopes of constructing a foundation for these or similar antenna designs to be used in the next generation of millimeter-wave detectors.

4.1 Motivation

As detailed in Section 1.2, the already faint signature of the CMB contains even fainter and smaller fluctuations of keen interest. These are worth close investigations to help determine cosmological constants and evolution parameters of the universe, in addition to detailed properties of galaxies and large-scale structure within the uni-

verse. In such an endeavor, increased sensitivity requires increasing an instrument's overall signal-to-noise characteristics.

Simply stated, this can be achieved by either increasing an instrument's signal, or decreasing noise. For a single-frequency band, upgrading the number of detectors or total observing time are the primary methods to increase signal. Meanwhile, decreased noise can be achieved through reducing noise contributions from sensors and readout electronics. The transition-edge sensor (TES) bolometer and kinetic inductance detector (KID) are the two prevalent low-noise sensors currently used in millimeter astronomy. For most cases now, these detectors approach background limited or photon-noise dominated levels in which they contribute minimally to measured noise compared to that of incident photons (Abitbol et al., 2017; Mauskopf, 2018). TES bolometers have been thoroughly studied and used in millimeter detectors for upwards of two decades (Irwin, 1995; Irwin and Hilton, 2005; Holland et al., 2013). Meanwhile, the slightly newer KIDs, first introduced in Day et al. (2003), show upside in ease of fabrication and scalability for large arrays. The most common forms of KIDs include microwave- (MKID), and lumped-element kinetic inductance detectors (LEKIDs) (Doyle, 2008; Abitbol et al., 2017).

Sensitivity to polarization is also an evermore important factor in millimeter astronomy to observe effects such as galaxy lensing and search for the elusive CMB B-mode polarization. By the use of detectors with dual-polarization capable antennas and a sensing element per polarization, the respective focal plane signal is effectively doubled. Deployment of multichroic detectors operating in more than one frequency band (see Section 1.5) similarly increases the total observable signal detected. As a result, multichroic dual-polarization detector arrays are now becoming standard to capitalize on both effects.

4.1.1 A Brief History of CMB Detectors and Antennas

The first such multichroic polarization-sensitive array to be used in a large-scale CMB experiment was deployed in 2015 as apart of ACTPol's third pixel array (PA3) at 97 and 148 GHz (Datta et al., 2016; Thornton et al., 2016). Since then most CMB instruments have been polarization-sensitive, and a handful including Advanced ACTPol (Simon et al., 2016) and SPT-3G (Posada et al., 2018) were also multichroic. SPT-3G in particular spans three bands, at 95, 150, and 220 GHz (Sobrin et al., 2022). Many planned upcoming instruments will also be using some form of multichroic dual-polarization detectors (e.g. Simon's Observatory, LiteBIRD, AliCPT, POLARBEAR-2; Westbrook et al., 2018; Xu et al., 2020; Salatino et al., 2020; Westbrook et al., 2021).

A standard in many polarization sensitive millimeter-wave detectors is the use of profiled or corrugated feedhorns coupled to planar probes or orthomode transducers (OMTs) (Dicker et al., 2014; Simon et al., 2016). The fabrication method and assembly of the feedhorns can vary, ranging from direct machined horn profiles to detailed stacking of etched silicon wafers (Simon et al., 2018). Such processes are also often multichroic, but can be costly and challenging for large arrays. Deep reactive-ion etching (DRIE) of the substrate between OMT probes and feedhorns adds a further necessary step in fabrication.

One alternative to feedhorns, planar antenna phased arrays have been developed and deployed in multiple CMB instruments including SPIDER, BICEP2, Keck Array, and BICEP3 (Ade et al., 2015a). Avoiding bulky feedhorns, these instead utilize an array of on-chip sub-antennas (Abitbol et al., 2017). To enable dual-polarization, each pixel consists of two orthogonal interleaving arrays, fed from separate microstrip feedlines. While they have been made up of simple slot antennas for single-band detectors,

broadband arrays are also under development. Challenges to antenna array pixels and scalability are primarily with the complex microstrip feed-lines. The efficacy of multichroic antenna arrays is also still undetermined, as feed-line complexity increases with required bandwidth. Antenna arrays do provide beam customization through phase adjustments which can be used to further optimize designs (Abitbol et al., 2017).

The other significant optical coupling method is the use of an individual antenna placed on the back of an anti-reflection (AR) coated lenslet. The aforementioned SPT-3G, the first large CMB array to span three frequency bands, utilizes a broadband sinusoidal log-periodic antenna paired with an alumina lenslet and detailed multi-layer AR coating (Posada et al., 2018; Nadolski, 2020). Other planned studies such as Simon's Observatory, LiteBIRD, and POLARBEAR-2 will use similar lenslet-coupled antennas for at least some of their bands Westbrook et al. (2018); Xu et al. (2020); Westbrook et al. (2021). In many cases, they are chosen for use in the lower-frequency bands where they provide a significant size benefit compared to their horn-coupled antenna counterparts. The lenslet-coupled method shows large potential and is the primary focus of this investigation, detailed below.

4.2 Lenslet Design

By placing a dielectric lenslet over a planar antenna, the main beam can be focused and gain greatly increased. With the antenna operating on a high-dielectric half-space (half air, half dielectric), a significant portion of the energy will radiate into the dielectric. For a thick (compared to λ) dielectric, the effective dielectric constant at the half-space interface approaches,

$$\epsilon_{eff} = \frac{\epsilon + \epsilon_0}{2}, \tag{4.1}$$

which also reduces the required physical antenna size for a desired frequency. An ideal lenslet geometry for detecting incident plane waves requires an ellipsoidal lens of eccentricity $e = 1/n$ with the detector residing at the opposing focal point (Filipovic et al., 1993; O'Brient, 2010). Hence, spherical waves emanating from an antenna would be transformed outside the ellipsoidal lens into planar waves. However, fabricating such a perfect ellipsoidal lens is both challenging and expensive, so one viable alternative is to use an extended hemispherical lenslet design. This is also commonly referred to as a synthesized ellipse (Filipovic et al., 1993).

Fig. 4.1 shows extended hemispherical lenslet diagrams both without and with a single layer anti-reflection (AR) coating. Rays are traced from the extended focal plane where a planar antenna would be located. An optimal synthesized elliptical lens seeks to minimize the zenith angle (Ψ) traced out from the extended focal point along all possible focal angles (θ'). This focal angle θ' can be redefined as:

$$\theta' = \arctan\left(\frac{\mathrm{R}\sin\theta}{\mathrm{L} + \mathrm{R}\cos\theta}\right), \tag{4.2}$$

where R is the hemispherical lens radius, L is the extension length from the hemisphere to focal plane, and θ is the hemispherical angle from zenith O'Brient (2010). Solving for a lenslet without an AR coating, an incident zenith angle Ψ is defined as

$$\Psi = \arcsin\left(\frac{\mathrm{L}(n_2/n_0)\sin\theta}{\sqrt{\mathrm{L}^2 + 2\mathrm{RL}\cos\theta + \mathrm{R}^2}}\right) - \theta, \tag{4.3}$$

with the lenslet refractive index n_2 and surrounding (air) index n_0. The inclusion of one AR coating of thickness T produces a lengthier solution,

$$\begin{aligned}\Psi = \arcsin\left(\frac{\mathrm{RL}(n_2/n_0)\sin\theta}{(\mathrm{R}+\mathrm{T})\sqrt{\mathrm{L}^2 + 2\mathrm{RL}\cos\theta + \mathrm{R}^2}}\right) + \arcsin\left(\frac{\mathrm{L}(n_2/n_1)\sin\theta}{\sqrt{\mathrm{L}^2 + 2\mathrm{RL}\cos\theta + \mathrm{R}^2}}\right) \\ - \arcsin\left(\frac{\mathrm{RL}(n_2/n_1)\sin\theta}{(\mathrm{R}+\mathrm{T})\sqrt{\mathrm{L}^2 + 2\mathrm{RL}\cos\theta + \mathrm{R}^2}}\right) - \theta,\end{aligned} \tag{4.4}$$

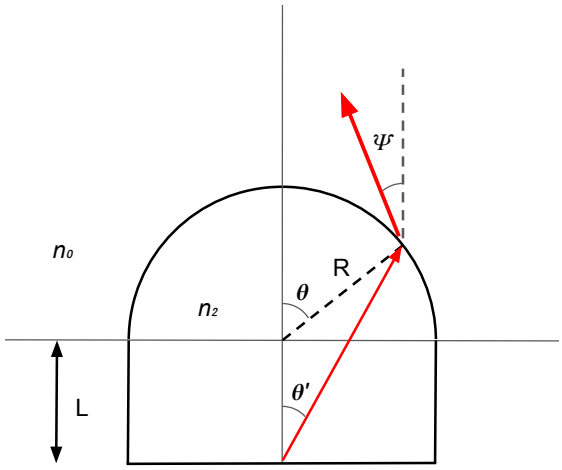

(a) Lenslet with no AR.

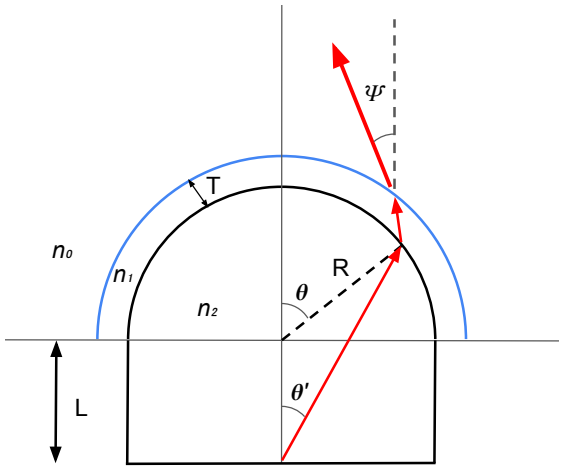

(b) Lenslet with 1-layer AR.

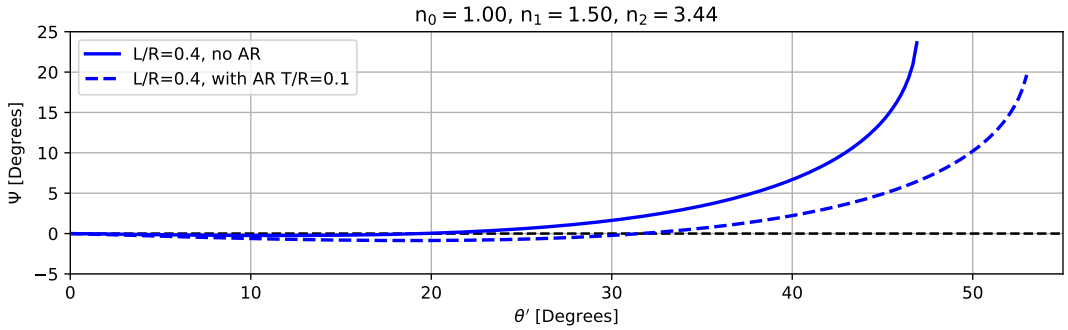

(c) Final (Ψ) vs focal (θ') zenith angle, for a lenslet without and with a 1-layer AR coating.

Figure 4.1: Ray tracing diagrams for an extended hemispherical lenslet (a) without and (b) with a single anti-reflection (AR) layer. Key parameters are labeled as follows: extension length L of the focal plane from the hemispherical plane, hemisphere radius R, hemispherical zenith angle θ, focal point zenith angle θ', final angle from zenith Ψ, and anti-reflection layer thickness T. (c) The addition of even a thin (T/R = 0.1) AR layer helps extend the viable final angle $\Psi \approx 0$ to larger focal angles θ'.

with refractive index of the AR coating, n_1. In the limiting cases of the AR coating being either thin relative to the lenslet radius (T$\ll$R) or with a similar index of refraction to the surrounding medium ($n_1 \rightarrow n_0$), eq. (4.4) becomes the simpler eq. (4.3). In the standard lenslet case where $n_0 < n_1 < n_2$, the addition of an AR coating also helps to create a more ideal near-ellipsoidal lens, as shown in Fig. 4.1c.

Of course, there are plenty of additional considerations that go beyond the scope of this derivation. This includes the physical size of the antenna residing at the focal plane, the model working in the ray-optics limit, lenslet quality, and effects of the curved hemispherical surface. For optimization, the extension-to-radius ratio L/R is often best near $\approx 0.38 - 0.46$ (O'Brient, 2010). Calculations can be analyzed further with desired AR coatings, but the thickness T is constrained by operating frequency. The antenna far-field radiation pattern can further be taken into consideration when defining lenslet parameters, but fluctuations with frequency limit the ability to optimize for broadband purposes. Many of these considerations depend on the size of the antenna, which can vary but should be smaller in radius than the hemispherical lenslet. In using a ray-optics limit, I also assume the lens' hemispherical surface is in the antenna's far-field. The standard far-field (Fraunhofer) radiation distance of an antenna is defined as:

$$R_{FF} = \frac{2\mathrm{D}^2}{\lambda}, \tag{4.5}$$

where D^2 is the effective area of the antenna. When the majority of radiation is along the lenslet axis (small θ'), effects from the lenslet curvature can also be considered negligible (Luhn and Hentschel, 2019).

Millimeter astronomy lenslet architecture was first used with crossed double-slot dipole antennas in POLARBEAR (Arnold et al., 2012). A subsequent deployment with sinuous log-periodic antennas was used in SPT-3G (Posada et al., 2018) with 3 multichroic bands. Similar sinuous lenslet designs are planned for low- to mid-frequency bands in Simons Observatory and LiteBIRD (Xu et al., 2020).

Lenslet coupled antenna pixels are extremely beneficial to increasing the size of telescope focal planes. It not only allows for smaller antennas thanks to the dielectric half-space, but saves weight without the need for additional feedhorns and enables custom antennas for broadband multichroic detectors. Similar to feedhorns however,

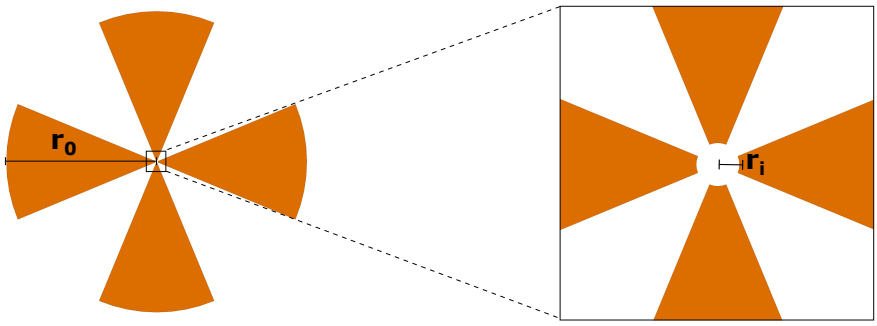

Figure 4.2: *Left:* A basic dual-bowtie self-complementary antenna layout. The arms are not directly connected in the center (close-up, *right*), but rather excited individually, normally as a slot antenna fed with a microstrip. No scale bar is included as this antenna can be scaled invariantly according to desired frequency.

the main drawback is the complexity of construction. Lenslets with a high dielectric constant require at least one layer of AR coating, while broadband pixels would be better served with multiple layers. Various coating methods have been used for lenslets that require specific and uniform AR thicknesses (Abitbol et al., 2017; Nadolski et al., 2018). The methods of carefully applying these AR coatings are still being improved, and show promise in scaling to large pixel arrays.

4.3 Self-Complementary Antenna Arm Geometry

The concept of self-complementary antennas for wide bandwidth applications has been around for decades, primarily investigated at radio frequencies (RF). Self-complementary antennas are also often considered frequency-independent due to their scalability and predicted impedance that follows an altered Babinet's Principle, shown by Deschamps (1959):

$$Z_{slot} Z_{metal} = \left(\frac{Z_0}{4 \sin\left(\frac{\pi}{n}\right)} \right)^2 , \tag{4.6}$$

which can be simplified for self-complementary planar layouts where the metal conductor arms are identical to the slots between them ($Z_{metal} = Z_{slot}$). For an $n = 4$ arm pattern in free space ($Z_0 = 120\pi = 377\ \Omega$), the arm impedance is roughly

133 Ω. When placed on a silicon dielectric half-space ($\epsilon = 11.7$, $\epsilon_{eff} \approx 6.35$, eq. 4.1), individual arm impedance becomes approximately 52.9 Ω.

The premise of most planar self-complementary antennas is rotational symmetry. A four-arm design places an identical arm every 90°, while the complementary property requires there to be an identical slot or gap between them. The most basic design is a dual-bowtie antenna (Fig. 4.2), with inner (r_i) and outer (r_0) arm radii scaled to operating wavelengths. The simplicity in geometry also grants uniform current density at constant radius, minimizing fluctuations in both impedance and polarization along zenith. The downsides that promote investigation into other designs include a weak beam efficiency and slightly noticeable cross-polarization.

4.3.1 Log-Periodic Geometry

Log-periodic self-complementary designs are one class of broadband planar antennas. The side of each arm is defined by a periodic unit cell pattern in radial log-space, oscillating between an angular amplitude of $\pm\omega$. The angular difference between arm sides is defined as δ, with a unit cell expansion rate of τ that characterizes half the length of the unit cell (from O'Brient, 2010). For M unit cells and an inner radius r_i, the outer radius is defined as:

$$r_o = r_i \tau^{2M}. \tag{4.7}$$

An $n = 4$ arm self-complementary layout requires $\delta = \frac{360^\circ}{2n} = 45^\circ$, while $\tau > 1$ can vary. Common examples are the sinuous and trapezoidal unit cells with $\omega = 45^\circ$ (ω often chosen as this for better polarization), shown in Fig. 4.3 alongside their respective antenna patterns. The sinuous design has been extensively analyzed at mm-scales for CMB detection (O'Brient, 2010; Edwards et al., 2012; Suzuki, 2013;

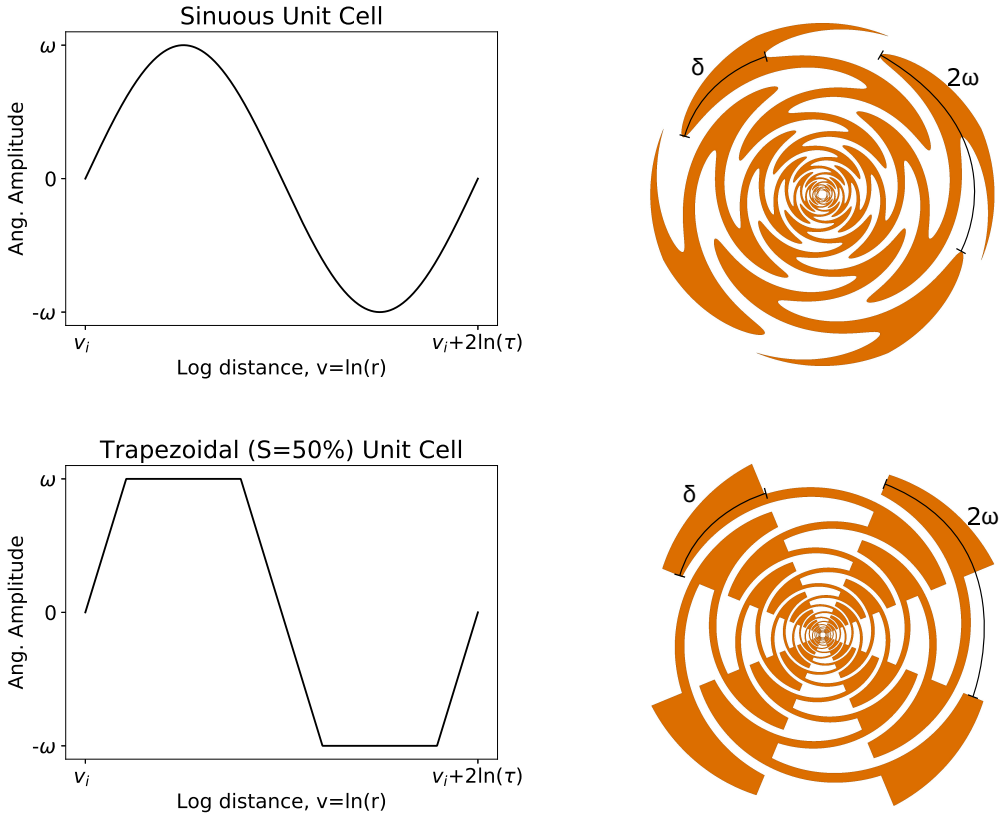

Figure 4.3: *Left:* Log-space unit cells for the Sinuous (*top*) and Trapezoidal (*bottom*) designs. Both respective antenna patterns (*right*) have $n = 4$ arms with $M = 7$ unit cells each. These can also be scaled invariantly. Note the trapezoidal design has an additional slope parameter S, that corresponds to the percentage of the unit cell at a max/min ($\pm\omega$, $S = 50\%$ shown). $S \to 100\%$ produces a rectangular unit cell, while $S = 0\%$ is triangular (Meinke et al., 2020).

Suzuki et al., 2014), while the trapezoidal has mainly undergone testing at larger wavelengths (Klemp et al., 2005, 2006).

Each sinuous arm's side/edge can be described from a continuous function in polar (r, ϕ) coordinates:

$$\phi = \omega \sin\left(\pi \frac{\ln r/r_i}{\ln \tau}\right) \pm \frac{\delta}{2}, \tag{4.8}$$

The deviation in expected polarization along the zenith direction (polarization wobble, see eq. 4.16) in these sinuous antennas has been shown to decrease with $\tau \to 1$ (Edwards et al., 2012).

The trapezoidal antenna is defined in a similar fashion, but with an additional slope parameter $0 \leq S < 100\%$ that designates the percentage the unit cell spends at a max/min ($\pm\omega$). It is not a continuous function, so must be defined piecewise:

$$\phi = \pm\frac{\delta}{2} + \omega \begin{cases} -1 + \frac{2}{(1-S)\ln\tau}\left(\ln r - \ln r_k\right) & r_k \leq r \leq r_k\tau^{\frac{1-S}{2}} \\ 1 & r_k\tau^{\frac{1-S}{2}} \leq r \leq r_k\tau^{\frac{1+S}{2}} \\ 1 - \frac{2}{(1-S)\ln\tau}\left(\ln r - \ln r_k - (\frac{1+S}{2})\ln\tau\right) & r_k\tau^{\frac{1+S}{2}} \leq r \leq r_k\tau^{\frac{3-S}{2}} \\ -1 & r_k\tau^{\frac{3-S}{2}} \leq r \leq r_k\tau^{\frac{3+S}{2}} \\ -1 + \frac{2}{(1-S)\ln\tau}\left(\ln r - \ln r_k - (\frac{3+S}{2})\ln\tau\right) & r_k\tau^{\frac{3+S}{2}} \leq r \leq r_k\tau^2 = r_{k+1}, \end{cases} \tag{4.9}$$

with the inner radius of the kth unit cell $r_k = r_i\tau^{2(k-1)}$ (for $k \geq 1$). Simulations in HFSS show polarization wobble decreases as $\tau \to 1$ and $S \to 100\%$ (towards a rectangular unit cell shape) (Meinke et al., 2020).

However, mask and fabrication resolution create more realistic expectations for antenna designs. The planar antennas need a feed structure in place, which must excite the arms near the center or else only high-order modes will be coupled (O'Brient, 2010). The best method of doing so involves running a microstrip feed down each antenna arm. At the center, this allows for opposing arms in the $n = 4$ pattern to connect and act as a differential feed-line, forming a virtual ground. An established feed design is shown in Fig. 4.4 that has been used in the sinuous pixels (Suzuki, 2013).

As fabrication resolution of a few microns is often required for consistent microstrip lines, log-periodic designs can have issues where the narrow switchback portions of the arms are below the necessary width to function as the microstrip line's ground plane. This issue arises as operating wavelength decreases (higher frequency), and is more

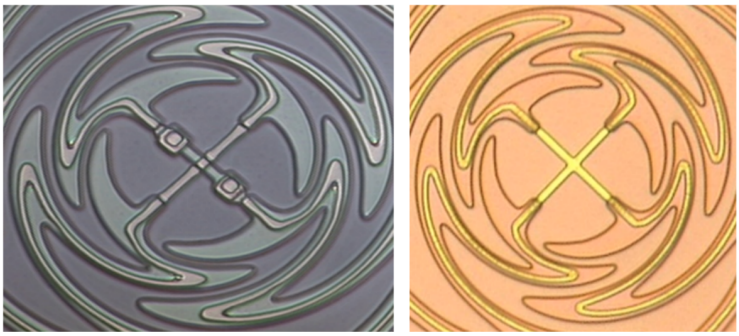

Figure 4.4: Center microstrip feed-line in sinuous (slot) antenna designs from Suzuki (2013). Orthogonality of the central feed connection (*right*) ensures reduced cross-talk between orthogonal polarizations even in the absence of a cross-over.

evident in the trapezoidal designs which have improved polarization with narrower switchbacks (due to slope parameter $S \to 100\%$).

4.3.2 Novel Hybrid Trapezoidal Design

A solution around the issue preventing microstrip feeds below a specific radii and parameter set is to modify the trapezoidal design. Narrow arm widths can be held constant by changing the slope parameter S with radius, such that S has the maximum allowed value at all radii for the desired microstrip in an attempt to also minimize polarization wobble. This removes the log-periodic classification, but maintains the self-complementary property. Here the hybrid trapezoidal designs were made to have a minimum width of $W = 4$ μm for a 2 μm wide microstrip plus padding on either side. This changes the first trapezoidal cell to look like Fig. 4.5 *left*, becoming more rectangular ($S \to 100\%$) as radius increases. The piecewise trapezoidal equation thus transforms into a 'hybrid' trapezoidal definition as shown in eq. (4.10) below. This is actually nicer than before but no longer log-periodic due to the $\pm W$ terms of the piecewise bounds.

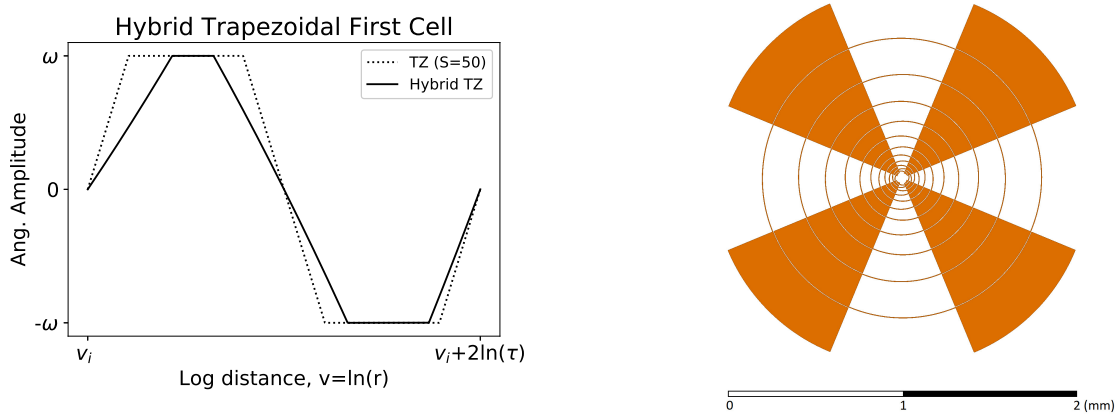

Figure 4.5: *Left:* First cell of the hybrid trapezoidal design (no longer log-periodic), compared to the previous trapezoidal (dashed, $S = 50\%$) unit cell. The goal of this design is to fix the narrow portions of the antenna arms (*right*), all 4 μm in width. The loss of periodicity also makes the design no longer invariantly scalable, the final design chosen and shown here has $r_i = 29.8$ μm, $M = 6$, and $\tau = 1.35$.

$$\phi = \pm\frac{\delta}{2} + \omega \begin{cases} \left[W(r - r_k)\right]^{-1} & r_k \leq r \leq r_k + W \\ 1 & r_k + W \leq r \leq r_k\tau - W \\ \left[W(r_k\tau - r)\right]^{-1} & r_k\tau - W \leq r \leq r_k\tau + W \\ -1 & r_k r_k \tau + W \leq r \leq r_k\tau^2 - W \\ \left[W(r - r_k\tau^2)\right]^{-1} & r_k\tau^2 - W \leq r \leq r_k\tau^2 = r_{k+1}, \end{cases} \tag{4.10}$$

4.4 Final Antenna Structure

The final antenna structure implemented within a millimeter-wave detector circuit requires a few additional modifications from the arm designs described above. As some of the arm features are small, it is often easier to instead create a complementary slot antenna out of a solid conducting ground plane, as done in other previous lenslet-coupled CMB antennas like the sinuous shown in Fig. 4.4. This is equivalent to

subtracting the arm designs (and central radius) from the ground plane. Via Babinet's principle, such subtraction is equivalent to the independent arm designs without a ground plane and is used to help simplify simulations as described in the following section.

Also as previously mentioned, difficulty can arise in ensuring correct routing of an antenna's signal. To avoid exciting only higher-order modes, the antennas must be fed from the lowest-order or smallest element, in this case meaning the center. A proven method of doing so involves careful routing of a microstrip feed-line down each arm (or slot antenna's ground plane "arm"). Thus at the center, each microstrip crosses over and excites the slot, converging to form a plus-shaped connection. Since each pair of opposing arms couples to an orthogonal linear polarization this creates a differential feed on opposing arm microstrip feed-lines, while minimizing cross-talk between the other polarization due identical central feeds oriented at 90°. Longer and winding feed-lines required for the more complex log-periodic antennas also lead to additional loss and cross-talk concerns, though attempts at modeling them have proven challenging.

4.5 HFSS Simulation Setup

Ansys High Frequency Structure Simulator[1] (HFSS) is a simulation software used to solve complex electromagnetic structures via the finite element method (FEM). The lenslet-coupled antennas are simulated with a driven modal HFSS solution type that is preferred for instances where higher-order modes may also be present. Each design is solved at the highest desired frequency of 230 GHz (smallest wavelength) for the finest mesh resolution. A linear frequency sweep is then conducted down to 130 GHz with a step size of 2 GHz. To slightly reduce memory for complex

[1] `https://www.ansys.com/products/electronics/ansys-hfss`

antennas such as the hybrid trapezoidal, the refinement percentage (mesh resolution increase) is kept at 10% per solution attempt, while the minimum ΔS is set to 0.01. A rectangular radiation boundary is used with a minimum $\lambda_{max}/4$ spacing from all lenslet and antenna components. An extra mesh constraint of $\lambda_{max}/16$ was applied on the radiation boundary to limit the maximum allowed mesh grid spacing for more consistent far-field calculations.

The general HFSS setup is shown in Fig. 4.6 for these antenna simulations. Lenslet designs as described overall in Section 4.2 are used, with two AR layers ($\epsilon_r = 2$ & 5) centered at 180 GHz for the final operational goal of covering both the 150 and 220 GHz bands. The prototype lenslet design used in chapter 5 will initially be a single-layer AR coated lenslet for testing focused on the 150 GHz band. Simulations of the dual-bowtie, sinuous, and hybrid trapezoidal designs are conducted following the design parameters listed in Table 4.1. A constant lenslet radius of R = 1.7 mm is used in all simulations.

To excite opposing arms, two non-overlapping lumped ports are placed in the center as in Fig. 4.6. A plus-shaped feed with four lumped ports could be used here, but the difference was found to be marginal while increasing total simulation resources needed.

Parameter	Dual-Bowtie	Sinuous	Hybrid TZ.
r_i [μm]	10	24	29.8
M	9	7	6
τ	1.3	1.3	1.35
L/R	0.38	0.46	0.42

Table 4.1: Antenna design parameters chosen for final simulations discussed in the following sections.

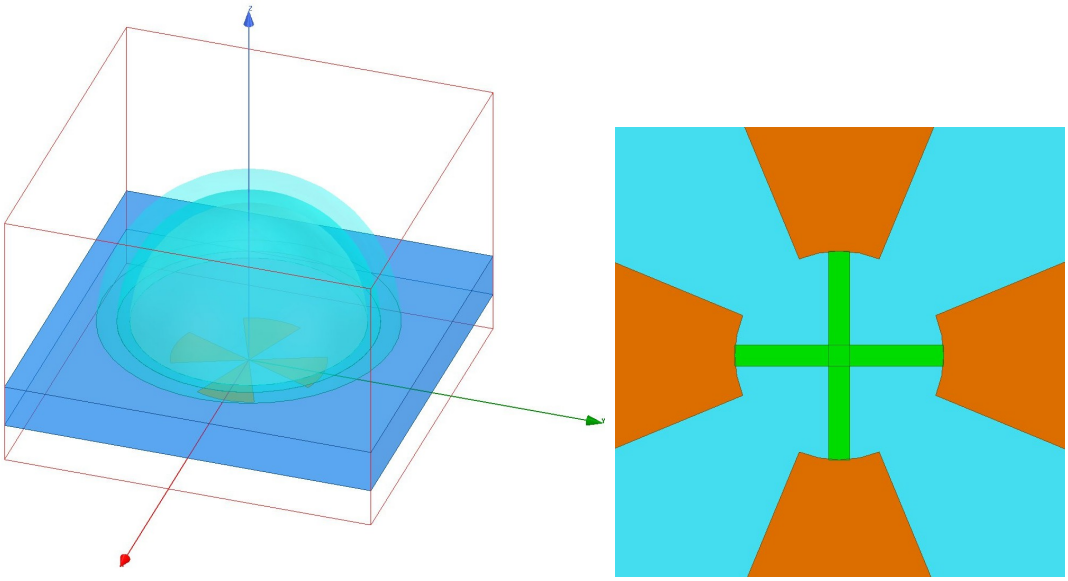

(a) Full Simulation Setup (b) Center Feed Setup

Figure 4.6: General HFSS setup for these antenna simulations. (a) Full view of simulation radiation box, silicon lenslet, single AR layer, and antenna location (dual-bowtie antenna shown). (b) Close-up of excitation present at the dual-bowtie antenna arm center. A pair of lumped ports (*green*) are used to excite each opposing arm pair. They do not physically overlap in the simulation, as one port is elevated slightly above the other.

HFSS solutions include field calculations at mesh-grid points within the radiation boundary, and scattering parameters in relation to the defined ports described in Pozar (2011) as the ratio of port output to input voltages

$$S_{ij} = \left.\frac{V_i^-}{V_j^+}\right|_{V_k=0,\ k\neq j}. \tag{4.11}$$

with the $+$ and $-$ denotes with respect to the incident and reflected port voltages. Reflections are often the most important in antenna simulations, with reflection at a port 1 defined as

$$S_{11} = \Gamma_1 = \frac{Z_1 - Z_{out}}{Z_1 + Z_{out}}, \tag{4.12}$$

where Z_{out} is the output impedance or defined port impedance within the simulation. For any $n = 4$ arm design with a lumped port as a differential feed for an opposing

pair of arms, each arm impedance is thus calculated from the reflection coefficient as

$$Z_1 = \frac{Z_{out}}{2}\frac{1+\Gamma_1}{1-\Gamma_1}. \tag{4.13}$$

For millimeter-wave detectors, the final product will be a slot antenna cut out of a superconducting ground plane as described above. Thus, simulations can simply define the complementary antenna arms as 2-dimensional sheets of perfect electrical conductors (PEC) with marginal expected differences.

4.5.1 Polarization

Consideration must be had to report an accurate representation of far-field polarization results obtained from simulations. While Stokes parameters are frequently used for polarization observation and analysis, they are not best suited for antenna characterization. Instead a Ludwig-3 definition is used for linear polarization, defined in Ludwig (1973) as

$$E_x(\theta,\phi) = E_\theta \cos\phi - E_\phi \sin\phi \tag{4.14}$$

$$E_y(\theta,\phi) = E_\theta \sin\phi + E_\phi \cos\phi, \tag{4.15}$$

where $\hat{z}$ is the direction of propagation of the light. This definition is good at describing an antenna's linear polarization in simulated projected far-fields and is often utilized in 3D electromagnetic simulation software like HFSS. Naming convention further divides polarizations into co- and cross- polarization compared to the desired or expected result. For an antenna sought to operate with linear polarization along $\hat{x}$, the "co-pol" term would be E_x (4.14), while "cross-pol" or "x-pol" would be considered the orthogonal E_y term (4.15).

Another prominent polarization metric for similar antennas is referred to as "polarization wobble" (O'Brient, 2010), defined as deviation of the far-field polarization

along the zenith direction from desired,

$$\text{Pol.Wob.} = \arctan\left(\frac{\mathrm{E_{x\text{-}pol}}(0,0)}{\mathrm{E_{co\text{-}pol}}(0,0)}\right) = \arctan\left(\frac{\mathrm{E_y}(0,0)}{\mathrm{E_x}(0,0)}\right), \tag{4.16}$$

with the rightmost definition valid in our example when the desired polarization is along the $\hat{x}$ or $\hat{\theta}$ direction. This value is useful in detectors when most of the incident signal received is expected along the zenith and identification of inherent "handedness" for an antenna versus frequency may be needed.

4.5.2 Radiation Patterns

A more complete picture can also be made by looking at an antenna's radiation patterns. The overall far-field radiation intensity [Watts per solid angle] can be defined in terms of E-fields as

$$U(\theta,\phi) = \frac{1}{2\eta}\left[\ \left|E_\theta(\theta,\phi)\right|^2 + \left|E_\phi(\theta,\phi)\right|^2\right], \tag{4.17}$$

where η is the intrinsic impedance of the far-field medium ($\eta = Z_0 = 377\ \Omega$ in our case) (Balanis, 2016). Following the same convention, co- and cross- polarization radiation intensities may be written from 4.14 & 4.15 as

$$U_x(\theta,\phi) = \frac{\left|E_x\right|^2}{2\eta} \tag{4.18}$$

$$U_y(\theta,\phi) = \frac{\left|E_y\right|^2}{2\eta}, \tag{4.19}$$

respectively, for again when the desired polarization is in the $\hat{x}$ direction. Antenna designs and simulations also benefit from inspecting the far-field directivity, or ratio of intensity compared to what would be expected from an isotropic source,

$$D(\theta,\phi) = \frac{4\pi U(\theta,\phi)}{\oiint_\Omega U(\theta,\phi)d\Omega} = \frac{U(\theta,\phi)}{U_0} \tag{4.20}$$

where Ω is the entire solid angle integrated over and $U_0 = \oiint_\Omega U(\theta,\phi)d\Omega/4\pi = P_{rad}/4\pi$ is the radiation intensity for an isotropic source or total radiated power averaged over

the entire solid angle sphere. Co- and cross- polarization directivities D_x and D_y may then be found by plugging in the definitions of 4.18 & 4.19 into the numerator, respectively (still assuming co-pol is in the $\hat{x}$ direction).

4.5.3 Beam Efficiency

Radiation patterns are the primary aids in identifying significant side-lobes and cross-polarization contamination that both harm the effectiveness of an antenna. To quantify such effects I report the co-pol beam efficiency of an antenna, often in percentage form,

$$\mathrm{BE}_x = \frac{\oiint\limits_{\Omega_{\mathrm{beam}}} U_x(\theta,\phi)d\Omega_{\mathrm{beam}}}{\oiint\limits_{\Omega} U(\theta,\phi)d\Omega} = \frac{\oiint\limits_{\Omega_{\mathrm{beam}}} U_x(\theta,\phi)d\Omega_{\mathrm{beam}}}{4\pi U_0} \tag{4.21}$$

where Ω_{beam} is the main or desired beam solid angle to integrate over. I elect to report the co-pol BE_x integrated over an Ω_{beam} defined as the main azimuthal beam to its first null or minimum. However, designs with an already identified telescope or instrument to pair with may instead prefer to define a specific angle from the azimuth. It is also worth noting a potential frequency-dependence, in which main beams often become narrower with frequency.

4.5.4 Polarization Ratio

Another useful metric is the ratio between integrated co- and cross- polarization intensities or directivities over the far-field sphere. This helps identify if reduced beam efficiencies are simply due to significant co-pol side-lobes or if cross-pol contamination may be a concern. Here the polarization ratio is defined as,

$$\text{Pol. Ratio} = \frac{\oiint\limits_{\Omega} U_x(\theta,\phi)d\Omega}{\oiint\limits_{\Omega} U_y(\theta,\phi)d\Omega} = \frac{\oiint\limits_{\Omega} D_x(\theta,\phi)d\Omega}{\oiint\limits_{\Omega} D_y(\theta,\phi)d\Omega} \tag{4.22}$$

where again co-polarization is considered synonymous with desired polarization in the $\hat{x}$ direction, and undesired cross-polarization in the $\hat{y}$.

4.6 Simulation Results

The parameters outlined in the previous section are used to carefully compare simulations for the dual-bowtie, sinuous, and hybrid trapezoidal antennas. Each design creates their own unique benefits and detriments, which must be carefully weighed for the final desired use. For each simulation, I focus on bands centered at 150 and 220 GHz with a two-layer AR coating with dielectric constants of 2 and 5. A constant lenslet radius of R = 1.7 mm is used in all simulations.

4.6.1 Impedance

Here I report the impedance as defined in 4.13 averaged between the two identical lumped ports. Impedance results are shown as real (resistance) and imaginary (reactance) in Fig. 4.7a. The real resistance corresponds to the far-field power radiated or absorbed, while the imaginary reactance corresponds to the near-field non-radiated power lost. The expected arm resistance for an $n = 4$ arm self-complementary design on a silicon dielectric half-space is 52.9 Ω (eq. 4.6). The dual-bowtie design stays very near this expected resistance. Meanwhile, both log-periodic designs suffer from impedance that oscillates with frequency. The hybrid trapezoidal has the widest fluctuations, which here were used to position the impedance peaks outside of the desired frequency bands.

4.6.2 Polarization Wobble

Polarization wobble is the alignment of polarization along the zenith, and does not provide any off-axis insights. The polarization wobble as defined in eq. (4.16)

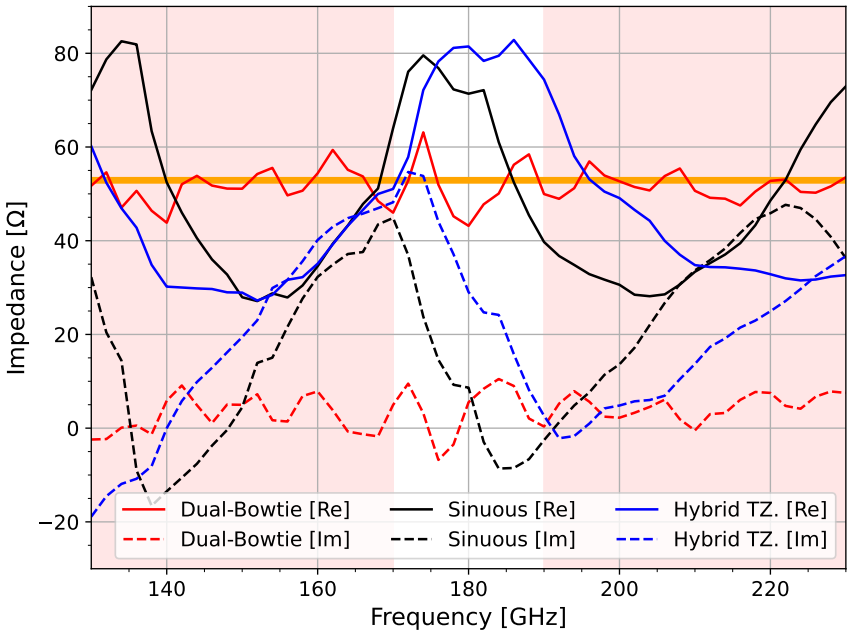

(a) Antenna Arm Impedance

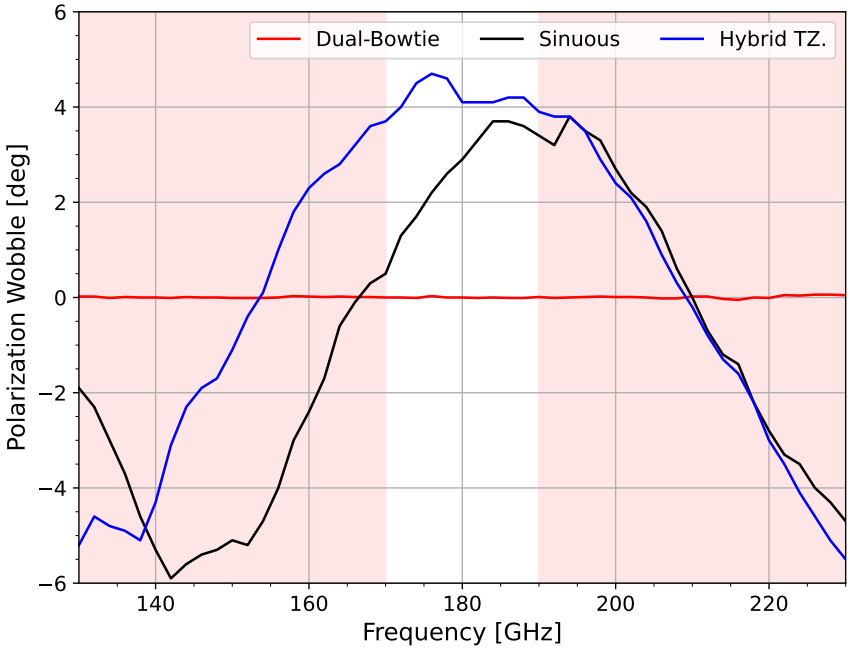

(b) Antenna Polarization Wobble

Figure 4.7: Dual-bowtie (*red*), sinuous (*black*), and hybrid trapezoidal (*blue*) simulation results of (a) antenna arm impedance eq. (4.13) with solid and dashed lines for resistance and reactance, respectively. A horizontal orange line indicating the expected impedance from eq. (4.6). (b) Polarization wobble, eq. (4.16), versus frequency.

is shown in Fig. 4.7b for the dual-bowtie, sinuous, and hybrid trapezoidal antennas. The dual-bowtie has minimal polarization wobble fluctuations with frequency. The log-periodic designs again share a similar result, oscillating between roughly $\pm 5^{\circ}$. The periodic fluctuations in impedance and polarization wobble indicate the log-periodic geometry is likely the cause.

4.6.3 Directivity Patterns

From just the impedance and polarization wobble results presented so far, it appears as if the dual-bowtie design would be the outright favorite. However, the entire radiation pattern must be taken into account. Here I report the directivity as defined in eq. (4.20). Table 4.2 lists the maximum co-polarization directivities found for each design at both 150 and 220 GHz, while Fig. 4.8 shows the relation versus all frequencies. The dual-bowtie has a noticeably lower max directivity than the sinuous and hybrid trapezoidal designs.

Freq.	Maximum Directivity		
[GHz]	Dual-Bowtie	Sinuous	Hybrid TZ.
150 GHz	14.7 dB	15.3 dB	15.8 dB
220 GHz	17.5 dB	19.2 dB	19.0 dB

Table 4.2: Maximum (co-polarization) directivities of each simulated antenna design at 150 and 220 GHz.

A further inspection of normalized directivity cross-section patterns in the E-, H-, and 45°- planes are shown in Figs. 4.9, 4.10 & 4.11, respectively. These reveal why the dual-bowtie has such a lower max directivity. There are obvious side-lobes present in all designs, but they exist at up to -10 dB for the dual-bowtie compared to only

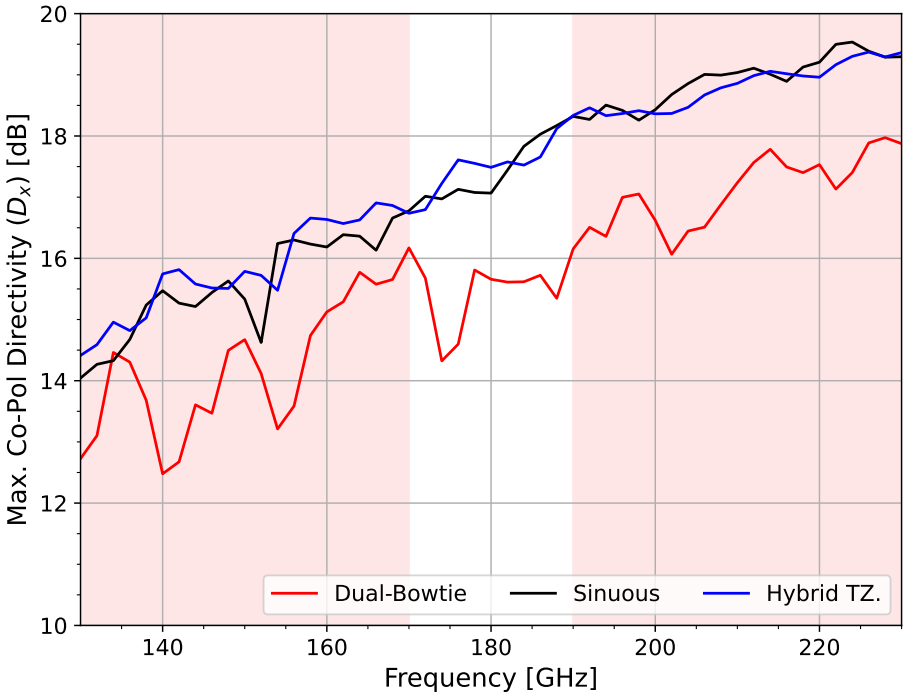

Figure 4.8: Simulated maximum co-pol directivity for each antenna design versus frequency. Dual-bowtie (*red*), sinuous (*black*), and hybrid trapezoidal (*blue*). The dual-bowtie has noticeably reduced peak directivity than the log-periodic designs.

-18 dB and -20 dB for the sinuous and hybrid trapezoidal, respectively. This is most evident in the E-plane patterns of Figs. 4.9a & 4.9b.

The sinuous and hybrid trapezoidal patterns show the cross-pol contamination responsible for producing polarization wobble also extends off the zenith at up to -20 dB. This indicates that their polarization wobble extremes are likely due to a constructive interference from the geometric and lenslet properties present. Meanwhile, the dual-bowtie design has extremely low cross-polarization below -55 dB in both E- and H- planes, but the 45°-plane is important in revealing off-axis side-lobes that reach almost -15 dB. As a result, the dual-bowtie antenna is not fully immune to cross-polarization contamination, only if looked at on-axis or along-zenith.

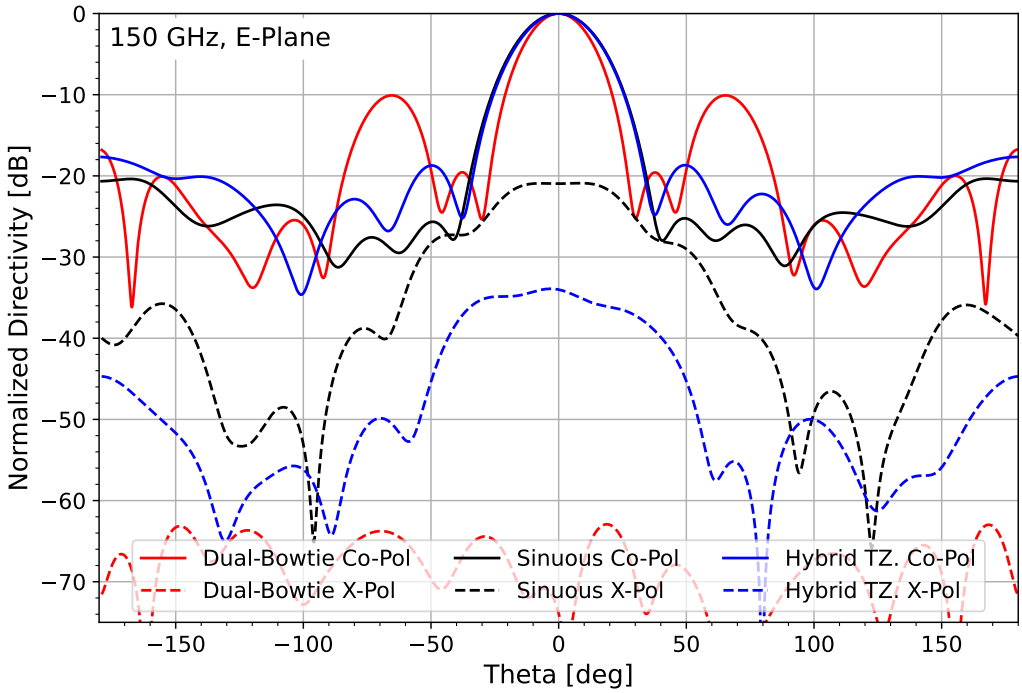

(a) Normalized Directivity, E-Plane, 150 GHz

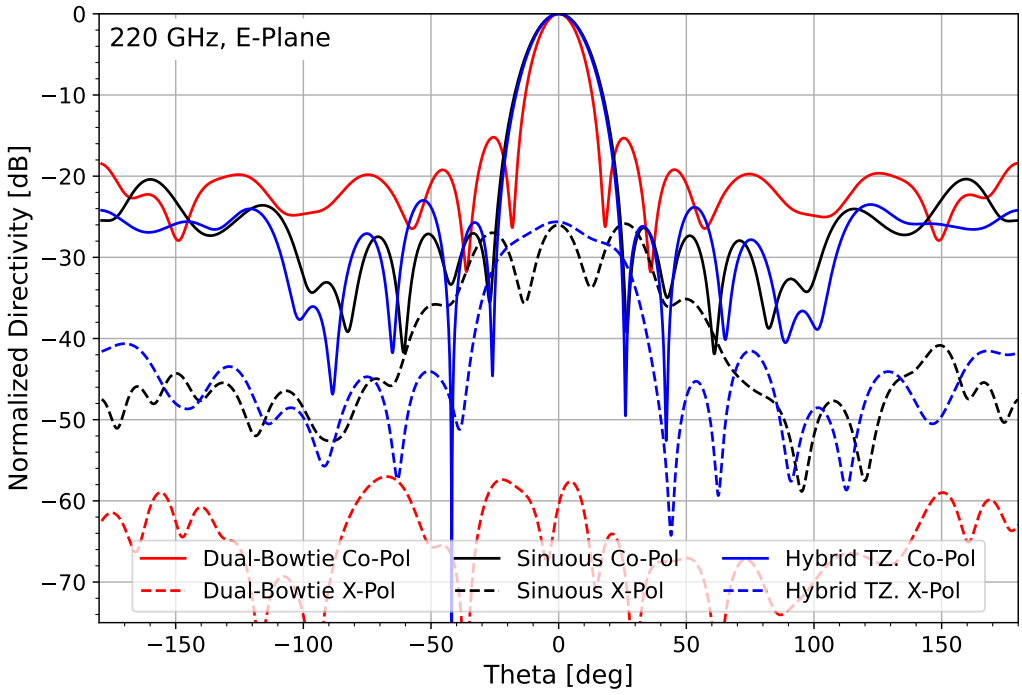

(b) Normalized Directivity, E-Plane, 220 GHz

Figure 4.9: Simulated normalized directivity patterns in the E-plane, for the dual-bowtie (*red*), sinuous (*black*), and hybrid trapezoidal (*blue*) antenna designs. Co- (*solid*) and cross- (x-, *dashed*) pol are both shown, for (a) 150 GHz and (b) 220 GHz.

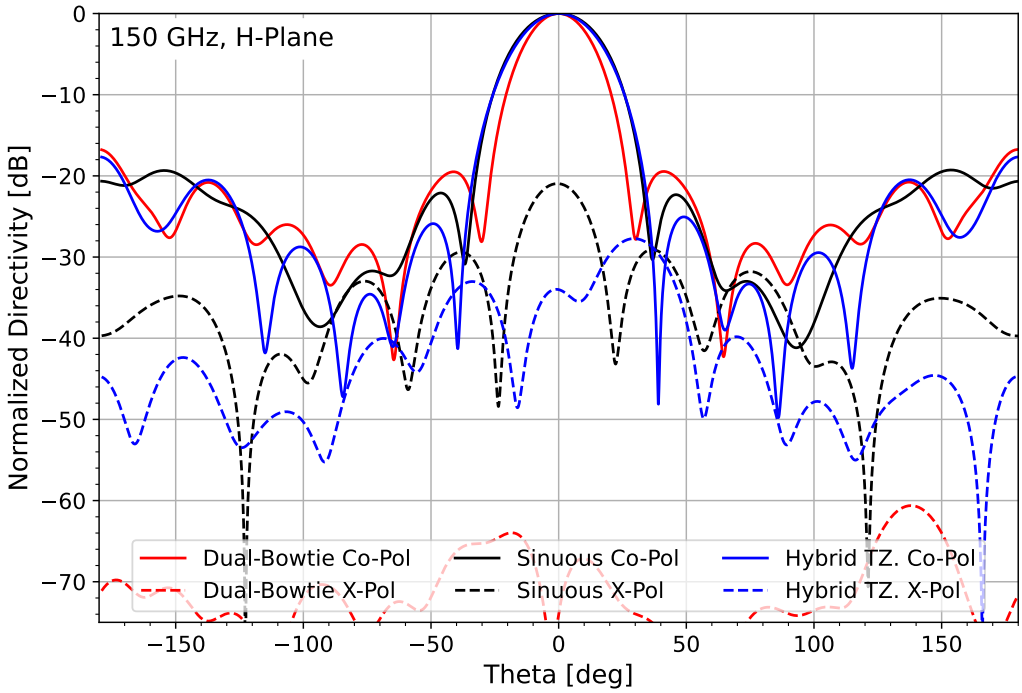

(a) Normalized Directivity, H-Plane, 150 GHz

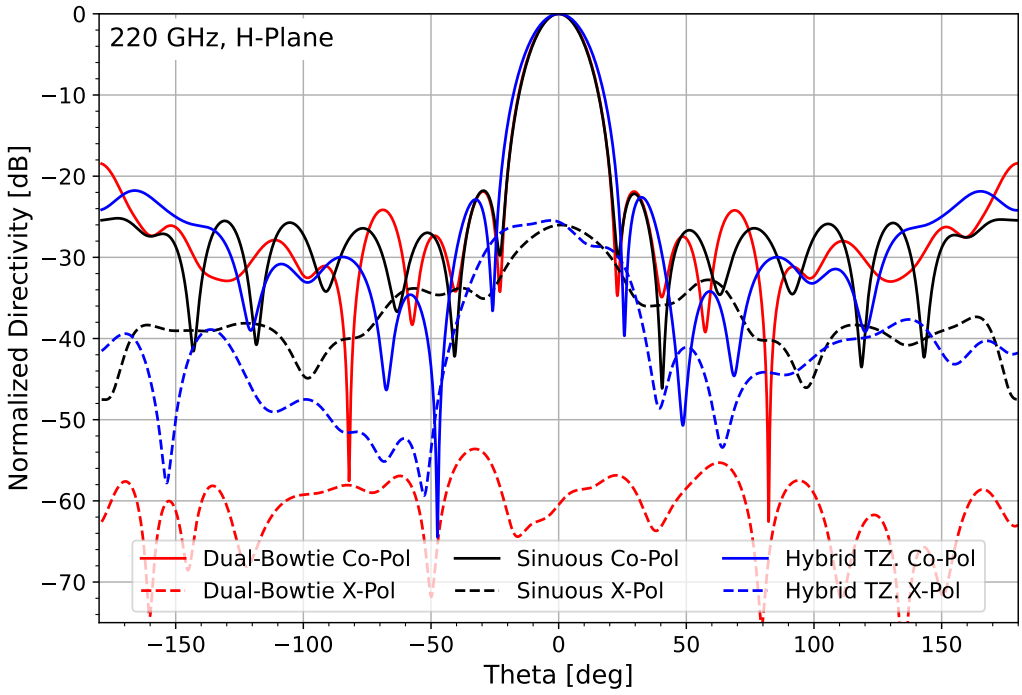

(b) Normalized Directivity, H-Plane, 220 GHz

Figure 4.10: Simulated normalized directivity patterns in the H-plane, for the dual-bowtie (*red*), sinuous (*black*), and hybrid trapezoidal (*blue*) antenna designs. Co- (*solid*) and cross- (x-, *dashed*) pol are both shown, for (a) 150 GHz and (b) 220 GHz.

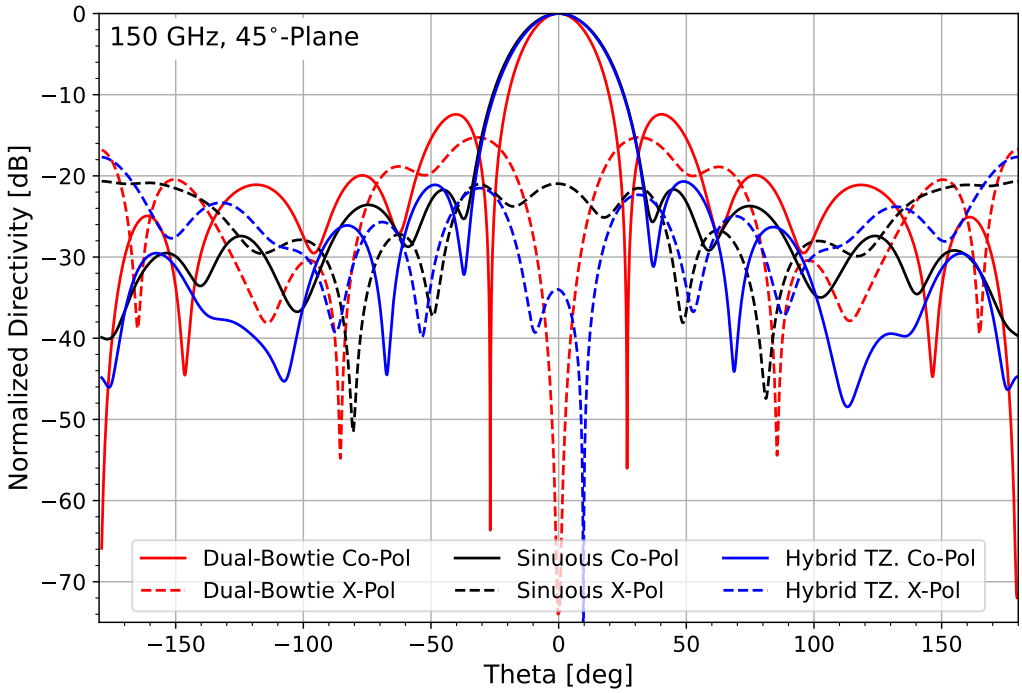

(a) Normalized Directivity, 45°-Plane, 150 GHz

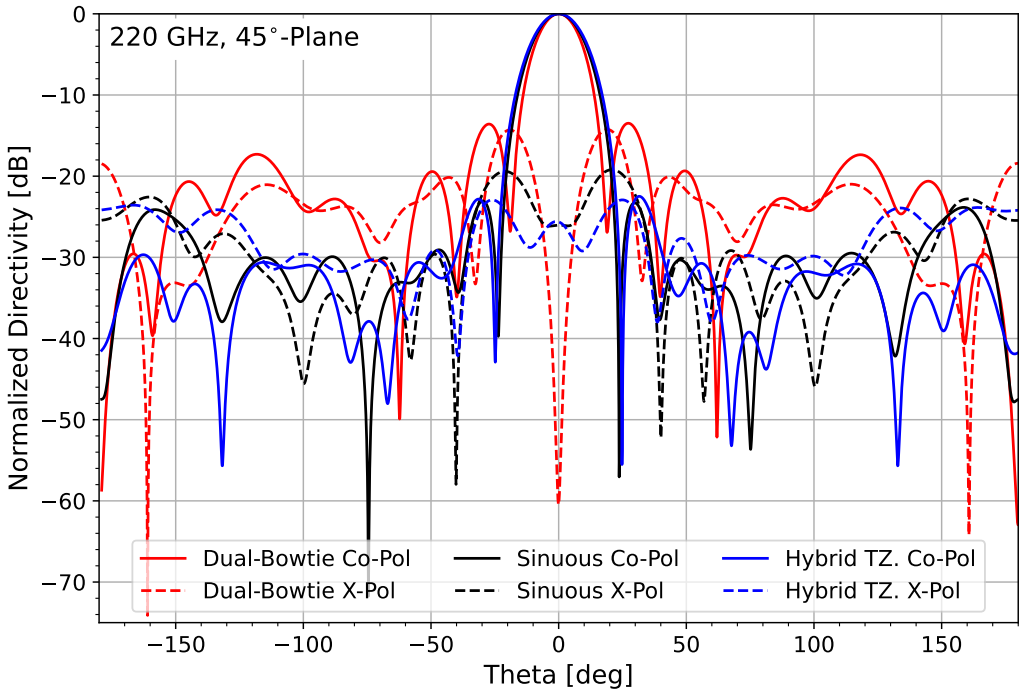

(b) Normalized Directivity, 45°-Plane, 220 GHz

Figure 4.11: Simulated normalized directivity patterns in the 45°-plane, for the dual-bowtie (*red*), sinuous (*black*), and hybrid trapezoidal (*blue*) antenna designs. Co- (*solid*) and cross- (x-, *dashed*) pol are both shown, for (a) 150 GHz and (b) 220 GHz.

Freq.	Band Avg. Beam Efficiency		
[GHz]	Dual-Bowtie	Sinuous	Hybrid TZ.
$130 - 170$ GHz	49.3%	82.6%	84.6%
$190 - 230$ GHz	45.0%	82.3%	84.2%

Table 4.3: Band averaged beam efficiencies for each antenna type at $130 - 170$ and $190 - 230$ GHz.

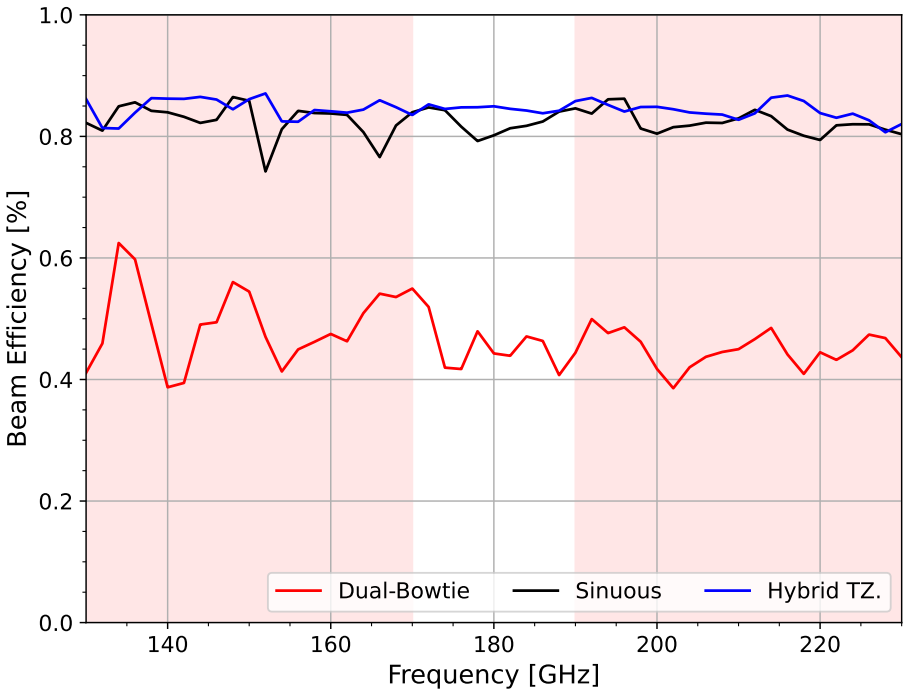

Figure 4.12: Simulated beam efficiency, eq. (4.21), for each antenna design versus frequency. Dual-bowtie (*red*), sinuous (*black*), and hybrid trapezoidal (*blue*). The dual-bowtie has reduced efficiency compared to both log-periodic designs.

4.6.4 Beam Efficiency

The co-polarization main beams are converted to a beam efficiency via integrating down to the first null following eq. (4.21). This evaluation helps quantify the impact of side-lobes and cross-polarization contamination evident in the directivity patterns discussed and shown above. The calculated beam efficiencies at 150 and 220 GHz are shown in Table 4.3, while also shown versus frequency in Fig. 4.12. It is evident that the dual-bowtie design with a beam efficiency of around 50% pales in comparison to the sinuous and hybrid trapezoidal designs with efficiencies upwards of 85%. When comparing the log-periodic antennas they are again extremely similar to one another, with the hybrid trapezoidal slightly better but likely within the simulation's margin of uncertainty. Minor differences in design parameters, as more time was spent optimizing the hybrid trapezoidal design in this investigation, could also play a role.

4.6.5 Polarization Ratio

Finally, the polarization ratio versus frequency is shown in Fig. 4.13. Both the sinuous and hybrid trapezoidal designs have ratios greater than 10 dB, or 10 times higher expected power in the co-polarization compared to the cross-polarization. The hybrid trapezoidal does show a slight $1-2$ dB improvement over the sinuous. Meanwhile, the dual-bowtie antenna has a ratio closer to 7 dB indicating that the cross-polarization side-lobes evident in the 45°-plane of Fig. 4.11 do significantly impact polarization.

4.7 Inferences and Future Potential

The multichroic dual-polarization antenna designs outlined in this chapter highlight a promising area for further advancement in the millimeter-wave detector and CMB astronomy community. The simulations here highlight how the three discussed

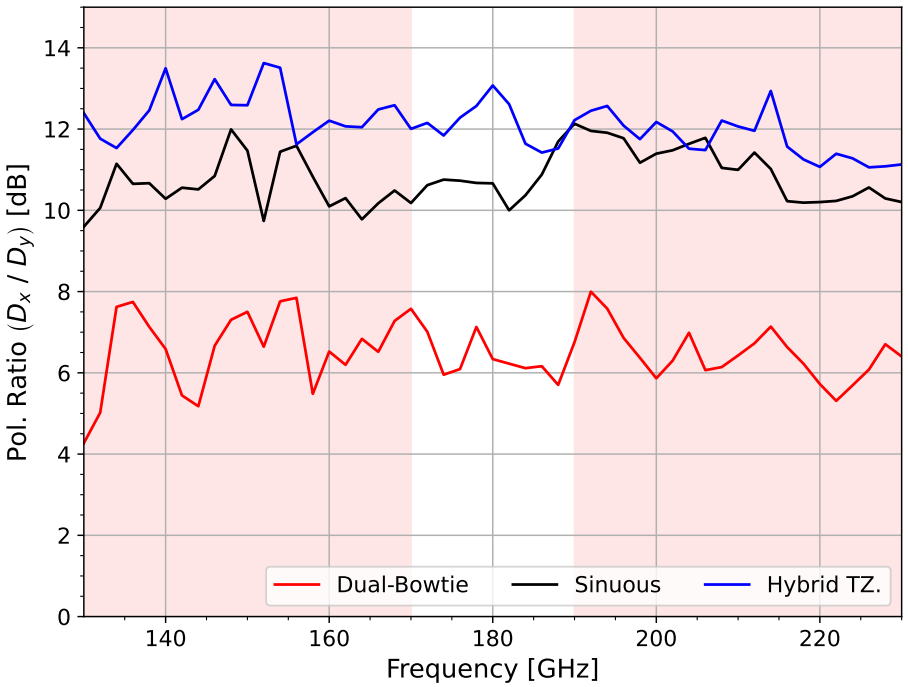

Figure 4.13: Simulated polarization ratio, eq. (4.22), for each antenna design versus frequency. Dual-bowtie (*red*), sinuous (*black*), and hybrid trapezoidal (*blue*). The dual-bowtie also has lower polarization ratio compared to both log-periodic designs, implying the 45° x-pol side-lobes in Fig. 4.11 are significant.

designs have their own unique pros and cons. The remainder of this chapter includes a summary of key takeaways, hindrances, and further comments on the gathered simulation results.

- The dual-bowtie antenna employs a simple design that allows for easy scaling down to even sub-millimeter wavelengths. Its constant impedance and minimal polarization along the zenith as shown in Fig. 4.7 allow for easy matching to reduce unnecessary loss. However, significant side-lobes increase the chance of cross-talk and lower overall efficiency, particularly in the E- and 45°- planes. These are likely due to multiple reasons, like arm width and cross-coupling between orthogonal arms. Thus, the dual-bowtie should be desired in cases where polarization (preferably near zenith) is important and efficiency is less

of a concern, such as when detecting a high occupation or concentration of photons. The dual-bowtie impedance can also be easily adjusted by dropping the self-complementary requirement and changing angular width of the arms.

- It is also worth noting that this broadband dual-bowtie antenna was designed to be multiple wavelengths larger than the operational maximum ($r_o \gtrsim 2\lambda_{max}$) to increase electrical length and reduce fluctuations with impedance. This is likely a partial cause in the increased side-lobes. For instance, decreasing the simulated design's outer radius by one factor of 1.3 so $M = 8$ instead of 9 in Table 4.1, drops side-lobes by $2 - 5$ dB. However it also then increases the maximum cross-pol by roughly 5 dB, the HPBW by $\approx 5°$, and impedance fluctuations by $\approx 5\%$.

- The sinuous and hybrid trapezoidal log-periodic designs share a multitude of similarities. They both have high overall beam efficiency, but less than desired fluctuations in impedance and cross-polarization versus frequency. The hybrid trapezoidal has a slight edge in both beam efficiency and polarization ratio, and may be marginally easier to geometrically adjust for better impedance matching. However, the sinuous antenna is an already proven design used in millimeter-wave detectors (Sobrin et al., 2022). A primary takeaway from these simulations is that the hybrid trapezoidal highlights potential for further improvement in the field, and show there are likely still many antenna designs yet to be found that would greatly benefit millimeter-wave astronomy.

4.7.1 Hindrances

Of course, it would be remiss to not also summarize many shortcomings of the current designs that have been described above. Some concerns have been addressed

or reduced in previous deployments for millimeter telescopes, but still remain an area for desired future improvement.

- A primary goal of these antenna designs is to minimize cross-polarization for accurate detections. Log-periodic designs in particular often have a "handedness" in the form of a polarization wobble with frequency. Experiments have corrected for this both during data analysis and by alternating pixels of opposite orientation/handedness (Abitbol et al., 2017). The challenge of improved co-pol gain or directivity along the main beam and minimized cross-pol is ever persistent.

- Long and winding microstrip feed-lines for the log-periodic designs introduce opportunities for undesired signal loss and cross-talk, while proving difficult to accurately simulate. Others have proposed solutions that reduce the antenna's physical size (increasing effective size), such as wavy sinuous arms discussed in Suzuki (2013). When routed down narrow portions of arms, difficulty also arises in accurate impedance matching.

- As evident in Fig. 4.7a, the frequency-dependent fluctuation in impedance is also a noticeable concern. Although centered around what is predicted by eq. (4.6), the log-periodic antenna impedances fluctuate significantly with frequency. This will cause a decrease in overall efficiency within any desired bandpasses unless well-matched.

- A further challenge arises in the required fabrication resolution of antenna patterns. The current standard fabrication resolution is often around $1 - 2$ μm, with increasing cost for increased resolution. As the central radii is the smallest feature for the simple dual-bowtie, it can be easily made down to sub-mm

operating wavelengths. On the other hand, the switchbacks and curves in the log-periodic designs discussed here likely limit them to mm or larger wavelengths. Instead, horn-coupled detectors are often selected at these limits, as echoed in the antenna choice for Simon's Observatory and LiteBIRD (Xu et al., 2020; Westbrook et al., 2021). One other alternative might be to switch out the silicon wafer and lenslet for a material with lower dielectric constant. Quartz, with a dielectric constant of $\epsilon = 4.5$ could be a viable alternative to avoid fabrication resolution limits and allow sub-mm operation in exchange for reduced forward gain due to larger back-lobes.

- Fabrication of the required lenslet designs discussed in Section 4.2 has proven to be a primary difficulty as well. Creation of a suitable hemisphere, inclusion of necessary AR layers, and the scalability to kilo-pixel sized arrays, are all costly endeavors that vary with each detector design but continue to improve.

4.7.2 Further Ideas and Comments

As outlined in the subsequent chapter, a prototype detector array with both dual-bowtie and hybrid trapezoidal antennas has been fabricated and under preparation for testing. A detailed analysis of each antenna design will yield promising insights into the best next steps. Here I will stick to a discussion about the antenna design process and emphasize a few key areas of desired improvement.

To begin with, the second and third hindrances listed in the above subsection only become an issue for the complex log-periodic antennas. The basic dual-bowtie design has the shortest possible microstrip feed path. With an outer radius large compared to the maximum wavelength, i.e. $r_o \gtrsim 2\lambda_{max}$, the dual-bowtie also has minimal variations in impedance with respect to frequency. However, that comes at a cost of lower overall efficiency due to higher side-lobes. In fact, any non-bowtie

self-complementary design will lack a reflection symmetry that amplifies impedance fluctuations when placed on a dielectric half-space.

From a wider perspective, I offer a simpler question: are self-complementary designs here truly beneficial? The usual primary benefit (aside from pleasing geometric patterns) is to produce an antenna with constant impedance. However, that property is significantly negated by combination of the dielectric half-space and any antenna's finite outer cutoff radius.

Furthermore, if the self-complementary characteristic is removed from consideration, what would an optimized design look like? The ideal antenna design would leave a narrow radial portion of the arm (or rather ground plane, if a slot antenna) for the required microstrip feed-line to travel over a shortest possible distance and excite the antenna center. This and an $n = 4$ arm dual-polarization layout would then constrain each antenna arm to non-overlapping regions of $\Delta\phi < 90^\circ$ angular width. Implementation of a log-periodic arm structure would still likely be beneficial, as it aids in creation of broadband antennas with long electrical lengths.

Finally, to entertain/propose an "out of the box" idea (and mainly get it out of my head), the inclusion of a vertical stack of parasitic elements could help facilitate improved forward gain for the types of antennas outlined in this chapter. It also allows for further domains of customization likely requiring a methodical approach via simulations to optimize. Such an idea could very well be poppycock, but it is not completely unfounded. A sequence of carefully spaced parasitic director elements are the foundation for the commonly used Yagi-Uda antenna (Uda, 1926). A few recent studies have also employed a multi-layer or vertical stacking of planar elements in a manner similar to proposed (e.g. Kramer et al., 2010; Choe and Lim, 2014; Ramos et al., 2018). However, the validity of a design to aid or even replace the lenslet

component discussed in this chapter, while still operating over a wide bandwidth, is unsupported and likely far-fetched.

Chapter 5

12-PIXEL PROTOTYPE ANTENNA-COUPLED MKID ARRAY

With potential lenslet-coupled antennas designed and simulated, the next steps are to find valid methods to fabricate and test them. This chapter describes the ongoing endeavor to do just that for both the dual-bowtie and hybrid trapezoidal (HTZ) designs described in Chapter 4. Here I outline the background, implementation, and fabrication of a 12-pixel prototype multichroic MKID array where each pixel is coupled to a lenslet-coupled multichroic antenna. At the time of this writing, the devices have been made and are present at Arizona State University. However, they are currently still under preparation for testing to fully begin. Here I shall describe the MKID array and the potential avenues for testing and development in the future.

5.1 MKID Overview

As these antennas are paired with superconducting microwave kinetic inductance detectors (MKIDs), I will first outline the processes present in such detectors.

5.1.1 Superconductivity

Superconductors are a classification of materials that exhibit zero DC resistance and an expulsion of magnetic fields below a given critical temperature T_c. The ground state of superconductors below T_c is made up of Cooper pairs, or electrons paired together through electron-phonon interaction. This is known as the Bardeen–Cooper–Schrieffer (BCS) theory of superconductivity (Bardeen et al., 1957). When at $T \ll T_c$, Cooper pairs have energies below that of the normal ground state

by an energy gap of

$$2\Delta_0 \approx 3.5 k_\mathrm{B} T_c, \tag{5.1}$$

where k_B is Boltzmann's constant. Breaking a Cooper pair requires energy above this $2\Delta_0$ gap. Conventional superconductors, with critical temperatures below roughly $T_c \lesssim 20$ K, thus have energy gaps on the order of $\mathcal{O}(10^{-3})$ eV or $\mathcal{O}(10^{-22})$ Joules. This translates to the capability to detect photons above a minimum frequency of $\nu_\mathrm{min} = 2\Delta_0/h \approx 73(T_c/1\mathrm{K})$ GHz, and is three orders of magnitude lower than charge-coupled devices (CCDs) used in optical and infrared observations (Mauskopf, 2018).

In addition to Cooper pairs, superconductors have a secondary charge carrier in the form of electron quasiparticles. The thermal properties of a superconductor and breaking of Cooper pairs dictate the quantity of quasiparticles present in a superconductor. These have a distribution $f(E)$ that when in thermal equilibrium follows a Fermi-Dirac distribution, with a quasiparticle number density shown in Zmuidzinas (2012) as

$$n_{qp} = 4N_0 \int_{\Delta(T)}^{\infty} \frac{f(E) E dE}{\sqrt{E^2 - \Delta(T)^2}} = 4N_0 \int_{\Delta(T)}^{\infty} \frac{1}{\exp\big(E/k_\mathrm{B}T\big) + 1} \frac{E dE}{\sqrt{E^2 - \Delta(T)^2}} \tag{5.2}$$

where N_0 is the single-spin density of states when at the Fermi energy. For low temperature ($T \ll T_c$), this becomes (Mauskopf, 2018)

$$n_{qp}(T) \approx 2N_0 \sqrt{2\pi k_\mathrm{B} T \Delta_0} \exp\left(\frac{-\Delta_0}{k_\mathrm{B}T}\right). \tag{5.3}$$

A superconductor's conductivity and thus impedance is dictated by the current carried by both such quasiparticles and Cooper pairs. Conductivity as defined in the Drude model with Ohm's law $\mathbf{J} = \sigma \mathbf{E}$, requires a complex form of $\sigma = \sigma_1 - i\sigma_2$ for superconductors (Glover and Tinkham, 1957). This is outlined via the Mattis-Bardeen theory (Mattis and Bardeen, 1958), of which the surface impedance for

thin-film superconductors approaches (Gao, 2008)

$$Z_s = \frac{1}{\sigma t} = \frac{1}{(\sigma_1 - i\sigma_2)t} = \frac{\sigma_1 + i\sigma_2}{(\sigma_1^2 + \sigma_2^2)t} \approx \frac{\sigma_1 + i\sigma_2}{\sigma_2^2 t} \tag{5.4}$$

for a given thickness t. The final approximation is made when at low temperatures where $\sigma_1 \ll \sigma_2$ is assumed.

5.1.2 Kinetic Inductance

Inductance within a conductor is present in two forms, magnetic and kinetic. The standard everyday inductance often discussed is the magnetic, corresponding to the magnetic energy stored within an ideal conductor,

$$\mathcal{E}_{mag} = \frac{1}{2} L_{mag} I^2 \tag{5.5}$$

as a function of current I. This can be considered as geometric or external inductance, where it is independent of the density of charge carriers present (Mauskopf, 2018). However, there is also energy stored in form of the charge carriers' kinetic motion,

$$\mathcal{E}_k = \frac{1}{2} N_{\text{tot}} m_e v^2 = \frac{1}{2} I^2 \frac{m_e l}{e^2 n_e A} = \frac{1}{2} L_k I^2, \tag{5.6}$$

for a wire of length l and cross section A with carrier density n_e, whose current can thus be described as $I = e n_e A v$ (Mauskopf, 2018). Thus kinetic inductance is defined as $L_k = m_e l/(e^2 n_e A)$. In normal metals the kinetic inductance is negligible due to a large number of charge carriers (n_e) present in a conductor. However in superconductors it becomes significant with fewer carriers below the critical temperature. The surface impedance in low temperature thin-film superconductors of eq. (5.4) can then in turn be characterized as a combination of surface resistance ($\mathcal{R}$) and kinetic inductance per unit square ($\mathcal{L}_k$),

$$Z_s \approx \frac{\sigma_1 + i\sigma_2}{\sigma_2^2 t} = \mathcal{R} + i\omega \mathcal{L}_k. \tag{5.7}$$

The resistance $\mathcal{R}$ is associated with the quasiparticle density (n_{qp}), while the inductance term $\mathcal{L}_k$ is related to the density of Cooper pairs (n_{cp}). Hence a superconducting transmission line resonator will consist of both geometric and kinetic inductances, $L = L_{mag} + L_k$.

5.1.3 Kinetic Inductance Detectors

Kinetic inductance detectors (KIDs) utilize the appreciable kinetic inductance (L_k) component of superconductors to fashion them into sensitive detection elements. The two most common forms are lumped-element KIDs (LEKIDs) and microwave KIDs (MKIDs). LEKIDs have lumped elements, i.e. elements shaped into respective components physically smaller than the operating wavelength. Meanwhile other KIDs, including most MKIDs, utilize distributed elements made of transmission line structures at sizes comparable to the target wavelength. To multiplex, KIDs may either be inductively or capacitively coupled to a main transmission line. The latter of which is increasingly common and used in this antenna-coupled prototype array.

A general schematic of a capacitively coupled KID is shown in Fig. 5.1a. It consists of an LC resonator circuit and coupling capacitor (C_c). Two potential types of loss are included in the form of a capacitive parallel shunt resistance ($R_{||}$) and inductive series resistance (R_s). The inclusion of both adds algebraic complexity that can frequently be simplified. Parallel shunt resistance $R_{||}$ of a KID geometry is often large, while series resistance R_s associated with quasiparticle density n_{qp} is small when operating at $T \ll T_c$. However the exclusion of both creates a fictional "perfect" LC circuit with no loss, so most models incorporate at least one form of resistance (see McCarrick, 2018; Mauskopf, 2018).

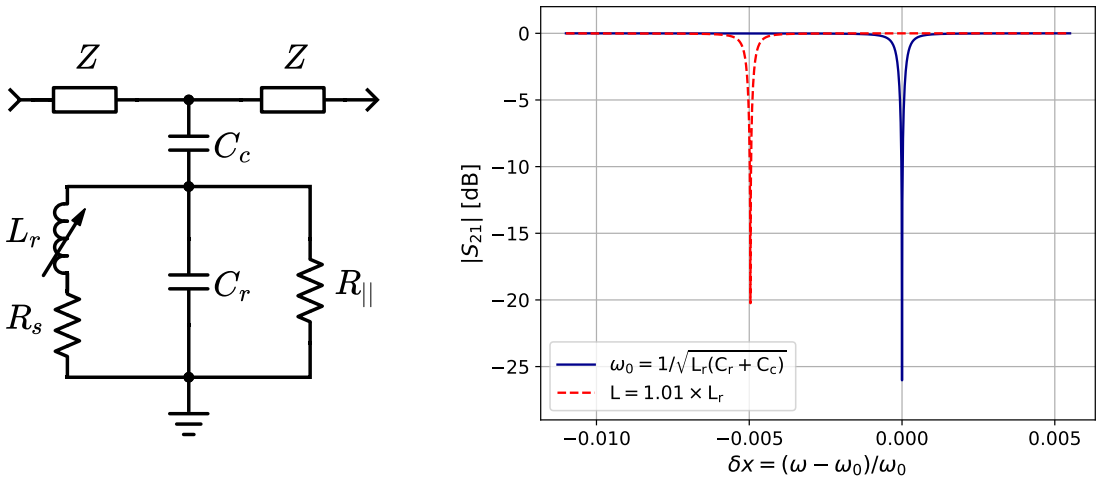

(a) (b)

Figure 5.1: (a) General schematic diagram of a single KID-style resonator. It consists of an RLC resonant circuit, capacitively coupled to a transmission line for it to be read out. (b) Simulated example S_{21} response versus fractional shift relative to resonant angular frequency ω_0 for such a resonator. *Blue* is the original design with resonance ω_0, while *red, dashed* is shifted via an increase in inductance by 1%.

5.1.4 Impedance, Quality Factors, and S_{21}

The resultant resonator impedance as in the circuit depicted in Fig 5.1a is

$$Z_{res}(\omega) = \frac{1}{i\omega C_c} + \left(\frac{1}{R_s + i\omega L_r} + \frac{1}{i\omega C_r} + \frac{1}{R_{||}} \right)^{-1}, \tag{5.8}$$

where $\omega = 2\pi\nu$ is the angular frequency. Expanding eq. (5.8) yields

$$Z_{res}(\omega) = \frac{R_s/R_{||} + 1 - \omega^2 L(C_r + C_c) + i\omega \left[R_s(C_r + C_c) + L/R_{||} \right]}{-\omega^2 C_c(R_s C_r + L/R_{||}) + i\omega C_c(R_s/R_{||} + 1 - \omega^2 L C_r)}. \tag{5.9}$$

An example scattering parameter transmission (S_{21}, see eq. 5.16 further below) for a resonator using this eq. (5.9) is shown in Fig. 5.1b. The dashed line corresponds to an increase in kinetic inductance as one would expect when a photon is detected by a KID via breaking of Cooper pair(s).

While eq. (5.9) appears daunting, it can be further simplified. Both R_s and $1/R_{||}$ are expected to be $\ll 1$, thus any second-order terms are negligible ($R_s/R_{||} \to 0$).

Near resonance, evaluation in terms of quality factors is an additional tool, where a quality factor is the ratio between the maximum energy in a system ($\mathcal{E}_{\rm sys}$) and the energy dissipated ($P_{\rm diss}$), per cycle,

$$Q = \frac{\omega_0 \mathcal{E}_{\rm sys}}{P_{\rm diss}}, \tag{5.10}$$

with the resonance angular frequency ω_0 is dependent upon the inductance and capacitance within the system,

$$\omega_0 = \frac{1}{\sqrt{L_r(C_r + C_c)}}. \tag{5.11}$$

Quality factors may be broken down into multiple sub-systems. First is the coupling between the transmission line (Z) and resonator capacitor (C_c) referred to as coupling quality factor (Barry, 2014),

$$Q_c = \frac{\omega_0(C_r + C_c)|V_{res}|^2/2}{|I_Z|^2 Z/4} = \frac{2(C_r + C_c)}{\omega_0 C_c^2 Z}, \tag{5.12}$$

where Z is the microwave transmission line impedance coupled to the KID under investigation. Furthermore, there is an internal quality factor of the RLC resonator indicative of the loss within resistance components R_s and $R_{||}$,

$$Q_i = \frac{\omega_0 L|I_L|^2/2}{P_s + P_{||}} = \frac{\omega_0 L|I_L|^2}{|I_L|^2 R_s + |I_L|^2|R_s + i\omega_0 L|^2/R_{||}} \simeq \frac{\omega_0 L}{R_s + \omega_0^2 L^2/R_{||}}. \tag{5.13}$$

Taking all of the above into account, eq. (5.9) at resonance can be rewritten as:

$$\begin{aligned} Z_{res}(\omega_0) &= \frac{i\omega\left[R_s(C_r + C_c) + L/R_{||}\right]}{-\omega^2 C_c(R_s C_r + L/R_{||}) + i\omega C_c(R_s/R_{||} + 1 - \omega^2 L C_r)} \\ &= \left(\frac{R_s + \omega_0^2 L^2/R_{||}}{\omega_0 L}\right)\left(\frac{C_r + C_c}{\omega_0 C_r^2}\right)\frac{1}{1 + i\omega_0(C_r + C_c)(R_s C_r + L/R_{||})/C_c} \\ &= \frac{ZQ_c}{2Q_i}\frac{1}{1 + i\epsilon_K} \end{aligned} \tag{5.14}$$

where $\epsilon_K = \omega_0(C_r + C_c)(R_s C_r + L/R_{||})/C_c$. A slight shift off-resonance is often represented as a $\delta x = (\omega - \omega_0)/\omega_0$, or $\omega = \omega_0(1 + \delta x)$. Substituting this into eq. (5.9)

for $\delta x \ll 1$ yields:

$$Z_{res}(\omega) \simeq \left(\frac{Q_c}{2Q_i + iQ_c\delta x}\right)\frac{Z}{1+i\epsilon_K}. \tag{5.15}$$

The expected scattering parameter transmission (S_{21}) through a network with one KID resonator thus becomes

$$S_{21} = \frac{2Z_{res}}{2Z_{res}+Z} = 1 - \frac{Z}{2Z_{res}+Z}, \tag{5.16}$$

which in combination with eq. (5.15) may be approximated as (Khalil et al., 2012),

$$S_{21} \simeq 1 - \frac{Q_{res}}{Q_c}\frac{1}{1+2iQ_{res}\delta x} \tag{5.17}$$

with Q_{res} being the overall resonator quality factor:

$$\frac{1}{Q_{res}} = \frac{1}{Q_c} + \frac{1}{Q_i} + \frac{1}{Q_{loss}}, \tag{5.18}$$

taking into account both coupling, internal, and parasitic loss Q_{loss} (Mauskopf, 2018). This Q_{loss} may include a variety of external factors such as parasitic reactances along with temperature- and optical load- dependent effects.

5.1.5 Thermal and Optical Response

The properties outlined above are all influenced by the density of charge carriers (Cooper pairs and quasiparticles) in the superconducting structures that make KIDs. The two most common properties that affect charge carrier density are temperature and optical loading.

A lower temperature (below T_c) creates more Cooper pairs, causing a lower kinetic inductance and thus shifts the resonance to higher frequencies. The change in resonant frequency ν_0 with temperature can be modeled as in Mauskopf (2018)

$$\begin{aligned}\frac{\mathrm{d}\nu_0}{\mathrm{d}T} =& \frac{L_k\nu_0\exp\left(-\Delta_0/k_\mathrm{B}T\right)}{L_{\mathrm{tot}}T}\sqrt{\frac{2\pi k_\mathrm{B}T}{\Delta_0}}\left(\frac{1}{2}+\frac{\Delta_0}{k_\mathrm{B}T}\right)\\ &\times\left[1+\sqrt{\frac{2\Delta_0}{\pi k_\mathrm{B}T}}\exp\left(-\frac{h\nu_0}{k_\mathrm{B}T}\right)I_0\left(\frac{h\nu_0}{k_\mathrm{B}T}\right)\right]\end{aligned} \tag{5.19}$$

where I_0 is the zeroth-order modified Bessel function of the first kind. Lower base temperatures are often desired, as they produce a higher overall resonator quality factor (Q_{res}).

Meanwhile, KIDs are also influenced by any absorbed power. This is most significant to determine the response of incident absorbed photons that are detected once pointed on-sky. The resonance frequency shift is described as a set of differential equations,

$$\frac{\mathrm{d}\nu_0}{\mathrm{d}P_{\mathrm{abs}}} = \frac{\mathrm{d}\nu_0}{\mathrm{d}\sigma_2}\frac{\mathrm{d}\sigma_2}{\mathrm{d}n_{qp}}\frac{\mathrm{d}n_{qp}}{\mathrm{d}P_{\mathrm{abs}}} \tag{5.20}$$

As shown in Mauskopf (2018), superconductors like aluminum have the product of:

$$\frac{\mathrm{d}\nu_0}{\mathrm{d}\sigma_2}\frac{\mathrm{d}\sigma_2}{\mathrm{d}n_{qp}} \simeq -\frac{L_k\nu_0}{4L_{\mathrm{tot}}N_0\Delta_0}\left(1+\sqrt{\frac{2\Delta_0}{\pi k_{\mathrm{B}}T}}\right), \tag{5.21}$$

with the final differential of eq. (5.20) being,

$$\frac{\mathrm{d}n_{qp}}{\mathrm{d}P_{\mathrm{abs}}} = \frac{1}{2}\sqrt{\frac{\eta}{\gamma P_{\mathrm{abs}}\Delta\Sigma}} \tag{5.22}$$

for an average quasiparticle generation efficiency η and superconductor volume Σ. This is under the assumption that the superconductor is dominated by optically excited quasiparticles, as expected for Al, and not thermal or background generated quasiparticles (Mauskopf, 2018; Gordon, 2019).

5.2 Array Specifications

The prototype antenna-coupled MKID array functions through the absorption of an incident photon via the antenna, filtered into its respective spectral band, sent to a MKID resonator where it breaks Cooper pair(s), changing the kinetic inductance and thus shifting the observed resonant frequency of the MKID. This process requires a detailed set of fabrication steps. All non-antenna designs were adapted from an existing multichroic MKID horn-coupled prototype design described in Johnson et al.

Layer	Material	Thickness	Info
6	Nb	400 nm	Microstrip & Gnd Straps
5	Au	100 nm	Term. R at 180° hybrid sum port
4	Vias	thru SiN (see 3)	For Microstrip & Gnd Straps
3	SiN_x	350 nm	Microstrip Dielectric/Insulator
2	Nb	200 nm	Bi-layer Gnd: CPWs, Slot Antenna
1	Al	40 nm	Bi-layer Gnd: CPWs, Slot Antenna
0	HRFZ Si Wafer	500 μm	Device Wafer

Table 5.1: Fabrication layer stack-up of the prototype lenslet-coupled antennas paired with multichroic MKIDs. *Note:* The MKID sensing elements are made of CPWs with exposed aluminum (layer 2 Nb removed).

(2018). The fabrication stack-up of all layers involved in the prototype array is listed in Table 5.1. These prototype arrays were fabricated at NIST (National Institute of Standards and Technology) and received here at ASU via Dr. Bradley Johnson (University of Virginia), the lead PI of this MKID collaboration.

The "uppermost" layers for the microstrip geometry consists of Nb on SiN_x dielectric, as fabrication layers 3 & 6 in Table 5.1. Each prototype array contains 6 dual-bowtie and 6 HTZ antennas. The antenna microstrip feed-lines have a minimum width of 1.0 and 1.3 μm at the dual-bowtie and HTZ antenna center, respectively. The feed-lines are then stepped in a Chebyshev-like impedance transformer towards the 5.0 μm-wide microstrip network, where each microstrip feed splits and filters incident signal into their respective 150 and 235 GHz bands per antenna arm. Differential signals from opposing arms are then recombined at a 180° hybrid tee, where the sum port signal is dissipated with a gold film terminator resistor (layer 5). A photo is shown in Fig. 5.2 of one such described pixel coupled to an HTZ antenna. The green region is the SiN_x microstrip substrate, with the thin yellow defining the Nb

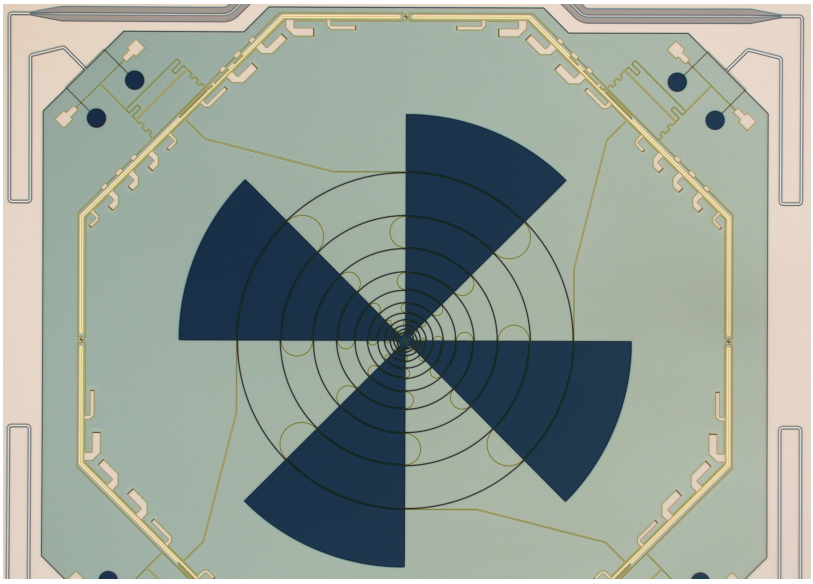

Figure 5.2: The center of one hybrid-trapezoidal MKID pixel in the prototype array. The green region is the SiN_x microstrip substrate, with the thin yellow defining the Nb microstrip edges. The thin regions extending from the center are the antenna microstrip feed-lines. The antenna slot (no Nb-over-Al ground plane) is dark blue. *Photo Credit: Dr. M. Vissers, NIST*

microstrip edges. The thin yellow stripes extending from the center are the antenna microstrip feed-lines. The antenna slot (no Nb-over-Al ground plane) is dark blue.

A microstrip to slotline transition transfers the 180° hybrid's difference signal to a coplanar waveguide (CPW) cut out of an Nb-over-Al bilayer ground plane. This occurs at each pixel corner, visible in Fig. 5.2. The CPW structure then constructs the MKID resonator, shown in Fig. 5.3. The CPW resonator starts narrow with an exposed Al center-line (no Nb) acting as the sensing element where Cooper pairs are broken due to aluminum's critical temperature of $T_c = 1.4$K. The rest of the CPW then widens and is made out of Nb-over-Al bilayer, with a measured $T_c = 8.3$K (Flanigan, 2018; Johnson et al., 2018). Breaking Cooper pairs at this T_c would require photon energies of ≈ 600 GHz, greater than the designed spectral bands and thus limiting destruction of Cooper pairs to only the narrow exposed Al resonator section.

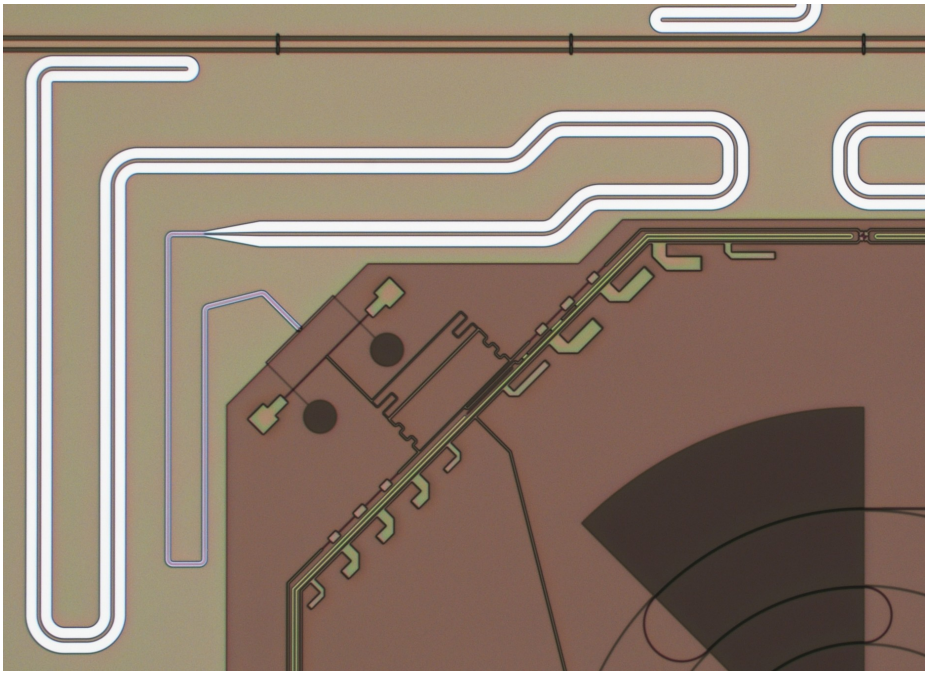

Figure 5.3: Closer view of one MKID resonator, made of an etched CPW geometry shown here as white. The thin CPW extending from the microstrip geometry transition (SiN_x here is the brown) has an exposed Al center-line where Cooper pairs are able to be broken. Also seen is the horizontal CPW transmission line (top) that the MKIDs are capacitively coupled to, with ground straps in an effort to reduce cross-talk between MKIDs. *Photo Credit: Dr. M. Vissers, NIST*

The Nb-over-Al portion of the resonator however helps set the base inductance and capacitance, which depend upon the over CPW length. Each MKID resonator is tuned to a unique resonance by varying this CPW length, for 4 per pixel or a total of 48 resonators in the prototype array. Their expected frequencies span from roughly $2.5 - 3.0$ MHz (Flanigan, 2018; Johnson et al., 2018). The CPW resonator end is then capacitively coupled to the main CPW transmission line that is routed around all pixels. Ground straps connecting the opposing CPW grounds, visible in Fig. 5.3, are placed over the main transmission line, via bridges made of Nb over SiN_x at frequent intervals. This is an attempt to minimize potential cross-talk between neighboring MKID resonators.

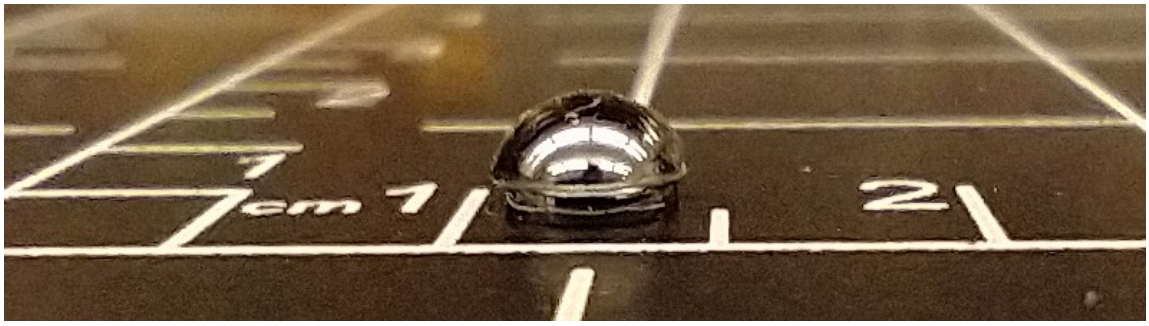

Figure 5.4: Side-view image of one prototype silicon lenslet with a single-layer glass AR cap/coating, with a $\lambda/4$ thickness centered at 150GHz.

5.2.1 Antenna and Lenslet Geometry

Echoed in the previous chapter, fabrication of AR-coated lenslets is one of the primary challenges for lenslet-coupled antennas. These prototype arrays will have a limited number of hyper-hemispherical silicon lenslets from *Hyperion Optics*[1] with a radius of R = 1.7 mm and thickness of 1.9 mm (0.2 mm hyper-extended from the hemispherical plane). Combined with the HRFZ silicon wafer, it creates a lenslet extension length of L = 0.7 mm for an L/R $\approx$ 0.41. Although not the optimized values used in the Chapter 4 simulations, this L/R value should be within near-optimal range for both dual-bowtie and hybrid trapezoidal antennas.

The two-layer AR coating was also unable to be easily obtained, so these first batch of lenslets instead use a single-layer of H-PZ33 glass ($n_d = 1.472$ or $\epsilon = 2.17$) with $T = \lambda/4$ thickness set at 150 GHz. As a result, the 150 GHz band will be the primary band under investigation, but the 235 GHz band can still be utilized to help improve efficiency estimations. This layer is also only applied to roughly 80° from zenith rather than a full 90° hemispherical cap due to fabrication limitations. An image of one such lenslet is shown in Fig. 5.4. Table 5.2 outlines the rest of

[1] http://www.hypoptics.com/

Parameter	Dual-Bowtie	Hybrid TZ.
r_i [μm]	10	29.8
M	9	6
τ	1.3	1.35
L/R	$0.7/1.7 \approx 0.41$	

Table 5.2: Design parameters for the prototype lenslet-coupled antennas paired with MKIDs. Both dual-bowtie and hybrid trapezoidal arm designs from Chapter 4 were chosen. However, the lenslet geometry was not able to be optimized per design, instead using an R = 1.7 mm radius lens with an extension length of L = 0.7 mm.

the antenna parameters, which do not otherwise differ from the previous simulation values.

5.3 Package Specifications

A device package was designed to hold the prototype array and lenslets for cryogenic testing. Machined out of aluminum, it must safely route an RF signal to the array's microwave transmission line. An SMA connector is soldered to a microstrip to CPW transition board that rests adjacent to the array. This is shown in Fig. 5.5a with an array placed (but not fully installed). Twelve circular cutouts reside behind the array that correspond to lenslet positions where incident light is to be observed from. A remaining difficulty is the accurate wire-bonding of the device array to the transition board and Al package. This requires Al wire-bonding between the upper bilayer of Nb to copper on the transition board and Al of the package. With limited Al wire-bonding experience and a manual wire-bonder that is currently experiencing issues, the many dozens of wire bonds necessary have proven difficult.

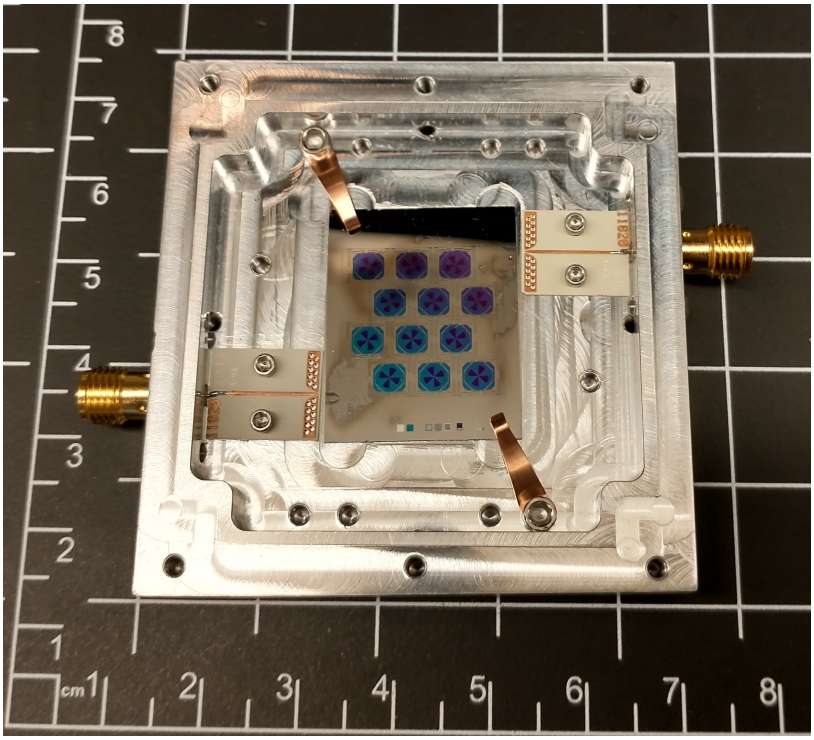

(a) Top

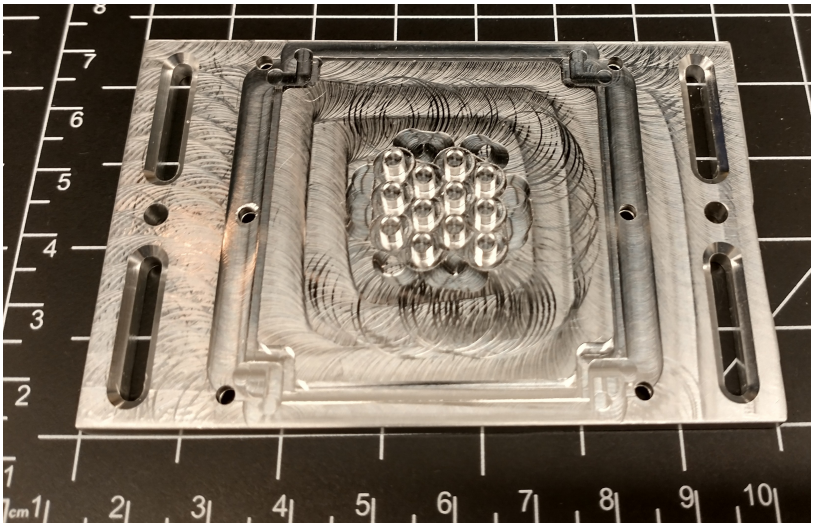

(b) Bottom

Figure 5.5: Device module package to hold the prototype lenslet antenna-coupled MKID array. (a) Inner top half of package, where the array is held and microwave transmission line is to be connected (Al wire-bonds not present). (b) Inner bottom half of the package, designed with a close-fit and individual 150 GHz $\lambda/4$ backshorts.

The bottom side of the device package, shown in Fig. 5.5b, contains individual $\lambda/4$ backshorts designed for 150 GHz. When assembled, the package top and bottom are tight-fitting to limit stray radiation from undesired directions.

Securing the device array is a primary concern, but securing and aligning individual lenslets over their respective pixel is of equal importance. A system has been devised to attach an aluminum holder to the outside of the module's top. Lenslets as previously shown in Fig. 5.4 may be placed within their circular cutouts of the package top and then secured from above via slightly narrower circular cutouts in the aluminum holder attachment. An image of this is shown in Fig. 5.6a resting upon the three available lenslets. Initial "dark" measurement testing where detectors are not illuminated may instead be conducted by simply placing a cover or tape over the package opening. Subsequent testing while illuminating the device array requires attaching the aluminum holder to the module package via a set of springs to hold the lenslets, shown in Fig. 5.6b, which allows for potential changes due to thermal expansion.

5.4 Future Steps

Testing has yet to fully commence on these prototype device arrays. That doesn't however prevent me from outlining potential steps in the testing timeline.

5.4.1 Dark Testing

The first and easiest test step would be to begin characterization of the MKID components. This involves keeping the array "dark" by minimizing any stray light and observing their base resonance frequencies. For accurate results, the array must be placed on a cryogenic stage at $T \lesssim 300$mK to be well below the 1.4K critical temperature of the aluminum. No lenslets nor their holder attachment are required

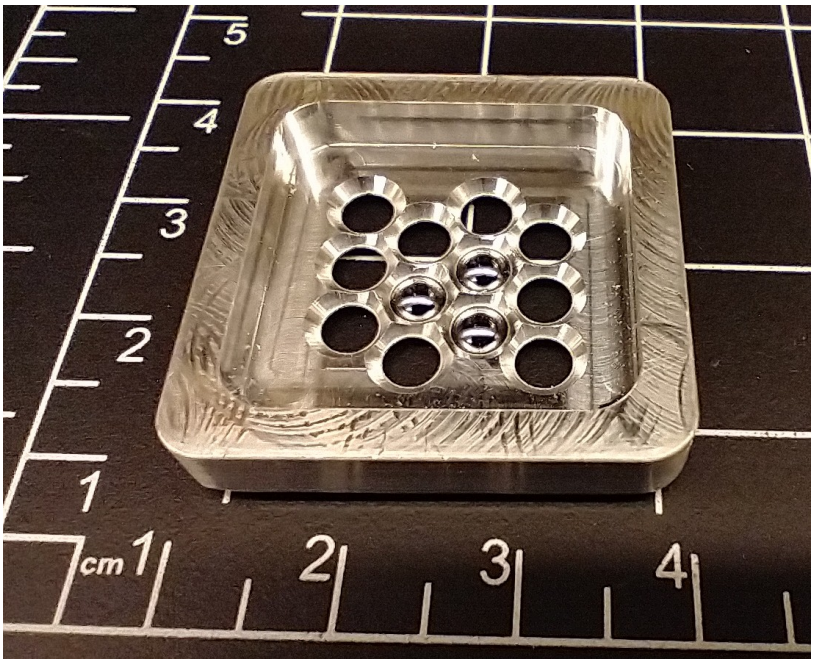

(a) Lenslet Holder

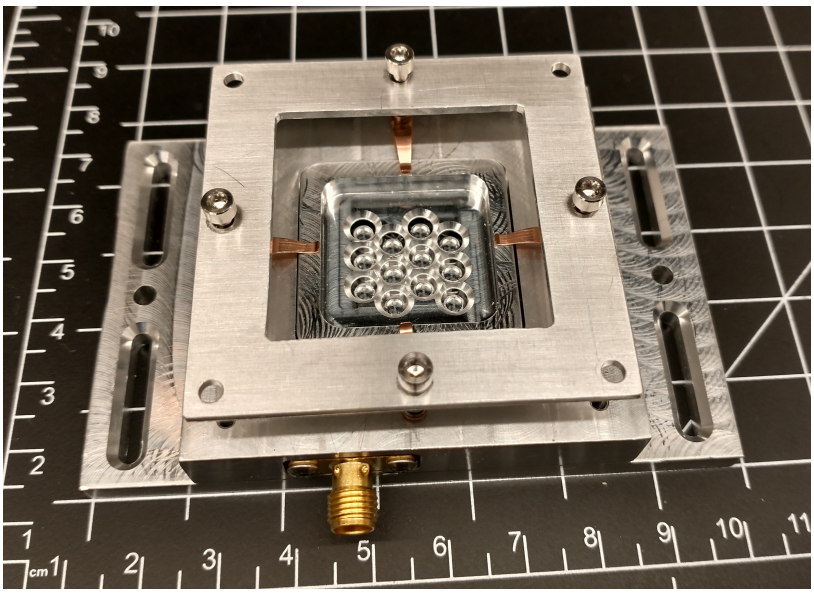

(b) Assembled Lenslet Holder

Figure 5.6: (a) Lenslet holder, resting upon the three available prototype lenslets. (b) Outer top side of the MKID device package, where a spring clamp setup is used on an aluminum holder to keep the individual lenslets in place (lenslets nor device array are present here).

for this step. The package's focal side can instead be covered or taped up to prevent stray light.

The temperature response, such as briefly described in Section 5.1.5 may also be characterized via the inclusion of a heater on the same ultra-cold cryogenic stage that the device is located. Paired with a reliable thermometer, the temperature can be controlled and dark resonator response recorded to help determine their kinetic inductance and energy gap Δ_0.

5.4.2 Illuminated Testing

Inclusion of the novel antenna designs was the primary motivation for these new MKID arrays, which unfortunately does not have direct influence on dark test results. Instead, the lenslet-coupled antennas must be illuminated to gauge antenna efficiency and overall optical response of the detectors. A clean manner of directing light onto the detectors would be using an external source outside the cryostat directed through a series of cryostat windows. However, most cryostats, including those in the lab here at ASU do not have that capability.

A standard alternative to cryogenic windows is to illuminate the detector array through a controllable external source routed into the cryostat. Waveguides are often preferred for millimeter wavelengths, as other methods such as RF coaxial cabling become lossy. The downsides are that waveguides can take up substantial amounts of space, and often require reconfiguration of parts within a cryostat. The second option involves placing a material inside the cryostat, normally at a higher temperature stage and directed towards the device to act as a blackbody source. This illuminates the device array with an incoherent broadband radiation, but is still partially controllable if placed with a heater to adjust its temperature.

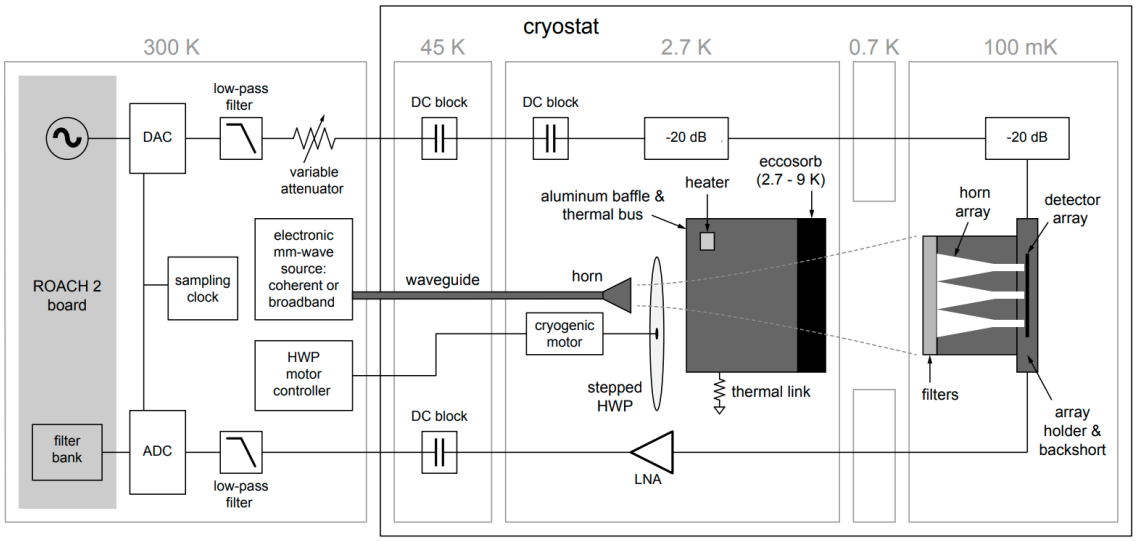

Figure 5.7: Test system schematic from McCarrick, H. et al. (2018), depicting two manners to radiate the focal plane of a detector array. The first option is the use of a controllable external coherent source sent in via a waveguide plus horn antenna, and further modulated by a half wave plate (HWP). The second option is to use Eccosorb coated with etched Teflon weakly coupled to a higher temperature stage (2.7K stage shown in image). This would emit a broadband blackbody radiation within the cryostat at its thermal temperature, which can be further adjusted by an adjacent heater.

A schematic containing both options is shown in Fig. 5.7, extracted from McCarrick, H. et al. (2018). Here the blackbody source (second option) is Eccosorb coated with etched Teflon, to ensure a sufficient but not excessive amount of blackbody radiation is generated within the cryostat. For initial testing, the blackbody source would be the easiest method to implement and compare overall responsivity between the dual-bowtie and hybrid trapezoidal antenna designs.

5.4.3 Antenna Considerations

If further antenna design modifications are conducted, such as some points raised in Section 4.7 of the previous chapter, the initial steps in fabrication and testing may benefit to differ from what was described and conducted here. Instead of full integration within a device array, antennas could first be fabricated individually or even

scaled to longer wavelengths and constructed out of valid normal room temperature conductors (i.e. copper). Then standard antenna testing in anechoic chambers could be conducted without the need for complex cryogenic systems. This was done for initial versions of the sinuous log-periodic designs (O'Brient, 2010). It may also then be more cost-effective, especially if any extremely novel untested designs are to be considered.

Chapter 6

CRYOGENIC READOUT DESIGN OF ALICPT

6.1 Scientific Motivation

A dominant portion of the current ground-based millimeter-wave telescopes are currently deployed in the Southern Hemisphere. More specifically, many reside at either the Atacama Desert in Chile; i.e. ACT (Choi et al., 2018; Mallaby-Kay et al., 2021), ALMA (Wootten and Thompson, 2009; ALMA Partnership et al., 2015), CLASS (Dahal et al., 2022), POLARBEAR (Westbrook et al., 2018; Kaneko et al., 2020), and the upcoming Simon's Observatory (Xu et al., 2020); or Antarctica; such as SPT (Anderson et al., 2018), and the BICEP/Keck instruments (Ade et al., 2015b; Moncelsi et al., 2020). Frequent balloon missions are also deployed near the South Pole, including BOOMERanG and SPIDER (Crill et al., 2003; Hubmayr et al., 2016).

For the Ali CMB Polarization Telescope (AliCPT), its location on the Tibetan Plateau shares many desired properties with the aforementioned sites, namely being dry, high altitude, and far from potential pollutants (Li et al., 2018). However, with AliCPT's presence in the Northern Hemisphere and resolutions of $19'$ and $11'$ for 90 and 150 GHz, respectively, it becomes an important counterpart to the BICEP/Keck family of Antarctic telescopes (Keating et al., 2003; Salatino et al., 2020). These are ideal instruments in the search for primordial gravitational waves via detection of the faint B-mode CMB polarization component, predicted to peak at moderate angular scales. They will also help to identify large-scale foreground contamination, such as galactic dust and synchrotron emission (Li et al., 2018). Shown in Fig. 6.1, AliCPT enables coverage in the Northern Hemisphere unreachable by instruments at

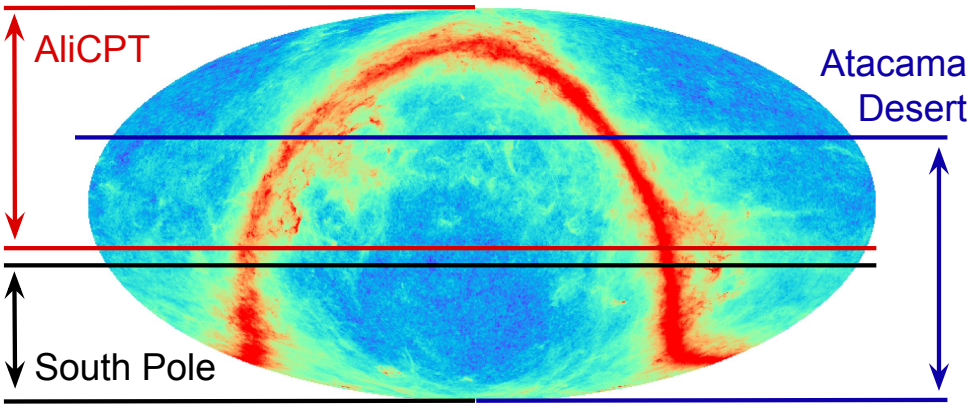

Figure 6.1: The general observational range of AliCPT compared to that of instruments at the South Pole and Atacama Desert, inspired by a similar graphic from the AliCPT IHEP team. AliCPT will unlock much of the less-studied Northern Hemisphere that these other instruments cannot observe. The background image is an equatorial Mollweide projected sky at 353 GHz from *Planck* (Planck Collaboration et al., 2020c).

the South Pole and Atacama Desert. It also provides opportunities for other analysis by overlapping with Northern Hemisphere sky surveys such as SDSS (Ahumada et al., 2020) and the Dark Energy Spectroscopic Instrument (DESI, Levi et al., 2019). Fig. 6.2 further highlights the lack of Northern Hemisphere CMB experiments, where AliCPT is a significant addition due to it's high sensitivity, detector count, and dedicated telescope (Salatino et al., 2020).

6.2 Overview of AliCPT

AliCPT is a dual-band polarimeter set to unlock large areas of the Northern Hemisphere sky via ground-based millimeter observations as part of an international collaboration led by the Institute of High Energy Physics (IHEP). AliCPT's telescope receiver development is led by Stanford University, with detector array development by NIST and readout electronics (both room temperature and cryogenic) from ASU. It will be deployed in the Tibetan Plateau with a 72 cm diameter aperture that illuminates a 63.6 cm diameter focal plane (Salatino et al., 2021). Cooled down to 280 mK,

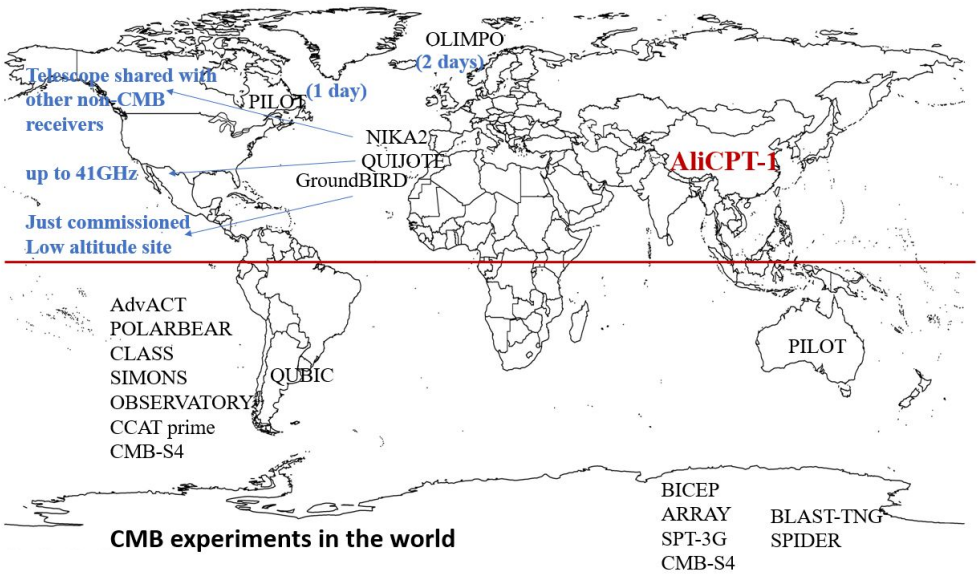

Figure 6.2: Various CMB experiments and their locations throughout the world, image created by Maria Salatino (Stanford University). AliCPT will be one of only a handful located in the Northern Hemisphere.

the focal plane will be populated by up to 19 detector modules, each of which contains 1704 transition-edge sensor (TES) bolometer detectors for a total of up to 32,376 detectors. These TES bolometers are voltage-biased superconducting devices that are operated just below their critical temperature (T_c). Thus, an increase in temperature produced by an incident photon creates a change in the TES electrical current. It then causes a resonance frequency shift in an inductively coupled RF superconducting quantum interference device (SQUID) resonator (Irwin and Hilton, 2005). AliCPT makes use of a microwave frequency-domain multiplexing μmux structure, where each TES-SQUID pair is tuned to a unique resonant frequency (Mates, 2011; Salatino et al., 2020). The final detector module design aims to operate on a single RF network, for a multiplexing factor of 1704. A complex system of cabling, components, and electronics are then required to accurately read out all signals detected.

Outside the cryostat at room temperature resides the warm readout electronics responsible for producing the frequency tones that probe the detector resonances. Al-

iCPT uses a Xilinx RF system, the RFSoC ZCU111 evaluation board, for all digital signal processing (DSP) demands (Sinclair et al., 2020; Salatino et al., 2021). An intermediate frequency (IF) transceiver board, from Alphacore Inc., is used in conjunction to up- and down- convert the RFSoC frequencies to the required 4-8 GHz detector resonator band (Salatino et al., 2020).

Fig. 6.3 shows the AliCPT cryostat vacuum jacket (VJ) during assembly at Stanford University and the SolidWorks model cross-section depicting most parts within the complete cryostat. The cryostat has temperature stages of approximately 50K, 4K, 1K, 350mK, and 280mK. The 50K and 4K stages are cooled down with a Cryomech PT420 2-stage pulse tube cryocooler[1].Meanwhile, a custom *Chase* 3-stage adsorption fridge is responsible for the three lower temperature stages (Salatino et al., 2020). Cryogenic readout pertains to all components in the signal chain between the electronic readout rack and TES detector array. The Mauskopf lab here at Arizona State University works on such readout design in collaboration with the AliCPT U.S. team, led by Stanford University.

6.3 Cryogenic Readout Overview

Of equal importance to detectors themselves is the ability to reliably read their signals out of the cryostat for detailed data analysis to begin. This relies upon a comprehensive set of cables and components routed from the room temperature readout electronics through the AliCPT cryostat, to the detectors at 280mK, and back out. The readout chain between the warm readout electronics and one such detector module is detailed in Fig. 6.4. This includes a set of RF coaxial (input

[1]Current thermal design predicts one PT420 cryocooler is sufficient the total deployment of 19 modules; however in the case of non-optimal performance, the receiver has been designed to host a second PT420 cryocooler.

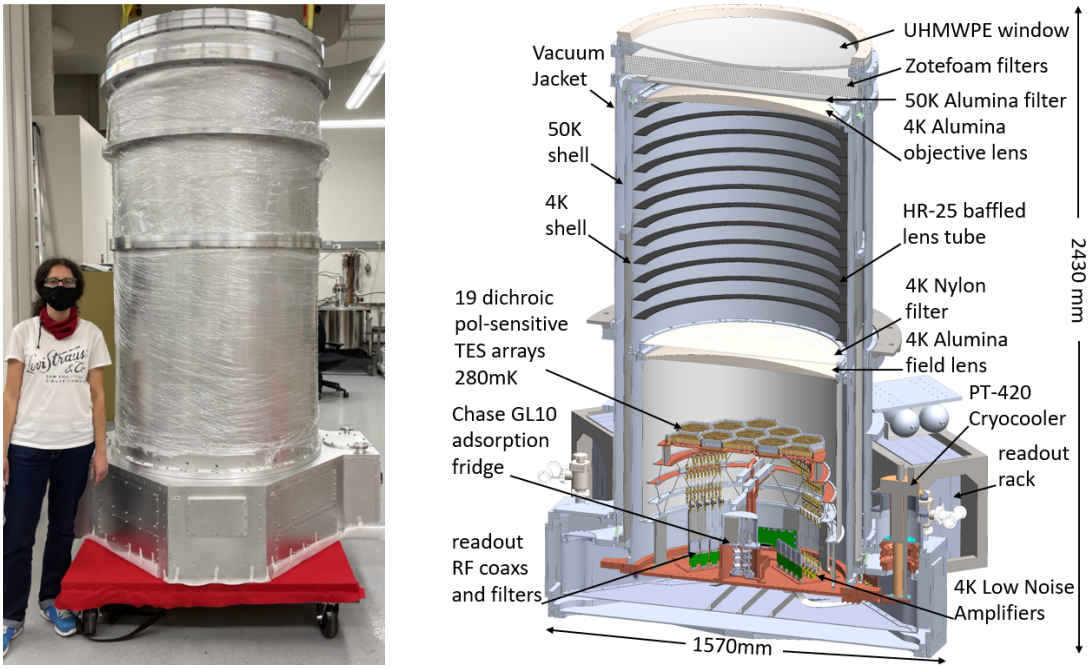

(a) 300K Vacuum Jacket (b) Cryostat Model

Figure 6.3: The AliCPT cryostat. (a) External view of 300K vacuum jacket and (b) SolidWorks model showing a cross section summary of the inner components. Originally published in Salatino et al. (2020).

and output) to successfully probe the resonance frequencies of the μmux resonators, and dedicated DC lines for the detectors and cryogenic readout electronics. These DC lines provide power to the low noise amplifiers (LNAs) situated on the RF chain output at 4K and 50K, along with providing TES voltage bias and RF SQUID ("flux ramp") bias at the detector module.

The RF input coaxial chain contains cryogenic attenuators starting at the 4K temperature stage and cooler. The resonators are optimally probed with a power of ≈ -70 dBm (Dober et al., 2017) at the detectors. However, to minimize noise temperature within the entire RF chain, a higher power tone (roughly -40 to -45 dBm) is input into the cryostat and then attenuated down at the colder stages. Ideally, this attenuation would be done at the coldest stage (280mK), but cryogenic loading also needs to be taken into account. Colder temperature stages have lower cooling

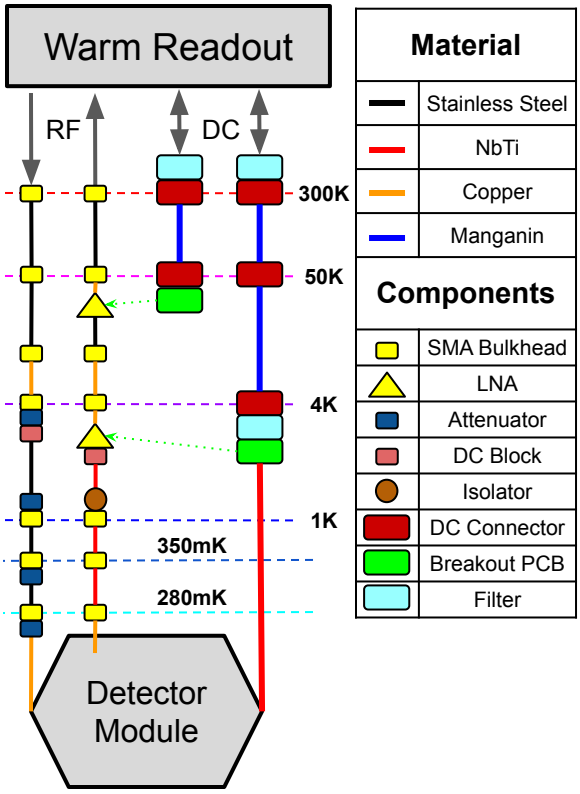

Figure 6.4: AliCPT cryogenic readout diagram, updated version from that originally published in Salatino et al. (2021) (cryogenic DC filter moved). It outlines all cabling and components needed to successfully read out one final AliCPT detector module. Initial detectors in AliCPT will require two sets of RF chains.

power, making the management of thermal loads a balancing act between cryostat capabilities and readout efficiency, particularly on the three lower stages cooled by the custom *Chase* adsorption fridge.

Listed in Table 6.1 are recent attenuator values used in AliCPT The 4K temperature stage has the largest attenuation (20 dB), due to its significantly higher cooling power of which RF attenuation uses only a marginal portion. The 1K and sub-Kelvin stages on the other hand, have lower cooling power from the adsorption fridge which allows for only $0-3$ dB attenuators. This is assuming the maximum of 1704 frequency-multiplexed tones through the RF cabling system.

Stage:	4K	1K	350mK	280mK
Attenuator:	20 dB	0 dB	3 dB	3 dB

Table 6.1: Recent attenuator selection within AliCPT (subject to change). As the 1K stage is nearest its net cooling power limit, no attenuation is assigned.

On the RF coaxial output, LNAs situated at 4K and 50K are made here at Arizona State University, providing nominal gains of roughly 25 dB and 15 dB, respectively. In combination, the two LNAs bring the RF signal back to readable power levels while minimizing noise contributions. An RF isolator is placed on the 1K output line before the first (4K) LNA to further reduce noise and limit any reflections at 4K from traveling back to the detector module. DC blocks are also utilized between the 4K and 1K stages, with available space at 300K and 280mK if deemed necessary, to limit DC and thermal propagation.

Similarly, the DC lines require minimal noise and as low electromagnetic interference (EMI) as possible within the cryostat. Unwanted EMI, especially near the focal plane, would interfere with both the readout cabling and the sensitive components of the detector module itself. Therefore, the DC lines incorporate a low-pass ferrite filter adapter at the cryostat VJ interface and a higher quality *Cristek* pi-type EMI filter at the 4K interface. The AliCPT cryostat also employs RF shielding around the sub-4K focal plane unit (FPU).

6.4 Mechanical Considerations

Cryostat temperature stages have minimal surface areas and volume, in part to minimize their required cooling power. This adds a spatial complexity to the already delicate balance between thermal limits and readout performance. Much of this space is allocated for general cryostat function and operation, while cabling between stages

must also incorporate either loops or flexibility to accommodate potential differences in thermal expansion. As a result, very deliberate cryogenic readout configurations must be designed. All AliCPT inter-stage RF cabling consists of semi-rigid coaxial cables with loops or turns for this reason. The cryogenic readout within AliCPT can be divided into three distinct portions. These pertain to a readout harness present from 300K to 4K, distribution of the 4K readout components on a panel mounted to the cryostat's 4K baseplate, and the 4K to 280mK cabling that traverses the FPU to/from the detector module.

6.4.1 Readout Harness

For AliCPT, a mechanical harness design is used, which includes the cryogenic readout VJ plate (room temperature, i.e. 300K) down to an intermediate "floating" 4K panel. In this manner, the readout harness can be assembled outside of the cryostat and then installed inside without further need to adjust any of the difficult semi-rigid inter-temperature coaxial cabling within it. The final deployment of AliCPT will have a total of four identical readout harnesses, each capable of carrying the components necessary for supporting up to 5× detector modules. Once installed, copper coax connects RF cabling from the "floating" 4K panel of the harness to a 4K readout panel attached to the cryostat's 4K baseplate. The initial and latest SolidWorks design iterations of the AliCPT readout harness are depicted in Fig 6.5.

The readout VJ plate is stainless steel, 448 by 123 mm, with hermetic feedthrough connectors for 10× SMAs, 5× 37-pin d-sub, 1× 25-pin d-sub, and two tapped extensions used during harness assembly. Fig. 6.6 shows the VJ readout plate from the side that is visible outside the cryostat when the harness is fully installed. The subsequently attached 50K panel is copper, roughly 357 by 68 mm, with mounting locations for 10× SMA bulkheads, the aforementioned DC cabling (converted to micro-d con-

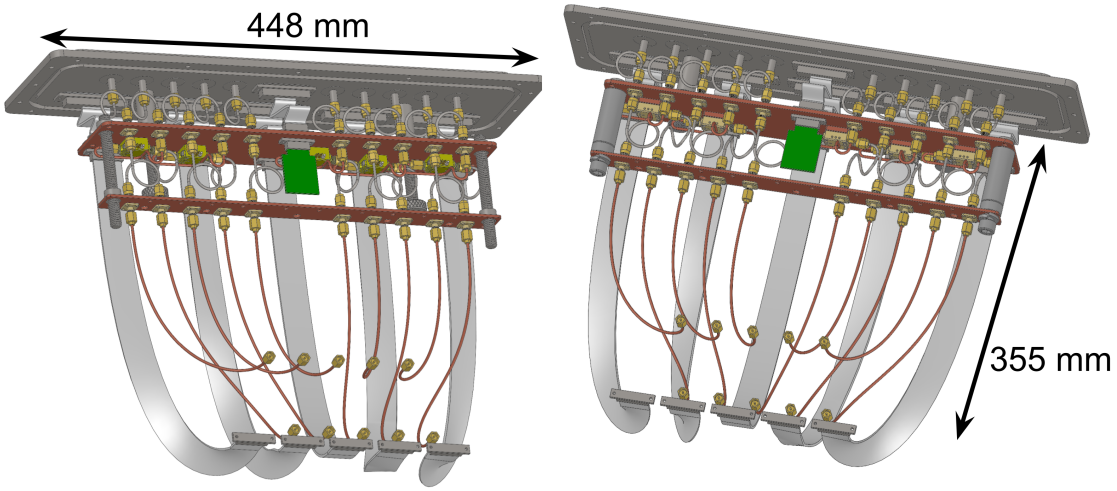

(a) First harness assembly model. (b) Latest harness assembly model.

Figure 6.5: 3D models of the AliCPT readout harness. (a) First assembled version. (b) Latest version, after identification of alignment difficulties. These latest modifications were implemented by Collaborators at Stanford University.

Figure 6.6: AliCPT VJ (300K) readout plate, the hermetic panel part of the readout harness design visible from outside the cryostat when fully installed.

nectors), and 4× through-holes for alignment legs during assembly. The 5× 50K LNAs and a breakout board from the 25-pin DC cable for all dedicated 50K LNA bias are also present on the 50K panel.

An intermediate "floating" 4K panel within the harness is implemented for the sole purpose of mounting 10× SMA bulkheads to constrain the 50K-4K semi-rigid coaxial cables within the harness design and simplify installation. It is not necessarily in complete thermal equilibrium with the 4K stage, as it is mounted via an

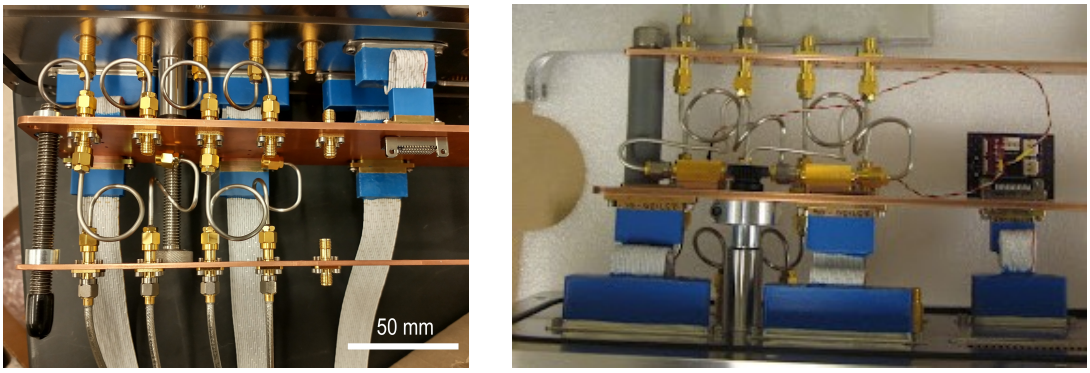

(a) First Readout Harness Assembly Test (b) Later Readout Harness Assembly Test

Figure 6.7: Initial readout harness assemblies of AliCPT with cabling for two RF chains. (a) The first assembly test, conducted at ASU (without 50K LNAs). (b) A later assembly conducted by Stanford University, with 50K LNAs and the updated assembly structure.

aluminum panel. Flexible copper coaxial cabling is then used to connect the harness once installed to the proper 4K panel (described in Section 6.4.2). Inserted into the cryostat the harness is secured, starting sequentially with the VJ plate, to each respective temperature stage. The alignment legs are then removed to help limit thermal conductivity between stages when cooled.

The VJ plate and 50K panel are separated by just 50.65 mm, while the 50K and intermediate 4K panels are only 59.75 mm apart. Such narrow distances restrict the number of possible coaxial cable configurations, especially when thermal properties are factored in (see Section 6.5). The 50K LNAs are placed on the 50K panel in a staggered manner that prevents physical interference between parts. Flexible copper coaxial is then carefully routed from the LNAs to the 50K SMA bulkhead outputs. Custom helically-looped 2.19 mm diameter stainless steel coaxial cables from *Coax-Co*[2] are used for all inter-temperature RF cabling within the readout harness. Images of the first test assembly and a later assembly are shown in Fig. 6.7, with an image of

[2]http://www.coax.co.jp/en/

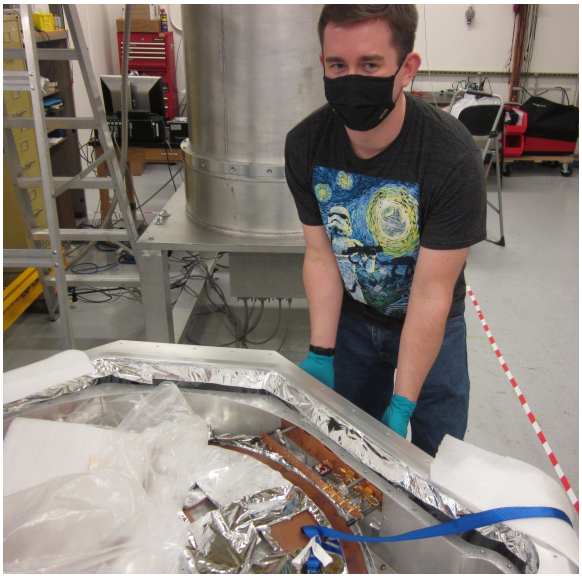

Figure 6.8: Image of me at Stanford University helping to conduct the first installation test of the AliCPT readout harness.

myself during the initial harness installation fit check at Stanford University is shown in Fig. 6.8.

6.4.2 4K Readout Panel

All AliCPT 4K readout components are situated on the 4K readout panel that resides upon the cryostat's 4K baseplate. This is the defining stage that spatially isolates the FPU from the rest of the cryostat. The intermediate "floating" 4K panel of the readout harness, mentioned above for simplicity in installation, connects to the 4K panel via flexible copper coaxial cabling. DC cables are also routed from the harness' 50K. Like the readout harness, each 4K readout panel is responsible for reading out up to 5 detector modules.

The 4K readout panel consists of the 5× 4K LNAs responsible for producing roughly 25 dB of gain on each RF output. The LNA bias is provided through individual breakout PCB boards, each routing bias for one LNA from a 37-pin micro-d DC cable. Before the breakout board, the DC cabling encounters a *Cristek* pi-type

EMI filter on the 4K stage. This is further protection for any residual EMI interference that could affect other electronics within the FPU. Each 37-pin DC cable then progresses through all FPU stages via thermal heat clamps and then connects to the detector module where it provides the TES and SQUID bias signals.

Other RF components are present on the 4K stage. As previously mentioned in Section 6.3, the largest attenuator (20 dB) is placed on the 4K input line, and DC blocks are placed on both RF input and output lines to help further isolate the FPU. Semi-rigid coaxial is then routed to the 1K stage, designed to avoid any potential interference with other equipment.

6.4.3 Sub-Kelvin Cabling

From the 4K panel, readout cabling must climb a stack of rings that constitute the three lowest temperature stages before reaching detectors at the focal plane. To maintain a high sense of modularity, all five RF chains (per harness side) are designed to be identical with interchangeable components between FPU stages. This is done with evenly spaced SMA bulkheads on a separate modular brass attachment for easy removal, designed by Stanford.

The primary difficulty for readout is the longer distances which the semi-rigid RF cables must traverse. Between 4K to 1K, the coaxial cabling must span a physical distance of roughly 280 mm. While distances of 77 mm and 94 mm are required from 1K to 350mK and 350mK to 280mK, respectively. Flexible copper coaxial cables are then employed for the 280mK isothermal connection to the detector modules. Custom 0.86 mm diameter coaxial cabling from *CryoCoax*[3] was used for these stages. Stainless steel was the material chosen for the input RF lines, while superconducting NbTi was selected for the output to minimize loss between the detectors and 4K

[3]https://cryocoax.com/

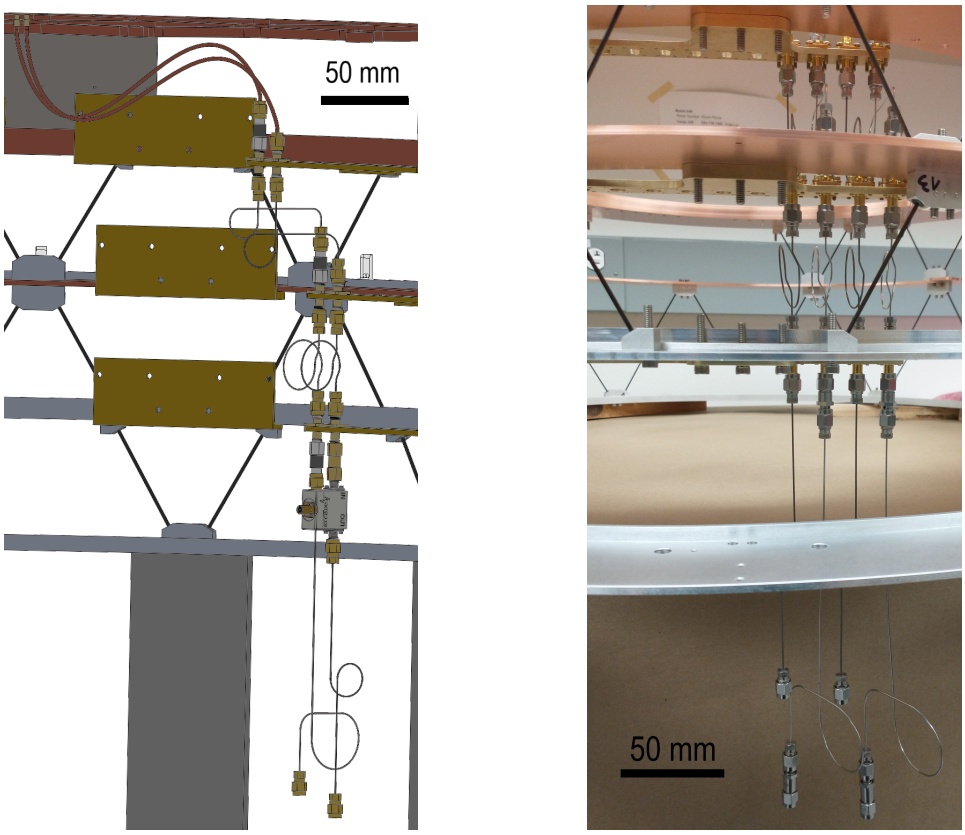

(a) Sub-Kelvin RF Solidworks 3D Model (b) Sub-Kelvin RF Physical Assembly

Figure 6.9: (a) SolidWorks 3D model of the AliCPT RF readout within the focal plane unit (4K-280mK). (b) Image of two assembled RF readout chains (four coax lines) within the focal plane unit. RF cryogenic isolator and DC cabling not shown.

LNA. The 3D model and initial assembly of AliCPT's sub-Kelvin RF coaxial chain is shown in Fig. 6.9.

Physical routing of the flexible DC cabling was easier. Since no breakout points past 4K are required, a long single cable can be directed along the FPU and thermally heat-sunk via copper clamps (designed by Stanford) at each stage.

6.5 Thermal Considerations

A cryostat's thermal load is highly dependent upon the selection of materials and parts present between temperature stages. This is often a balancing act for cabling, as

higher electrical conductivity is preferred to reduce loss, but is normally accompanied by higher thermal conductivity. For non-superconducting material, this is described via the Wiedemann-Franz law (Franz and Wiedemann, 1853),

$$\frac{\kappa}{\sigma} = LT \tag{6.1}$$

where T is temperature and L is the Lorenz number (itself related to Boltzmann's constant and the elementary charge). A material spanning some temperature range T_1 to T_2 will carry a thermal load

$$\Delta Q = \frac{A}{l} \int_{T_1}^{T_2} \kappa(T) dT \tag{6.2}$$

where A is the cross-sectional area and l is the material length between situated temperatures. The standard units of conductivity used here are [W/m/K].

Therefore, cryogenic loading limits must also be taken into account. RF and DC cables within AliCPT make use of multiple material types between stages. For the RF coaxial cables, stainless steel and NbTi are used with two diameter sizes and a Polytetrafluoroethylene (PTFE or Teflon) dielectric insulator. Meanwhile, the DC lines use custom *Tekdata*[4] cabling. These employ a proprietary sequence of shielding and PTFE around individually-shielded twisted pairs of 36-AWG conductors. Manganin was used for all DC cabling between 300K to 4K, while the 4K to 280mK DC cables are made of NbTi and thermally heat-sunk via clamps at the FPU rings of 1K, 350mK, and 280mK.

To approximate the thermal loads expected to be produced from all readout cabling, existing thermal conductivity data and fits are utilized. The predominant source is the public cryogenic materials database from NIST[5] (NIST; Marquardt et al.,

[4]https://www.tekdata-interconnect.com/

[5]https://trc.nist.gov/cryogenics/materials/materialproperties.htm

2002). This database encompasses material properties for a large set of commonly used cryogenic materials.

For stainless steel (304) coaxial cabling, the NIST database fit is employed down to 1K, below which a basic fit of a $T^{1.2}$ relation is used as follows,

$$\kappa_{SS} = \begin{cases} 10^{-1.4087+1.3982(\log_{10}\mathrm{T})+0.2543(\log_{10}\mathrm{T})^2-0.6260(\log_{10}\mathrm{T})^3+0.2334(\log_{10}\mathrm{T})^4+\ldots} \\ \ldots+0.4256(\log_{10}\mathrm{T})^5-0.4658(\log_{10}\mathrm{T})^6+0.1650(\log_{10}\mathrm{T})^7-0.0199(\log_{10}\mathrm{T})^8, & \mathrm{T} \geq 1\mathrm{K} \\ 0.039\ \mathrm{T}^{1.2}, & \mathrm{T} < 1\mathrm{K} \end{cases} \tag{6.3}$$

For PTFE or Teflon dielectric insulator, the NIST database fit is employed down to 4K, below which a $T^{1.88}$ fit is used,

$$\kappa_{PTFE} = \begin{cases} 10^{2.738-30.677(\log_{10}\mathrm{T})+89.430(\log_{10}\mathrm{T})^2-136.99(\log_{10}\mathrm{T})^3+124.69(\log_{10}\mathrm{T})^4+\ldots} \\ \ldots-69.556(\log_{10}\mathrm{T})^5+23.320(\log_{10}\mathrm{T})^6-4.3135(\log_{10}\mathrm{T})^7+0.33829(\log_{10}\mathrm{T})^8, & \mathrm{T} \geq 4\mathrm{K} \\ 3.40\times10^{-3}\ \mathrm{T}^{1.88}, & \mathrm{T} < 4\mathrm{K} \end{cases} \tag{6.4}$$

Unfortunately, NIST does not have any superconducting NbTi data. Instead, results from Olson (1993) are used. As the data is reported only up to 2K, the range between $2 < \mathrm{T} < 4\mathrm{K}$ should be considered over-estimated and diverging for $\mathrm{T} > 4\mathrm{K}$,

$$\kappa_{NbTi} \approx 0.015\mathrm{T}^2, \mathrm{T} \leq 4\mathrm{K} \tag{6.5}$$

AliCPT does not use any NbTi above 4K, so this approximation is deemed sufficient. In comparison with other reported thermal conductivity measurements of NbTi near 4K (Bychkov et al., 1981), this approximation is anywhere between a 60% overestimation or 20% underestimation depending on NbTi concentration. Lower Nb concentrations in Bychkov et al. (1981) were seen to have lower overall conductivities, but with differences between different states of structure as well.

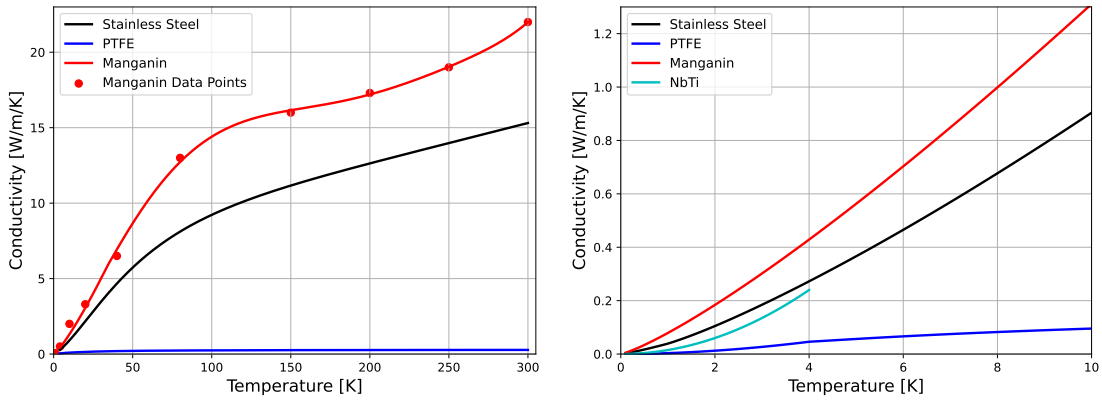

(a) $4-300$K Thermal Conductivity (b) $0.1-10$K Thermal Conductivity

Figure 6.10: Thermal conductivity of materials used for all readout cabling within AliCPT. (a) From $4-300$K, manganin points (*red circles*) shown are for the polynomial fit used. (b) From $0-10$K, including NbTi below 4K (*cyan*).

Manganin is also not included in the NIST cryogenic materials database, so thermal conductivity is determined via a polynomial fit of data points from [6] and [7] for large T, then switched to a fit from Peroni et al. (1999) below when the curves intersect at 34.26K:

$$\kappa_{Mang.} \approx \begin{cases} .0412 + .1251\mathrm{T} + .0025\mathrm{T}^2 - 4.136\times10^{-5}\mathrm{T}^3 + ... \\ +2.380\times10^{-7}\mathrm{T}^4 - 6.120\times10^{-10}\mathrm{T}^5 + 5.977\times10^{-13}\mathrm{T}^6, & \mathrm{T}\geq 34.26\mathrm{K} \\ 0.079\ \mathrm{T}^{1.22}, & \mathrm{T} < 34.26\mathrm{K} \end{cases} \tag{6.6}$$

The thermal conductivities of all these materials are shown in Fig. 6.10 versus temperature.

[6] https://www.lakeshore.com/products/categories/specification/temperature-products/cryogenic-accessories/cryogenic-wire

[7] https://nvlpubs.nist.gov/nistpubs/Legacy/NSRDS/nbsnsrds8.pdf

6.6 Cryogenic Link Budget

A helpful aid in the AliCPT readout design was a cryogenic link budget Python code[8] originally produced by Adrian Sinclair (Sinclair, 2021). The thermal info described above was incorporated into the link budget calculator to help outline all potential thermal and RF considerations of a design. It also now allows one to optimize a coaxial cable's length according to thermal demand via balancing expected attenuation and thermal load. However, the best optimized lengths determined in such a manner were found to be out of the physical limitations required for AliCPT (as described in Section 6.4).

Two potential RF configurations are shown in Figs. 6.11 & 6.12, calculated at the 6 GHz center frequency and with an input power of -40 dBm. In Fig. 6.11, all semi-rigid RF cabling as discussed in Sections 6.3 & 6.4, and attenuator values as listed in Table 6.1 are assumed. The detector module would expect to see a power of roughly -76.4 dBm, with the power out of the cryostat at -38.06 dBm ($\approx$ 2 dBm increase from input).

For an alternative comparison, Fig. 6.12 is identical with exception of the $4-1$K input coax, where stainless steel is replaced by NbTi to help alleviate potential loading concerns on the 1K stage. However the trade-off is additional loading from attenuation on sub-Kelvin stages. This configuration provides an expected power of -71.8 dBm at the detector module, and final cryostat output of -33.46 dBm ($\approx$ 6.5 dBm increase from input). Combined with the four possible attenuators that may be easily changed, this allows for future RF chain customization to ensure the cryostat stays within cooling limits once the focal plane is populated with the maximum 19 detector modules.

[8] https://github.com/ASU-Astronomical-Instrumentation/CryoChainCalc

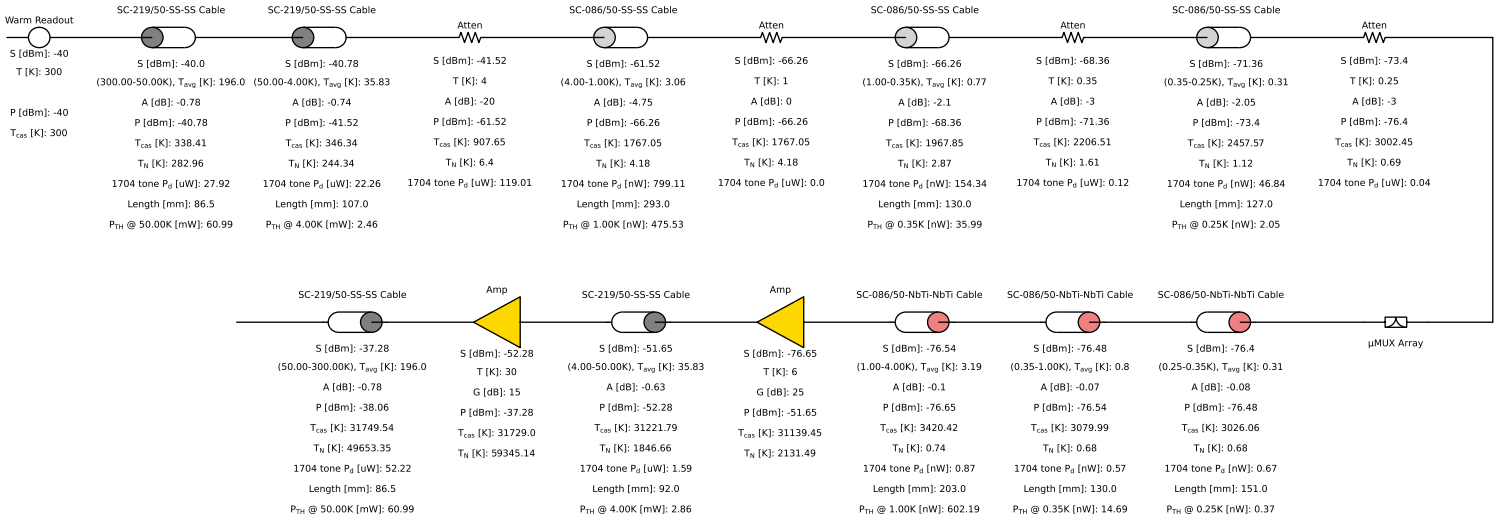

Figure 6.11: AliCPT RF cryogenic chain model for the default RF chain order, at the 6 GHz center frequency. Per component, input power is shown as S, temperature T of the component (or estimate noise temperature for LNAs), attenuation is given as A (or gain G), and output power shown as P. Further values include T_{cas} for cascaded noise temperature in reference to the first chain component, T_N for output noise temperature, P_d for power dissipated due to attenuation, and P_{TH} for cooling power required due to thermal conductivity of cabling (see Section 6.5).

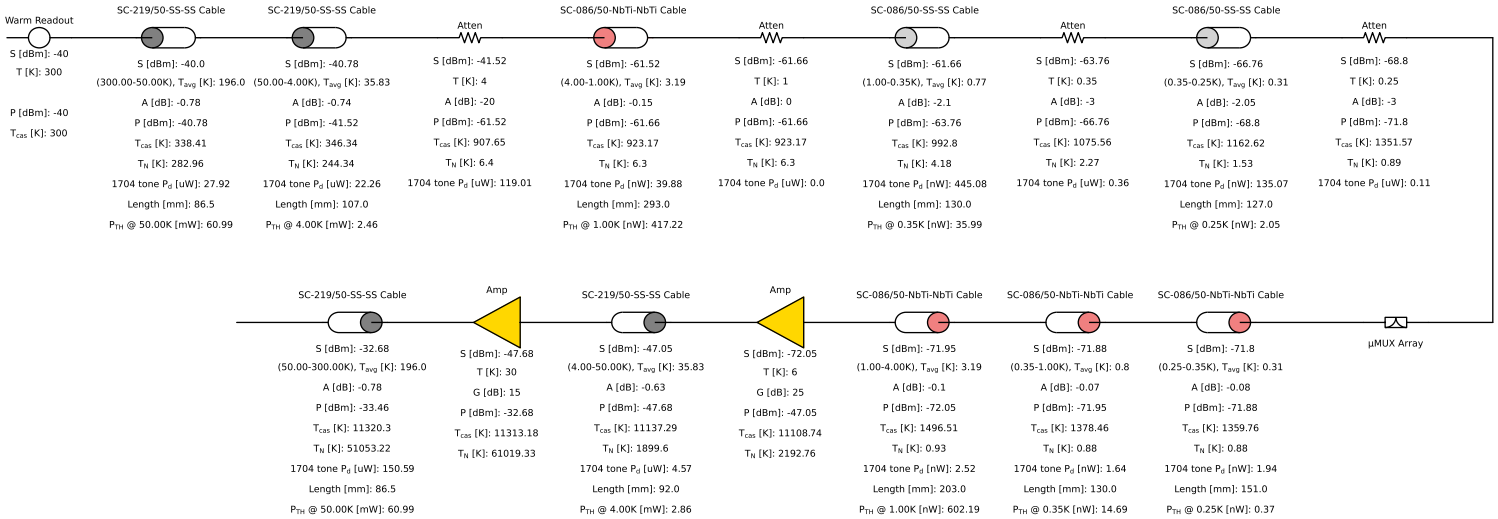

Figure 6.12: AliCPT RF cryogenic chain model with 2.19mm NbTi coax in place of the stainless steel between $4-1$K. This modification could be a beneficial alternative due to reduced cooling demand of the 1K stage, and less overall system loss. However it also results in higher cooling power needed for the sub-Kelvin stages and a higher cabling price. Also calculated at the 6 GHz center frequency.

Chapter 7

CONCLUSION

7.1 Future Millimeter-Wave Endeavors

Technology for millimeter-wave astronomy is at a very prosperous time, driven by ambitious scientific goals. The push for improved detection of the CMB temperature and polarization anisotropies has led to a simultaneously notable advancement in related millimeter-wave astronomical studies.

Galaxy stacking and tSZ analysis, like those discussed in Chapters 2 & 3, will greatly benefit from reduced noise, improved resolution, and larger survey fields of future instruments. The latest thermal energy measurements shown here for $z \approx 1$ quiescent galaxies support AGN feedback models. In addition, detection of dust following the large-scale clustering of matter in the universe also helps highlight the potential in upcoming surveys. These results also emphasize the need for continued improvements to theory and galaxy simulations to correctly identify all observations being documented.

The investigations into new antenna designs, such as the promising hybrid trapezoidal design described in Chapter 4, and prototype MKID-paired test arrays as in Chapter 5, play another important role in identifying continued avenues of detector development. Novel antenna designs lead to further evaluation of current and new architectures. Meanwhile the cryogenic readout development of Chapter 6 in support of AliCPT will allow for better CMB B-mode polarization constraints. Similar telescopes designed for the specific goal of B-mode detection, like BICEP Array, are also key for the next steps in CMB polarimetry.

Competing forms of detector technology in TES bolometers and KIDs play a role as well. Simon's Observatory will utilize large and small aperture telescopes with TES bolometers, followed by its even larger successor in the CMB-S4 project (Abitbol et al., 2017). These will be used for the search of primordial gravitational waves alongside the characterization of polarized dust, neutrino mass constraint, gravitational lensing, mapping of dark matter and more (Abazajian et al., 2016; Hensley et al., 2022). At the same time, technological up-scaling of KIDs is happening. TolTEC has recently become operational, observing at sub-arcminute resolutions. Its future beneficiary, CMB-HD, will act in a further manner with high sensitivity. In this way, both will differ from CMB-S4 and allow finer detailed analysis of gravitational lensing, thermal and kinetic Sunyaev-Zel'dovich effects, inflation models, and much more (The CMB-HD Collaboration et al., 2022).

With these various projects all working in parallel, millimeter-wave astronomy and the detector systems that make it possible will continue to flourish and find new creative paths to success.

Abazajian, K. N., Adshead, P., Ahmed, Z., et al., "CMB-S4 Science Book, First Edition", arXiv e-prints p. arXiv:1610.02743 (2016).

Abbott, T. M. C., Abdalla, F. B., Allam, S., et al., "The Dark Energy Survey: Data Release 1", ApJS **239**, 2, 18 (2018).

Abitbol, M. H., Ahmed, Z., Barron, D., et al., "CMB-S4 Technology Book, First Edition", (2017).

Addison, G. E., Dunkley, J., & Bond, J. R., "Constraining Thermal Dust Emission in Distant Galaxies With Number Counts and Angular Power Spectra", MNRAS **436**, 2, 1896–1917 (2013).

Ade, P. A. R., Aikin, R. W., Amiri, M., et al., "Antenna-Coupled TES Bolometers Used in BICEP2, Keck Array, and SPIDER", ApJ **812**, 2, 176 (2015a).

Ade, P. A. R., Aikin, R. W., Barkats, D., et al., "BICEP2/Keck Array. IV. Optical Characterization and Performance of the BICEP2 and Keck Array Experiments", ApJ **806**, 2, 206 (2015b).

Ade, P. A. R., Aikin, R. W., Barkats, D., et al., "Detection of B-Mode Polarization at Degree Angular Scales by BICEP2", Phys. Rev. Lett. **112**, 241101 (2014).

Ahumada, R., Allende Prieto, C., Almeida, A., et al., "The 16th Data Release of the Sloan Digital Sky Surveys: First Release from the APOGEE-2 Southern Survey and Full Release of eBOSS Spectra", ApJS **249**, 1, 3 (2020).

ALMA Partnership, Fomalont, E. B., Vlahakis, C., et al., "The 2014 ALMA Long Baseline Campaign: An Overview", ApJL **808**, 1, L1 (2015).

Amodeo, S., Battaglia, N., Schaan, E., et al., "Atacama Cosmology Telescope: Modeling the gas thermodynamics in BOSS CMASS galaxies from kinematic and thermal Sunyaev-Zel'dovich measurements", PhRvD **103**, 063514 (2021).

Amvrosiadis, A., Valiante, E., Gonzalez-Nuevo, J., et al., "Herschel-Atlas : The Spatial Clustering of Low- and High-Redshift Submillimetre Galaxies", MNRAS **483**, 4, 4649–4664 (2018).

Anderson, A. J., Ade, P. A. R., Ahmed, Z., et al., "SPT-3G: A Multichroic Receiver for the South Pole Telescope", Journal of Low Temperature Physics **193**, 5-6, 1057–1065 (2018).

Arnold, K., Ade, P. A. R., Anthony, A. E., et al., "The Bolometric Focal Plane Array of the POLARBEAR CMB Experiment", in "Millimeter, Submillimeter, and Far-Infrared Detectors and Instrumentation for Astronomy VI", edited by W. S. Holland, vol. 8452, pp. 381 – 392, International Society for Optics and Photonics (SPIE, 2012).

Austermann, J. E., Beall, J. A., Bryan, S. A., et al., "Millimeter-Wave Polarimeters Using Kinetic Inductance Detectors for TolTEC and Beyond", Journal of Low Temperature Physics **193**, 3, 120–127 (2018).

Balanis, C., *Antenna Theory: Analysis and Design* (John Wiley & Sons, Inc., New Jersey, 2016), 4 edn.

Bardeen, J., Cooper, L. N., & Schrieffer, J. R., "Theory of Superconductivity", Phys. Rev. **108**, 1175–1204 (1957).

Barry, P. S., *On the development of SuperSpec; a Fully Integrated On-chip Spectrometer for Far-infrared Astronomy*, Ph.D. thesis, Cardiff University (2014).

Battaglia, N., Bond, J. R., Pfrommer, C., Sievers, J. L., & Sijacki, D., "Simulations Of The Sunyaev-Zel'dovich Power Spectrum With Active Galactic Nucleus Feedback", ApJ **725**, 1, 91–99 (2010).

Behroozi, P., Wechsler, R. H., Hearin, A. P., & Conroy, C., "UNIVERSEMACHINE: The Correlation Between Galaxy Growth and Dark Matter Halo Assembly From z = 0-10", MNRAS **488**, 3, 3143–3194 (2019).

Behroozi, P. S., Conroy, C., & Wechsler, R. H., "A Comprehensive Analysis of Uncertainties Affecting the Stellar Mass-Halo Mass Relation for 0 <z <4", ApJ **717**, 1, 379–403 (2010).

Bennett, C. L., Bay, M., Halpern, M., et al., "The Microwave Anisotropy Probe Mission", ApJ **583**, 1, 1–23 (2003).

Benson, B. A., Ade, P. A. R., Ahmed, Z., et al., "SPT-3G: A Next-Generation Cosmic Microwave Background Polarization Experiment on the South Pole Telescope", in "Millimeter, Submillimeter, and Far-Infrared Detectors and Instrumentation for Astronomy VII", vol. 9153 of *Proc. SPIE* , p. 91531P (2014).

Berta, S., Lutz, D., Genzel, R., Förster-Schreiber, N. M., & Tacconi, L. J., "Measures of Galaxy Dust and Gas Mass With Herschel Photometry and Prospects for ALMA", A&A **587**, A73 (2016).

BICEP2/Keck Collaboration, Planck Collaboration, Ade, P. A. R., et al., "Joint Analysis of BICEP2/Keck Array and Planck Data", PhRvL **114**, 10, 101301 (2015).

BICEP/Keck Collaboration, :, Ade, P. A. R., et al., "The Latest Constraints on Inflationary B-modes from the BICEP/Keck Telescopes", arXiv e-prints p. arXiv:2203.16556 (2022).

Birkinshaw, M., Gull, S. F., & Hardebeck, H., "The Sunyaev-Zeldovich Effect Towards Three Clusters of Galaxies", Nature **309**, 34–35 (1984).

Blanton, M. R., & Roweis, S., "K-Corrections and Filter Transformations in the Ultraviolet, Optical, and Near-Infrared", AJ **133**, 2, 734–754 (2007).

Blanton, M. R., Schlegel, D. J., Strauss, M. A., et al., "New York University Value-Added Galaxy Catalog: A Galaxy Catalog Based on New Public Surveys", ApJ **129**, 6, 2562–2578 (2005).

Bleem, L. E., Stalder, B., de Haan, T., et al., "Galaxy Clusters Discovered via the Sunyaev-Zel'dovich Effect in the 2500-Square-Degree SPT-SZ Survey", ApJS **216**, 27 (2015).

Bocquet, S., Dietrich, J. P., Schrabback, T., et al., "Cluster Cosmology Constraints from the 2500 deg^2 SPT-SZ Survey: Inclusion of Weak Gravitational Lensing Data from Magellan and the Hubble Space Telescope", ApJ **878**, 1, 55 (2019).

Borthakur, S., Heckman, T., Tumlinson, J., et al., "Connection between the Circumgalactic Medium and the Interstellar Medium of Galaxies: Results from the COS-GASS Survey", ApJ **813**, 1, 46 (2015).

Bower, R. G., Benson, A. J., Malbon, R., et al., "Breaking the Hierarchy of Galaxy Formation", MNRAS **370**, 645–655 (2006).

Brammer, G. B., van Dokkum, P. G., & Coppi, P., "EAZY: A Fast, Public Photometric Redshift Code", ApJ **686**, 2, 1503–1513 (2008).

Bregman, J. N., Hodges-Kluck, E., Qu, Z., et al., "Hot Extended Galaxy Halos around Local L* Galaxies from Sunyaev-Zeldovich Measurements", ApJ **928**, 1, 14 (2022).

Brownson, S., Maiolino, R., Tazzari, M., Carniani, S., & Henden, N., "Detecting the Halo Heating From AGN Feedback with ALMA", MNRAS **490**, 4, 5134–5146 (2019).

Bruzual, G., & Charlot, S., "Stellar Population Synthesis at the Resolution of 2003", MNRAS **344**, 4, 1000–1028 (2003).

Bryan, S., Austermann, J., Ferrusca, D., et al., "Optical Design of the TolTEC Millimeter-Wave Camera", in "Millimeter, Submillimeter, and Far-Infrared Detectors and Instrumentation for Astronomy IX", vol. 10708 of *Proc. SPIE* , p. 107080J (2018).

Bychkov, Y., Herzog, R., & Khukhareva, I., "Thermal Conductivity and Electrical Resistivity of Nbti Alloys at Low Temperatures", Cryogenics **21**, 12, 741–745 (1981).

Calafut, V., Gallardo, P. A., Vavagiakis, E. M., et al., "The Atacama Cosmology Telescope: Detection of the Pairwise Kinematic Sunyaev-Zel'dovich Effect With SDSS DR15 Galaxies", PhRvD **104**, 4, 043502 (2021).

Calura, F., Pozzi, F., Cresci, G., et al., "The Dust-to-Stellar Mass Ratio as a Valuable Tool to Probe the Evolution of Local and Distant Star-Forming Galaxies", MNRAS **465**, 1, 54–67 (2016).

Carlstrom, J. E., Ade, P. A. R., Aird, K. A., et al., "The 10 Meter South Pole Telescope", Publications of the Astronomical Society of the Pacific **123**, 903, 568–581 (2011).

Carlstrom, J. E., Holder, G. P., & Reese, E. D., "Cosmology with the Sunyaev-Zel'dovich Effect", ARA&A **40**, 643–680 (2002).

Casey, C. M., "Far-Infrared Spectral Energy Distribution Fitting for Galaxies Near and Far", MNRAS **425**, 4, 3094–3103 (2012).

Ceverino, D., & Klypin, A., "The Role of Stellar Feedback in the Formation of Galaxies", ApJ **695**, 1, 292 (2009).

Chamberlain, C., Arav, N., & Benn, C., "Strong Candidate for AGN Feedback: VLT/X-Shooter Observations of BALQSO SDSS J0831+0354", MNRAS **450**, 1085–1093 (2015).

Chartas, G., Brandt, W. N., Gallagher, S. C., & Proga, D., "XMM-Newton and Chandra Spectroscopy of the Variable High-Energy Absorption of PG 1115+080: Refined Outflow Constraints", AJ **133**, 1849–1860 (2007).

Chatterjee, S., Ho, S., Newman, J. A., & Kosowsky, A., "Tentative Detection of Quasar Feedback from WMAP and SDSS Cross-correlation", ApJ **720**, 299–305 (2010).

Cheng, E. S., Saulson, P. R., Wilkinson, D. T., & Corey, B. E., "Large-Scale Anisotropy in the 2.7K Radiation.", ApJL **232**, L139–L143 (1979).

Choe, H., & Lim, S., "Directivity and Diversity Dual-Mode Stacked Antenna Array Using Directors of Yagi–Uda Antenna as Monopole Antennas", IEEE Antennas and Wireless Propagation Letters **13**, 575–578 (2014).

Choi, S. K., Austermann, J., Beall, J. A., et al., "Characterization of the Mid-Frequency Arrays for Advanced ACTPol", Journal of Low Temperature Physics **193**, 3-4, 267–275 (2018).

Chown, R., Omori, Y., Aylor, K., et al., "Maps of the Southern Millimeter-wave Sky from Combined 2500 deg 2 SPT-SZ and Planck Temperature Data", ApJS **239**, 1, 10 (2018).

Churazov, E., Brüggen, M., Kaiser, C. R., Böhringer, H., & Forman, W., "Evolution of Buoyant Bubbles in M87", ApJ **554**, 261–273 (2001).

Coil, A. L., Mendez, A. J., Eisenstein, D. J., & Moustakas, J., "PRIMUS+DEEP2: The Dependence of Galaxy Clustering on Stellar Mass and Specific Star Formation Rate at $0.2 < z < 1.2$", ApJ **838**, 2, 87 (2017).

Coleman, G. D., Wu, C. C., & Weedman, D. W., "Colors and Magnitudes Predicted for High Redshift Galaxies", ApJS **43**, 393–416 (1980).

Condon, J. J., & Matthews, A. M., "Λ CDM Cosmology for Astronomers", Publications of the Astronomical Society of the Pacific **130**, 989, 073001 (2018).

Conklin, E. K., "Velocity of the Earth with Respect to the Cosmic Background Radiation", Nature **222**, 5197, 971–972 (1969).

Corey, B. E., & Wilkinson, D. T., "A Measurement of the Cosmic Microwave Background Anisotropy at 19 GHz", in "Bulletin of the American Astronomical Society", vol. 8, p. 351 (1976).

Costa, T., Sijacki, D., & Haehnelt, M. G., "Feedback From Active Galactic Nuclei: Energy- versus Momentum-driving", MNRAS **444**, 2355–2376 (2014).

Cowie, L. L., Songaila, A., Hu, E. M., & Cohen, J. G., "New Insight on Galaxy Formation and Evolution From Keck Spectroscopy of the Hawaii Deep Fields", AJ **112**, 839 (1996).

Crichton, D., Gralla, M. B., Hall, K., et al., "Evidence for the thermal Sunyaev-Zel'dovich effect associated with quasar feedback", MNRAS **458**, 1478–1492 (2016).

Crill, B. P., Ade, P. A. R., Artusa, D. R., et al., "BOOMERANG: A Balloon-borne Millimeter-Wave Telescope and Total Power Receiver for Mapping Anisotropy in the Cosmic Microwave Background", ApJS **148**, 2, 527–541 (2003).

Croton, D. J., Springel, V., White, S. D. M., et al., "The Many Lives of Active Galactic Nuclei: Cooling Flows, Black Holes and the Luminosities and Colours of Galaxies", MNRAS **365**, 11–28 (2006).

CSO, http://www.submm.caltech.edu/cso/weather/ (2007).

Cunha, C. E., Lima, M., Oyaizu, H., Frieman, J., & Lin, H., "Estimating the Redshift Distribution of Photometric Galaxy Samples – II. Applications and Tests of a New Method", MNRAS **396**, 4, 2379–2398 (2009).

Dahal, S., Appel, J. W., Datta, R., et al., "Four-year Cosmology Large Angular Scale Surveyor (CLASS) Observations: On-sky Receiver Performance at 40, 90, 150, and 220 GHz Frequency Bands", ApJ **926**, 1, 33 (2022).

Das, S., Sherwin, B. D., Aguirre, P., et al., "Detection of the Power Spectrum of Cosmic Microwave Background Lensing by the Atacama Cosmology Telescope", Phys. Rev. Lett. **107**, 021301 (2011).

Datta, R., Austermann, J., Beall, J. A., et al., "Design and Deployment of a Multichroic Polarimeter Array on the Atacama Cosmology Telescope", Journal of Low Temperature Physics **184**, 3, 568–575 (2016).

Day, P. K., LeDuc, H. G., Mazin, B. A., Vayonakis, A., & Zmuidzinas, J., "A Broadband Superconducting Detector Suitable for Use in Large Arrays", Nature **425**, 6960, 817–821 (2003).

de Bernardis, P., Ade, P. A. R., Bock, J. J., et al., "A flat Universe From High-Resolution Maps of the Cosmic Microwave Background Radiation", Nature **404**, 6781, 955–959 (2000).

de Kool, M., Arav, N., Becker, R. H., et al., "Keck HIRES Observations of the QSO FIRST J104459.6+365605: Evidence for a Large-Scale Outflow", ApJ **548**, 609–623 (2001).

Deschamps, G., "Impedance Properties of Complementary Multiterminal Planar Structures", IRE Transactions on Antennas and Propagation **7**, 5, 371–378 (1959).

Dicker, S. R., Ade, P. A. R., Aguirre, J., et al., "MUSTANG 2: A Large Focal Plane Array for the 100 m Green Bank Telescope", Journal of Low Temperature Physics **176**, 5, 808–814 (2014).

Dober, B., Becker, D. T., Bennett, D. A., et al., "Microwave Squid Multiplexer Demonstration for Cosmic Microwave Background Imagers", Applied Physics Letters **111**, 24, 243510 (2017).

Donevski, D., Lapi, A., Małek, K., et al., "In Pursuit of Giants. I. The Evolution of the Dust-to-Stellar Mass Ratio in Distant Dusty Galaxies", A&A **644**, A144 (2020).

Doyle, S., *Lumped Element Kinetic Inductance Detectors*, Ph.D. thesis, Cardiff University (2008).

Draine, B. T., "Interstellar Dust Grains", ARA&A **41**, 241–289 (2003).

Draine, B. T., *Physics of the Interstellar and Intergalactic Medium* (Princeton, NJ: Princeton Univ. Press, 2011).

Draine, B. T., & Lazarian, A., "Diffuse Galactic Emission from Spinning Dust Grains", ApJ **494**, 1, L19–L22 (1998).

Drory, N., & Alvarez, M., "The Contribution of Star Formation and Merging to Stellar Mass Buildup in Galaxies", ApJ **680**, 41–53 (2008).

Dunn, J. P., Bautista, M., Arav, N., et al., "The Quasar Outflow Contribution to AGN Feedback: VLT Measurements of SDSS J0318-0600", ApJ **709**, 611–631 (2010).

Dunne, L., Eales, S., Ivison, R., Morgan, H., & Edmunds, M., "Type II Supernovae as a Significant Source of Interstellar Dust", Nature **424**, 6946, 285–287 (2003).

Dunne, L., & Eales, S. A., "The SCUBA Local Universe Galaxy Survey - II. 450-μm Data: Evidence for Cold Dust in Bright IRAS Galaxies", MNRAS **327**, 3, 697–714 (2001).

Edwards, J. M., O'Brient, R., Lee, A. T., & Rebeiz, G. M., "Dual-Polarized Sinuous Antennas on Extended Hemispherical Silicon Lenses", IEEE Transactions on Antennas and Propagation **60**, 9, 4082–4091 (2012).

Eftekharzadeh, S., Myers, A. D., White, M., et al., "Clustering of Intermediate Redshift Quasars Using the Final SDSS III-BOSS Sample", MNRAS **453**, 3, 2779–2798 (2015).

Fabian, A. C., "Observational Evidence of Active Galactic Nuclei Feedback", ARA&A **50**, 455–489 (2012).

Ferrarese, L., "Beyond the Bulge: A Fundamental Relation between Supermassive Black Holes and Dark Matter Halos", ApJ **578**, 90–97 (2002).

Feruglio, C., Maiolino, R., Piconcelli, E., et al., "Quasar Feedback Revealed by Giant Molecular Outflows", A&A **518**, L155 (2010).

Filipovic, D., Gearhart, S., & Rebeiz, G., "Double-Slot Antennas on Extended Hemispherical and Elliptical Silicon Dielectric Lenses", IEEE Transactions on Microwave Theory and Techniques **41**, 10, 1738–1749 (1993).

Fixsen, D. J., "The Temperature of the Cosmic Microwave Background", ApJ **707**, 2, 916–920 (2009).

Flanigan, D., *Kinetic Inductance Detectors for Measuring the Polarization of the Cosmic Microwave Background*, Ph.D. thesis, Columbia University (2018).

Franz, R., & Wiedemann, G., "Ueber die Wärme-Leitungsfähigkeit der Metalle", Annalen der Physik **165**, 8, 497–531 (1853).

Gao, J., *The Physics of Superconducting Microwave Resonators*, Ph.D. thesis, California Institute of Technology (2008).

Glover, R. E., & Tinkham, M., "Conductivity of Superconducting Films for Photon Energies between 0.3 and 40kTc", Physical Review **108**, 2, 243–256 (1957).

Gobat, R., Daddi, E., Magdis, G., et al., "The Unexpectedly Large Dust and Gas Content of Quiescent Galaxies at z >1.4", NatAs **2**, 3, 239–246 (2018).

Gordon, S., *Highly Multiplexed Superconducting Detectors and Readout Electronics for Balloon-Borne and Ground-Based Far-Infrared Imaging and Polarimetry*, Ph.D. thesis, Arizona State University (2019).

Gralla, M. B., Crichton, D., Marriage, T. A., et al., "A Measurement of the Millimetre Emission and the Sunyaev-Zel'dovich Effect Associated With Low-Frequency Radio Sources", MNRAS **445**, 460–478 (2014).

Granato, G. L., De Zotti, G., Silva, L., Bressan, A., & Danese, L., "A Physical Model for the Coevolution of QSOs and Their Spheroidal Hosts", ApJ **600**, 580–594 (2004).

Greco, J. P., Hill, J. C., Spergel, D. N., & Battaglia, N., "The Stacked Thermal Sunyaev–Zel'dovich Signal of Locally Brightest Galaxies in Planck Full Mission Data: Evidence for Galaxy Feedback?", ApJ **808**, 151 (2015).

Greene, J. E., Pooley, D., Zakamska, N. L., Comerford, J. M., & Sun, A.-L., "Extended X-Ray Emission from a Quasar-driven Superbubble", ApJ **788**, 54 (2014).

Hall, K. R., Zakamska, N. L., Addison, G. E., et al., "Quantifying the Thermal Sunyaev-Zel'dovich Effect and Excess Millimetre Emission in Quasar Environments", MNRAS **490**, 2, 2315–2335 (2019).

Hanany, S., Ade, P., Balbi, A., et al., "MAXIMA-1: A Measurement of the Cosmic Microwave Background Anisotropy on Angular Scales of 10[arcmin]–5°", ApJ **545**, 1, L5–L9 (2000).

Hand, N., Addison, G. E., Aubourg, E., et al., "Evidence of Galaxy Cluster Motions with the Kinematic Sunyaev-Zel'dovich Effect", PhRvL **109**, 4, 041101 (2012).

Hand, N., Appel, J. W., Battaglia, N., et al., "The Atacama Cosmology Telescope: Detection of Sunyaev-Zel'Dovich Decrement in Groups and Clusters Associated with Luminous Red Galaxies", ApJ **736**, 39 (2011).

Hanson, D., Hoover, S., Crites, A., et al., "Detection of B-Mode Polarization in the Cosmic Microwave Background with Data from the South Pole Telescope", PhRvL **111**, 14, 141301 (2013).

Harrison, C. M., Alexander, D. M., Mullaney, J. R., & Swinbank, A. M., "Kiloparsec-Scale Outflows Are Prevalent Among Luminous AGN: Outflows and Feedback in the Context of the Overall AGN Population", MNRAS **441**, 3306–3347 (2014).

Henry, P. S., "Isotropy of the 3 K Background", Nature **231**, 5304, 516–518 (1971).

Hensley, B. S., Clark, S. E., Fanfani, V., et al., "The Simons Observatory: Galactic Science Goals and Forecasts", ApJ **929**, 2, 166 (2022).

Hill, J. C., Baxter, E. J., Lidz, A., Greco, J. P., & Jain, B., "Two-Halo Term in Stacked Thermal Sunyaev-Zel'dovich Measurements: Implications for Self-Similarity", PhRvD **97**, 083501 (2018).

Hilton, M., Hasselfield, M., Sifón, C., et al., "The Atacama Cosmology Telescope: The Two-season ACTPol Sunyaev-Zel'dovich Effect Selected Cluster Catalog", ApJS **235**, 1, 20 (2018).

Hojjati, A., Tröster, T., Harnois-Déraps, J., et al., "Cross-Correlating Planck tSZ With RCSLenS Weak Lensing: Implications for Cosmology and AGN Feedback", MNRAS **471**, 2, 1565–1580 (2017).

Holland, W. S., Bintley, D., Chapin, E. L., et al., "SCUBA-2: The 10 000 Pixel Bolometer Camera on the James Clerk Maxwell Telescope", MNRAS **430**, 4, 2513–2533 (2013).

Hotinli, S. C., Holder, G. P., Johnson, M. C., & Kamionkowski, M., "Cosmology From the Kinetic Polarized Sunyaev Zel'dovich Effect", JCAP **2022**, 10, 026 (2022).

Hu, W., & Dodelson, S., "Cosmic Microwave Background Anisotropies", Annual Review of Astronomy and Astrophysics **40**, 1, 171–216 (2002).

Hu, W., & White, M., "A CMB Polarization Primer", New Astronomy **2**, 4, 323–344 (1997).

Hubmayr, J., Austermann, J. E., Beall, J. A., et al., "Design of 280 GHz Feedhorn-Coupled TES Arrays for the Balloon-Borne Polarimeter SPIDER", in "Millimeter, Submillimeter, and Far-Infrared Detectors and Instrumentation for Astronomy VIII", edited by W. S. Holland and J. Zmuidzinas, vol. 9914, pp. 185 – 198, International Society for Optics and Photonics (SPIE, 2016).

Hubmayr, J., Austermann, J. E., Beall, J. A., et al., "Low-Temperature Detectors for CMB Imaging Arrays", Journal of Low Temperature Physics **193**, 3-4, 633–647 (2018).

International Telecommunication Union, "International Telecommunication Union Radio Regulations, Edition 2020", http://handle.itu.int/11.1002/pub/814b0c44-en (2020).

Irwin, K., & Hilton, G., *Transition-Edge Sensors*, pp. 63–150 (Springer Berlin Heidelberg, Berlin, Heidelberg, 2005).

Irwin, K. D., "An Application of Electrothermal Feedback for High Resolution Cryogenic Particle Detection", Applied Physics Letters **66**, 15, 1998–2000 (1995).

Ishihara, D., Onaka, T., Kataza, H., et al., "The AKARI/IRC mid-infrared all-sky survey*", A&A **514**, A1 (2010).

Jarosik, N., Bennett, C. L., Dunkley, J., et al., "Seven-Year Wilkinson Microwave Anisotropy Probe (WMAP) Observations: Sky Maps, Systematic Errors, and Basic Results", ApJS **192**, 2, 14 (2011).

Johnson, B. R., Flanigan, D., Abitbol, M. H., et al., "Development of Multi-chroic MKIDs for Next-Generation CMB Polarization Studies", Journal of Low Temperature Physics **193**, 3, 103–112 (2018).

Joint IRAS Science, W. G., "VizieR Online Data Catalog: IRAS catalogue of Point Sources, Version 2.0 (IPAC 1986)", yCat **2**, 125 (1994).

Kamionkowski, M., Kosowsky, A., & Stebbins, A., "Statistics of Cosmic Microwave Background Polarization", Phys. Rev. D **55**, 7368–7388 (1997).

Kaneko, D., Adachi, S., Ade, P. A. R., et al., "Deployment of Polarbear-2A", Journal of Low Temperature Physics **199**, 3, 1137–1147 (2020).

Keating, B. G., Ade, P. A. R., Bock, J. J., et al., "BICEP: a large angular-scale CMB polarimeter", in "Polarimetry in Astronomy", edited by S. Fineschi, vol. 4843, pp. 284 – 295, International Society for Optics and Photonics (SPIE, 2003).

Khalil, M. S., Stoutimore, M. J. A., Wellstood, F. C., & Osborn, K. D., "An Analysis Method for Asymmetric Resonator Transmission Applied to Superconducting Devices", Journal of Applied Physics **111**, 5, 054510 (2012).

King, I., "The Structure of Star Clusters. I. An Empirical Density Law", AJ **67**, 471 (1962).

Kinney, A. L., Calzetti, D., Bohlin, R. C., et al., "Template Ultraviolet to Near-Infrared Spectra of Star-forming Galaxies and Their Application to K-Corrections", ApJ **467**, 38 (1996).

Klemp, O., Damnoen, P., & Eul, H., "Miniaturized Antenna-Arrays for Combined Wideband Polarization- and Space Diversity", in "2006 IEEE Antennas and Propagation Society International Symposium", pp. 161–164 (2006).

Klemp, O., Schultz, M., & Eul, H., "Novel Logarithmically Periodic Planar Antennas for Broadband Polarization Diversity Reception", AEU - International Journal of Electronics and Communications **59**, 5, 268–277 (2005).

Koopman, B. J., Cothard, N. F., Choi, S. K., et al., "Advanced ACTPol Low-Frequency Array: Readout and Characterization of Prototype 27 and 39 GHz Transition Edge Sensors", Journal of Low Temperature Physics **193**, 5-6, 1103–1111 (2018).

Kosowsky, A., "Cosmic Microwave Background Polarization", Annals of Physics **246**, 1, 49–85 (1996).

Kovac, J. M., Leitch, E. M., Pryke, C., et al., "Detection of Polarization in the Cosmic Microwave Background Using DASI", Nature **420**, 6917, 772–787 (2002).

Kramer, O., Djerafi, T., & Wu, K., "Vertically Multilayer-Stacked Yagi Antenna With Single and Dual Polarizations", IEEE Transactions on Antennas and Propagation **58**, 4, 1022–1030 (2010).

Kravtsov, A. V., Vikhlinin, A. A., & Meshcheryakov, A. V., "Stellar Mass—Halo Mass Relation and Star Formation Efficiency in High-Mass Halos", Astronomy Letters **44**, 1, 8–34 (2018).

Lacy, M., Mason, B., Sarazin, C., et al., "Direct Detection of Quasar Feedback via the Sunyaev-Zeldovich Effect", MNRAS **483**, L22–L27 (2019).

Lansbury, G. B., Jarvis, M. E., Harrison, C. M., et al., "Storm in a Teacup: X-Ray View of an Obscured Quasar and Superbubble", ApJL **856**, L1 (2018).

Levi, M., Allen, L. E., Raichoor, A., et al., "The Dark Energy Spectroscopic Instrument (DESI)", in "Bulletin of the American Astronomical Society", vol. 51, p. 57 (2019).

Lewis, A., & Challinor, A., "Weak Gravitational Lensing of the CMB", Physics Reports **429**, 1, 1–65 (2006).

Lewis, A., & Challinor, A., "CAMB: Code for Anisotropies in the Microwave Background", (2011).

Li, A., & Draine, B. T., "Infrared Emission from Interstellar Dust. II. The Diffuse Interstellar Medium", ApJ **554**, 2, 778–802 (2001).

Li, H., Li, S.-Y., Liu, Y., et al., "Probing primordial gravitational waves: Ali CMB Polarization Telescope", National Science Review **6**, 1, 145–154 (2018).

Lokken, M., Hložek, R., Engelen, A. v., et al., "Superclustering with the Atacama Cosmology Telescope and Dark Energy Survey. I. Evidence for Thermal Energy Anisotropy Using Oriented Stacking", ApJ **933**, 2, 134 (2022).

Lu, Z., Mo, H. J., Lu, Y., et al., "Star Formation and Stellar Mass Assembly in Dark Matter Haloes: From Giants to Dwarfs", MNRAS **450**, 2, 1604–1617 (2015).

Ludwig, A., "The Definition of Cross Polarization", IEEE Transactions on Antennas and Propagation **21**, 1, 116–119 (1973).

Luhn, S., & Hentschel, M., "Analytical Fresnel Laws for Curved Dielectric Interfaces", Journal of Optics **22**, 1, 015605 (2019).

Magdis, G. E., Gobat, R., Valentino, F., et al., "The Interstellar Medium of Quiescent Galaxies and Its Evolution With Time", A&A **647**, A33 (2021).

Mainzer, A., Bauer, J., Grav, T., et al., "Preliminary Results from NEOWISE: An Enhancement to the Wide-field Infrared Survey Explorer for Solar System Science", ApJ **731**, 1, 53 (2011).

Mallaby-Kay, M., Atkins, Z., Aiola, S., et al., "The Atacama Cosmology Telescope: Summary of DR4 and DR5 Data Products and Data Access", ApJS **255**, 1, 11 (2021).

Maoz, D., *Astrophysics in a Nutshell* (Princeton University Press, 2016).

Marconi, A., & Hunt, L. K., "The Relation between Black Hole Mass, Bulge Mass, and Near-Infrared Luminosity", ApJL **589**, L21–L24 (2003).

Marquardt, E. D., Le, J. P., & Radebaugh, R., *Cryogenic Material Properties Database*, pp. 681–687 (Springer US, Boston, MA, 2002).

Masi, S., Ade, P. A. R., Artusa, R., et al., "BOOMERanG: a scanning telescope for 10 arcminutes resolution CMB maps", AIP Conference Proceedings **476**, 1, 237–248 (1999).

Mates, J. A. B., *The Microwave SQUID Multiplexer*, Ph.D. thesis, University of Colorado Boulder (2011).

Mather, J. C., Cheng, E. S., Eplee, R. E., J., et al., "A Preliminary Measurement of the Cosmic Microwave Background Spectrum by the Cosmic Background Explorer (COBE) Satellite", ApJL **354**, L37 (1990).

Mattis, D. C., & Bardeen, J., "Theory of the Anomalous Skin Effect in Normal and Superconducting Metals", Physical Review **111**, 2, 412–417 (1958).

Mauskopf, P. D., "Transition Edge Sensors and Kinetic Inductance Detectors in Astronomical Instruments", Publications of the Astronomical Society of the Pacific **130**, 990, 082001 (2018).

Mauskopf, P. D., Ade, P. A. R., Allen, S. W., et al., "A Determination of the Hubble Constant Using Measurements of X-Ray Emission and the Sunyaev-Zeldovich Effect at Millimeter Wavelengths in the Cluster Abell 1835", ApJ **538**, 2, 505–516 (2000).

Mauskopf, P. D., Bock, J. J., Castillo, H. D., Holzapfel, W. L., & Lange, A. E., "Composite infrared bolometers with Si3N4 micromesh absorbers", Appl. Opt. **36**, 4, 765–771 (1997).

McCarrick, H., *Design and Performance of Kinetic Inductance Detectors for Cosmic Microwave Background Polarimetry*, Ph.D. thesis, Columbia University (2018).

McCarrick, H., Jones, G., Johnson, B. R., et al., "Design and Performance of Dual-Polarization Lumped-Element Kinetic Inductance Detectors for Millimeter-Wave Polarimetry", A&A **610**, A45 (2018).

McNamara, B. R., Russell, H. R., Nulsen, P. E. J., et al., "A Mechanism for Stimulating AGN Feedback by Lifting Gas in Massive Galaxies", ApJ **830**, 79 (2016).

McNamara, B. R., Wise, M., Nulsen, P. E. J., et al., "Chandra X-Ray Observations of the Hydra A Cluster: An Interaction between the Radio Source and the X-Ray-emitting Gas", ApJL **534**, L135–L138 (2000).

Meier Valdés, E. A., Morris, B. M., & Demory, B.-O., "Monitoring Precipitable Water Vapour in Near Real-Time to Correct Near-Infrared Observations Using Satellite Remote Sensing", A&A **649**, A132 (2021).

Meinke, J., Böckmann, K., Cohen, S., et al., "The Thermal Sunyaev–Zel'dovich Effect from Massive, Quiescent $0.5 \leq z \leq 1.5$ Galaxies", ApJ **913**, 2, 88 (2021).

Meinke, J., Mauskopf, P., Johnson, B. R., et al., "Planar Self-similar Antennas for Broadband Millimeter-Wave Measurements", Journal of Low Temperature Physics **199**, 1, 281–288 (2020).

Miller, T. R., Arav, N., Xu, X., & Kriss, G. A., "The Contribution of Quasar Absorption Outflows to AGN Feedback", MNRAS **499**, 1, 1522–1529 (2020).

Mo, H. J., & White, S. D. M., "An Analytic Model for the Spatial Clustering of Dark Matter Haloes", MNRAS **282**, 2, 347–361 (1996).

Moncelsi, L., Ade, P. A. R., Ahmed, Z., et al., "Receiver Development for BICEP Array, a Next-Generation CMB Polarimeter at the South Pole", in "Millimeter, Submillimeter, and Far-Infrared Detectors and Instrumentation for Astronomy X", edited by J. Zmuidzinas and J.-R. Gao, vol. 11453 of *Society of Photo-Optical Instrumentation Engineers (SPIE) Conference Series*, p. 1145314 (2020).

Moster, B. P., Naab, T., & White, S. D. M., "Galactic Star Formation and Accretion Histories From Matching Galaxies to Dark Matter Haloes", MNRAS **428**, 4, 3121–3138 (2013).

Moster, B. P., Naab, T., & White, S. D. M., "EMERGE - An Empirical Model for the Formation of Galaxies Since z $\sim$ 10", MNRAS **477**, 2, 1822–1852 (2018).

Mroczkowski, T., Dicker, S., Sayers, J., et al., "A Multi-wavelength Study of the Sunyaev-Zel'dovich Effect in the Triple-merger Cluster MACS J0717.5+3745 with MUSTANG and Bolocam", ApJ **761**, 1, 47 (2012).

Mroczkowski, T., Nagai, D., Basu, K., et al., "Astrophysics with the Spatially and Spectrally Resolved Sunyaev-Zeldovich Effects. A Millimetre/Submillimetre Probe of the Warm and Hot Universe", SSRv **215**, 17 (2019).

Muzzin, A., Marchesini, D., Stefanon, M., et al., "The Evolution of the Stellar Mass Functions of Star-forming and Quiescent Galaxies to z = 4 from the COSMOS/UltraVISTA Survey", ApJ **777**, 1, 18 (2013).

Nadolski, A., Kofman, A. M., Vieira, J. D., et al., "Broadband Anti-Reflective Coatings for Cosmic Microwave Background Experiments", in "Millimeter, Submillimeter, and Far-Infrared Detectors and Instrumentation for Astronomy IX", edited by J. Zmuidzinas and J.-R. Gao, vol. 10708, pp. 719 – 731, International Society for Optics and Photonics (SPIE, 2018).

Nadolski, A. W., *Broadband, Millimeter-Wave Antireflection Coatings for Cryogenic Sintered Aluminum Oxide Optics*, Ph.D. thesis, University of Illinois at Urbana-Champaign (2020).

Naess, S., Aiola, S., Austermann, J. E., et al., "The Atacama Cosmology Telescope: Arcminute-Resolution Maps of 18 000 Square Degrees of the Microwave Sky From ACT 2008–2018 Data Combined with Planck", JCAP **2020**, 12, 046–046 (2020).

Oke, J. B., & Gunn, J. E., "Secondary Standard Stars for Absolute Spectrophotometry", ApJ **266**, 713–717 (1983).

Olson, J., "Thermal Conductivity of Some Common Cryostat Materials Between 0.05 and 2 K", Cryogenics **33**, 7, 729–731 (1993).

Otarola, A., Breuck, C. D., Travouillon, T., et al., "Precipitable Water Vapor, Temperature, and Wind Statistics At Sites Suitable for mm and Submm Wavelength Astronomy in Northern Chile", Publications of the Astronomical Society of the Pacific **131**, 998, 045001 (2019).

O'Brient, R. C., *A Log-Periodic Focal-Plane Architecture for Cosmic Microwave Background Polarimetry*, Ph.D. thesis, University of California, Berkeley (2010).

Page, L., Jackson, C., Barnes, C., et al., "The Optical Design and Characterization of the Microwave Anisotropy Probe", ApJ **585**, 1, 566–586 (2003).

Pandey, S., Baxter, E. J., Xu, Z., et al., "Constraints on the Redshift Evolution of Astrophysical Feedback With Sunyaev-Zel'dovich Effect Cross-Correlations", PhRvD **100**, 6, 063519 (2019).

Pardo, J., Cernicharo, J., & Serabyn, E., "Atmospheric Transmission at Microwaves (ATM): An Improved Model for Millimeter/submillimeter Applications", IEEE Transactions on Antennas and Propagation **49**, 12, 1683–1694 (2001).

Pascale, E., Ade, P. A. R., Bock, J. J., et al., "The Balloon-borne Large Aperture Submillimeter Telescope: BLAST", ApJ **681**, 1, 400–414 (2008).

Pathria, R. K., & Beale, P. D., *Statistical Mechanics* (Elsevier Ltd., Amsterdam, 2011), 3 edn.

Penzias, A. A., & Wilson, R. W., "A Measurement of Excess Antenna Temperature at 4080 Mc/s", ApJ **142**, 419–421 (1965).

Peroni, I., Gottardi, E., Peruzzi, A., Ponti, G., & Ventura, G., "Thermal Conductivity of Manganin Below 1 K", Nuclear Physics B - Proceedings Supplements **78**, 1, 573–575 (1999).

Piffaretti, R., Arnaud, M., Pratt, G. W., Pointecouteau, E., & Melin, J. B., "The MCXC: A Meta-Catalogue of X-Ray Detected Clusters of Galaxies", A&A **534**, A109 (2011).

Pillepich, A., Nelson, D., Hernquist, L., et al., "First Results from the IllustrisTNG simulations: The Stellar Mass Content of Groups and Clusters of Galaxies", MNRAS **475**, 1, 648–675 (2018).

Planck Collaboration, Ade, P. A. R., Aghanim, N., et al., "Planck Intermediate Results. XI. The Gas Content of Dark Matter Halos: The Sunyaev-Zeldovich-Stellar Mass Relation for Locally Brightest Galaxies", A&A **557**, A52 (2013).

Planck Collaboration, Ade, P. A. R., Aghanim, N., et al., "Planck Early Results. VIII. The All-Sky Early Sunyaev-Zeldovich Cluster Sample", A&A **536**, A8 (2011).

Planck Collaboration, Ade, P. A. R., Aghanim, N., et al., "Planck 2015 Results. XXIV. Cosmology From Sunyaev-Zeldovich Cluster Counts", A&A **594**, A24 (2016a).

Planck Collaboration:, Ade, P. A. R., Aghanim, N., et al., "Planck Intermediate Results. XIV. Dust Emission at Millimetre Wavelengths in the Galactic Plane", A&A **564**, A45 (2014).

Planck Collaboration, Ade, P. A. R., Aghanim, N., et al., "Planck 2013 Results. XXVIII. The Planck Catalogue of Compact Sources", A&A **571**, A28 (2014).

Planck Collaboration, Ade, P. A. R., Aghanim, N., et al., "Planck 2015 Results - XXVII. The Second Planck Catalogue of Sunyaev-Zeldovich Sources", A&A **594**, A27 (2016b).

Planck Collaboration, Ade, P. A. R., Aghanim, N., et al., "Planck 2015 Results - XIII. Cosmological Parameters", A&A **594**, A13 (2016c).

Planck Collaboration, Ade, P. A. R., Aghanim, N., et al., "Planck 2015 Results - XXVIII. The Planck Catalogue of Galactic Cold Clumps", A&A **594**, A28 (2016d).

Planck Collaboration, Aghanim, N., Akrami, Y., et al., "Planck 2018 Results - I. Overview and the Cosmological Legacy of Planck", A&A **641**, A1 (2020a).

Planck Collaboration, Aghanim, N., Akrami, Y., et al., "Planck 2018 Results - VI. Cosmological Parameters", A&A **641**, A6 (2020b).

Planck Collaboration, Aghanim, N., Akrami, Y., et al., "Planck 2018 Results - III. High Frequency Instrument Data Processing and Frequency Maps", A&A **641**, A3 (2020c).

Planck Collaboration, Aghanim, N., Arnaud, M., et al., "Planck 2015 Results - XXII. A Map of the Thermal Sunyaev-Zeldovich Effect", A&A **594**, A22 (2016e).

Planck Collaboration, Akrami, Y., Ashdown, M., et al., "Planck 2018 Results - IV. Diffuse Component Separation", A&A **641**, A4 (2020d).

Posada, C. M., Ade, P. A. R., Ahmed, Z., et al., "Fabrication of Detector Arrays for the SPT-3G Receiver", Journal of Low Temperature Physics **193**, 5, 703–711 (2018).

Pozar, D. M., *Microwave Engineering; 4th ed.* (Wiley, Hoboken, NJ, 2011).

Pratt, C. T., Qu, Z., & Bregman, J. N., "The Resolved Sunyaev–Zel'dovich Profiles of Nearby Galaxy Groups", ApJ **920**, 2, 104 (2021).

Press, W. H., & Schechter, P., "Formation of Galaxies and Clusters of Galaxies by Self-Similar Gravitational Condensation", ApJ **187**, 425–438 (1974).

Rabii, B., Winant, C. D., Collins, J. S., et al., "MAXIMA: A Balloon-Borne Cosmic Microwave Background Anisotropy Experiment", Review of Scientific Instruments **77**, 7, 071101 (2006).

Ramos, A., Varum, T., & Matos, J. N., "Compact Multilayer Yagi-Uda Based Antenna for IoT/5G Sensors", Sensors **18**, 9 (2018).

Rees, M. J., & Ostriker, J. P., "Cooling, Dynamics and Fragmentation of Massive Gas Clouds - Clues to the Masses and Radii of Galaxies and Clusters", MNRAS **179**, 541–559 (1977).

Reichardt, C. L., Stalder, B., Bleem, L. E., et al., "Galaxy Clusters Discovered Via the Sunyaev-Zel'dovich Effect in the First 720 Square Degrees of the South Pole Telescope Survey", ApJ **763**, 2, 127 (2013).

Ruan, J. J., McQuinn, M., & Anderson, S. F., "Detection of Quasar Feedback from the Thermal Sunyaev–Zel'dovich Effect in Planck", ApJ **802**, 135 (2015).

Sachs, R. K., & Wolfe, A. M., "Perturbations of a Cosmological Model and Angular Variations of the Microwave Background", ApJ **147**, 73 (1967).

Salatino, M., Austermann, J., Meinke, J., et al., "Current Status of the Ali CMB Polarization Telescope Focal Plane Camera", IEEE Transactions on Applied Superconductivity **31**, 5, 1–5 (2021).

Salatino, M., Austermann, J., Thompson, K. L., et al., "The design of the Ali CMB Polarization Telescope receiver", in "Millimeter, Submillimeter, and Far-Infrared Detectors and Instrumentation for Astronomy X", edited by J. Zmuidzinas and J.-R. Gao, vol. 11453, pp. 341 – 360, International Society for Optics and Photonics (SPIE, 2020).

Santini, P., Ferguson, H. C., Fontana, A., et al., "Stellar Masses from the CANDELS Survey: The GOODS-South and UDS Fields", ApJ **801**, 2, 97 (2015).

Santini, P., Maiolino, R., Magnelli, B., et al., "The Evolution of the Dust and Gas Content in Galaxies", A&A **562**, A30 (2014).

Savage, B. D., Kim, T. S., Wakker, B. P., et al., "The Properties of Low Redshift Intergalactic O VI Absorbers Determined from High S/N Observations of 14 QSOs with the Cosmic Origins Spectrograph", ApJS **212**, 1, 8 (2014).

Sazonov, S. Y., & Sunyaev, R. A., "Microwave Polarization in the Direction of Galaxy Clusters Induced by the CMB Quadrupole Anisotropy", MNRAS **310**, 3, 765–772 (1999).

Scannapieco, E., & Oh, S. P., "Quasar Feedback: The Missing Link in Structure Formation", ApJ **608**, 62–79 (2004).

Scannapieco, E., Thacker, R. J., & Couchman, H. M. P., "Measuring AGN Feedback with the Sunyaev-Zel'dovich Effect", ApJ **678**, 674–685 (2008).

Schaan, E., Ferraro, S., Amodeo, S., et al., "Atacama Cosmology Telescope: Combined Kinematic and Thermal Sunyaev-Zel'dovich Measurements From BOSS CMASS and LOWZ Halos", PhRvD **103**, 063513 (2021).

Schaffer, K. K., Crawford, T. M., Aird, K. A., et al., "The First Public Release of South Pole Telescope Data: Maps of a 95 deg^2 Field from 2008 Observations", ApJ **743**, 1, 90 (2011).

Schaye, J., Crain, R. A., Bower, R. G., et al., "The EAGLE project: Simulating the Evolution and Assembly of Galaxies and Their Environments", MNRAS **446**, 1, 521–554 (2015).

Schlafly, E. F., Meisner, A. M., & Green, G. M., "The unWISE Catalog: Two Billion Infrared Sources from Five Years of WISE Imaging", ApJS **240**, 2, 30 (2019).

Silk, J., "Cosmic Black-Body Radiation and Galaxy Formation", ApJ **151**, 459 (1968).

Silk, J., & Rees, M. J., "Quasars and Galaxy Formation", A&A **331**, L1–L4 (1998).

Simon, S. M., Austermann, J., Beall, J. A., et al., "The Design and Characterization of Wideband Spline-Profiled Feedhorns for Advanced ACTPol", in "Millimeter, Submillimeter, and Far-Infrared Detectors and Instrumentation for Astronomy VIII", edited by W. S. Holland and J. Zmuidzinas, vol. 9914, pp. 277 – 289, International Society for Optics and Photonics (SPIE, 2016).

Simon, S. M., Golec, J. E., Ali, A., et al., "Feedhorn Development and Scalability for Simons Observatory and Beyond", in "Millimeter, Submillimeter, and Far-Infrared Detectors and Instrumentation for Astronomy IX", edited by J. Zmuidzinas and J.-R. Gao, vol. 10708, pp. 787 – 798, International Society for Optics and Photonics (SPIE, 2018).

Sinclair, A. K., *In-flight Performance of the BLAST-TNG Balloon-borne Far-infrared Telescope and Development of a Reconfigurable Readout on the RFSoC Platform for Frequency Multiplexed Superconducting Detector Arrays*, Ph.D. thesis, Arizona State University (2021).

Sinclair, A. K., Stephenson, R. C., Hoh, J., Gordon, S. B., & Mauskopf, P. D., "On the Development of a Reconfigurable Readout for Superconducting Arrays", in "Society of Photo-Optical Instrumentation Engineers (SPIE) Conference Series", vol. 11453 of *Society of Photo-Optical Instrumentation Engineers (SPIE) Conference Series*, p. 114531T (2020).

Smoot, G., Bennett, C., Weber, R., et al., "COBE Differential Microwave Radiometers: Instrument Design and Implementation", ApJ **360**, 685 (1990).

Smoot, G. F., Gorenstein, M. V., & Muller, R. A., "Detection of Anisotropy in the Cosmic Blackbody Radiation", Phys. Rev. Lett. **39**, 898–901 (1977).

Smoot, G. F., & Lubin, P. M., "Southern Hemisphere Measurements of the Anisotropy in the Cosmic Microwave Background Radiation", ApJL **234**, L83–L86 (1979).

Sobrin, J. A., Anderson, A. J., Bender, A. N., et al., "The Design and Integrated Performance of SPT-3G", ApJS **258**, 2, 42 (2022).

Soergel, B., Flender, S., Story, K. T., et al., "Detection of the Kinematic Sunyaev-Zel'dovich Effect with DES Year 1 and SPT", MNRAS **461**, 3172–3193 (2016).

Soliman, A., Ade, P. A. R., Ahmed, Z., et al., "Design and performance of wideband corrugated walls for the BICEP Array detector modules at 30/40 GHz", in "Millimeter, Submillimeter, and Far-Infrared Detectors and Instrumentation for Astronomy IX", edited by J. Zmuidzinas and J.-R. Gao, vol. 10708, pp. 331 – 342, International Society for Optics and Photonics (SPIE, 2018).

Somerville, R. S., & Davé, R., "Physical Models of Galaxy Formation in a Cosmological Framework", ARA&A **53**, 51–113 (2015).

Spacek, A., Scannapieco, E., Cohen, S., Joshi, B., & Mauskopf, P., "Constraining AGN Feedback in Massive Ellipticals with South Pole Telescope Measurements of the Thermal Sunyaev-Zel'dovich Effect", ApJ **819**, 128 (2016).

Spacek, A., Scannapieco, E., Cohen, S., Joshi, B., & Mauskopf, P., "Searching for Fossil Evidence of AGN Feedback in WISE-selected Stripe-82 Galaxies by Measuring the Thermal Sunyaev–Zel'dovich Effect with the Atacama Cosmology Telescope", ApJ **834**, 102 (2017).

Springel, V., Pakmor, R., Pillepich, A., et al., "First Results From the IllustrisTNG Simulations: Matter and Galaxy Clustering", MNRAS **475**, 1, 676–698 (2018).

Strukov, I. A., & Skulachev, D. P., "Deep-Space Measurements of the Microwave Background Anisotropy - First Results of the Relikt Experiment", Pisma v Astronomicheskii Zhurnal **10**, 3–13 (1984).

Sunyaev, R. A., & Zeldovich, Y. B., "The Observations of Relic Radiation as a Test of the Nature of X-Ray Radiation from the Clusters of Galaxies", Comments on Astrophysics and Space Physics **4**, 173 (1972).

Sunyaev, R. A., & Zeldovich, Y. B., "The Velocity of Clusters of Galaxies Relative to the Microwave Background - The Possibility of Its Measurement.", MNRAS **190**, 413–420 (1980).

Suzuki, A., *Multichroic Bolometric Detector Architecture for Cosmic Microwave Background Polarimetry Experiments*, Ph.D. thesis, University of California, Berkeley (2013).

Suzuki, A., Arnold, K., Edwards, J., et al., "Multi-Chroic Dual-Polarization Bolometric Detectors for Studies of the Cosmic Microwave Background", Journal of Low Temperature Physics **176**, 5, 650–656 (2014).

Thacker, R. J., Scannapieco, E., & Couchman, H. M. P., "Quasars: What Turns Them Off?", ApJ **653**, 86–100 (2006).

The CMB-HD Collaboration, :, Aiola, S., et al., "Snowmass2021 CMB-HD White Paper", arXiv e-prints p. arXiv:2203.05728 (2022).

Thornton, R. J., Ade, P. A. R., Aiola, S., et al., "The Atacama Cosmology Telescope: The Polarization-Sensitive ACTPol Instrument", ApJS **227**, 2, 21 (2016).

Treu, T., Ellis, R. S., Liao, T. X., & van Dokkum, P. G., "Keck Spectroscopy of Distant GOODS Spheroidal Galaxies: Downsizing in a Hierarchical Universe", ApJL **622**, L5–L8 (2005).

Tumlinson, J., Peeples, M. S., & Werk, J. K., "The Circumgalactic Medium", ARA&A **55**, 1, 389–432 (2017).

Uda, S., "On the Wireless Beam Of Short Electric Waves. (I)", The Journal of the Institute of Electrical Engineers of Japan **46**, 452, 273–282 (1926).

van Dokkum, P. G., Whitaker, K. E., Brammer, G., et al., "The Growth of Massive Galaxies Since z = 2", ApJ **709**, 2, 1018–1041 (2010).

Vavagiakis, E. M., Gallardo, P. A., Calafut, V., et al., "The Atacama Cosmology Telescope: Probing the Baryon Content of SDSS DR15 Galaxies with the Thermal and Kinematic Sunyaev-Zel'dovich Effects", PhRvD **104**, 4, 043503 (2021).

Veilleux, S., Meléndez, M., Sturm, E., et al., "Fast Molecular Outflows in Luminous Galaxy Mergers: Evidence for Quasar Feedback from Herschel", ApJ **776**, 27 (2013).

Voges, W., Aschenbach, B., Boller, T., et al., "The ROSAT All-Sky Survey Bright Source Catalogue", A&A **349**, 389–405 (1999).

Walter, F., Carilli, C., Neeleman, M., et al., "The Evolution of the Baryons Associated with Galaxies Averaged over Cosmic Time and Space", ApJ **902**, 2, 111 (2020).

Wampler, E. J., Chugai, N. N., & Petitjean, P., "The Absorption Spectrum of Nuclear Gas in Q0059-2735", ApJ **443**, 586–605 (1995).

Wang, L., Farrah, D., Oliver, S. J., et al., "Connecting Stellar Mass and Star-Formation Rate to Dark Matter Halo Mass out to z $\sim$ 2", MNRAS **431**, 1, 648–661 (2013).

Werk, J. K., Prochaska, J. X., Cantalupo, S., et al., "The COS-Halos Survey: Origins of the Highly Ionized Circumgalactic Medium of Star-Forming Galaxies", ApJ **833**, 1, 54 (2016).

Werk, J. K., Prochaska, J. X., Tumlinson, J., et al., "The COS-Halos Survey: Physical Conditions and Baryonic Mass in the Low-redshift Circumgalactic Medium", ApJ **792**, 1, 8 (2014).

Werner, N., McNamara, B. R., Churazov, E., & Scannapieco, E., "Hot Atmospheres, Cold Gas, AGN Feedback and the Evolution of Early Type Galaxies: A Topical Perspective", SSRv **215**, 5 (2019).

Westbrook, B., Ade, P. A. R., Aguilar, M., et al., "The POLARBEAR-2 and Simons Array Focal Plane Fabrication Status", Journal of Low Temperature Physics **193**, 5-6 (2018).

Westbrook, B., Raum, C., Beckman, S., et al., "Detector Fabrication Development for the LiteBIRD Satellite Mission", (2021).

White, S. D. M., & Frenk, C. S., "Galaxy Formation Through Hierarchical Clustering", ApJ **379**, 52–79 (1991).

White, S. D. M., & Rees, M. J., "Core Condensation in Heavy Halos: A Two-Stage Theory for Galaxy Formation and Clustering", MNRAS **183**, 341–358 (1978).

Wilson, G. W., Abi-Saad, S., Ade, P., et al., "The TolTEC Camera: An Overview of the Instrument and In-Lab Testing Results", in "Society of Photo-Optical Instrumentation Engineers (SPIE) Conference Series", vol. 11453 of *Proc. SPIE* , p. 1145302 (2020).

Wootten, A., & Thompson, A. R., "The Atacama Large Millimeter/Submillimeter Array", Proceedings of the IEEE **97**, 8, 1463–1471 (2009).

Wright, E. L., Eisenhardt, P. R. M., Mainzer, A. K., et al., "The Wide-field Infrared Survey Explorer (WISE): Mission Description and Initial On-orbit Performance", AJ **140**, 6, 1868–1881 (2010).

Xu, Z., Bhandarkar, T., Coppi, G., et al., "The Simons Observatory: The Large Aperture Telescope Receiver (LATR) Integration and Validation Results", in "Millimeter, Submillimeter, and Far-Infrared Detectors and Instrumentation for Astronomy X", edited by J. Zmuidzinas and J.-R. Gao, vol. 11453, pp. 207 – 226, International Society for Optics and Photonics (SPIE, 2020).

Yamamura, I., Makiuti, S., Ikeda, N., et al., "VizieR Online Data Catalog: AKARI/FIS All-Sky Survey Point Source Catalogues (ISAS/JAXA, 2010)", yCat **2**, 298 (2010).

Zeldovich, Y. B., & Sunyaev, R. A., "The Interaction of Matter and Radiation in a Hot-Model Universe", Ap&SS **4**, 3, 301–316 (1969).

Zmuidzinas, J., "Superconducting Microresonators: Physics and Applications", Annual Review of Condensed Matter Physics **3**, 1, 169–214 (2012).

APPENDIX A

PREVIOUSLY PUBLISHED WORK

All co-authors have granted permission to allow the inclusion of these previously published works in their present form for this dissertation.

The results shown in Chapters 2 and 3 detail research previously published or currently submitted to a reputable journal, respectively. Slight modifications were made in each chapter to incorporate expanded details and comply with format guidelines. Additionally, listed below are the titles and abstracts as they appear (or were initially submitted) for publication.

A.1 The Thermal Sunyaev-Zel'dovich Effect from Massive, Quiescent $0.5 \leq z \leq 1.5$ Galaxies

Abstract, Meinke et al. (2021):

We use combined South Pole Telescope (SPT)+Planck temperature maps to analyze the circumgalactic medium (CGM) encompassing 138,235 massive, quiescent $0.5 \leq z \leq 1.5$ galaxies selected from data from the Dark Energy Survey (DES) and Wide-Field Infrared Survey Explorer (WISE). Images centered on these galaxies were cut from the 1.85 arcmin resolution maps with frequency bands at 95, 150, and 220 GHz. The images were stacked, filtered, and fit with a gray-body dust model to isolate the thermal Sunyaev-Zel'dovich (tSZ) signal, which is proportional to the total energy contained in the CGM of the galaxies. We separate these $M_\star = 10^{10.9} M_\odot$ - $10^{12} M_\odot$ galaxies into 0.1 dex stellar mass bins, detecting tSZ per bin up to 5.6σ and a total signal-to-noise ratio of 10.1σ. We also detect dust with an overall signal-to-noise ratio of 9.8σ, which overwhelms the tSZ at 150GHz more than in other lower-redshift studies. We correct for the 0.16 dex uncertainty in the stellar mass measurements by parameter fitting for an unconvolved power-law energy-mass relation, $E_{\rm therm} = E_{\rm therm,peak} \left(M_\star / M_{\star,\rm peak}\right)^\alpha$, with the peak stellar mass distribution of our selected galaxies defined as $M_{\star,\rm peak} = 2.3 \times 10^{11} M_\odot$. This yields an $E_{\rm therm,peak} = 5.98^{+1.02}_{-1.00} \times 10^{60}$ ergs and $\alpha = 3.77^{+0.60}_{-0.74}$. These are consistent with $z \approx 0$ observations and within the limits of moderate models of active galactic nuclei (AGN) feedback. We also compute the radial profile of our full sample, which is similar to that recently measured at lower-redshift by Schaan et al. (2021).

A.2 Evidence of Extended Dust and Feedback around $z \approx 1$ Quiescent Galaxies via Millimeter Observations

Abstract, Meinke et al. 2023 (Submitted and under revision with The Astrophysical Journal):

We use public data from the South Pole Telescope (SPT) and Atacama Cosmology Telescope (ACT) to measure radial profiles of the thermal Sunyaev-Zel'dovich (tSZ) effect and dust emission around massive quiescent galaxies at $z \approx 1$. Using survey data from the Dark Energy Survey (DES) and Wide-Field infrared Survey Explorer (WISE), we selected $387,627$ quiescent galaxies within the ACT field, with a mean stellar $\log_{10}(M_\star/\mathrm{M}_\odot)$ of 11.40. A subset of $94,452$ galaxies, with a mean stellar $\log_{10}(M_\star/\mathrm{M}_\odot)$ of 11.36, are also covered by SPT. In $0.5'$ bins around these galaxies, we detect the tSZ profile at levels up to 11.6σ, and the dust profile up to 21.5σ. Both profiles are extended, and the dust profile slope at large radii is consistent with galaxy clustering. We analyze the thermal energy and dust mass versus stellar mass via integration within $R = 2.0'$ circular apertures and fit them with a forward-modeled power-law to correct for our photometric stellar mass uncertainty. For galaxies at the mean log stellar mass of each respective catalog, we extract thermal energies from the tSZ of $E_{\mathrm{pk}} = 6.66^{+1.60}_{-1.46} \times 10^{60}$ erg and $8.00^{+0.51}_{-0.50} \times 10^{60}$ erg, most consistent with moderate to high levels of active galactic nuclei feedback acting upon the circumgalactic medium. Dust masses at the mean log stellar mass are $M_{\mathrm{d,pk}} = 6.18^{+0.66}_{-0.66} \times 10^8$ $\mathrm{M}_\odot$ and $6.70^{+0.56}_{-0.55} \times 10^8$ $\mathrm{M}_\odot$, and we find a greater than linear dust-to-stellar mass relation, which indicates that the more massive galaxies in our study retain more dust. Our work highlights current capabilities of stacking millimeter data around individual galaxies and potential for future use.